

INFORMATION TO USERS

This manuscript has been reproduced from the microfilm master. UMI films the text directly from the original or copy submitted. Thus, some thesis and dissertation copies are in typewriter face, while others may be from any type of computer printer.

The quality of this reproduction is dependent upon the quality of the copy submitted. Broken or indistinct print, colored or poor quality illustrations and photographs, print bleedthrough, substandard margins, and improper alignment can adversely affect reproduction.

In the unlikely event that the author did not send UMI a complete manuscript and there are missing pages, these will be noted. Also, if unauthorized copyright material had to be removed, a note will indicate the deletion.

Oversize materials (e.g., maps, drawings, charts) are reproduced by sectioning the original, beginning at the upper left-hand corner and continuing from left to right in equal sections with small overlaps. Each original is also photographed in one exposure and is included in reduced form at the back of the book.

Photographs included in the original manuscript have been reproduced xerographically in this copy. Higher quality 6" x 9" black and white photographic prints are available for any photographs or illustrations appearing in this copy for an additional charge. Contact UMI directly to order.

UMI

A Bell & Howell Information Company
300 North Zeeb Road, Ann Arbor MI 48106-1346 USA
313/761-4700 800/521-0600

University of Alberta

**Optimization of Metal-Semiconductor-Metal
Photodetectors and Advanced Photodetector Structures**

By

Ray George DeCorby



A thesis submitted to the Faculty of Graduate Studies and Research in partial fulfillment of the requirements for the degree of **Doctor of Philosophy**

Department of Electrical and Computer Engineering

Edmonton, Alberta

Spring 1998



National Library
of Canada

Acquisitions and
Bibliographic Services

395 Wellington Street
Ottawa ON K1A 0N4
Canada

Bibliothèque nationale
du Canada

Acquisitions et
services bibliographiques

395, rue Wellington
Ottawa ON K1A 0N4
Canada

Your file Votre référence

Our file Notre référence

The author has granted a non-exclusive licence allowing the National Library of Canada to reproduce, loan, distribute or sell copies of this thesis in microform, paper or electronic formats.

The author retains ownership of the copyright in this thesis. Neither the thesis nor substantial extracts from it may be printed or otherwise reproduced without the author's permission.

L'auteur a accordé une licence non exclusive permettant à la Bibliothèque nationale du Canada de reproduire, prêter, distribuer ou vendre des copies de cette thèse sous la forme de microfiche/film, de reproduction sur papier ou sur format électronique.


L'auteur conserve la propriété du droit d'auteur qui protège cette thèse. Ni la thèse ni des extraits substantiels de celle-ci ne doivent être imprimés ou autrement reproduits sans son autorisation.

0-612-29029-8

University of Alberta

Faculty of Graduate Studies and Research

The undersigned certify that they have read, and recommend to the Faculty of Graduate Studies and Research for acceptance, a thesis entitled **Optimization of Metal-Semiconductor-Metal Photodetectors and Advanced Photodetector Structures** submitted by **Ray George DeCorby** in partial fulfillment of the requirements for the degree of **Doctor of Philosophy**.



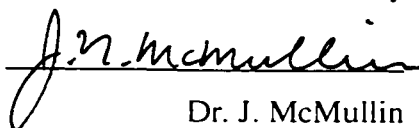
Dr. R.I. MacDonald, Supervisor



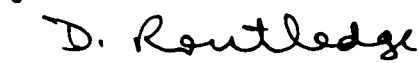
Dr. S. Dew



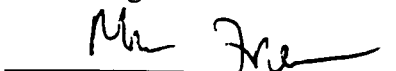
Dr. I. Filanovsky



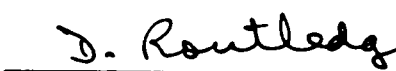
Dr. J. McMullin



Dr. D. Routledge, Committee Chair



Dr. M.R. Freeman



Dr. K. McGreer, External

Date: 13/4/98

To my parents, Henry and Finna, and the importance of caring deeply

Abstract

This thesis addresses some of the inherent disadvantages of MSM photodetectors, in the interest of obtaining an optimized technology on GaAs and InP. The planar structure of the MSM detector, coupled with the sub-optimal electronic surface characteristics of III-V semiconductors, has resulted in a lack of performance reliability and predictability. Deleterious surface effects were reviewed, and techniques for minimizing these effects were investigated experimentally. For MSM detectors operating at 1550 nm wavelength, two material systems were compared. An InGaAsP/InP device with a pseudomorphic InGaP cap layer produced state-of-the-art performance. A 3 dB bandwidth of 12 GHz was determined in the frequency domain, for a finger spacing of 2 μm , and an active region area of $(100 \mu\text{m})^2$. On InAlGaAs/InP, the passivating effects of a suitable surface etch, followed by deposition of silicon nitride, are presented.

For operation at 800 nm wavelength, an optimized AlGaAs/GaAs epitaxial structure was investigated, based on a theoretical treatment of hole pileup at the cap layer heterojunction. Subsequently, 18 GHz bandwidth at 2 to 3 V bias was demonstrated experimentally for an MSM detector with 1 μm finger spacing, and an active region area of $(50 \mu\text{m})^2$.

Another disadvantage traditionally associated with MSM detectors is low responsivity, due to shadowing by opaque metal fingers. The second part of this thesis is dedicated to resonant-cavity techniques. Resonant-cavity epitaxial structures were designed in several material systems, for operation at 800, 1300, and 1550 nm wavelength. In particular, a novel device was fabricated in the

InGaP/GaAs material system, employing a Burstein-Moss shifted mirror. Heavy n-type doping of GaAs shifts its band edge to approximately 810 nm wavelength, extending its transparency into a range where the most ubiquitous sources operate.

Finally, significant progress towards the realization of broadband photodetector arrays was made. Transmission-line concepts were used to design impedance-matched MSM photodetector arrays (IMMPA); the arrays are configured as loaded transmission lines, with characteristic impedance matched to the external load. A uniform 12 GHz bandwidth was obtained, for an array of 8 MSM photodetectors on GaAs. A full theoretical treatment is provided, and several diverse experiments were conducted to verify the theory.

Acknowledgments

The author wishes to first thank Dr. Ian MacDonald, whose ideas provided the impetus for much of this thesis. I appreciate having been allowed to pursue my own interests within the framework of a vibrant and successful research program, under the supervision of Dr. MacDonald.

I am indebted to David Clegg, for valuable and practical advice relating to electrical engineering research, and for his expertise in the laboratory. I am grateful to Julian Noad and Francois Gouin of the Communications Research Centre, for their patience and willingness to collaborate. I also thank Tom Pinnington, Mario Beaudoin, and Tom Tiedje at UBC department of physics, and Jim Broughton of AMC, for assisting in device fabrication.

Many of my fellow students at TRILabs made direct and indirect contributions to this research. I especially thank Rohit Sharma, Alan Hnatiw, Dave Boertjes, Mike Sieben, Craig Unick, Rajkumar Nagarajan, and Sheldon Walklin. I am grateful to all of the past and present staff at TRILabs, including Dino Corazza, Dr. Jim McMullin, and Dr. Barrie Keyworth.

I owe the greatest debt of gratitude to my wife, Maureen Douglas, for her constant love and support.

Finally, I would like to acknowledge the financial support of TRILabs, NSERC, and the University of Alberta, which facilitated this research. TRILabs provided an excellent environment in which to conduct graduate work, and is a unique blend of the academic and the professional.

Table of Contents

1. APPLICATIONS FOR METAL-SEMICONDUCTOR-METAL PHOTODETECTORS.....	1
1.1. Introduction – Photodetectors.....	1
1.1.1. Photocurrent Gain – Deleterious Effects.....	2
1.2. Metal-Semiconductor-Metal Photodetectors.....	4
1.3. Optoelectronic Matrix Switches.....	7
1.3.1. Optoelectronic Space-Division Switching.....	7
1.3.2. Optoelectronic Signal Processing.....	12
1.4. Optoelectronic Integrated Circuits.....	13
1.5. Comparison of MSM and p-i-n Photodetectors.....	16
1.6. Fundamental Properties of MSM Photodetectors.....	19
1.6.1. Sources of Capacitance in MSM Photodetectors.....	19
1.6.2. Transit-Time-Limited Speed of MSM Photodetectors.....	21
1.7. High-Frequency Test System.....	24
1.8. Thesis Organization.....	26
2. TECHNOLOGICAL CONSIDERATIONS FOR MSM PHOTODETECTORS	28
2.1. Introduction- Materials for MSM Photodetectors.....	28
2.2. Technological Challenges for MSM Photodetectors.....	31
2.2.1. Deleterious Surface and Interface Effects.....	31
2.2.2. Heterojunctions.....	33
2.3. Double-Heterostructure MSM Photodetectors.....	36
2.3.1. Surface (Cap) Layer.....	36
2.3.2. Absorption Region.....	38
2.3.3. Substrate Isolation Layer.....	39
2.3.4. Graded Layers.....	39
2.3.5. Dark Current-Voltage Characteristics.....	41
2.4. Alternative Epitaxial Materials for InP-based MSM Detectors.....	45
2.4.1. InAlAs/InGaAs Material System.....	45
2.4.2. InP/InGaAs Material System.....	47
2.4.3. $In_xGa_{1-x}P/InP/InGaAs$ Material System.....	48

2.5. Alternative Epitaxial Materials For GaAs-based MSM detectors.....	49
2.5.1. AlGaAs/GaAs Material System	50
2.5.2. In _{0.49} Ga _{0.51} P/GaAs Material System.....	52
2.6. III-V Semiconductor Interfaces	54
2.6.1. Introduction.....	54
2.6.2. Semiconductor Surfaces - General.....	55
2.6.3. Metal-Semiconductor Interfaces – The Schottky Barrier.....	57
2.6.4. Bias-Dependent Barrier-Lowering Mechanisms	63
2.6.5. Dielectric Layers on III-V Semiconductors.....	65
2.6.6. Passivation of III-V Semiconductors.....	67
2.6.6.1. Passivation of Arsenides.....	68
2.7. Hole Pile-Up in Double-Heterostructure MSM Photodetectors.....	70
2.7.1. Bias Requirements for Saturation Bandwidth, in the Absence of Carrier Pileup	71
2.7.2. Hole Transport.....	72
2.8. Design of an MSM Mask Set and Development of a Fabrication Process ..	75
2.9. Summary of Technology Issues	78
3. EXPERIMENTAL RESULTS FOR DOUBLE-HETEROSTRUCTURE MSM PHOTODETECTORS	80
3.1. Introduction	80
3.2. InGaP/InP/InGaAs/InP Material System – Experimental Results	81
3.3. InAlAs/InGaAs/InP Material System – Experimental Results	88
3.3.1. Dark-Current Study of InP-based MSM Photodetectors	90
3.3.2. Reduction of Low-Frequency Gain by Silicon Nitride Passivation	96
3.4. AlGaAs/GaAs Material System – Experimental Results	102
3.5. Summary and Conclusions	107
4. RESONANT-CAVITY-ENHANCED MSM PHOTODETECTORS.....	109
4.1. Introduction – Improving the Responsivity of MSM photodetectors	109
4.2. Semiconductor Quarter-Wave-Stacks as Distributed Bragg Reflectors.....	112
4.3. Resonant-Cavity-Enhancement of Absorption - Theory	116
4.3.1. Analytical Formulae for Resonant-Cavity Photodetectors.....	119

4.4. Top-Illuminated Resonant-Cavity Enhanced MSM photodetectors - Design Criterion.....	121
4.5. Recommended Structures.....	125
4.5.1. <i>GaAs/AlGaAs Resonant-Cavity Detector Operating Near 800 nm</i>	126
4.5.1.1. Epitaxial Design.....	126
4.5.1.2. Fabrication and Experimental Results	131
4.5.2. <i>GaAs/InGaP Resonant-Cavity Detector Operating Near 800 nm</i>	134
4.5.2.1. Introduction	134
4.5.2.2. Doping-Induced Changes in Optical Constants	136
4.5.2.3. Epitaxial Design.....	141
4.5.2.4. Fabrication.....	144
4.5.2.5. Experimental Results and Discussion.....	145
4.5.3. <i>InP/InGaAsP Resonant-Cavity Detector Operating Near 1300 nm</i>	151
4.5.4. <i>InP/InAlGaAs Resonant-Cavity Detector Operating Near 1300 nm</i> ...	154
4.5.5. <i>InP/InGaAs Resonant-Cavity Detector Operating Near 1550 nm</i>	157
4.6. Summary and Conclusions	159
5. MSM PHOTODETECTOR ARRAYS	162
5.1. Introduction	162
5.2. Photodetector Arrays - General	163
5.3. Experimental Results for Single-Output Arrays.....	165
5.3.1. <i>16 detector arrays – ('squid' arrays)</i>	167
5.3.2. <i>8 detector arrays – type 1 ('goalpost' arrays)</i>	172
5.3.3. <i>8 detector arrays –type 2 ('rake' arrays)</i>	174
5.3.4. <i>Summary of results for single-output arrays</i>	176
5.4. Impedance-Matched MSM Photodetector Arrays (IMMPA).....	177
5.4.1. <i>Introduction</i>	177
5.4.2. <i>Lumped-element treatment of a photodetector array</i>	179
5.4.3. <i>Semi-distributed treatment of a photodetector array</i>	181
5.4.3.1. Periodic structures	181
5.4.3.2. Termination of periodic structures.....	184
5.4.4. <i>Properties of microstrip transmission lines on III-V semiconductors</i> .	186
5.5. Experimental Results –Impedance-Matched Detector Arrays	189

5.5.1. <i>Selecting an appropriate array</i>	189
5.5.2. <i>Experimental results – 16 detector array</i>	195
5.5.3. <i>Experimental results – 8-detector arrays</i>	198
5.6. Limits on Array Length – Microwave Loss	204
5.7. Comparison of Impedance-Matched and Single-Output Arrays	207
5.8. Conclusions and Summary	209
6. CONCLUSIONS AND RECOMMENDATIONS	211
6.1. Overview of Significant Results.....	211
6.2. Suggestions for Future Work.....	213
7. REFERENCES	215
 APPENDIX A: MSM PHOTODETECTORS FOR OPTOELECTRONIC SIGNAL	
PROCESSING – BIAS CONTROL OF RESPONSIVITY	230
A.1. Introduction	230
A.2. Electric Fields Near Interdigitated Electrodes.....	232
A.2.1. <i>Device Operating Range – Bandwidth Saturation</i>	235
A.3. Semiconductor Quantum Wells.....	236
A.3.1. <i>Electronic States in Semiconductor Quantum Wells</i>	236
A.3.2. <i>Absorption in Quantum Wells</i>	240
A.3.3. <i>Electro-Optic Effects in Semiconductor Quantum Wells</i>	241
A.3.3.1. Electro-Optic Effects Due to Perpendicular Fields	242
A.3.3.2. Electro-Optic Effects due to Parallel Fields.....	245
A.4. Semi-Empirical Simulations.....	248
A.4.1. <i>Model for Absorption in Quantum Wells</i>	249
A.4.2. <i>Predicted Results for a Rear-Illuminated MSM Photodetector</i>	252
A.4.3. <i>Suggestions to Improve the Model</i>	254
A.5. Summary and Conclusions	254
A.6. Appendix A References.....	255
 APPENDIX B: MATLAB FILE FOR CALCULATING OPTICAL SPECTRA OF A MULTI-LAYER SEMICONDUCTOR (IN GAP/GAAS)	
	258

List of Figures

- Figure 1.1.** A useful classification system for photodetectors is shown. While vacuum tube devices are still used, for example in ultra-sensitive photon-counting applications, solid-state devices dominate the overall market. MSM photodetectors fall in the category of solid-state devices, without gain. These are the devices used for the highest speed applications..... 1
- Figure 1.2.** A one-dimensional metal-semiconductor-metal structure. A semiconductor material is sandwiched by back-to-back Schottky electrodes. The structure can exhibit interesting current-voltage characteristics, due to its bipolar nature. Electrons are injected over the Schottky barrier at the cathode, holes at the anode. Depending on the relative heights of electron and hole barriers, the current is dominated by one or the other carrier. 5
- Figure 1.3.** Schematic top and cross-sectional views of an interdigitated photodetector are shown. The important geometrical parameters of the electrode structure are finger spacing, finger width, and side length. The operation of the device is illustrated in the cross-sectional view: light generates carriers between the fingers, and the holes and electrons are swept along two-dimensional field lines, to the cathode and anode respectively. 6
- Figure 1.4.** The optoelectronic switching technique is illustrated schematically. A 2x2 space-switch is shown, but the matrix size is generally m rows by n columns. The input channels are optical signals, which can derive from local or remote laser transmitters. The output channels are electrical signals, and typically travel on the common bus of a photodetector array (see Chapter 5). The accepted symbol for an MSM photodetector (back-to-back rectifying junctions) is shown at the crosspoints of the switch. Bias is used to control the responsivity of the photodetectors, thereby enabling a crosspoint function. Broadband electrical signals must be accommodated by the photodetector array, as discussed in Chapter 5. 9
- Figure 1.5.** A schematic illustration of an optoelectronic signal-processing element is shown. A transversal filter (or other function) can be realized by using optical delay lines and weighted taps, followed by summation of the delayed and weighted components of the input signal. The broadband signal summation is provided by a photodetector array (see Chapter 5). More advanced processing functions can be realized using an entire optoelectronic matrix [20]. The technique is predicated on photodetectors that have variable responsivity (controlled by bias), but sufficient bandwidth over the required range of responsivity..... 13
- Figure 1.6.** A schematic illustration of an OEIC is shown, incorporating a high electron mobility transistor (HEMT) and an MSM photodetector. The HEMT layers are very thin (typically 100 to 200 nm), so the structure is very nearly planar. The entire structure can be formed in a single epitaxial growth, followed by selective etching for access to the MSM detector layers. Inter-device isolation is provided by the wide band-gap, MSM cap layer. After [16]. 15
- Figure 1.7.** A typical p-i-n photodetector is shown schematically, in cross-section. The fabrication process starts with growth of at least five epitaxial layers, with both heavily doped n- and p-type layers required. Two separate ohmic metal layers are deposited, as the technology for ohmic contacts is unique for p- and n-type layers. A third metal layer is required, for circuit interconnects. The structure is vertical, so contacts must be made on more than one level. This complicates the definition of fine features..... 17
- Figure 1.8.** A typical MSM photodetector is shown, in cutout view. The structure is planar (lateral), with both contacts lying on the surface. Also, the device is symmetrical, and can be biased in either direction. As shown, the active region is isolated by formation of a mesa (see Chapter 2). The absence of doped layers greatly simplifies the epitaxial growth. 18

- Figure 1.9.** Sources of excess charge polarization, and thus excess capacitance, are shown. Two MSM detector fingers are shown in cross-section. Free charge carriers can increase capacitance by interacting with each other (P1), or with dopant atoms (P2). Stored charge at an interface can interact with free charge or with dopant atoms (P3). P1 and P2 increase with illumination intensity, and decrease with bias. P3 may be relatively insensitive to bias or illumination conditions. 20
- Figure 1.10.** The saturation bandwidth of an MSM photodetector with 1 μm finger spacing and width is plotted, versus the thickness of the absorption region. The plot illustrates the benefit of reducing this thickness: for a 0.5 μm absorber, the bandwidth is enhanced by more than a factor of 2, compared to an infinite absorber. The data were adapted from [42]. 22
- Figure 1.11.** A frequency response derived from the approximate analytical expression of equation (1.2) is shown. The hole and electron transit-times were assumed to be 15 ps and 30 ps, respectively. These values should be reasonably representative of an MSM photodetector with 1 μm finger spacing, and biased such that all carriers are traveling at saturation velocity. Note the good agreement with the experimental result for a similar device in Figure 3.21. 23
- Figure 1.12.** Schematic block diagram of the high-frequency test system is shown. A temperature-stabilized, fiber-pigtailed semiconductor laser drives a lithium niobate electro-optic modulator. The RF power for the modulator is provided by an amplified signal from one port of the network analyzer. The other port of the network analyzer extracts the RF signal from the photodetector under test. The system is calibrated with a Schottky photodetector (New Focus, model number 1434), with a -3 dB bandwidth in excess of 25 GHz. 25
- Figure 2.1.** Diagram of band-gap energy vs. lattice-constant, for the column IV, III-V, and II-VI semiconductors. The left vertical axis indicates the minimum band-gap energy, and the right vertical axis indicates the corresponding wavelength (photon energy) of light. The horizontal axis shows the lattice-constant of the semiconductor crystal. Solid lines indicate direct band-gap alloys, dotted lines indicate indirect band-gaps. Also shown is the strained-layer epitaxial (SLE) and lattice-mismatched (bulk) growth of germanium on silicon. The Figure is from reference [49]. 29
- Figure 2.2.** A cross-sectional view of a generic double-heterostructure MSM detector is shown (see section 2.3). While the lateral (planar) structure of the device is relatively simple to fabricate, and integrate with other devices, it also implies that surface effects can dominate device performance. 31
- Figure 2.3.** Two fingers of an interdigitated MSM detector are shown, in cross-section. A bias is applied between the adjacent fingers, and the field lines tend to cluster at their peripheries, near the surface. Unfortunately, the surface is often the site of unwanted charge storage in III-V semiconductors. As an example, positive charge storage is shown at the surface. This can produce a high field at the periphery of the cathode (-V) fingers. The Schottky barrier is reduced by the high field, resulting in excessive dark current and low-frequency gain. 33
- Figure 2.4.** An idealized band diagram at a heterojunction between two semiconductors. The semiconductors have band-gaps given by E_{G1} and E_{G2} , respectively. Their corresponding electron affinities are χ_1 and χ_2 , respectively. Alignment of the Fermi level in equilibrium implies that band offsets, ΔE_C and ΔE_V , are formed. 34
- Figure 2.5.** Representative band diagram at the surface of an MSM photodetector, with a barrier-enhancement layer. Φ_n and Φ_p are the electron and hole barriers, respectively, for the contact. Interface states can dominate the behavior of Schottky barriers and heterojunctions. 35

Figure 2.6. A Generic double-heterostructure MSM detector is shown. The absorption region has a band-gap of E_{gA} . In general, it should be isolated from both the free surface and the substrate, by wider band-gap layers. Graded layers may be included, to minimize free carrier pileup and trapping at the heterojunctions.....	36
Figure 2.7. One-dimensional representation of carrier transport is shown. The wider band-gap cap layer may present a barrier to the efficient collection of photogenerated carriers. This can cause problematic low-frequency gain, and generally slow the speed of the device. It may also affect responsivity, as some carriers will be lost to recombination. Carrier pileup is discussed in detail in Section 2.7.....	37
Figure 2.8. A band diagram is shown, for a barrier-enhanced MSM detector, with a superlattice grade designed to minimize free carrier pileup. The quantum wells are potential locations for carrier confinement.....	40
Figure 2.9. Elimination of carrier pileup at the cap layer, by addition of a compositional grade, is shown. The example considers hole collection at the cathode fingers of the MSM.....	40
Figure 2.10. A conduction band notch is shown, for the InAlAs/InGaAs heterojunction. A notch of this type, at the bottom of the absorption region, can cause delayed collection of photogenerated carriers, and lower responsivity.....	41
Figure 2.11. Limiting cases are shown, for the dark I-V characteristic of an MSM structure. Φ_n and Φ_p are the electron and hole barriers, respectively, of the Schottky contacts. V_{rt} and V_{fb} are the reach-through and flat-band voltages, respectively, discussed in the text.....	42
Figure 2.12. The one-dimensional band diagram for an InAlAs/InGaAs MSM detector is shown. The band-gap offset is apportioned primarily to the conduction band. The Fermi level of a typical Schottky contact lies near mid-gap, which is ideal for minimizing dark current in an MSM photodetector.....	46
Figure 2.13. The one-dimensional band diagram for an InP/InGaAs MSM detector is shown. The band offset is apportioned primarily to the valence band. The electron barrier of a typical Schottky contact is relatively low, much lower than the corresponding hole barrier.....	48
Figure 2.14. The one-dimensional band diagram for an InGaP/InP/InGaAs MSM detector is shown. The inclusion of the strained InGaP layer results in a higher electron barrier at the Schottky contact, compared to an InP surface layer alone.....	49
Figure 2.15. Simplified one-dimensional band diagram for an AlGaAs/GaAs MSM detector. The hole barrier at the Schottky junctions is much lower than the electron barrier, so hole transport is expected to dominate dark current.....	52
Figure 2.16. A simplified one-dimensional band diagram, for an InGaP/GaAs MSM detector, is shown. InGaP exhibits high Schottky barriers, and should produce a device with very low dark current. The high valence band offset may hinder efficient collection of photogenerated holes, as discussed in Section 2.7.....	53
Figure 2.17. A band diagram is shown, at the surface of a semiconductor. Surface states are represented as two-dimensional bands, which may reside within or outside the band-gap of the semiconductor. Φ_s is the work function of the semiconductor. The work function includes a surface contribution, due to dipole-induced band bending at the surface. Φ_0 is the charge-neutrality level, a theoretical abstraction that allows the net charge at the surface to be inferred from the occupancy of the surface state bands. In the example shown, the surface contains a	

net-negative charge, so the bands bend upwards towards the surface. The excess electrons at the surface derive from the donor atoms in the n-type semiconductor shown..... 56

Figure 2.18. A band diagram is shown, for an interface between an n-type semiconductor and a metal, where the metal has a larger work function. Charge transfer establishes equilibrium (as indicated by the flat Fermi level), between the metal, the semiconductor surface states, and the semiconductor bulk. An idealized interfacial layer is assumed: it is insulating, thin enough that electrons can tunnel through unobstructed, but thick enough to withstand the applied field without breaking down. V_i is the voltage drop across the interfacial layer. 58

Figure 2.19. The variation of Schottky barrier height with metal work function (Φ_m) is illustrated schematically, for various limiting cases. D_s is the energy-density of surface-states, assumed for simplicity to be constant over the entire band-gap. Φ_{nf} is the flat-band barrier height, as defined in [68]. The curves intersect for a metal work function that is coincident with the charge neutrality level of the semiconductor surface states. 61

Figure 2.20. A typical relationship between Schottky barrier height and metal work function is illustrated schematically. The semiconductor surface states are distributed as sub-bands of acceptors and donors, as in Figure 2.17. Depending on the work function of the deposited metal, the surface Fermi level is pinned or not pinned. 62

Figure 2.21. A Maxwellian hole distribution is shown schematically, incident on the valence band offset near the cathode. The holes are heated by the applied field, and have a characteristic mean energy. By comparing this mean energy to the valence band offset, as a function of bias voltage, an estimate of hole pileup can be obtained. The Maxwellian carrier distribution is never strictly valid, but is a commonly used approximation [114]. 73

Figure 2.22. Mean hole energy near the cathode vs. bias is shown, per the model described in the text (solid) and extrapolated from data in reference [116] (dash). Dotted lines show band offsets for $Al_{0.2}Ga_{0.8}As/GaAs$ (0.09 eV), $InAlAs/InGaAs$ (0.2 eV), $InP/InGaAs$ (0.35 eV), and $InGaP/GaAs$ (0.31 eV). It is predicted that the phosphorus-based material systems will require higher bias for saturated speed. 74

Figure 2.23. The figure provides a legend for the mask set designed as part of this research. The arrays of photodetectors were named for their physical appearance, as shown in Figure 2.24. The size of the MSM detectors in each array is also indicated. The labeling corresponds to 'finger width x finger spacing _ active region side length'. Each photodetector on the mask has an adjacent label, following the same convention. 76

Figure 2.24. A unit cell of the mask set is shown. The features are described by the legend in Figure 2.23. 77

Figure 2.25. The process for fabrication of MSM photodetectors is shown schematically. The mesa mask is light field, and requires a positive resist. Following mesa formation, an insulator is deposited, and the window mask is used to open active regions. The window mask is dark field, and also requires a positive resist. Both metal layers are light field masks, and liftoff is performed with a negative resist. As an option, an anti-reflection or passivation layer can be deposited last, and defined with either the mesa or metal2 mask. 78

Figure 3.1. The epitaxial layer structure is shown, for the devices discussed in the present section. All layers were grown nominally undoped, by MOVPE, on a Fe doped (semi-insulating) InP substrate. The surface layer is slightly mismatched, but thin enough to avoid dislocations. 82

- Figure 3.2.** A microscope photograph is shown, of a 3x2 InGaAsP/InP MSM photodetector. The active region was defined by opening a window in a silicon nitride dielectric layer, and appears light grey. The area of the active region is $(100 \mu\text{m})^2$ 83
- Figure 3.3.** The relevant features of the OTM-8 mask set, used to fabricate the devices discussed in this section. The discrete photodetectors are labeled 1 to 20. Each has $3 \mu\text{m}$ finger width, and an active region area of $(100 \mu\text{m})^2$. The finger spacing ranges from $1 \mu\text{m}$ to $20 \mu\text{m}$. Most of the results were obtained for devices with $2 \mu\text{m}$ finger spacing. An array of ten detectors is also shown, but was not studied in detail here. 83
- Figure 3.4.** A typical photocurrent characteristic is shown, for a '3x2' MSM photodetector, fabricated in the InGaAsP/InP material system. The DC response is nearly ideal: The photocurrent saturates at a very low bias, and shows little bias-dependence thereafter. This is characteristic of a device for which low-frequency gain is negligible. The curves are labeled, to indicate the optical power and wavelength (λ) for each measurement 84
- Figure 3.5.** An activation energy plot is shown, for a '3x2', InGaAsP/InP device. The plot format is described in Section 2.3.5. The slope of the plots indicates the effective Schottky barrier height ($\Phi_{n,\text{eff}}$) of the MSM electrodes, at various bias voltages. As shown, Schottky barrier lowering effects were minimal..... 85
- Figure 3.6.** A frequency response is shown, for a typical 3x2 InGaAsP device. The upper trace was for a bias of 12 V, the lower trace was for a bias of 0 V. The wavelength of the incident light was 1320 nm, the average power was 1 mW. The on/off isolation was greater than 40 dB, across the entire 20 GHz measurement band. The vertical scale is in dB, relative to the photodetector used to calibrate the test system. 0 dB corresponded to 0.1 A/W. 86
- Figure 3.7.** -3dB Bandwidth as a function of bias is shown, for a typical 3x2 device on the InGaAsP/InP wafer. The device bandwidth was nearly saturated for bias as low as 7 to 8 V. The saturation bandwidth indicated (12 GHz) is in good agreement with the transit-time limited estimates discussed in Chapter 1. 87
- Figure 3.8.** The epitaxial structure is shown, for the devices discussed in the present section. All layers were nominally undoped and nominally lattice-matched. The thin surface layer of InGaAs was grown to protect the aluminum-rich cap layer. InAlAs has a high affinity for atmospheric oxygen, which generally degrades the electronic characteristics of its free surface. Prior to deposition of the MSM electrodes, the surface InGaAs layer was selectively etched to expose the underlying InAlAs. 89
- Figure 3.9.** Typical dark current characteristics of '3x2' devices are shown; for the InAlGaAs/InP (dashed) and the InGaAsP/InP (solid) material systems. The magnitude of the dark current was similar, at moderate bias, but the curve shapes were different. The InGaAsP/InP characteristic is representative of an ideal Schottky contact, under reverse bias, as discussed in the text..... 91
- Figure 3.10.** Dark current of an InAlGaAs '3x2' device is shown, as measured at various temperatures. Heating the device facilitated a better determination of the dark current characteristic, at low bias. At least three separate dark current regimes were observed: a rapid increase at low bias, followed by quasi-saturation, followed by soft breakdown at high bias... 92
- Figure 3.11.** An ideality factor plot (see Chapter 2) for an InGaAsP/InP detector is shown. The data were taken at room temperature. The zero bias intercept indicated a Schottky barrier for electrons (Φ_m) of 0.46 eV, with a typical value assumed for the modified Richardson constant. The reverse-bias ideality factor (n), determined from the slope of the plot, was 1.04..... 93

- Figure 3.12.** An ideality factor plot for an InAlGaAs '3x2' device is shown. The data were obtained at a temperature of 120 C. The zero-bias barrier height (Φ_{n0}) was estimated as 0.59 eV. From the slope of the curve, a reverse-bias ideality factor of 1.07 was estimated. 94
- Figure 3.13.** An activation energy plot for an InAlGaAs/InP '3x2' device is shown. From the slope of the curves, Schottky barrier lowering was observed in the 0 to 3 V bias range. The effective Schottky barrier at 1, 2, 3, and 6 V was estimated as 0.58 eV, 0.47 eV, 0.34 eV, and 0.33 eV, respectively..... 95
- Figure 3.14.** Photocurrent characteristics for a 3x2 InAlGaAs/InP MSM detector are shown: before passivation (dashed line), and after passivation (solid line). The photocurrent curves revealed much less recombination and low-frequency gain for the passivated device. The dark current was nearly identical before and after passivation. The photocurrent was measured for several optical powers, at 1320 nm wavelength, as indicated by the labels..... 98
- Figure 3.15.** Plots of responsivity as a function of optical power are shown, for the passivated (solid line) and non-passivated (dashed lines) InAlGaAs/InP detectors. A responsivity that is independent of optical power indicates a gain-free MSM detector, as explained in the text. The plots were obtained at various bias voltages, as indicated by the labels..... 98
- Figure 3.16.** High-frequency measurements for the passivated (upper scan) and non-passivated (lower scan) InAlGaAs/InP MSM detectors are shown. The devices had finger width of 3 μm , finger spacing of 2 μm , and an active region area of $(100 \mu\text{m})^2$. Results were obtained with an optical power of 0.3 mW, at a wavelength of 1320 nm, and for a bias voltage of 12 V. Marker 2 indicates the bandwidth of the non-passivated device, 2.6 GHz. For the passivated device, the bandwidth exceeded 10 GHz. This was due to the absence of a peaked response at low frequency. The vertical scale is relative to the responsivity of the photodetector used to calibrate the system. 0 dB corresponds to approximately 0.15 A/W. 100
- Figure 3.17.** The bandwidth as a function of bias is shown, for the passivated (solid line) and non-passivated (dashed line) InAlGaAs/InP MSM detectors. The devices had finger width of 3 μm , finger spacing of 2 μm , and an active region area of $(100 \mu\text{m})^2$. The bandwidth of the non-passivated devices was limited by low-frequency gain, as shown in Figure 3.16. 100
- Figure 3.18.** The epitaxial structure is shown, for the wafer discussed in the present section. The design of the epitaxy was described in Section 2.5.1. MSM fingers are shown schematically, at the top surface, in cross-section. The layers were grown on a semi-insulating (S.I.) GaAs substrate. Not shown is a 5 nm GaAs surface layer, grown to protect the AlGaAs cap layer from severe oxidation, and etched prior to metal deposition and passivation. The passivation layer (silicon nitride) is also not shown..... 103
- Figure 3.19.** A microscope photograph of an AlGaAs/GaAs MSM detector is shown. The edge of the mesa is labeled. The device has 1 μm finger spacing and width (1x1), and an active region area of $(50 \mu\text{m})^2$ 104
- Figure 3.20.** DC photoresponse characteristics are shown, for an AlGaAs/GaAs MSM detector, with 1 μm finger width and spacing. The curves were relatively flat up to 5 V, but show a gradual increase at higher bias. This is indicative of the onset of low-frequency gain. The photoresponse was measured for several different optical powers, at a wavelength of 830 nm, as indicated by the labels. 104
- Figure 3.21.** A frequency scan, for a 1x1 AlGaAs/GaAs device, is shown. The bias voltage for the measurement was 3 V, and the optical power was 1 mW, at 830 nm wavelength. Marker 2 indicates the -3 dB bandwidth, which was greater than 18 GHz. The vertical axis is relative to the photodetector used to calibrate the test system. 0 dB corresponds to 0.15 A/W. 105

- Figure 3.22.** The -3dB bandwidth as a function of bias is shown, for the devices described in the present section (solid curve) and for the InAlAs/InGaAs devices described in [128] (dashed curve). The AlGaAs/GaAs devices reported here exhibited exceptional bandwidth at low bias. This was attributed to reduced hole pileup, as described in Section 2.7..... 106
- Figure 4.1.** A quarter-wave-stack distributed Bragg reflector, with alternating refractive indices, n_{d1} and n_{d2} . The stack is embedded in semi-infinite media, with refractive index n_i at the input, n_o at the output. The stack may have an even number of layers (starting with layer n_{d1} , ending with layer n_{d2}) or an odd number of layers (starting and ending with layer n_{d1}). N is the number of periods, each consisting of one n_{d1} and one n_{d2} layer. 113
- Figure 4.2.** The effect on reflectivity of varying refractive index (a) and of varying number of periods in a GaAs/AlAs stack (b). The data are from reference [145]..... 115
- Figure 4.3.** Total field quantities in adjacent dielectric media. E_i and E_{ii} (and the corresponding magnetic fields) are related by a transfer-matrix, based on the boundary conditions for material interfaces..... 118
- Figure 4.4.** Simplified model of a resonant-cavity photodetector, used to obtain analytical design formulae. R_1 and R_2 are the reflectivity of the top and bottom mirrors, respectively. The reflectors are treated as ‘hard’ mirrors, not penetrated by the internal field in the cavity. Correction factors, including the phase of each mirror, are required for wavelengths other than the center wavelength of the quarter-wave-stacks. 119
- Figure 4.5.** Model structure used for design of top-illuminated resonance-enhanced MSM photodetectors. E 's are band-gaps, n 's are refractive indices, and t 's are layer thickness'. L_{cav} is the effective cavity length, which must satisfy the resonance condition. It is dependent on the ratio of refractive indices for the first and second layers of the quarter-wave-stack. This is to satisfy the phase condition for the resonant-cavity, as discussed in the text..... 122
- Figure 4.6.** Recommended epitaxial structure for an AlGaAs/GaAs resonant-cavity-enhanced MSM detector, with a center wavelength of 800 nm. All layers are nominally undoped..... 127
- Figure 4.7.** The simulated spectral characteristic of the resonant cavity structure illustrated in Figure 4.6, with an absorption region thickness of $t_{\text{abs}}=389$ nm. The horizontal scale is fraction of power absorbed (solid), transmitted (dot), and reflected (dash-dot). This absorption region thickness is near the optimal value, as given by (4.12)..... 128
- Figure 4.8.** Variation of absorbed power for the structure of Figure 4.6, with different absorption region thickness. $t_{\text{abs}}=171$ nm (dash), 280 nm (dot), 498 nm (solid), and 716 nm (dash-dot). In keeping with the theory in Section 4.4, the peak absorption is maximized by a layer thickness of approximately 400 nm. A reduction or increase in this thickness reduces peak absorption... 129
- Figure 4.9.** Effect of a silicon nitride passivation layer on the absorption characteristics of the device of Figure 4.6, with $t_{\text{abs}}=389$ nm. $t_{\text{SiN}}=205$ nm (solid), 40 nm (dot), 75 nm (dash). Note that the passivation layer, having an intermediate refractive index, cannot improve the reflectivity of the front mirror. Thus, a passivation layer should be made ‘vanishing’ by restricting its thickness to a multiple of a half wavelength at the design frequency. This is the case for the 205 nm layer. 130
- Figure 4.10.** Photograph of a fabricated MSM device, on the GaAs/AlGaAs resonant-cavity wafer. The finger spacing and width are 2 and 1 μm , respectively, for the device shown. The active region appears light gray, and was defined by opening a window in a silicon nitride layer... 131

- Figure 4.11.** Frequency response for a resonant-cavity-enhanced MSM detector, with $(50 \mu\text{m})^2$ active regions, $1 \mu\text{m}$ finger width, and $2 \mu\text{m}$ finger spacing. Comparing to the results in Chapter 3, the detectors on this wafer did not exhibit transit-time-limited bandwidth. Rather, the bandwidth is limited by low frequency gain. The scan was obtained for 0.4 mW of modulated light, at 830 nm wavelength. The device was biased at 5 V . The plot is the screen output of a network analyzer. The horizontal scale is linear in frequency, starting at 50 MHz and ending at 10 GHz . The vertical scale is logarithmic, 3 dB per division. The 0 dB reference line is marked by the 'greater-than' symbol at the left, and represents 0.1 A/W 132
- Figure 4.12.** An experimental reflectivity scan is shown, for the AlGaAs/GaAs resonant cavity structure (solid line). Also shown is a theoretical fit to the data (dashed line). The theoretical fit was obtained by assuming the GaAs absorption region to be grown as specified, and all AlGaAs layers to be under-grown by 4% . The observed resonant peak was typically at 785 nm wavelength, compared to the design target of 800 nm 133
- Figure 4.13.** Band-filling in a degenerately n-doped, direct band-gap semiconductor. E_F is the Fermi-level, $h\nu_g$ is the band-gap energy, and $h\nu_{\text{min}}$ is the minimum photon energy for absorption. $h\nu_{fc}$ is a typical free-carrier transition, and hhb, lhb, and cb are the heavy-hole, light-hole and conduction bands, respectively. 137
- Figure 4.14.** The shift of the absorption band-edge due to band filling in a heavily doped semiconductor. Transparency is increased for photon energy slightly greater than the nominal band gap. 138
- Figure 4.15.** The shift of the absorption edge in a degenerately doped semiconductor due to band-gap shrinkage. The nominal band gap is shifted, due to potential energy screening by free carriers in the crystal lattice. 139
- Figure 4.16.** Changes in refractive index (relative to undoped case) for a degenerately n-doped semiconductor, due to band filling, band-gap shrinkage, and free-carrier absorption. Depending on the particular semiconductor, and the doping level, one or more of the three effects can dominate. 139
- Figure 4.17.** Absorption edge of intrinsic (dash-dot line) and heavily doped ($n \sim 7 \times 10^{18} \text{ cm}^{-3}$) (solid line) GaAs. The band edge is effectively shifted, due to band-filling by donor electrons. 140
- Figure 4.18.** Resonant-cavity epitaxial structure, using a buried n-type InGaP/GaAs DBR mirror, with a target center wavelength of 830 nm . Doping the GaAs layers in the mirror makes them effectively transparent at 830 nm 141
- Figure 4.19.** Modeled real parts of the refractive indices for the various layers in Figure 4.18. The indices shown are for undoped GaAs (solid line), doped GaAs (dash-dot line), undoped InGaP (dash line), and doped InGaP (dot line). 142
- Figure 4.20.** For the structure of Figure 4.18: the percentage of incident power absorbed in the absorption layer (dash line), absorbed in the mirror (solid line), reflected from the surface (dash-dot line), and transmitted into the substrate (dot line). Peak absorption of 88% is predicted at 830 nm . This is limited primarily by the reflectivity of the bottom mirror (90%). Less than 2% of the power is absorbed in the mirror, for wavelengths of 810 nm and above. 143
- Figure 4.21.** Spectral response for the structure of Figure 4.18, with a 25 period buried mirror. The legend is the same as in Figure 4.20. Peak absorption greater than 96% is predicted. 144

- Figure 4.22.** An experimental power reflectivity scan is shown, for the epitaxial structure illustrated in Figure 4.18. The spectrum was obtained with a Varian spectrophotometer. Away from the center of the wafer, the resonant wavelength of the structure was 796 nm +/- 2 nm..... 145
- Figure 4.23.** A comparison of experimental (solid line) and theoretical (dashed line) reflectivity spectra is shown. For the theoretical spectra, a -17 % growth error was assumed for the InGaP layers, while the GaAs layers were assumed to be as specified. This assumption did not produce a good match to the secondary features of the experimental spectrum..... 147
- Figure 4.24.** A comparison of experimental (solid line) and theoretical (dashed line) spectra is shown. For the theoretical spectra, a fixed growth thickness error of -4.8 % was assumed, for all of the layers in Figure 4.18. The excitonic feature at the GaAs band edge is labeled on the experimental spectrum. It is present, but less resolved in the theoretical plot. This might reflect the fact that the refractive index data for the simulation correspond to melt-grown GaAs samples, as discussed in the text..... 148
- Figure 4.25.** A scanning electron microscope (SEM) image is shown, of the grown epitaxial structure in cross-section. The structure is illustrated schematically in Figure 4.18. As indicated by the label, the absorption region thickness was estimated as 410 nm, from the SEM image. This represents a - 4.5 % growth error, which supports the simulation of Figure 4.24..... 150
- Figure 4.26.** Simulated power spectra for the layer structure of Figure 4.18, with all layers undergrown by 4.8 %. The legend is as given in Figure 4.20. The mirror layers absorb about 15 % of the incident power, and only 77 % is absorbed in the in the intended absorption region. This corresponds to responsivity (neglecting finger shadowing) of 0.5 A/W, for a photodetector operating at approximately 800 nm wavelength..... 151
- Figure 4.27.** Recommended epitaxial structure of an InGaAsP/InP resonant-cavity-enhanced MSM detector, with a center wavelength of 1320 nm. All layers nominally undoped. The total epitaxy exceeds the specifications in Section 4.4, but is the minimum required for an efficient device..... 152
- Figure 4.28.** The reflected (dot), transmitted (dash-dot), and absorbed (solid) power as a fraction of incident power, for the device illustrated in Figure 4.27. 154
- Figure 4.29.** Recommended structure for a resonant-cavity MSM photodetector, using the InAlGaAs material system. The target center-wavelength is 1320 nm. All layers are nominally undoped. 155
- Figure 4.30.** The predicted spectral response for the device of Figure 4.29 is shown. The traces are for absorbed (solid), reflected (dash-dot), and transmitted (dot) percentages of incident optical power. 156
- Figure 4.31.** A Recommended structure for operation in the 1550 nm wavelength region. A Burstein-Moss shifted InGaAs/InP DBR mirror is used. The relevant theory is contained in Section 4.5.2. The target center-wavelength is 1535 nm. 158
- Figure 4.32.** Simulated power spectra for the device of Figure 4.31: Absorption (solid), reflection (dash-dot), and transmission into the substrate (dot). 159
- Figure 5.1.** A generic MSM photodetector array. Several photodetectors are interconnected, by a common bus. This accommodates an electrical and/or summation of their signals. The opposite side of each MSM detector is selectively biased, providing a control function, useful for switching or weight-setting. The bus must interface to an external system, generally a 50 Ω load. 165

- Figure 5.2.** Frequency scans for a single $(75\ \mu\text{m})^2$ MSM detector, with $2\ \mu\text{m}$ finger spacing and width. The top scan is for a device with $(100\ \mu\text{m})^2$ bond pads, as for the device results in Chapter 3. The lower scan is for the same detector in a 'skinny squid' detector array (see Section 5.3.1). Each scan was obtained with a ground-signal RF probe, making contact across the detector. The plot is the screen output of a HP-8510B network analyzer. The horizontal scale is linear in frequency, starting at 45 MHz and ending at 15 GHz. The vertical scale is logarithmic, 3 dB per division. The 0 dB reference represents 0.15 A/W responsivity..... 166
- Figure 5.3.** A photograph of a packaged 'skinny squid' array. The array contains 16 MSM detectors, each with $(75\ \mu\text{m})^2$ active regions. The arrows identify the numbering of the MSM detectors, for discussion purposes. Also indicated are the adjacent metal strips relevant to the discussion of coupled-line effects in the text..... 168
- Figure 5.4.** The scans show the typical frequency response for detectors in the 'fat' or 'skinny' 'squid' arrays. This particular plot was for a 'skinny squid' array, and shows the response of detectors 1,4,6,11, and 16 in the array. The frequency responses exhibit a strong RC roll-off, and position-dependent spurious features above 2 GHz. The plot is the screen output of a HP-8510B network analyzer, see Figure 5.2..... 168
- Figure 5.5.** A typical frequency response for an MSM detector in one of the 16 detector 'squid' arrays. The upper trace was a frequency scan for a discrete detector of identical geometry, on the same wafer, for reference. The lower scan was for MSM #1 in a 'skinny squid' array, with the adjacent detector bonded to ground. The bias voltage was 8 V, and the optical power was 1 mW, at 830 nm wavelength. See Figure 5.2 for a description of the plot format..... 169
- Figure 5.6.** A schematic illustration of coupled microstrip lines (a), and a simple equivalent circuit (b). The lines have width w , spacing s , and are a distance d from the ground plane. They lie on a dielectric with relative permittivity, ϵ_r . C_{11} and C_{22} are the capacitances (per unit length) between each strip and the ground plane, in the absence of the other strip. C_{12} is the coupling capacitance between the adjacent strips, in the absence of the ground plane..... 170
- Figure 5.7.** A coupled-line directional coupler model for the adjacent lines indicated in Figure 5.3. The length of the adjacent sections is L . The bias pads are connected to AC ground. Each microstrip line is terminated, by the low-impedance output section of the array..... 170
- Figure 5.8.** Schematic illustration of the periodic nature of power transfer in a coupled-line directional coupler. The minima occur at the frequencies shown, and are determined by the adjacent length (L) of the coupled-lines, and the phase velocity (v_{ph})..... 171
- Figure 5.9.** Photograph of a packaged 'goalpost' array. The bond wires appear black in the image. The MSM detectors are numbered for discussion purposes. The array contains eight MSM photodetectors, with $(75\ \mu\text{m})^2$ active regions, and a finger spacing and width of $2\ \mu\text{m}$. The inter-detector spacing is $500\ \mu\text{m}$. Asymmetric frequency responses for detectors on either side of center suggested that coupled-line effects were present at the location indicated..... 172
- Figure 5.10.** Frequency responses for several detectors in the packaged 'goalpost' array. The upper scan was for a discrete MSM detector of the same size, for reference. The lower scans revealed unique characteristics for detectors on either side of the line of symmetry, in the 'goalpost' array. The scans that are indicated by marker 2 were for detectors 2,3, and 4. The others were for detectors 5,7, and 8. The optical power was 0.8 mW, at 830 nm wavelength. The bias voltage was 10 V. See Figure 5.2 for a description of the plot format..... 173
- Figure 5.11.** The frequency response of MSM #8 in the 'goalpost' array. The traces show decreasing roll-off in the response of MSM #8, as bond wires of the neighboring detectors

(starting with MSM #7) were successively removed. The optical power was 0.8 mW, at 830 nm. MSM #8 was biased at 10 V. See Figure 5.2 for a description of the plot format. 174

Figure 5.12. Photograph of a packaged 'rake' array. The array contains 8 MSM photodetectors, each with a $(75 \mu\text{m})^2$ active region. The detectors are numbered for discussion purposes. The location of coupled-line effects, revealed by experiment, is also indicated. 175

Figure 5.13. The frequency response of MSM #8 in the 'rake' array. The upper trace is the frequency response of a single isolated detector, for reference. The lower traces show decreasing roll-off in the response of MSM #8, as bond wires of the neighboring detectors (starting with MSM #7) were successively removed. The optical power was 0.8 mW, at 830 nm wavelength. MSM #8 was biased at 10 V. The plot is a screen output from a HP-8510B network analyzer. The horizontal scale is linear in frequency, starting at 45 MHz and ending at 10 GHz. The vertical scale is logarithmic, 5 dB/division. 175

Figure 5.14. A lumped-element representation of an array of photodetectors, such as in Figure 5.1. A simple equivalent circuit is used for the photodetector, including the capacitance and resistive losses associated with the device. For MSM photodetectors, R_S is generally the series resistance associated with the thin metal fingers, and R_L is the conductive loss associated with free and interfacial charge in the epitaxial layers. C_d is the total capacitance associated with each photodetector. Adjacent photodetectors are interconnected by a conductive element with high AC impedance, modeled simply as an inductor with some associated loss. Each end of the array is terminated in the system impedance. 179

Figure 5.15. (a). A portion of a common-bus MSM photodetector array. The bus is equivalent to a high impedance microstrip line. The MSM detectors, to first order, are capacitive loads, periodically spaced along the line. (b). An equivalent circuit for the periodically loaded line. The unloaded microstrip line has impedance Z_H , and effective propagation index n_H . The susceptance of the photodetector loads is b 182

Figure 5.16. A periodically loaded transmission line, terminated by an external system impedance, Z_T . Γ is the reflection coefficient at the load. 184

Figure 5.17. Microstrip transmission line in cross-section. In general, ϵ_r is complex, accounting for dielectric loss. For a semiconductor, conductivity is the primary source of loss. 187

Figure 5.18. Simplified equivalent circuit for an individual detector in an array. The devices are probed between the common bus and their bias pad. The measured capacitance is approximately the entire amount attributable to that detector. In a wire-bonded array, there may be an additional small component due to adjacent bias pads. The inductance is due primarily to the extended metal patterns attached to each side of a detector, see Figure 5.19. 190

Figure 5.19. Layout of the photodetector array used to demonstrate impedance-matched photodetector concepts. The MSM detectors have active regions of $(26 \mu\text{m})^2$, finger width and spacing of 2 μm . The arrays lie on a semi-insulating GaAs substrate. Arrays of eight and sixteen photodetectors were studied. 191

Figure 5.20. Experimental S_{22} characteristic for one of the detectors in the array of Figure 5.19. The trace lies very close to the open-circuit point on the Smith-chart, indicating the device has very low capacitance and negligible resistive loss. Reflection measurements were made over the frequency range 45 MHz to 5 GHz. The marker indicates that the device impedance at 5 GHz ($23.3-j652 \Omega$) is almost completely reactive, and corresponds to a capacitance of approximately 49 fF. The measured capacitance was not bias-dependent. 192

- Figure 5.21.** The solid line shows free-space propagation constant vs. loaded-line propagation constant (k - β relationship), predicted for the detector array described in this section. The dashed line is the nominal cutoff propagation constant, as determined from (5.6). The dotted line is for propagation at the speed of light, for reference. 194
- Figure 5.22.** The predicted phase velocity on the detector array, as a function of frequency. The loaded-line is very nearly free of dispersion up to the nominal cutoff frequency, 86 GHz. 195
- Figure 5.23.** A photograph of a packaged, 16-detector array is shown. A $47\ \Omega$ chip resistor (not visible) terminated one end of the common bus, while the other end interfaced to a $50\ \Omega$ system. Multiple bond wires were used to connect each end of the bus to coplanar waveguide lines on the RF substrate. A single bond wire connected each detector's bias pad to the ground plane on the RF substrate. 195
- Figure 5.24.** The upper scans are the frequency response of all 16 detectors, for the array in Figure 5.23. The lower scan indicates the noise floor of the test system. Good response uniformity was observed up to the measured 3 dB bandwidth, 6.5 GHz, which is indicated by the markers. Pass-band ripple and position-dependence were observed in the 6 to 16 GHz range. The plot is the screen output of a HP-8510B network analyzer (see Figure 5.2). 197
- Figure 5.25.** A microscope photograph of an 8-detector array, as discussed in the present section. Each MSM photodetector has an active region of $(26\ \mu\text{m})^2$, and finger spacing and width of $2\ \mu\text{m}$. The chip was mounted on a gold-deposited alumina substrate, with $50\ \Omega$ coplanar waveguide access lines. Each end of the bus was bonded to an identical coplanar line on the RF substrate, with a pair of wire bonds approximately 0.5 mm in length. 199
- Figure 5.26.** Frequency response of all detectors in an 8-detector array, measured sequentially. The traces are arranged (top to bottom) in order of increasing distance from the load, and are offset for clarity. The top trace is not offset, and 0 dB represents approximately 0.1 A/W, determined by the detector used to calibrate the measurement system. The frequency response varies by less than 3 dB up to 12 GHz, for each photodetector. The wavelength of measurement was 830 nm, and the detectors were illuminated with 0.4 mW average optical power. The bias voltage was 5 V. 200
- Figure 5.27.** The measured return loss characteristic is shown, for the packaged 8-detector array. The return loss was measured at the point of contact to the RF substrate. As such, it represents the total mismatch for the packaged array, including that due to the bond wires at each end of the common bus. In the low frequency range, where the bond wires have relatively negligible impedance, the return loss is due to the impedance of the detector array alone. 201
- Figure 5.28.** A schematic illustration of an experiment conducted to investigate electrical propagation along the photodetector array. As shown, the termination was removed from one end of the array, producing an open-circuit condition. The photocurrent from an active detector splits approximately equally in each direction. The photocurrent wave incident at the open circuit is reflected back towards the load end of the device. At the load, the total photocurrent is the sum of two signals of equal frequency, but unequal phase, which interfere. 202
- Figure 5.29.** A result for the experiment described by Figure 5.28. The detectors are in an 8-detector array. The trace indicated by marker 2 is for detector 6, the other is for detector 2. The notch frequencies are approximately 4.7 GHz and 6.6 GHz, respectively. The bottom of the notches is off the display, but is about 30 dB below the DC response. The plot is the screen output of a HP-8510B network analyzer, see Figure 5.2 for details of the plot format. 203
- Figure 5.30.** Losses for a microstrip line on GaAs, with an electron concentration of $3 \times 10^{13}\ \text{cm}^{-3}$. The conductor loss is not sensitive to the underlying material, and is shown by the dotted line.

The dielectric loss dominates, and is shown by the dashed line. The total loss is shown by the solid line, and is approximately 1.5 dB/mm, independent of frequency..... 205

Figure 5.31. The maximum number of detectors in an array is plotted against the cutoff frequency, as determined by microstrip attenuation alone. Two limiting cases are considered. The first assumes a carrier concentration of $3 \times 10^{13} \text{ cm}^{-3}$ in the semiconductor underlying the microstrip (solid line). This is representative of the wafers discussed in Section 5.5. The second case assumes the microstrip lies on a semi-insulating semiconductor, so that dielectric losses are negligible (dashed line)..... 206

Figure A.1. The desired characteristics of MSM photodetectors for switching versus signal processing applications are illustrated schematically. For switching, it is desirable that the detector's bandwidth and responsivity saturate at low bias, so that a large and stable operating region is available. For signal processing, it is required that the detector has a bias-dependent responsivity, to accommodate the setting of tap weights. Ideally, this bias dependent responsivity is introduced without altering the bias-independent bandwidth of the switching detector. 230

Figure A.2. A schematic illustration of the equipotential surfaces and electric field lines, near a single finger (shown in cross-section) of an interdigitated MSM detector, with finger spacing equal to finger width. The field lines are shown for a single unit cell only, with bias applied between the MSM finger and its neighboring finger (not shown). If background doping is neglected in the layers (zero space charge), an equipotential plane lies midway between adjacent fingers, as shown. In this case, all of the relevant information is contained in the unit cell shown (the field lines on the other side of the vertical equipotential plane are a mirror image). In reality, residual n-type dopants typically enhance the field near the cathode fingers, and reduce it near the anode fingers. Note that the field is strongest near the semiconductor surface, and especially near the peripheries of the electrodes. Also, the electric field is mostly lateral (parallel to the plane of the layers) in the non-shadowed regions between MSM fingers. 232

Figure A.3. The coordinate system is shown, for the conformal transformations used to determine the electric field in the vicinity of the MSM fingers. The transformations are valid for coordinates within the unit cell shown. The field pattern is identical in other unit cells. The origin lies at the semiconductor surface, midway between neighboring fingers. Lateral field components are directed along the x direction, and are also termed parallel (to the plane of the epitaxial layers). Vertical fields are directed along the y direction, and are also termed perpendicular (to the plane of the epitaxial layers)..... 233

Figure A.4. The total electric field magnitude in the vicinity of adjacent MSM fingers. The coordinate system is as shown in Figure A.3, and the plot is for a 1x1 device, biased at 10 V. Data is plotted to a depth of $0.5 \mu\text{m}$, which represents a typical absorption region thickness for the devices in Chapters 3 and 4. The field is peaked at the semiconductor surface, near the peripheries of the fingers. Away from these locations, the total field magnitude is quite uniform, and about half the nominal value (bias/finger spacing). 234

Figure A.5. The transverse (lateral) electric field is plotted, for the same geometry as in Figure A.4. Note that the lateral field is strongest in the regions between fingers, and is relatively weak beneath the fingers..... 235

Figure A.6. The vertical electric field is plotted, for the same geometry as in Figure A.4. The strongest vertical fields exist in the regions beneath and near the MSM fingers. The regions between fingers primarily contain lateral fields (parallel to the plane of the layers). 236

- Figure A.7.** Epitaxial layers (top) and band diagram (bottom) for a GaAs/AlGaAs multiple quantum well (MQW) structure. The quantized energy levels shown are labeled $e1$ and $e2$ for the electron states, $hh1$ for the lowest heavy-hole state, and $lh1$ for the lowest light-hole state. ... 237
- Figure A.8.** Schematic illustration of the two lowest bound states in a finite quantum well. V_0 is the well depth, E_2 and E_1 are the eigen-energies, k and κ are wave-numbers in the well and barrier material, respectively, and L_w is the well width. Note that the overlap integral between states of opposite parity (symmetry about the well center) is nearly zero. 238
- Figure A.9.** The transition wavelength between ground state confinement energies, $e1$ to $hh1$, in a GaAs/Al_xGa_{1-x}As quantum well. The data are plotted as a function of well width, for $x=0.2$ (dotted line), $x=0.3$ (solid line), and $x=0.4$ (dashed line)..... 239
- Figure A.10.** A semi-empirical model for absorption at the band edge of a 9.6 nm wide GaAs/Al_{0.3}Ga_{0.7}As MQW. Three contributions to absorption are included as described in the text: heavy-hole exciton (dashed line), light-hole exciton (dotted line), and broadened continuum (dash-dotted line). The solid line represents total absorption. The fitting parameters are the peak absorption coefficients, the linewidths, and the energy position of each contribution. For the heavy-hole exciton, the assumptions are a peak absorption coefficient of $1.1 \mu\text{m}^{-1}$, a linewidth (half-width at half-maximum) of 3 meV, and a peak position of 1.4575 eV. For the light-hole exciton, the peak absorption is $0.63 \mu\text{m}^{-1}$, the linewidth is 3 meV, and the peak position is 1.466 eV. For the continuum, a linewidth of 5 meV was assumed, and the band edge is at 1.4675 eV. After reference [23]..... 241
- Figure A.11.** Schematic illustration of the red-shift of the optical band-edge in a quantum-well. At zero field (left), the wells are rectangular in shape, and both the electron and hole ground state have highest probability at the center of the well. For a finite perpendicular field (right), the confined particles reside in a trapezoidal well, with sloping potential. The ground-state hole has highest probability near the left barrier, the ground-state electron near the right. The band edge is red-shifted by the field ($h\nu_2 < h\nu_1$), and the exciton oscillator strengths (peak absorption) are reduced, due to a reduction in the overlap of electron and hole wavefunctions in the well..... 242
- Figure A.12.** The tunneling-resonance technique is illustrated schematically. The technique is used to estimate the quantized energy levels in a quantum well, with field applied perpendicular to the plane of the layers. Each layer is divided into multiple steps, each step having a constant potential. This allows simple exponential solutions to be assumed at each step. The energy of an incident electron wave is varied, and resonant peaks in the transmission or reflection spectra indicate the quantized energy levels in the well. 243
- Figure A.13.** The result of a tunneling resonance simulation, as described in the text, for a 10 nm GaAs well. A barrier width of 10 nm was used, and the barrier material was Al_{0.3}Ga_{0.7}As. The resonance shown indicates the approximate position of the ground-state confinement energy for electrons, $e1$, with no applied field. 245
- Figure A.14.** The sub-band gap, given by (A.9), is plotted as a function of electric field applied perpendicular to the plane of the quantum well layers. The parameters of the well are the same as indicated for Figure A.13. The gap was determined using the tunneling resonance technique described in the text. 246
- Figure A.15.** Semi-empirical fits to the experimental data in [5] are shown. The data are for parallel fields in a 10 nm GaAs well: $1.6 \text{ V } \mu\text{m}^{-1}$ (dotted line), $4.8 \text{ V } \mu\text{m}^{-1}$ (dashed line). The fitted curves are similar to that shown in Figure A.10. A continuum band-edge at 1.465 eV, with linewidth (HWHM) of 5.5 meV, was used. The continuum parameters were assumed insensitive to the applied field. The heavy-hole exciton is located at 1.4532 eV, and the light-hole exciton at 1.4642 eV. The positions of the excitons were also assumed insensitive to

parallel field. A zero-field exciton linewidth of 4.6 meV [5] was used, and they were broadened according to (A.17). The peak absorption of each exciton was subsequently adjusted to match the experimental data..... 247

Figure A.16. Representative structure proposed to achieve bias-dependent responsivity for a gain-free MSM photodetector. Both front and back mirrors are included, to increase the quality factor of the resonant cavity as needed. Also, both top and rear illumination are considered, since the opaque fingers shadow regions of high vertical field (see Section A.2) in the top illumination case. For rear-illumination, the substrate must be transparent or removed. 248

Figure A.17. Schematic illustration of the model used to estimate absorption in an MSM photodetector, with a MQW active region. The case shown is for top-illumination, with opaque metal fingers. A unit cell of the device (see Figure A.3) is divided into a two-dimensional matrix, with rows defined by the center point of each quantum well. The two-dimensional field is calculated at each point in the matrix, and the components are used to estimate the local absorption characteristics. Next, the total absorption spectra are calculated for each column of the matrix, separately, using the transfer-matrix technique described in Chapter 4. Finally, the spectra from all columns are averaged, to provide an estimate of the overall absorption spectra for the MSM detector. 249

Figure A.18. The reduction in exciton peak amplitude is shown as a function of electric field perpendicular to the wells (solid line) and parallel to the wells (dashed line). The amplitude is expressed as a fraction of the zero-field peak amplitude. In the simulation, the contributions due to both field components are multiplied. 250

Figure A.19. Band-edge absorption features, as predicted by the semi-empirical model described in the text. The solid line is for no applied field. The dashed line is for a field of $5 \text{ V } \mu\text{m}^{-1}$, applied perpendicular to the plane of the wells. In that case, the band-edge shifts to the red. The dotted line is for field components of $5 \text{ V } \mu\text{m}^{-1}$, both perpendicular and parallel to the plane of the wells. While the band edge is red-shifted by the perpendicular field, the exciton features are broadened and obscured by the parallel field. 251

Figure A.20. MSM structure, in cross-section, used to simulate the electro-optic effects for rear-illumination. The entire structure is designed to resonate near the zero-field band edge of the quantum wells, at approximately 860 nm. The incident-side mirror is a semiconductor quarter-wave stack, with a reflectivity of approximately 75 %. The other mirror was assumed to have 97 % reflectivity, and to be constructed of a multi-layer dielectric coating. The mirror reflectivities were determined using (4.11), with the absorption coefficients modeled in Figure A.21. The MSM detector was assumed to have finger width and spacing of $1 \mu\text{m}$ 252

Figure A.21. The net absorption characteristics for the structure of Figure A.20, with no mirrors, as a function of bias: 2 V (dashed line), 4 V (dotted line), 6 V (dashed-dotted line), and 10 V (solid line). A representative absorption coefficient was determined from the data, using the total thickness of absorbing material (300 nm). 253

Figure A.22. The wavelength-dependent quantum efficiency, simulated for the device of Figure A.20. The data are for bias voltages of 2, 3, 4, 6, 8, and 10 V, from bottom to top. Bias-dependent quantum efficiency is predicted, over a wavelength band of 5 nm. 254

Figure A.23. Predicted quantum efficiency at 860 nm, as a function of bias, is shown. The quantum efficiency varies from 20 % to over 90 %, with increase of bias voltage from 2 to 10 V. 255

List of Abbreviations

ADM	anti-site defect model
AlGaAs	aluminum gallium arsenide
APD	avalanche photodetector
AR	anti-reflection
DBR	distributed Bragg reflector
DH-MSM	double-heterostructure MSM
DX	donor-related
E-beam	electron beam
EDFA	erbium doped fiber amplifier
EFA	envelope function approximation
EMA	effective mass approximation
FET	field effect transistor
GaAs	gallium arsenide
HBT	heterojunction bipolar transistor
HDTV	high-definition television
HEMT	high electron mobility transistor
HRXRD	high-resolution X-ray diffraction
HP	Hewlett Packard
IMMPA	impedance-matched MSM photodetector array
InAlAs	indium aluminum arsenide
InAlGaAs	indium aluminum gallium arsenide
InGaAs	indium gallium arsenide
InGaAsP	indium gallium arsenide phosphide
InGaP	indium gallium phosphide
InP	indium phosphide
MBE	molecular beam epitaxy
MESFET	metal-semiconductor field effect transistor
MOCVD	metal-organic chemical vapor deposition
MODFET	modulation-doped field effect transistor
MOVPE	metal-organic vapor-phase epitaxy

MQW	multiple quantum well
MSM	metal semiconductor metal photodetector
OC-48	optical carrier modulated at 2.488 Gb/s
OC-192	optical carrier modulated at 9.953 Gb/s
OEIC	optoelectronic integrated circuit
PECVD	plasma-enhanced chemical vapor deposition
p-i-n	p-type-intrinsic-n-type photodetector
Q	quality factor
QCSE	quantum-confined Stark effect
QWS	quarter-wave stack
RCEPD	resonant-cavity-enhanced photodetector
RF	radio frequency
SEM	scanning electron microscope
TEM	transmission electron microscope
UV	ultraviolet
TWPA	traveling-wave photodetector array
VCSEL	vertical-cavity surface-emitting laser
VMPA	velocity-matched photodetector array
WDM	wavelength-division multiplexing

1. Applications for Metal-Semiconductor-Metal Photodetectors

1.1. Introduction – Photodetectors

A photodetector is a device that converts the energy of photons into some other form of energy, such as thermal or electrical energy. The modern applications of photodetectors are numerous, and they are important for fiber optics, photography, astronomy, spectroscopy, plasma physics, high-energy physics, sensors and monitoring, and many increasingly pedestrian devices such as grocery store scanners.

This thesis is concerned mainly with metal-semiconductor-metal (MSM) photodetectors, and this section is intended to give some perspective on their particular strengths and applications. Figure 1.1 provides a useful starting point for discussion. It is a common classification system [1] for photon detectors, including both the tube devices, which still find modern application, and the increasingly popular solid-state devices, generally employing a photosensitive semiconductor.

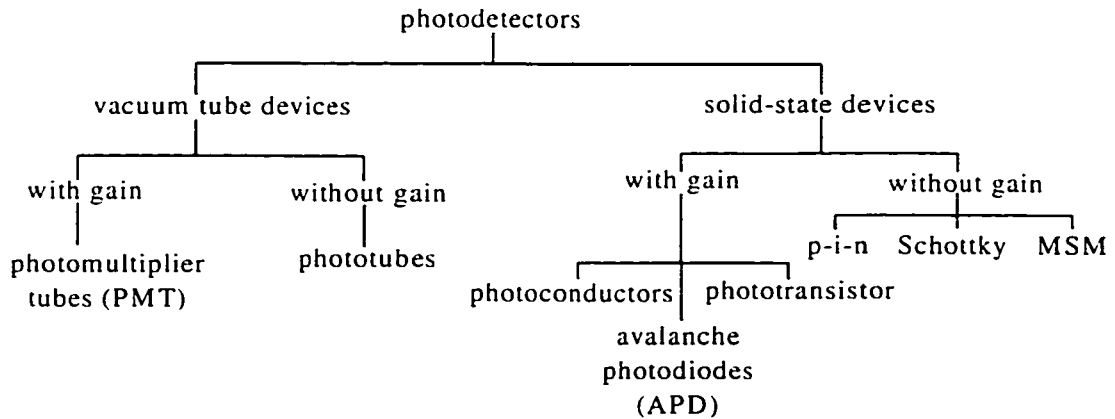


Figure 1.1. A useful classification system for photodetectors is shown. While vacuum tube devices are still used, for example in ultra-sensitive photon-counting applications, solid-state devices dominate the overall market. MSM photodetectors fall in the category of solid-state devices, without gain. These are the devices used for the highest speed applications.

Figure 1.1 does not include the so-called thermal detectors [2], such as thermoelectric detectors and bolometers. In thermal detectors, the absorption of light raises the temperature of a portion of the device, which results in a change in

some property of the device that can be conveniently detected by electrical circuitry. In photon detectors, the linkage between the light absorption and a resultant electrical signal is direct, and is provided by some quantum event. Examples are the emission of an electron from the surface of a metal, or the raising of an electron from the valence to the conduction band in a semiconductor.

As shown in Figure 1.1, the main criterion used to classify photodetectors, aside from their physical structure, is whether or not they exhibit photocurrent gain. Good general discussions on the nature and sources of photocurrent gain can be found elsewhere [3],[4]. The most important details are briefly reviewed here. In the discussion to follow, only solid-state devices are considered.

1.1.1. Photocurrent Gain – Deleterious Effects

It is perhaps most illustrative to describe a gain-free photodetector first. In that type of device, each photon absorbed in the photosensitive semiconductor creates one electron and one hole. Further, in the absence of internal gain or loss mechanisms, each photogenerated carrier contributes to current in the external circuitry attached to the photodetector. The responsivity is a measure of the conversion efficiency, and for a gain-free photodetector (with unity external quantum efficiency) is given by [2]

$$R = \frac{e}{h\nu} [A/W], \quad (1.1)$$

where e is the electron charge, h is the Planck constant, and ν is the frequency of the incident photons.

Equation (1.1) is the transducer relationship for the photodetector, and quantifies the conversion of photons into charge carriers. In a photodetector with gain, there is not a one-to-one relationship between the generated charge carriers and the incident photons, as suggested by (1.1). Rather, some physical process in the photodetector results in multiple charge carriers for each incident photon.

The most basic example of this is photoconductive gain, which occurs in photoconductors. Photoconductors are simply a region of photosensitive semiconductor, with ohmic electrodes. Absorption of photons lowers the

resistivity of the semiconductor, so that a photocurrent flows between positive (anode) and negative (cathode) electrodes [5]. The photocurrent is produced by holes flowing towards the cathode, and by electrons flowing towards the anode. Photoconductive gain occurs as a result of different transit-times for electrons and holes. The primary electrons (those created by photon absorption) are swept out very quickly, relative to the time it takes the holes to be swept out. To preserve charge balance in the semiconductor, the ohmic cathode electrodes inject electrons into the semiconductor until the primary holes have been completely removed. The electrons injected by the cathode are termed *secondary charge carriers*.

In photoconductors, and in other photodetectors, gain can result from more complex physical processes. For example, if some of the primary charge carriers are trapped, or pileup at heterojunctions, their collection is delayed. In this case, secondary carriers may be injected until the trapped carriers emit or recombine. This illustrates why gain is treated as a deleterious mechanism for the high-speed devices of interest here. The slowest (or most delayed) carriers determine the ultimate speed of the detector.

In time domain experiments, gain is often manifested as a long, slowly decaying tail in the impulse response of the detector. In the frequency domain, it correspondingly appears as a peaked response at the lowest frequencies, falling off dramatically with increasing frequency. Thus, it is often termed *low-frequency gain*. The slope of the roll-off is dependent on the characteristic lifetimes of the mechanisms causing the gain. For example, carriers might have an emission lifetime, once trapped, on the order of a few nanoseconds. This implies that the gain will manifest itself for frequencies less than 1 GHz.

The effect of low-frequency gain is that the bandwidth linearity of a device is degraded. In simple terms, the device is slower as a result of the gain process. For this reason, the devices used for the highest speed applications are designed to suppress gain, by preventing secondary carrier injection. In the p-i-n photodetectors, secondary carrier injection is prevented by the presence of a reverse-biased p-n junction. In Schottky and MSM photodetectors, rectifying

Schottky contacts prevent secondary carrier injection. Ideally, speed in these devices is determined only by the transit-times of primary photogenerated carriers. As the results in Chapter 3 indicate, rectifying contacts do not completely nullify secondary carrier injection. This is especially true if trapping or carrier pileup creates a charge imbalance in the device, and strong fields are present at the contacts. Thus, careful design is often required to minimize the physical mechanisms that cause secondary carrier injection.

Gain is not always an undesirable device characteristic. Over a limited bandwidth, it can greatly increase the sensitivity of a photodetector. For this reason, avalanche photodetectors (APD) have traditionally been the device of choice in receivers for long-haul fiber optic systems [6]. They generally allow higher signal to noise ratio, as compared to p-i-n photodetectors, in high speed, low-power systems [7]. However, APD's require high bias voltage and are not suitable for integration. In addition, the avalanche gain process limits device speed to 10-20 GHz at present [8], for reasons similar to those described above.

As discussed in the following sections, the trend in optoelectronics is towards higher speeds (40 Gb/s and beyond) and higher levels of integration. Only the gain-free solid-state detectors can provide the required bandwidths at present. Also, they are the most suitable for optoelectronic integration, as discussed in Section 1.4. Unless suitable APD's (with low bias requirements and higher speed) are developed, new systems will increasingly rely on p-i-n or MSM photodetectors, and electronic devices will provide the necessary gain.

1.2. Metal-Semiconductor-Metal Photodetectors

The metal-semiconductor-metal (MSM) structure consists of back-to-back Schottky contacts, separated by a layer of semiconductor, as shown in Figure 1.2. Sze et al. [9] originally studied this structure for its interesting dark current-voltage characteristics, which arise due to the bipolar nature of the device. Depending on the Schottky barrier heights of each contact, minority or majority carriers can be made to dominate the current characteristic over a particular voltage range. These

attributes are apparent only for thin semiconductor layers, where the depletion region of the reverse-bias contact can reach through to the other contact, prior to the onset of avalanche breakdown in the semiconductor. A detailed discussion of the relevant band diagrams and current characteristics is contained in reference [4].

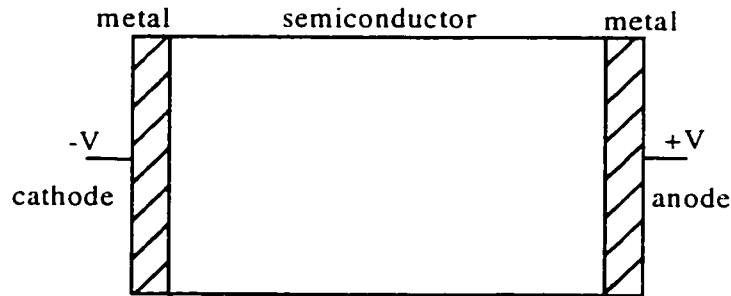


Figure 1.2. A one-dimensional metal-semiconductor-metal structure. A semiconductor material is sandwiched by back-to-back Schottky electrodes. The structure can exhibit interesting current-voltage characteristics, due to its bipolar nature. Electrons are injected over the Schottky barrier at the cathode, holes at the anode. Depending on the relative heights of electron and hole barriers, the current is dominated by one or the other carrier.

If the Schottky contacts in Figure 1.2 are replaced by ohmic contacts, and if the semiconductor is photosensitive at a wavelength of interest, we have the simple photoconductor type of detector, discussed in the preceding section. In the photoconductor, photogenerated carriers are swept out by a field applied between the ohmic contacts, with holes drifting to the cathode (negative) contact, and electrons to the anode contact. The speed of such a device is ultimately limited by the ohmic contact spacing, which determines the maximum transit-time of carriers contributing to the photocurrent. The speed can be increased by reducing the inter-contact distance, but at the expense of reducing the area of photosensitive semiconductor. Interdigitated electrodes, which find application as capacitors in microwave circuits [10], were introduced to alleviate the inherent trade-off between speed and photosensitive area [11]. The interdigitated structure is illustrated in Figure 1.3.

In this structure, carrier transit-times are approximately determined by the finger spacing, while the entire electrode structure can be illuminated, thus easing the area limitation. It also turns out that the interdigitated structure exhibits low

intrinsic capacitance [12], as discussed further in Section 1.6. The major drawback is that the electrodes are typically an opaque metal, and shadow a portion of the illuminated region, reducing responsivity.

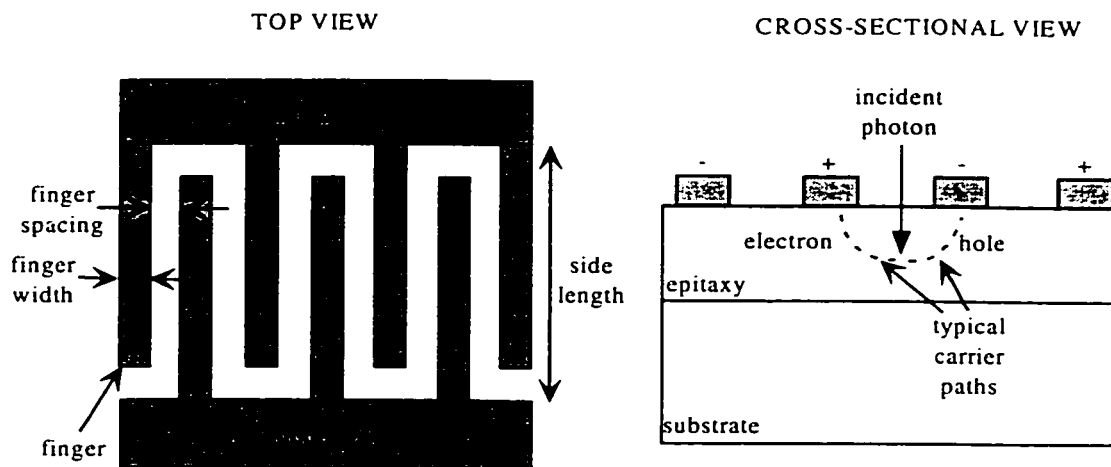


Figure 1.3. Schematic top and cross-sectional views of an interdigitated photodetector are shown. The important geometrical parameters of the electrode structure are finger spacing, finger width, and side length. The operation of the device is illustrated in the cross-sectional view: light generates carriers between the fingers, and the holes and electrons are swept along two-dimensional field lines, to the cathode and anode respectively.

The photoconductive device has several limitations for high-sensitivity, high-speed optoelectronic applications. First, with ohmic electrodes, the dark current is limited by the resistivity of the semiconductor, and is typically a couple of orders of magnitude higher than is desirable [13]. The dark current of the photodetector is important in determining the overall noise performance in modern optical receiver and signal processing circuitry [14]. Second, the devices exhibit low-frequency gain, as discussed above. The low-frequency gain problem is exacerbated in many applications, since the optical carrier of the high frequency photonic signal typically has a large DC background light level. When these signals are incident on a photodetector with low-frequency gain, the resulting shot-noise level is much greater than that due to dark current alone [14]. Therefore, photoconductors cannot deliver the speed or noise performance required in modern optoelectronic systems.

Around 1980 [11],[15], researchers began to investigate the advantages of using rectifying, Schottky contacts in the interdigitated electrode structure. The motivation was to produce a gain-free, fast, low-noise photodetector while maintaining the inherent advantages (low capacitance and ease of fabrication) of the interdigital photoconductor. With Schottky contacts, dark current is determined by thermionic emission at the metal-semiconductor junctions [9]. In addition, these barriers greatly reduce secondary carrier injection, thereby reducing or eliminating gain [16]. This produces benefits in terms of speed and noise performance, as discussed above. The terminology *metal-semiconductor-metal (MSM)* photodetector, while an accurate description of the photoconductive detector, is traditionally restricted to those devices that incorporate Schottky contacts.

MSM photodetectors currently compete with p-i-n photodetectors [17], in the highest-speed and highest sensitivity telecommunications applications. The key advantages of MSM photodetectors relative to p-i-n photodetectors are summarized in Section 1.5. However, in the following section we introduce the main applications to which this thesis has been addressed, optoelectronic switching and signal processing techniques.

1.3. Optoelectronic Matrix Switches

1.3.1. Optoelectronic Space-Division Switching

MSM photodetectors are of general interest for high-speed optical communications, as discussed further in Section 1.4. However, the devices discussed in this thesis were designed primarily for application to optoelectronic switching and signal processing systems. This is especially true of the MSM photodetector arrays discussed in Chapter 5. In this section, the basic concepts of optoelectronic switching and signal processing are reviewed. The purpose here is not to give a detailed treatment of the optoelectronic switching architecture [18]. Rather, the main strengths and weaknesses are highlighted, to facilitate the discussion of MSM photodetectors in the remainder of the thesis.

The optoelectronic switching technique was originally conceived [19] as a technique for the switched distribution of analog video signals. Since that first demonstration, the basic structure has been applied to numerous other systems, including digital switches, analog and digital signal processors, and artificial neural networks [20]. A key element in all of these systems is a broadband array of photodetectors. The term *array* refers to an architecture in which several photodetectors drive a common load. In simplest form, the array is several photodetectors interconnected by a common bus, so that there is an electrical summation of their signals. The basic optoelectronic switching architecture is illustrated in Figure 1.4.

The structure is a hybrid of photonic and electronic elements. It is apparent that the architecture is that of a crosspoint (space) switch. In the optoelectronic version shown, the input signals are distributed to the crosspoints by an optical distribution network. The optical power distribution can be designed using multi-mode fiber power splitters [21], polymer or other waveguides [22], or free-space beams and diffractive optics [23].

The crosspoints are photodetectors, and the switching function is achieved by controlling their photosensitivity, by means of their bias voltage. One photodetector corresponding to each input path is associated with a given output port. The photodetectors for each output port are passively summed, using a simple hard-wired arrangement. In this way, one or more of the input signals can appear at a given output port, in electronic form. The device in Figure 1.4 has been termed a matrix switch [18], which reflects its architecture of row-wise inputs and column-wise outputs.

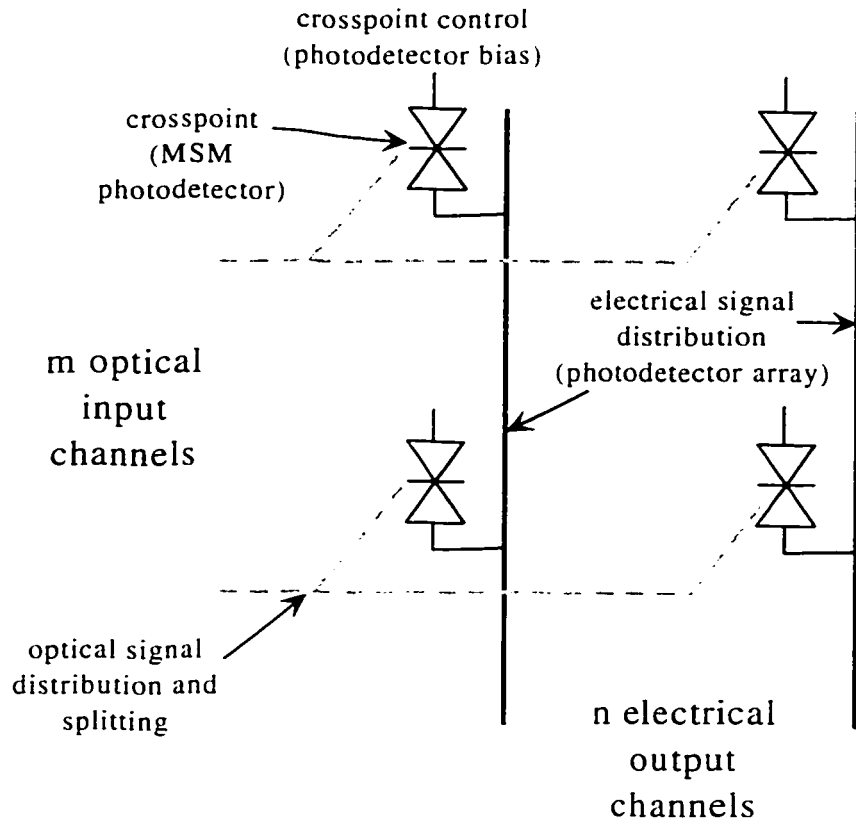


Figure 1.4. The optoelectronic switching technique is illustrated schematically. A 2x2 space-switch is shown, but the matrix size is generally m rows by n columns. The input channels are optical signals, which can derive from local or remote laser transmitters. The output channels are electrical signals, and typically travel on the common bus of a photodetector array (see Chapter 5). The accepted symbol for an MSM photodetector (back-to-back rectifying junctions) is shown at the crosspoints of the switch. Bias is used to control the responsivity of the photodetectors, thereby enabling a crosspoint function. Broadband electrical signals must be accommodated by the photodetector array, as discussed in Chapter 5.

Optoelectronic switching has, to some extent, remained a good idea awaiting the appropriate application. It competes both with purely electronic and purely photonic switching methods. As data speeds have escalated rapidly over the past decade, electronic switches have kept pace. This has represented a major engineering challenge, and it is expected that purely electronic methods may become cost-prohibitive to implement [24] for digital data rates targeted in the near future. A major research effort has been applied to the search for all-optical switching fabrics [25], in which fiber-based signals are routed without conversion to electronic form. In this sense, the optoelectronic technique has been squeezed

out, by the familiar and surprisingly adaptable electronic techniques on one end, and by the nirvana promised by optical techniques on the other.

There is reason to believe that the markets for optoelectronic switching may just now be emerging, however. In the foreseeable future, a portion of the switching fabric in telephone company central offices will be electronic [26]. This is because telecommunications networks provide connections on demand, and require dynamic routing and circuit assignment capabilities. This is achieved by time and packet switching techniques. The logical elements (computers) which provide these functions are likely to remain as electronic devices. Thus, it is not entirely certain that all-optical switches will play a key role in the short term.

On the other hand, all large switching fabrics incorporate one or more space-division switching elements, like the matrix switch illustrated in Figure 1.4. The matrix switch fills various roles, including switching of entire broadband circuits. This can be part of the routine operation of the switching center, as in the provision of circuit-switched services (for example, a digital cross-connect function). Alternatively, the matrix switch may be used for network restoration, by switching broadband circuits to backup facilities. Another emerging application for broadband switching fabrics is in wavelength-division-multiplexed (WDM) networks [27],[28]. The erbium-doped fiber amplifier (EDFA) band limits the number of available wavelengths in a network, and EDFA's are not likely to be replaced for some time (they represent a large capital investment). Thus, wavelength reassignment will be necessary for WDM implementations in the near future. There is a need for broadband, wavelength routing nodes in these networks [29].

In a matrix (space-division) switch, the input and output signal paths must be physically close, since they intersect at the crosspoints. In purely electronic switches, electromagnetic coupling between and amongst input and output paths can be a severe problem. Each time a new aggregate data rate is targeted, the technological challenge of reducing crosstalk in such a switch is magnified many times [24]. For the OC-48 (2.5 Gb/s) channel rate of current optical networks,

various manufacturers have successfully implemented purely electronic matrix switches, typically with a maximum size of 16x16 [30]. The next generations of fiber systems will have aggregate data speeds of 10 Gb/s (OC-192), and beyond. The feasibility of electronic matrix switches for these data rates is not presently clear.

The main advantage in moving to the optoelectronic matrix is a reduction in electromagnetic coupling effects. As shown in Figure 1.4, the input paths consist of guided optical signals, and do not suffer from crosstalk problems. The output paths are electronic, but are interconnected only by optical paths. Thus, the output channels can be isolated from each other, almost arbitrarily. Optoelectronic crosspoint switches therefore have potential for much higher channel rates, and much larger matrix size. In addition, the cost of implementing the optoelectronic switch may be much less, due to the reduction in isolation requirements. Thus, optoelectronic switches may be viable and economical components, for the next one or two generations of fiber communications systems [18]. They have potential to achieve the required bit rates, while inherently providing electronic access to the aggregate channels.

Since electromagnetic coupling may be negligible in an optoelectronic switch, the inter-channel isolation is ultimately determined by the on-off contrast of the photodetector crosspoints [18]. In this regard, it is extremely advantageous if the photodetector crosspoints are non-responsive at zero bias. This is a key advantage of the MSM photodetector, as discussed in Section 1.5.

In the arguments presented above, it was implicit that the elements of the optoelectronic matrix can accommodate broadband signals, as necessary. In practice, the channel speed is limited by the bandwidth of the optoelectronic transducers. Obviously, the first requirement is that the individual photodetectors in the matrix have the required bandwidth. Development of broadband MSM photodetectors was the primary focus of this work, and is reported in Chapters 2 and 3. A greater challenge is achieving a broadband response for an array of photodetectors, electrically summed as in Figure 1.4. It has proven difficult to

realize such an array for operation at frequencies in the GHz range. Significant progress was made in the course of this research, and is detailed in Chapter 5.

Optoelectronic switches have some inherent disadvantages. Typically, they are configured for electrical signals at both the inputs and outputs. Thus, laser transmitters (or similar) are modulated, and drive the optical input ports in Figure 1.4. The overall signal path for the optoelectronic switch comprises an electrical to optical power conversion, a 1 to n power split, and an optical to electrical power conversion. Given the limited efficiency of the power conversions, and the significant splitting loss for a reasonably large matrix, signal loss through the switch can be as much as 60 dB [18]. Since it is generally desired that a switch not introduce loss, significant amplification is required at the output of each photodetector array.

Broadband electronic amplifiers with 60 dB of gain are neither trivial nor inexpensive. For this reason, it is important to minimize the sources of loss in the switch. One way to do this is to maximize the responsivity of the photodetector crosspoints. This motivated the development of resonant-cavity-enhanced MSM photodetectors (RCEPD), as discussed in Chapter 4.

1.3.2. Optoelectronic Signal Processing

The basic architecture of Figure 1.4 can be used to construct broadband signal processing elements. Previous demonstrations included an optoelectronic transversal filter [31], and an optoelectronic equalizer [32] for compensation of dispersion in fiber waveguides. The essential concept is illustrated in Figure 1.5.

In Figure 1.5, a single photodetector array is used to implement a delay-line filter. The input signal is split, and the subsequent paths have variable optical delays. The individual photodetectors are used to weight the contribution of each signal path, and the components are summed electrically by the array. More complex signal processing can be accomplished with an entire optoelectronic matrix [18].

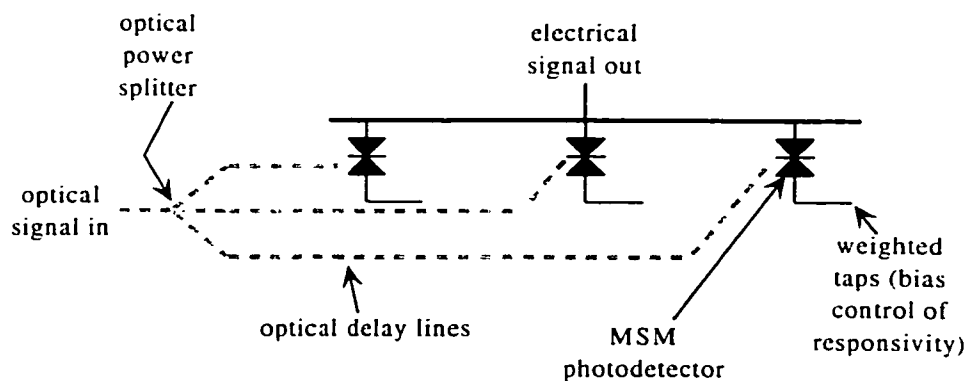


Figure 1.5. A schematic illustration of an optoelectronic signal-processing element is shown. A transversal filter (or other function) can be realized by using optical delay lines and weighted taps, followed by summation of the delayed and weighted components of the input signal. The broadband signal summation is provided by a photodetector array (see Chapter 5). More advanced processing functions can be realized using an entire optoelectronic matrix [20]. The technique is predicated on photodetectors that have variable responsivity (controlled by bias), but sufficient bandwidth over the required range of responsivity.

A key requirement here is that the photodetector responsivity is variable, and controlled by bias voltage. As shown in Chapters 2 and 3, the photoresponse of an optimized gain-free photodetector actually saturates at very low bias, and is insensitive to bias thereafter. Previously, signal processing demonstrations have relied on MSM photodetectors with significant low-frequency gain. Such devices have a bias-dependent responsivity as required. However, as discussed in Section 1.1, low-frequency gain is associated with limited bandwidth and high device noise. In addition, the bandwidth of such a device is likely to vary with bias.

In appendix A, a novel MSM device is proposed. The goal was to obtain a photodetector with the inherent attributes of the optimized MSM detector, but with bias-dependent responsivity. Such a device would be beneficial for broadband, optoelectronic signal processors.

1.4. Optoelectronic Integrated Circuits

As mentioned, a key motivation for the development of MSM photodetectors has been their suitability for integration with other devices. An

increasing amount of research and development resources are being assigned to optoelectronic integrated circuits (OEICs) [33],[34], at research facilities worldwide. In this section the issues surrounding the development of OEICs, especially as they relate to MSM photodetectors, are briefly reviewed.

The term *optoelectronics* emerged as part of the fiber optics revolution. It reflects the requirement, in modern telecommunications and computing, to interface between optical and electrical signal paths. Discrete optoelectronic components have traditionally met the basic requirements of point-to-point fiber communications. However, fiber networks are evolving into multi-point architectures, and the point of optical access is moving from the central office out to the subscriber [35]. In the future, the requirement for optoelectronic components, such as lasers and photodetectors, is likely to increase exponentially.

The technology pull is being provided by demands for broadband networking services, such as internet access and high definition television (HDTV). There is a need to achieve higher levels of integration of optoelectronic and electronic devices, to reduce component costs per subscriber. Optoelectronic integrated circuits (OEIC) combine electronic, optoelectronic, and potentially photonic devices, on a single semiconductor chip [33],[36]. The potential benefits are exactly those that accrued from the monolithic integration of electronic devices: higher performance, lower unit costs, greater reliability, and increased yields.

For OEICs to achieve these goals, a robust technology is required. The maturity of the technology must eventually meet and exceed that of present day silicon microelectronics. Simple and integrable devices, which are tolerant to process variations, are required. The MSM photodetector is potentially such a device, and their use in OEICs has been the main focus of research [37-40]. A simple example is given in Figure 1.6, which shows the monolithic integration of a high-speed FET and an MSM detector [16].

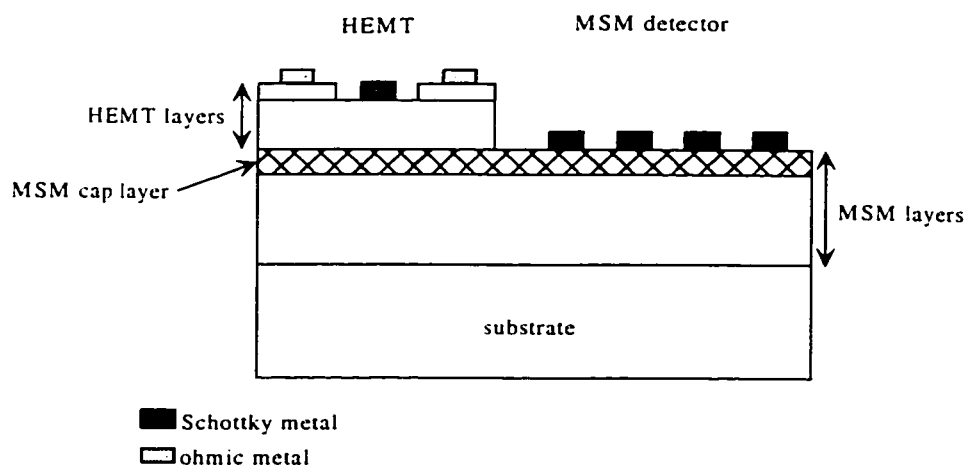


Figure 1.6. A schematic illustration of an OEIC is shown, incorporating a high electron mobility transistor (HEMT) and an MSM photodetector. The HEMT layers are very thin (typically 100 to 200 nm), so the structure is very nearly planar. The entire structure can be formed in a single epitaxial growth, followed by selective etching for access to the MSM detector layers. Inter-device isolation is provided by the wide band-gap, MSM cap layer (see Chapter 2). After [16].

There are generally two approaches to designing OEICs [33]: vertical devices, such as p-i-n photodetectors and HBTs, are combined, or lateral devices, such as MSM photodetectors and HEMTs, are combined. Vertical devices potentially offer higher circuit density. Also, there is greater control over the critical dimensions, which are defined by epitaxial growth rather than lithography. The fabrication complexity is much greater, however, as different devices typically require unique epitaxial structures. Regrowth or selective etching of many layers is required, and the surface may be very non-planar in the end [41]. As a result, fine tolerance control of electrical interconnections is more difficult.

Integration of planar devices is potentially much simpler, and circuit density is increased by use of advanced lithographic techniques. As shown in Figure 1.6, the high-speed HEMT requires a thin epitaxial structure only. The cap layer of the double-heterostructure MSM detector (see Chapter 2) isolates the transistor and photodetector active regions. The device is very nearly planar, so high-resolution photolithography is possible.

This section provided only a brief introduction to the current research in OEICs. Many novel material combinations and fabrication processes have been suggested, and are discussed in the references [37-40].

1.5. Comparison of MSM and p-i-n Photodetectors

As mentioned in Section 1.1, MSM photodetectors are generally viewed as an alternative to p-i-n photodetectors for the highest-speed applications. In this section the main comparison points are briefly reviewed, and the advantages of the MSM photodetector are highlighted.

The main attributes of interest for a high-speed photodetector are its bandwidth, its responsivity, and its noise properties. The bandwidths of both p-i-n and MSM photodetectors are ultimately limited by carrier transit-times. For p-i-n detectors, the relevant carrier transit is across the intrinsic region of the device. In the MSM detector, it is the transit-time between adjacent fingers (Figure 1.3) that is relevant. Without going into great detail, it can be stated that similar speeds are accessible for each type of detector [16],[17],[42]. In either case, higher speeds are generally obtained at the expense of lower responsivity.

With regards to responsivity, p-i-n detectors have a definite advantage. This is due to the partial shadowing of the absorption region by opaque metal fingers, in the top-illuminated MSM. This was discussed in Section 1.2. The lower responsivity of the MSM is somewhat compensated by its lower inherent capacitance. In a typical optoelectronic receiver, a transimpedance amplifier follows the photodetector. The capacitance of the photodetector is important in determining the overall sensitivity of the receiver [39]. Rogers [37] has shown that, in spite of the lower responsivity, MSM photodetectors improve the sensitivity of optoelectronic receivers, at least up to a certain bandwidth. Improvements in MSM detector responsivity, as discussed in Chapter 4, increase the bandwidth over which the MSM photodetector maintains an advantage, relative to the p-i-n detector.

Figure 1.7 is a schematic illustration of a typical, vertical p-i-n photodetector. In Figure 1.8, a schematic illustration of a typical, planar MSM photodetector is shown.

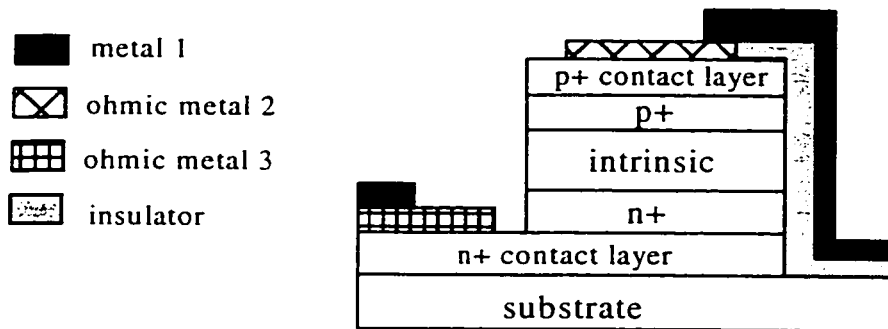


Figure 1.7. A typical p-i-n photodetector is shown schematically, in cross-section. The fabrication process starts with growth of at least five epitaxial layers, with both heavily doped n- and p-type layers required. Two separate ohmic metal layers are deposited, as the technology for ohmic contacts is unique for p- and n-type layers. A third metal layer is required, for circuit interconnects. The structure is vertical, so contacts must be made on more than one level. This complicates the definition of fine features.

Three primary advantages can be identified for the MSM detector: fabrication and integration are simplified, the device is inherently symmetric, and the capacitance is lower. The p-i-n photodetector requires up to twice as many processing steps. In addition, many of the features of the p-i-n detector are more complicated to realize in practice: it is more difficult to grow heavily doped layers accurately and repeatedly, ohmic electrodes require closely controlled recipes, and contacts must be made to two layers of the epitaxial structure. As a result, the p-i-n photodetector will generally cost more to fabricate.

Device symmetry is a key advantage of the MSM detector, in light of the discussion on optoelectronic switching and signal processing in Section 1.3. The on-off contrast of the photodetector determines the inter-channel isolation in the optoelectronic switch. Since p-i-n photodetectors are single junction devices, they exhibit a photoresponse at zero bias. It is necessary to forward bias a p-i-n photodetector to turn it off. This represents a complication, as well as a problematic dissipation of power, in the realization of practical systems [19]. The MSM photodetector, on the other hand, is very non-responsive at zero bias, due to

the opposing Schottky junctions. Very good contrast is possible, by simply removing bias from the detector. Some of the discrete MSM devices discussed in Chapter 3 exhibit at least 40 dB of on-off contrast up to 20 GHz.

For signal processing applications, the device symmetry allows bipolar weighting of the MSM photodetector response. Bipolar tap weights are required to realize bandpass and high pass transversal filters [19].

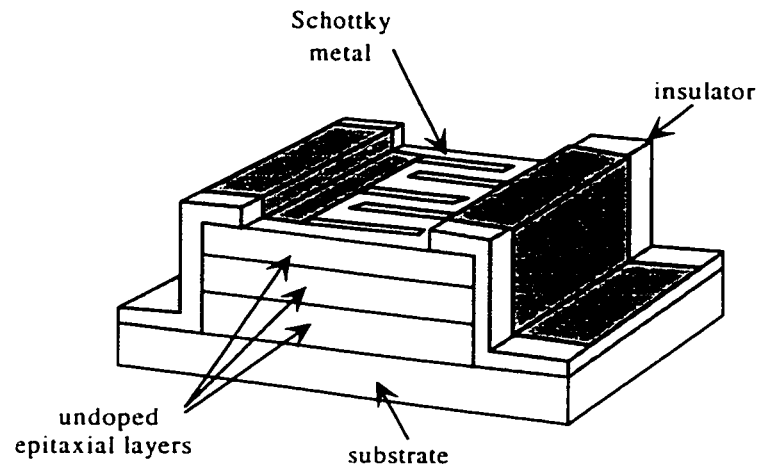


Figure 1.8. A typical MSM photodetector is shown, in cutout view. The structure is planar (lateral), with both contacts lying on the surface. Also, the device is symmetrical, and can be biased in either direction. As shown, the active region is isolated by formation of a mesa (see Chapter 2). The absence of doped layers greatly simplifies the epitaxial growth.

Finally, the low capacitance of the MSM detector is an advantage in optoelectronic receivers, as discussed above. In addition, it is generally desirable for high-speed devices to have low parasitic capacitance. This is illustrated in the design of broadband photodetector arrays, in Chapter 5. It is important to understand all sources of parasitic capacitance, however. The analysis by Rogers [37], discussed above, only considered the geometrical capacitance associated with the MSM detector's interdigitated electrodes. In Section 1.6.1, other potential sources of capacitance are discussed.

1.6. Fundamental Properties of MSM Photodetectors

For an extensive introduction to the properties of MSM photodetectors, good reviews are available elsewhere [4],[16],[42]. However, it is worthwhile to briefly mention some fundamental properties here. The capacitance exhibited by a telecommunications device is always of primary importance. For the MSM photodetector arrays of Chapter 5, an understanding of the sources of capacitance is critical. These are reviewed in Section 1.6.1.

The capacitance of MSM photodetectors is very low, generally, so the speed of discrete devices is determined by transit-times. In Section 1.6.2, some models for transit-time-limited speed are discussed. These are useful for interpreting the results presented in Chapter 3.

1.6.1. Sources of Capacitance in MSM Photodetectors

The capacitance of MSM photodetectors is often underestimated [43], as the finite conductivity of the epitaxial layers is routinely neglected. In that approximation, the capacitance of the interdigitated electrodes can be estimated using conformal transformations, derived by Lim and Moore [44]. Those analytical expressions are described in [4], and the associated capacitance will be termed the *geometrical* capacitance of the active region.

Generally, two other sources of capacitance must be considered. First, the interdigitated electrodes invariably have attached bond pads or interconnect metal. Because the interdigitated electrodes exhibit very low geometrical capacitance (typically 10 to 100 fF), the capacitance associated with interconnect metal can often dominate [42]. This is especially critical when several MSM photodetectors are integrated as part of an array, as discussed in Chapter 5. In that case, a relatively large metal pattern is attached to one side of the MSM photodetector, so the associated parasitic capacitance can be large.

Both sources of capacitance discussed above are essentially geometrical in nature; they would be present even if the semiconductor were a perfect dielectric.

In reality, the semiconductor is not a perfect dielectric, and the observed capacitance exceeds the geometrical estimate, for both the bond pads and the interdigitated electrodes. This increase is due to charge storage in the semiconductor layers, and is generally called depletion capacitance [45],[46]. Depletion capacitance is illustrated schematically in Figure 1.9.

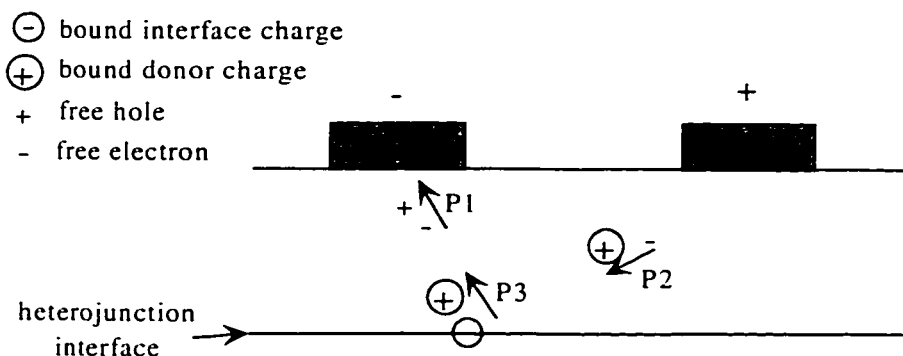


Figure 1.9. Sources of excess charge polarization, and thus excess capacitance, are shown. Two MSM detector fingers are shown in cross-section. Free charge carriers can increase capacitance by interacting with each other (P1), or with dopant atoms (P2). Stored charge at an interface can interact with free charge or with dopant atoms (P3). P1 and P2 increase with illumination intensity, and decrease with bias. P3 may be relatively insensitive to bias or illumination conditions.

The capacitance of metal electrodes on a dielectric is determined by polarization of bound atomic charges. In an epitaxial semiconductor, many sources of excess charge are possible, and each may make a polarization contribution, increasing the device capacitance over a certain range of bias and frequency. Three sources of polarization are shown in Figure 1.9. The first two, labeled P1 and P2, are always present in a non-depleted semiconductor, and result from free charge carriers. Generally speaking, the free charge density in the MSM photodetector will depend on bias and illumination conditions, as well as the doping level of the layers.

In the MSM detector there is usually a weak-field region far beneath the contacts, which may not be fully depleted at the operating bias of the device. Thus the geometrical capacitance estimate will be slightly low, even under low-level illumination. A space charge (depletion) capacitance contribution should always be considered in accurate device models [46].

The third source of polarization, labeled P3 in Figure 1.9, arises from charge storage at interfaces. This is common in III-V semiconductors, as discussed in Chapter 2. Polarization contributed by interface states is especially problematic, as it may be due entirely to quasi-bound charges. For example, a negative charge stored at the interface can interact with adjacent, depleted donor atoms in the bulk. The resultant capacitance contribution might not be reduced with the application of bias, unlike the contributions due to free charges. Rather, high quality interfaces are required, with few charged states, to minimize this source of excess capacitance. As an example, Ralph et al. [45] reported that an InAlAs buffer layer on InP, grown prior to an InGaAs absorption region, was effective in reducing capacitance.

In summary, several factors must be considered in estimating the capacitance of MSM photodetectors. Geometrical capacitance, due to interdigitated electrodes and attached pad metal, can generally be approximated by analytical or numerical methods. In operation, the device will have capacitance slightly or even much greater than those estimates imply, especially for high illumination and/or low bias. Some of this excess depletion capacitance is due to free charge carriers, and is inevitable. However, highly resistive (lightly doped) epitaxial layers with high quality interface characteristics are beneficial. As discussed in Chapter 5, this can be critical to the accurate prediction of detector capacitance.

1.6.2. Transit-Time-Limited Speed of MSM Photodetectors

In the past decade, several theoretical treatments have been reported for estimating the transit-time limited bandwidth of MSM photodetectors. These techniques vary in their rigor, and the alternative approaches were reviewed in [4]. A couple of key points are raised here, to facilitate discussion in the remainder of the thesis.

First, for photolithographically defined MSM photodetectors, carrier transport is well described by steady-state, carrier velocity versus electric field

relationships [47]. This holds for devices with finger spacing as small as $0.5\ \mu\text{m}$, and therefore encompasses all of the devices discussed in this thesis. Two comprehensive studies of transit-time limited speed are available, based on this steady-state velocity model [16],[42].

In Figure 1.10, the data of Bottcher et al. [42] have been adapted to a convenient form. The bandwidth of an MSM photodetector with $1\ \mu\text{m}$ finger spacing and width ('1x1') is plotted versus the thickness of the absorption region. The data were obtained assuming a bias voltage of 10 V. They should represent the saturation bandwidth of the device, as carriers will move at saturation velocity for such a large applied field.

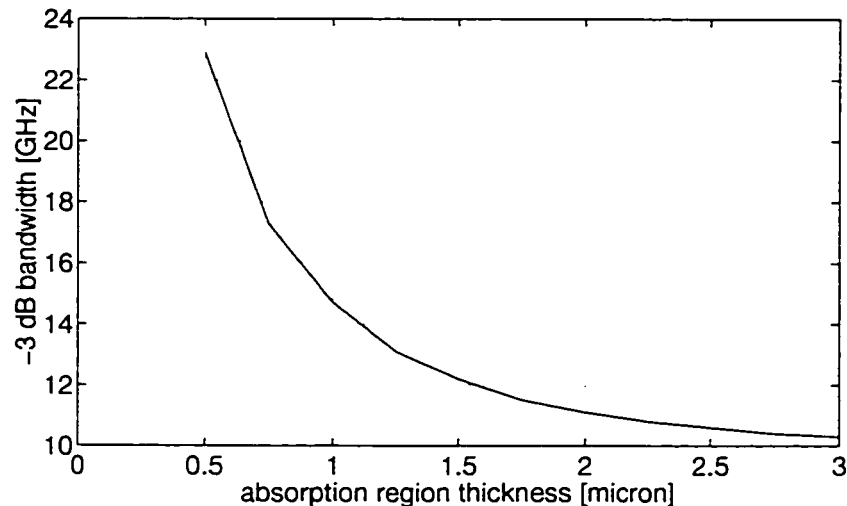


Figure 1.10. The saturation bandwidth of an MSM photodetector with $1\ \mu\text{m}$ finger spacing and width is plotted, versus the thickness of the absorption region. The plot illustrates the benefit of reducing this thickness: for a $0.5\ \mu\text{m}$ absorber, the bandwidth is enhanced by more than a factor of 2, compared to an infinite absorber. The data were adapted from [42].

Roughly speaking, for finger spacing other than $1\ \mu\text{m}$, the transit-time limited bandwidth can be estimated by dividing the numbers in Figure 1.10 by the finger spacing in μm . For example, $2\ \mu\text{m}$ finger spacing would correspond to approximately 12 GHz bandwidth, for a $0.5\ \mu\text{m}$ absorption region. This is a very rough approximation only, but is useful for obtaining a quick estimate.

For devices with thin absorption regions, such as most of the devices discussed in Chapters 3 and 4, the frequency response can be estimated analytically, as [48]

$$\frac{I(\omega)}{I(0)} = \frac{1}{j\omega\tau_n} \left[1 - \frac{1 - \exp(-j\omega\tau_n)}{j\omega\tau_n} \right] + \frac{1}{j\omega\tau_p} \left[1 - \frac{1 - \exp(-j\omega\tau_p)}{j\omega\tau_p} \right] \quad (1.2)$$

$I(0)$ is the DC photocurrent, and τ_n and τ_p are the mean electron and hole transit-times, respectively. Equation (1.2) is semi-empirical, as it requires prior knowledge of the transit-times. However, it is useful for illustrating the typical frequency response of a transit-time limited MSM photodetector. As an example, consider an MSM detector with 1 μm finger spacing. Typical saturation velocities for holes and electrons, in GaAs, are on the order of $5 \times 10^4 \text{ m s}^{-1}$ and 10^5 m s^{-1} , respectively [49]. The corresponding mean transit-times are on the order of 10-20 ps for electrons, and 20-40 ps for holes. The high estimates include a factor of two, to account for the finite thickness of the absorbing layer. Using the middle of range values in (1.2), a frequency response is plotted in Figure 1.11.

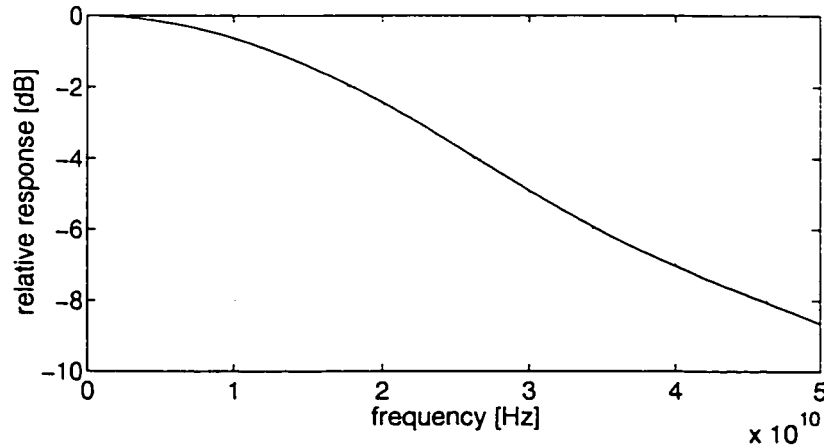


Figure 1.11. A frequency response derived from the approximate analytical expression of equation (1.2) is shown. The hole and electron transit-times were assumed to be 15 ps and 30 ps, respectively. These values should be reasonably representative of an MSM photodetector with 1 μm finger spacing, and biased such that all carriers are traveling at saturation velocity. Note the good agreement with the experimental result for a similar device in Figure 3.21.

An experimental bandwidth in agreement with a transit-time limited estimate provides strong evidence that a device has optimized speed. In other words, it shows that physical speed-limiting mechanisms, other than the saturation velocity of carriers, have been minimized. Note the good agreement between Figure 1.11 and the experimental result in Figure 3.21, for an MSM detector with similar geometry.

1.7. High-Frequency Test System

High-frequency results are reported for many of the devices in Chapters 3 and 4. In this section, the test system is described briefly. All results were obtained in the frequency domain, using a Hewlett-Packard 8510-B vector network analyzer. The test system is illustrated schematically in Figure 1.12. A detailed description of the test system can be found in [4], including the optical and RF powers at every point in the circuit.

The discrete MSM photodetectors discussed in Chapters 3 and 4 were contacted with a broadband, on-wafer, ground-signal probe. The probe was manufactured by Picobrobe, located in Naples, Florida, and was model number 40A-GS-150-P. Picobrobe provided a calibration plot for the probe, showing less than 1 dB insertion loss up to 40 GHz. The photodetector arrays discussed in Chapter 5 were mounted on high-frequency test jigs, the descriptions of which are left for that chapter.

The test system was calibrated by inserting a commercially available Schottky photodetector, with known response, in place of the device under test. Two calibrated photodetectors were used, both New Focus model 1434. New Focus provided a plot for each photodetector, showing less than 2 dB of ripple up to 25 GHz. The system calibration was always performed with one device, and confirmed with the other. The confirmation is important, since the commercial photodetectors are the only portion of the test system that cannot be calibrated out by the network analyzer. Thus, a damaged or non-functioning calibration detector would lead to erroneous results.

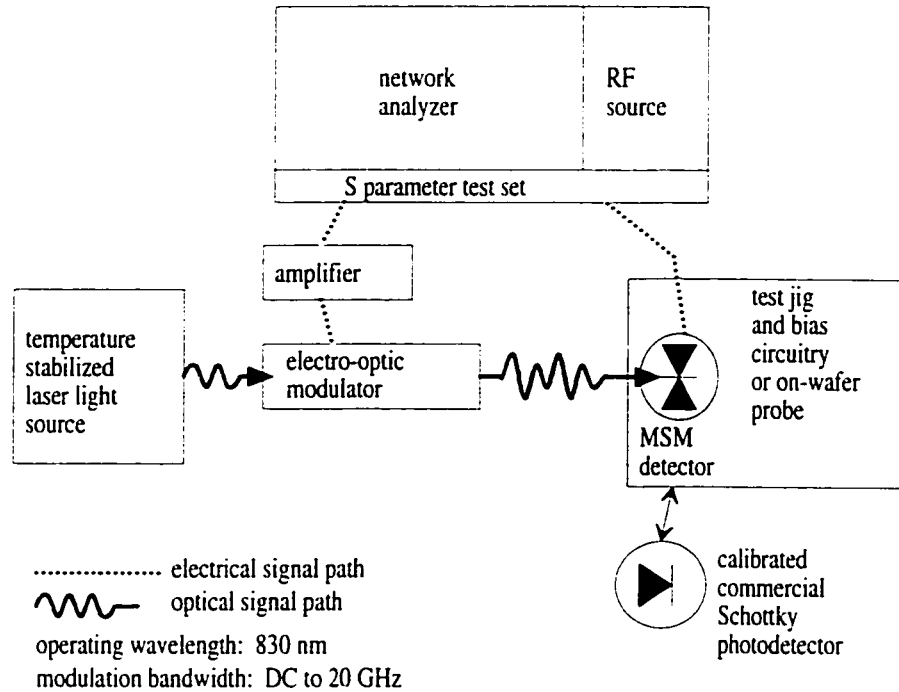


Figure 1.12. Schematic block diagram of the high-frequency test system is shown. A temperature-stabilized, fiber-pigtailed semiconductor laser drives a lithium niobate electro-optic modulator. The RF power for the modulator is provided by an amplified signal from one port of the network analyzer. The other port of the network analyzer extracts the RF signal from the photodetector under test. The system is calibrated with a commercially available Schottky photodetector (New Focus, model number 1434), with a -3 dB bandwidth in excess of 25 GHz.

It is worth mentioning a couple of details that were neglected in the previous description of the test system [4]. First, as can be verified from the power levels given in [4], the light illuminating the device under test typically had a 20 % depth of modulation at low frequency, dropping to 10 % depth of modulation at 15 to 20 GHz. Thus, a considerable amount of DC background light is always present in the measurements. From the discussion in Section 1.1.1, this can affect device performance, via low-frequency gain mechanisms. The test procedure represents a worst-case scenario, in that sense, since a large amount of continuous-wave light increases the potential for carrier trapping and pileup, which will tend to slow a device. Thus, the results presented in Chapters 3 and 4 should represent modest estimates of how the devices will perform in real systems. Still, it would be useful to quantify the effects of changes in modulation depth in future work.

A second point of interest is the mismatch at the discrete photodetectors under test. The commercial photodetectors are mounted in an enclosed package, with an internal $50\ \Omega$ matching resistor, and an external microwave connector. During system calibration, the network analyzer is therefore matched at both ports. Subsequently, the discrete devices were probed, as described above, without a matching resistor. A slight calibration error could result from this change in matching conditions. Commercial test sets, such as Hewlett-Packard's Lightwave Test Set attachments [50], use calibrated sources and detectors as a means of removing this error. In an attempt to quantify this error, a 10 dB attenuator was inserted in the experimental circuit, adjacent to the on-wafer probe. This provided 20 dB of round-trip attenuation to any signals spuriously reflected at the probed device. No change in the shape of the frequency response was observed, for several devices tested. This indicated that the error associated with the mismatch was negligible, for the range of frequencies considered in this thesis (0 to 20 GHz). Compensating this error would be a refinement of the test system, however, for future work.

Finally, it is mentioned that three similar test systems were used, operating at 830 nm, 1320 nm, and 1535 nm. The 830 nm test system was described in detail in [4]. The others were obtained from the Communications Research Centre in Ottawa, and are essentially identical except for the wavelength of operation.

1.8. Thesis Organization

This thesis is divided into seven chapters, organized as follows. Chapter 1 introduces the MSM photodetector and its applications. Chapter 2 describes technological issues and challenges for the realization of high-performance, reliable MSM photodetectors. Emphasis is placed on device attributes that remain to be optimized, especially the elimination of deleterious surface effects. In addition, proposals are made for high-performance MSM photodetectors in various material systems. Devices were fabricated based on those proposals, and Chapter 3 describes the experimental results.

Chapter 4 describes techniques to improve the responsivity of MSM photodetectors, and detailed theory and proposals for resonant-cavity-enhanced detectors are developed. Based on those proposals, two resonant-cavity wafers were obtained, and the experimental results are also discussed in Chapter 4.

In appendix A, a novel device is proposed, based on the resonant-cavity techniques of Chapter 4 and the electro-optic effects made possible by multiple-quantum wells (MQW). A theoretical analysis and a semi-empirical simulation are included.

In Chapter 5, progress in the development of broadband MSM photodetector arrays is presented. Several alternative layouts were studied experimentally. A new technique is suggested and experimentally verified. The technique involves treating the photodetector array as a periodically loaded transmission line, and matching it to the external system.

Finally, Chapter 6 contains a summary of the results, and recommendations for future work.

2. Technological Considerations for MSM Photodetectors

2.1. Introduction- Materials for MSM Photodetectors

A semiconductor is characterized by mechanical, electrical, optical, thermal, and electro-optical attributes. There are myriad applications for semiconductors, in fiber optics, electronics and optoelectronics. No single material has optimal characteristics for all of these applications. Rather, for almost every particular application, a unique material system has taken on the primary role. An excellent discussion of the comparison points for semiconductors, and of the strengths and weaknesses of each material system, has been provided by Bean [49].

Silicon dominates the very-large-scale-integrated electronics market, due to its good electrical transport characteristics, its excellent mechanical and thermal attributes, and the ubiquity of the raw material. In addition, many silicon devices (especially MOS devices) rely on the excellent and controllable properties of its free surfaces and interfaces.

On the other hand, if one sets out to define an ideal semiconductor [49], silicon has several apparent weaknesses. Foremost is its indirect band-gap, which limits its usefulness in optoelectronics, where efficient light emitters and detectors are required. Also, the electron and hole transport properties of silicon are mediocre, in comparison with GaAs and $\text{In}_{0.53}\text{Ga}_{0.47}\text{As}$. Thus, for the highest speed applications, such as monolithic microwave integrated circuits (MMICs), GaAs MESFETs, and increasingly $\text{In}_{0.53}\text{Ga}_{0.47}\text{As}$ -based MODFETs and HBTs, are favored. Finally, while impressive progress has been made in the area of strained silicon-germanium heterostructures [51], the lack of a lattice-matched alloy compatible with silicon is a major drawback. The advances in device performance owing to band-gap engineering in III-V semiconductors are too numerous to list.

For optoelectronics, the starting point in choosing a semiconductor family is to match the operational wavelengths of a system to the available band-gaps. It is convenient to plot the minimum band-gaps and lattice constants of the various semiconductors on a two-dimensional grid, as in Figure 2.1. The semiconductors

shown are the commonly used material combinations, from columns II to VI of the periodic table.

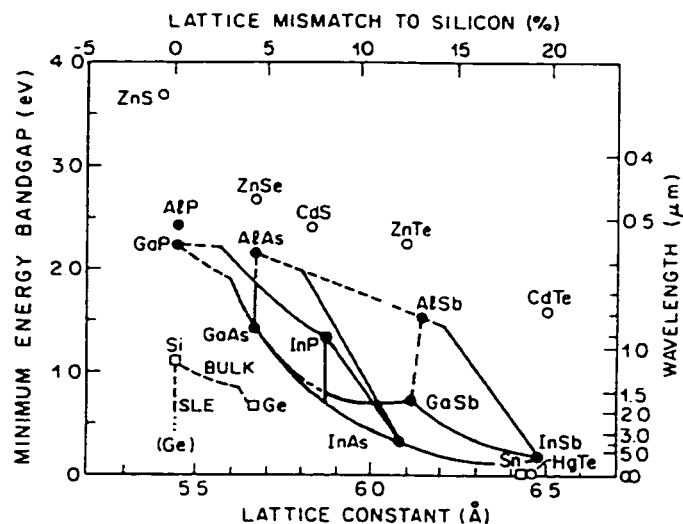


Figure 2.1. Diagram of band-gap energy vs. lattice-constant, for the column IV, III-V, and II-VI semiconductors. The left vertical axis indicates the minimum band-gap energy, and the right vertical axis indicates the corresponding wavelength (photon energy) of light. The horizontal axis shows the lattice-constant of the semiconductor crystal. Solid lines indicate direct band-gap alloys, dotted lines indicate indirect band-gaps. Also shown is the strained-layer epitaxial (SLE) and lattice-mismatched (bulk) growth of Si-Ge on silicon. The figure is from reference [49].

After silicon and germanium, the most common substrate materials available are GaAs and InP. GaAs has become a relatively mature material system, due to the success of the GaAs MESFET process. InP was developed extensively in the 1980s, to fill a need for optoelectronic devices in fiber optic systems. All of the devices proposed and fabricated here were grown on one of these III-V substrates.

For each of GaAs and InP substrates, there are two common, alternative material systems that can be grown lattice-matched. In each case, a fairly large and continuous range of direct band-gaps is possible with these materials. The most-mature hetero-epitaxial material system is the $\text{Al}_x\text{Ga}_{1-x}\text{As}/\text{GaAs}$ family, owing to its nearly perfect lattice-match for all values of x . It is popular for fabrication of heterojunction transistors, and for light sources operating in the 800 nm wavelength region. $\text{In}_x\text{Ga}_{1-x}\text{As}_y\text{P}_{1-y}/\text{GaAs}$ has received some attention of late,

due to the superior interface characteristics of the phosphorus alloys [52]. Also, $\text{In}_{0.49}\text{Ga}_{0.51}\text{P}$ has higher breakdown fields than AlGaAs, and is attractive as an emitter material in high-power GaAs-based HBTs [53].

On InP, the most-mature material system is $\text{In}_x\text{Ga}_{1-x}\text{As}_y\text{P}_{1-y}/\text{InP}$, which dominates the laser and detector market for fiber optic applications [54],[55]. An alternative is $\text{In}_x\text{Al}_y\text{Ga}_{1-x-y}\text{As}/\text{InP}$, which has produced the fastest transistors demonstrated to date [56]. This can be attributed in part to a high conduction-band offset, inherent to $\text{In}_{0.52}\text{Al}_{0.48}\text{As}/\text{In}_{0.53}\text{Ga}_{0.47}\text{As}$, which is an advantage in n-MODFET design. Also, the Schottky barrier height on InAlAs is higher than on InP.

Proposals for MSM photodetectors, using each of these material systems, are outlined in the following sections. Based on these proposals, representative epitaxy was obtained. The experimental results for MSM photodetectors fabricated on these epitaxial structures are contained in Chapter 3.

In addition to describing epitaxial alternatives, this chapter deals with a variety of technological issues relevant to MSM fabrication and optimization. In section 2.2, some technological problems traditionally associated with MSM photodetectors are discussed. In Section 2.3, the basic structure of a state-of-the-art, double-heterostructure MSM photodetector is reviewed. In Section 2.4, epitaxial proposals are made for MSM detectors on InP, for operation at the fiber communication wavelengths. In Section 2.5, epitaxial proposals for GaAs-based MSM detectors are outlined.

As mentioned in Section 2.2, MSM photodetector performance is very dependent on the quality of the epitaxial interfaces and surfaces. In Section 2.6, the two most important semiconductor interfaces are discussed. The first important interface is the Schottky junction, which must be of high quality if the MSM detector is to exhibit low dark current and minimal low-frequency gain (see Section 1.1.1). The second critical interface is the free surface of the semiconductor, which interfaces to air or a dielectric passivant. The requirements of a good passivant are reviewed briefly in Section 2.6.6.

The effects of abrupt heterojunctions on detector performance are mentioned in Section 2.3. In Section 2.7, this is treated in more detail, with emphasis on the pileup of photogenerated holes, at valence band offsets in the double-heterostructure. Section 2.8 contains a description of a new mask set, which was designed to facilitate detailed study of MSM photodetectors and photodetector arrays. Also in Section 2.8, the fabrication process is described. Finally, a brief summary of technological issues is contained in Section 2.9.

2.2. Technological Challenges for MSM Photodetectors

2.2.1. Deleterious Surface and Interface Effects

MSM photodetectors are touted for their simplicity, as discussed in Section 1.5. In spite of this, the implementation of a high quality MSM photodetector can be more challenging than for a p-i-n photodetector. This is supported by the continued dominance of p-i-n detectors, even in OEIC's [41], where MSM detectors are supposed to have their greatest advantage. The purpose of the current section is to illuminate this apparent dichotomy, somewhat.

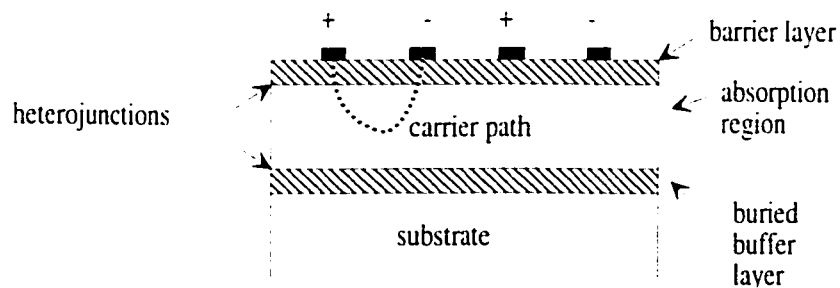


Figure 2.2. A cross-sectional view of a generic double-heterostructure MSM detector is shown (see section 2.3). While the lateral (planar) structure of the device is relatively simple to fabricate, and integrate with other devices, it also implies that surface effects can dominate device performance.

A key advantage of MSM photodetectors is their lateral structure; interdigitated electrodes are formed on the surface of a photosensitive, epitaxial stack. Planar (lateral) devices are generally simpler to fabricate, as it is not necessary to make contacts to different layers (see Section 1.5). While this is

advantageous in terms of fabrication and integration simplicity, it also means that the performance of MSM detectors is often dominated by surface and interface effects. A cross-section of a generic MSM is shown in Figure 2.2.

The interdigitated metal electrodes form a Schottky contact to the top layer. Carriers are photogenerated in the absorption region, and their subsequent motion can be reasonably well understood by a one-dimensional representation of the carrier path shown in Figure 2.2. However, the MSM is more correctly treated as a two-dimensional device. An applied bias produces a two-dimensional electric field distribution, between the device fingers, with the strongest field near the edges and tips of the fingers (see Appendix A).

As discussed in Section 1.1.1, poor quality Schottky barriers can produce excessive dark current and low-frequency gain. Barrier lowering, and resultant secondary carrier injection, is most likely to occur at the regions of high field described above. The field at a Schottky junction is greatly dependent on charge storage in the semiconductor, near the junction. This is discussed in Section 2.6: high dopant density or trap density in the vicinity of the contact generally degrades the rectifying properties of the contact.

In the MSM photodetector, there are several potential sources of high charge density in the region of the contacts. With a thin barrier enhancement layer, a heterojunction (between the cap layer and the absorption layer) lies very near the contacts. Depending on the quality of the epitaxy, a heterojunction is a potential site for charged traps. This is discussed in the following sub-section.

More often, however, it is the free epitaxial surface that is the site of unwanted charge storage in III-V semiconductors. This is discussed in greater detail in Section 2.6. This fact, along with the tendency of field lines to cluster near the finger peripheries, is most responsible for the inconsistent performance of MSM photodetectors to date. The problem is illustrated in Figure 2.3.

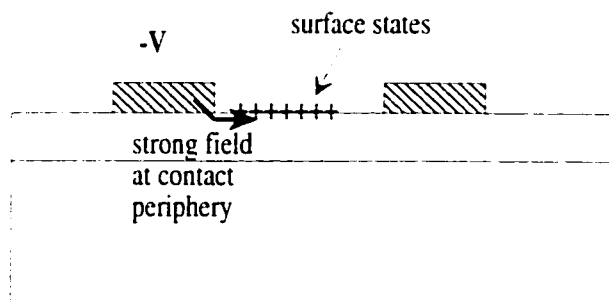


Figure 2.3. Two fingers of an interdigitated MSM detector are shown, in cross-section. A bias is applied between the adjacent fingers, and the field lines tend to cluster at their peripheries, near the surface. Unfortunately, the surface is often the site of unwanted charge storage in III-V semiconductors. As an example, positive charge storage is shown at the surface. This can produce an extremely high field at the periphery of the cathode (-V) fingers. The Schottky barrier is reduced by the high field, resulting in excessive dark current and low-frequency gain.

The majority of device research on MSM detectors has been aimed at minimizing surface-related problems [57-59]. Since a reliable technology has remained elusive, both on GaAs and InP, MSM photodetectors have continued to play a secondary role in optoelectronics. There are also issues relating to responsivity, as discussed in Chapter 1, but several methods exist to alleviate that problem (see Chapter 4).

An important goal of the work reported here was to investigate reliable technologies, exhibiting a minimum of the deleterious surface effects. To that end, the essential features of a high performance MSM detector are outlined in Section 2.3. Based on that, alternative materials were investigated, and their inherent surface properties were compared. Also, dielectric passivation techniques were attempted, in order to improve the surface conditions of sub-optimal devices. The experimental results are contained in Chapter 3.

2.2.2. Heterojunctions

As discussed in Section 2.3, MSM photodetectors are usually heterostructure devices. Most deleterious effects are due to unwanted charge storage near the metal fingers, as discussed in the preceding sub-section. The

fundamental properties of heterojunctions are reviewed here, as they can represent sites of unwanted charge trapping or pileup.

The essential band diagram characteristics of an abrupt interface between two different semiconductors may be approximated using a model proposed in 1960 by Anderson [60-62]. The details are illustrated in Figure 2.4. The model neglects charged interface states, and the band diagram is determined solely by the electron affinities, work functions, and band gaps of the two bulk semiconductors. A discontinuity (offset) in the conduction and valence bands is implied (ΔE_c and ΔE_v , respectively). This model is approximately valid for lattice-matched heterointerfaces, for which dislocations and defects due to strain are not present. Also, sufficiently thin mismatched layers (with lattice misfits of a few percent) may be grown without introduction of dislocations. Such growth is termed pseudomorphic.

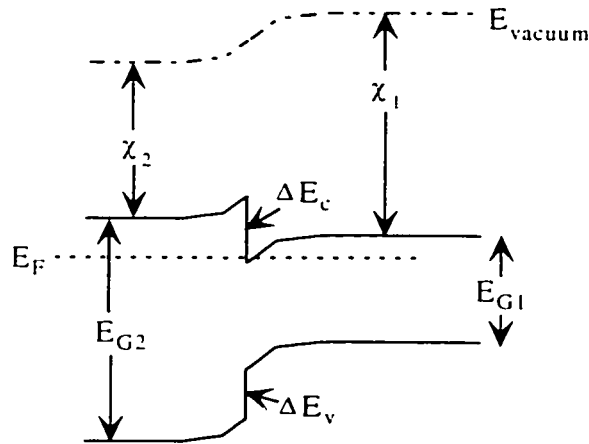


Figure 2.4. An idealized band diagram at a heterojunction between two semiconductors. The semiconductors have band-gaps given by E_{G1} and E_{G2} , respectively. Their corresponding electron affinities are χ_1 and χ_2 , respectively. Alignment of the Fermi level in equilibrium implies that band offsets, ΔE_c and ΔE_v , are formed.

Even in the lattice-matched cases, interface states may be important. If the lattice constant differs by more than a fraction of a percent, or if the two crystals have different growth characteristics, misfit dislocations can be formed. These produce localized interface states, which can play a dominant role in charge transport across the interface. Also, the interface states can be charged, thus

distorting the band profile. Finally, they may act as recombination and trapping centres.

Thus, real heterojunctions are more complex than indicated by Figure 2.4. The situation near the surface of a barrier-enhanced MSM detector is further complicated, since a semiconductor heterojunction and a Schottky barrier junction are formed in close proximity. The characteristics of the metal-semiconductor junction are also determined by interface states, as discussed in Section 2.6. A simple one-dimensional band diagram, which incorporates interface states for both the metal-semiconductor junction and the heterojunction, is shown in Figure 2.5.

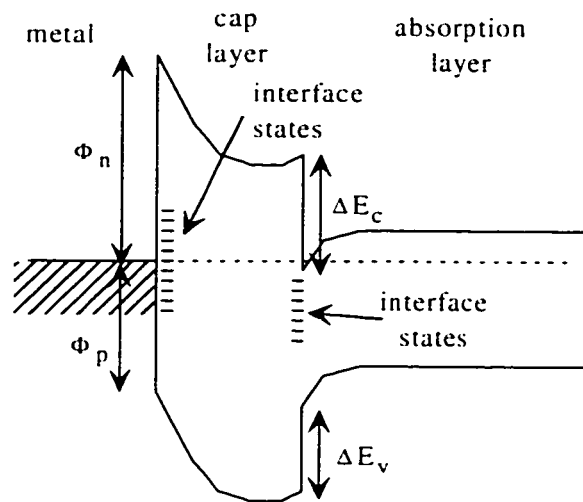


Figure 2.5. Representative band diagram at the surface of an MSM photodetector, with a barrier-enhancement layer. Φ_n and Φ_p are the electron and hole barriers, respectively, for the Schottky contact. Interface states can dominate the behavior of Schottky barriers and heterojunctions.

The band bending illustrated in Figure 2.5 assumes that the thin interfacial barrier layer transfers electrons to both the metal and the absorption semiconductor, and as a result is very nearly depleted at zero bias. Other band profiles are possible, depending on the combination of metal and semiconductors, the density of interfacial states, the conductivity of the semiconductors, and the thickness of the barrier layer.

Bias transforms the equilibrium band diagram. Simplified band diagrams, which generally assume depleted semiconductors, are used in the remainder of the chapter.

2.3. Double-Heterostructure MSM Photodetectors

Almost all state-of-the-art MSM detectors are based on the generic heterostructure shown in Figure 2.6.

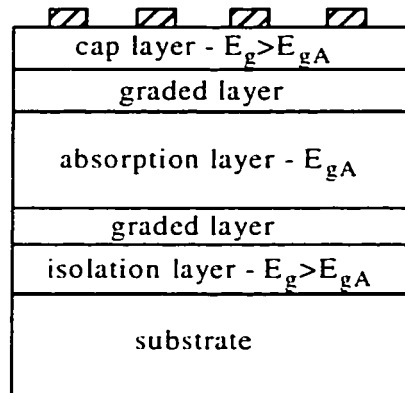


Figure 2.6. A Generic double-heterostructure MSM detector is shown. The absorption region has a band-gap of E_{gA} . In general, it should be isolated from both the free surface and the substrate, by wider band-gap layers. Graded layers may be included, to minimize free carrier pileup and trapping at the heterojunctions.

In the following, the rationale for each layer in Figure 2.6 is discussed.

2.3.1. Surface (Cap) Layer

For InGaAs-based MSM detectors, a surface layer is required to enhance the Schottky barrier height, as the low barrier for most metals on InGaAs results in excessive dark current and low-frequency gain. Reasonably good results are possible on GaAs without a cap layer [63], owing to the high Schottky barriers possible. However, those simple devices generally suffer from various surface-related effects; traps at the surface contribute to excessive dark current and speed-limiting gain [57],[59], and recombination centers at the surface can reduce the device responsivity by as much as 50 % [64]. A wide band-gap, non-absorbing surface layer serves to eliminate or reduce carrier generation and transport near the free surface, thus greatly improving the low frequency characteristics of the MSM device [65].

The barrier enhancement layer has other effects on MSM detector performance. First, it may introduce traps in its bulk or at the interface with the

absorption layer, depending on the quality of growth and the degree of lattice matching achieved. Second, the band offsets, at the heterojunction between the absorption region and the cap layer, can act as a site for pileup of free carriers, as illustrated in Figure 2.7. Figure 2.7 is a one-dimensional representation of the primary path of carrier flow in the MSM detector (see Figure 1.3); photogeneration in the absorption region, and transport of electrons to the anode and holes to the cathode, across the wider band-gap surface layer.

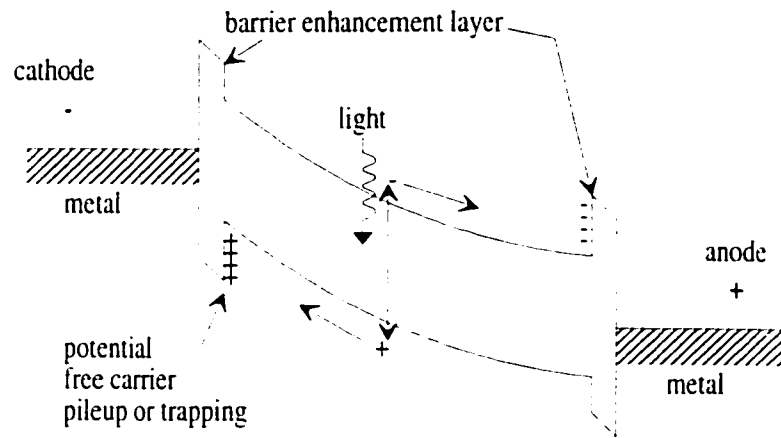


Figure 2.7. One-dimensional representation of carrier transport is shown. The wider band-gap cap layer may present a barrier to the efficient collection of photogenerated carriers. This can cause problematic low-frequency gain, and generally slow the speed of the device. It may also affect responsivity, as some carriers will be lost to recombination. Carrier pileup is discussed in detail in Section 2.7.

Either trapping or free carrier pileup can produce an asymmetric charge distribution, resulting in an enhanced field near the contacts and a screened field in the interior of the absorption region. Increased secondary carrier injection, hence increased gain and dark current, and degraded speed and responsivity, can result. The ideal surface layer for a double-heterostructure MSM should repel photogenerated charge from the free surface, while introducing no barrier to hole and electron collection, by the cathode and anode, respectively. As discussed in Section 2.7, it is generally desirable for the surface layer to have a band-gap offset that is apportioned primarily to the conduction band. This is because of the much higher mobility and lower effective mass of electrons, which allows them to reach their collecting electrode more easily, either by thermionic emission or tunneling.

Note that the requirements of surface isolation and minimal pileup are at odds. A thick surface layer with large band discontinuities is best for isolating the surface, but will result in greater carrier pileup.

2.3.2. Absorption Region

Most often, higher bandwidth in MSM detectors is obtained by a reduction in finger spacing. This is limited by the resolution of the photolithographic method used. Also, capacitance rises with decreasing finger spacing, and finger resistance increases with decreasing finger width. As a result, RC transients may limit the detector speed for very narrow finger spacing.

Higher bandwidth can also be obtained by using a thinner absorption region. This is traditionally avoided since it produces a corresponding reduction in responsivity, which is already a concern for the MSM detector. However, a close look at the available theoretical treatments leads to a few conclusions. The results in [42] show that the electric field strength falls very rapidly with depth beneath the fingers. For a thick absorption region (2 μm), a significant bias (10 to 20 V) is necessary to saturate the bandwidth of a device, regardless of the finger spacing. In order to achieve high speeds at low bias, it is crucial to reduce the absorption region thickness. This can be accompanied by relatively wide finger spacing, since the applied field is concentrated near the surface.

In light of this analysis, an absorption region thickness of approximately 0.5 μm was generally recommended. Several of the devices in Chapter 3 showed high bandwidths at low bias. This is expected to be important for integration of the devices, in the future. Several methods exist to enhance the responsivity of MSM detectors with thin absorption regions, including use of transparent electrodes, or use of resonant-cavity techniques (Chapter 4).

2.3.3. Substrate Isolation Layer

Growth of a wide band-gap isolation layer, between the substrate and the absorption region, serves a couple of different purposes. First, by blocking the collection of carriers that are generated deep in the substrate, the device speed is greatly enhanced, with little loss of responsivity. This is because most of the carriers are generated near the surface in a top-illuminated MSM detector. Second, the isolation layer provides a higher quality surface for the epitaxial growth of the absorption region, so defects from the wafer are not propagated into the regions of carrier generation and transport. This also improves device speed, by minimizing trapping of carriers deep in the absorption region, and enhances efficiency, by maximizing the recombination lifetime in the absorbing layer.

The band offsets of the isolation layer determine the extent to which carriers generated in the absorption region are confined to the absorption region. From this perspective, large conduction and valence band offsets are desirable, as they block photogenerated carriers from passing into the substrate, and thereby enhance device speed [16]. Also important is that the isolation layer does not introduce centers for charge localization, such as traps or band notches. This will be discussed further in the next sub-section.

2.3.4. Graded Layers

In some cases, a graded layer has been grown between the cap and absorption layers, in order to minimize free carrier pileup. The superlattice grade, which grades the effective band-gap by varying the width ratio of alternating layers, is easier to grow, but introduces wells which are potential locations for carrier trapping. This may offset the intended advantage somewhat [66]. This is illustrated by means of a simplified flat-band diagram in Figure 2.8.

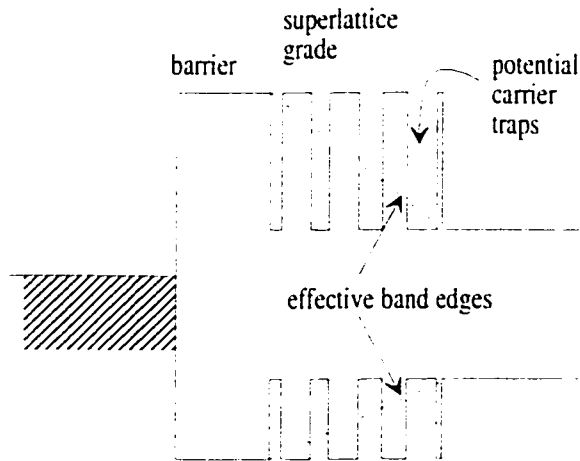


Figure 2.8. A band diagram is shown, for a barrier-enhanced MSM detector, with a superlattice grade designed to minimize free carrier pileup. The quantum wells are potential locations for carrier confinement.

A compositional grade [67] can theoretically eliminate free carrier pileup completely, as illustrated in Figure 2.9. At sufficient bias, for a given graded layer thickness and finger spacing, the photogenerated carriers face no barrier to collection by the metal contacts.

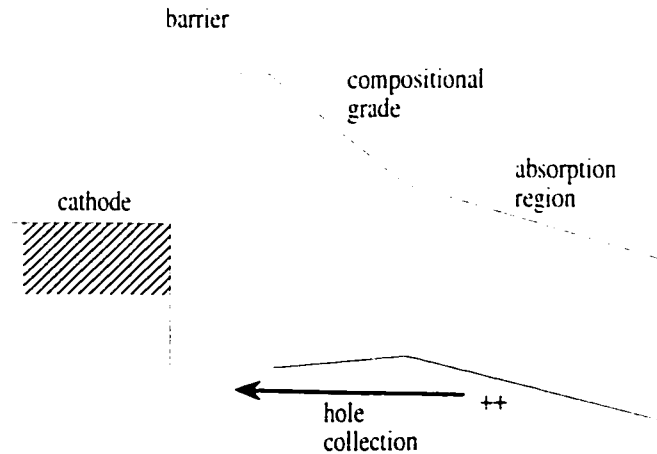


Figure 2.9. Elimination of carrier pileup at the cap layer, by addition of a compositional grade, is shown. The example considers hole collection at the cathode fingers of the MSM detector

The main disadvantage of introducing graded layers is an increase in fabrication complexity. Also, such devices are less compatible for integration with abrupt heterojunction devices, such as HEMT's and HBT's.

A rarely incorporated feature is a graded layer between the absorption region and the substrate isolation layer [66]. The heterojunction may exhibit a notch, in either the conduction or valence band, at low bias. This is shown schematically in Figure 2.10, for the InAlAs/InGaAs heterojunction. Since the field at the substrate is relatively low in MSM detectors, this notch represents a trapping site for photogenerated electrons. Besides slowing the device, electrons may accumulate in the notch, attract photogenerated holes, and produce recombination events that degrade device responsivity.

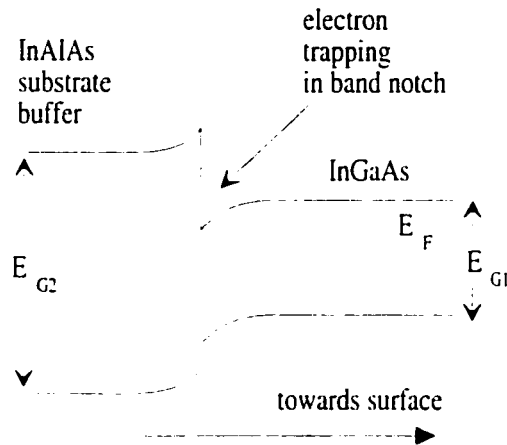


Figure 2.10. A conduction band notch is shown, for the InAlAs/InGaAs heterojunction. A notch of this type, at the bottom of the absorption region, can cause delayed collection of photogenerated carriers, and lower responsivity.

In any case, a quasi-abrupt heterojunction should be maintained. Otherwise, the isolation layer will not provide an adequate barrier to carrier transport into the substrate, which is one of its primary purposes. This is especially important in devices with narrow absorption regions, where significant vertical field components exist at the bottom of the absorbing layer.

2.3.5. Dark Current-Voltage Characteristics

The one-dimensional band diagram, shown in Figure 2.7, is a very useful tool for understanding the operation and performance of an MSM detector. The basic dark current properties of the MSM photodetector were studied originally by

Sze et al. [9], and were reviewed in [4]. Some of the essentials are mentioned here, to facilitate the discussion of experimental results in Chapter 3. The one-dimensional approximation is representative of a typical carrier path, as illustrated in Figure 1.3. The Schottky barriers are subject to various field-dependent barrier lowering mechanisms, and the representative band diagram will vary at different locations of the real two-dimensional structure.

The dark conduction characteristic of the MSM structure is determined by electron injection at the cathode contact and hole injection at the anode contact, and thus by the height and nature of the electron and hole Schottky barriers. A good analysis of the I-V characteristic for such a structure was provided by Sze [9]. Under applied bias, the depletion region near the cathode grows, and the depletion region at the anode shrinks. Eventually, the cathode depletion region reaches through to the anode, and the semiconductor is entirely depleted (at the reach-through voltage, V_{rt}). At higher bias, a point is reached for which the field in the semiconductor becomes unidirectional between cathode and anode (at the flat-band voltage, V_{fb}). In Figure 2.7, bias exceeds the flat-band voltage, which is typical for the MSM detector in operation.

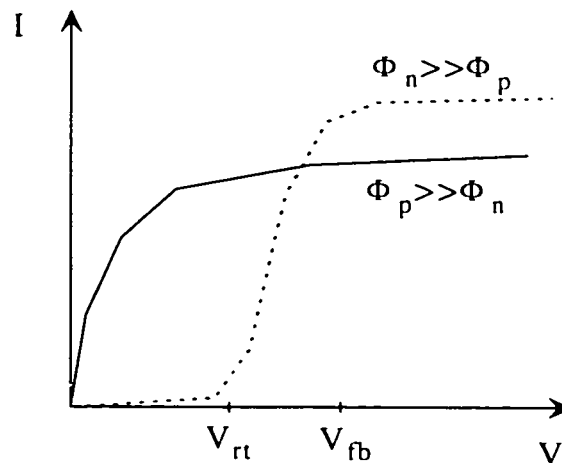


Figure 2.11. Limiting cases are shown, for the dark I-V characteristic of an MSM structure. Φ_n and Φ_p are the electron and hole barriers, respectively, of the Schottky contacts. V_{rt} and V_{fb} are the reach-through and flat-band voltages, respectively, discussed in the text.

The dark I-V characteristic of the one-dimensional device can be represented by one of two limiting cases, depending on the relative heights of the electron and hole barriers. This is illustrated in Figure 2.11.

The analytical expressions from [3] are somewhat complex for $V < V_n$, as the applied bias is shared unequally between the cathode and anode depletion regions. However, for $V > V_n$, the dark current characteristic is well represented by a simple, thermionic-emission rivalry relation, given by

$$J = A_n^{**} T^2 \exp\left(\frac{-\Phi_{n,eff}}{kT}\right) + A_p^{**} T^2 \exp\left(\frac{-\Phi_{p,eff}}{kT}\right). \quad (2.1)$$

The constants are the modified Richardson constants, and $\Phi_{n,eff}$ and $\Phi_{p,eff}$ are the effective barrier heights (bias-dependent), incorporating various barrier lowering mechanisms. In practice, one term generally dominates over the other, as per the limiting cases in Figure 2.11.

In studying the Schottky contacts of an MSM structure, one never has access to the forward bias characteristic, due to the back-to-back nature of the Schottky contacts. This hinders characterization, but considerable information can be gleaned from the experimental I-V characteristic. For the case $\Phi_p \gg \Phi_n$, the experimental curve is reasonably representative of the reverse characteristic of the cathode Schottky contact. This is only true for moderate to large bias, since initially a significant portion of the bias is dropped across the anode depletion region. In an ideal Schottky barrier study, the anode contact is ohmic, so that the measured I-V characteristic is attributable entirely to the Schottky contact forming the cathode. In MSM structures, a good approximation is that the anode contact is effectively ohmic (in terms of electron transport) for applied bias on the order of the contact potential of the anode.

Consider a dark current characteristic dominated by electron transport. At a given bias voltage ($>3kT/q$), a plot of $\ln(I/T^2)$ versus $1/T$ yields a straight line, with slope $q\Phi_{n,eff}/k$. By plotting the I-T data in this manner, with bias voltage as a parameter, it is possible to get a sense of how the effective barrier height varies with bias. This is generally referred to as an activation-energy plot. These plots

are used in Chapter 3, to analyze the surface characteristics of InP-based MSM structures.

Most Schottky contacts have I-V characteristics that deviate from the predictions of the thermionic-emission expression. A slightly modified equation is often used to fit experimental data:

$$J = J_0 \exp(eV / nkT) [1 - \exp(-eV / kT)] . \quad (2.2)$$

n is called the ideality factor and is a measure of the extent to which the I-V characteristic deviates from ideal behavior [68]. The deviation is attributable to various physical mechanisms, including Schottky effect (image force) barrier lowering, tunneling (field emission), recombination in the depletion region, and the presence of an unintentional interfacial layer between metal and semiconductor. For the case of injection of electrons,

$$J_0 = A^* T^2 \exp[-\Phi_{n0} / kT] , \quad (2.3)$$

where Φ_{n0} is the effective barrier height for electrons, at zero bias. Φ_{n0} incorporates some intrinsic image force effects, which are small for a moderately doped semiconductor.

Equation 2.2 can be manipulated, to analyze the quality of a Schottky contact. A plot of $\ln\{I / [\exp(qV/kT) / \exp(qV/kT) - 1]\}$ versus V should yield a straight line, if n is constant, for all values of V . The slope of such a graph is q/nkT , from which the ideality factor can be determined at a given temperature. In addition, using a known value for the modified Richardson constant, the zero-bias barrier height can be approximated, since the intercept with the zero-bias axis is equal to J_0 .

In general, large deviation of n from unity, or a bias-dependent n , indicates that the Schottky contact is not ideal (not well represented by thermionic-emission theory), due to the presence of significant barrier lowering and tunneling mechanisms. It is important to note that the ideality factor described here, from reverse bias characteristics, is not equivalent to the more commonly determined ideality factor, from the forward bias characteristic [68]. However, the ideality

factor plot described is a useful method for determining Schottky barrier height, if only the reverse-bias characteristic is accessible.

2.4. Alternative Epitaxial Materials for InP-based MSM Detectors

In the GaAs material system, high performance MSM detectors have been demonstrated both in isolation [63],[69], and as part of a wideband integrated receiver [38]. In some ways, the development of good devices for detection at the fiber wavelengths (1300 and 1550 nm) has been a greater challenge, due to the relative immaturity of the material systems. In spite of results reported for alternative material systems such as GaSb [70] and HgCdTe [71], InGaAs lattice-matched to InP (or potentially mismatched on GaAs) will initially form the basis of commercially realizable MSM detectors at 1300 and 1550 nm.

The Schottky contact that InGaAs ($E_g \sim 0.76$ eV) forms with most metals exhibits a low electron barrier of about 0.2 eV. As a result, MSM detectors formed directly on InGaAs display excessive dark current and gain, due to injection of electrons from the reverse biased cathode contact. Research has focused on the search for an appropriate barrier-enhancement material, which doubles as the cap layer discussed in Section 2.3.

A review of the literature revealed that three materials had shown promise as a barrier enhancement layer on InGaAs: InP, $\text{In}_{0.52}\text{Al}_{0.48}\text{As}$, and pseudomorphically grown $\text{In}_x\text{Ga}_{1-x}\text{P}$. In a previous report [72], the best results in the literature were summarized, and epitaxial proposals were outlined for each material system. In the following sub-sections, the one-dimensional band diagrams relevant to each system are briefly discussed.

2.4.1. InAlAs/InGaAs Material System

Many good results have been reported for devices with an InAlAs barrier layer. However, the high aluminum content of $\text{In}_{0.52}\text{Al}_{0.48}\text{As}$ is a potential disadvantage [73], owing to affinity of Al for oxygen. This can hinder growth, degrade surface conditions, and limit the long-term aging characteristics of a

device. Still, carefully grown InAlAs/InGaAs has demonstrated a low defect and trap density, derived from X-ray, photoluminescence, and two-dimensional mobility analysis [16].

The experimentally determined conduction and valence band offsets are approximately 0.5 eV and 0.2 eV, respectively [74]. The Schottky barrier height for most metals on n-In_{0.52}Al_{0.48}As is approximately 0.65 to 0.7 eV, although the value is dependent on the growth conditions of the semiconductor [74] and on the particular contact metals used [75],[76]. In addition, for lattice-matched barrier enhancement layers, the effective Schottky barrier height is found to depend on the thickness of the enhancement layer. The value saturates, for layers greater than a few tens of nm thick, to that found on the bulk semiconductor [77]. The barrier enhancement layers reported in the literature are greater than 30 nm thick in all cases. For discussion purposes a Schottky barrier height of 0.7 eV is assumed [74]. The resultant one-dimensional band diagram for the InAlAs/InGaAs MSM is shown in Figure 2.12.

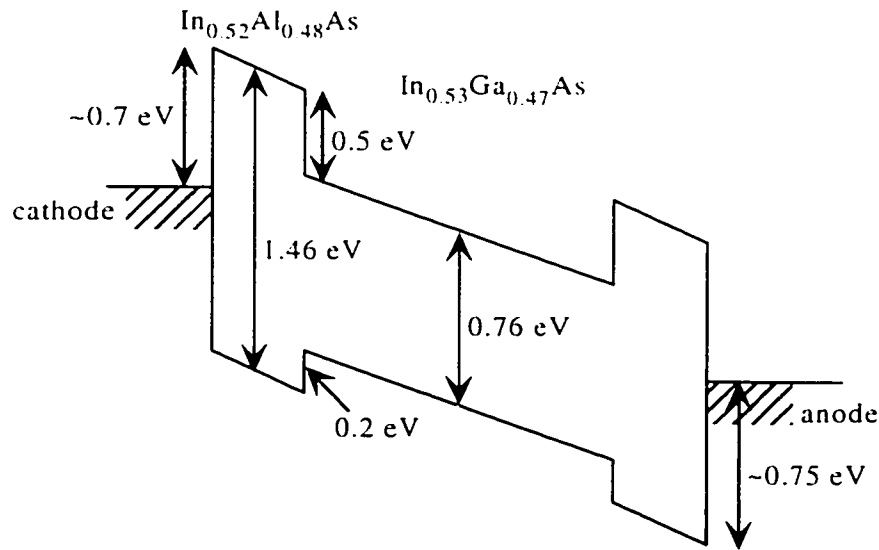


Figure 2.12. The one-dimensional band diagram for an InAlAs/InGaAs MSM detector is shown. The band-gap offset is apportioned primarily to the conduction band. The Fermi level of a typical Schottky contact lies near mid-gap, which is ideal for minimizing dark current in an MSM photodetector.

For the Schottky barrier height shown, electron conduction should dominate the dark current, per the discussion in Section 2.3.5. However, an electron barrier height as high as 0.8 eV has been reported on n-InAlAs [16], for which hole transport would dominate the dark current. In any case, a Schottky barrier that lies near mid-gap is generally ideal in terms of minimizing dark current in MSM detectors [12], per the thermionic emission rivalry relation discussed in Section 2.3.5. InAlAs cap layers have produced the lowest reported dark current for InGaAs-based MSM detectors [67].

As a final note, the small valence band offset is advantageous in terms of minimizing hole pileup. Hole pileup is discussed in Section 2.7. Essentially, higher performance at lower bias is predicted for a cap layer with a small valence band offset.

2.4.2. InP/InGaAs Material System

InP barrier-enhancement layers result in higher dark current, as compared to InAlAs barrier layers. This is due to a lower Schottky barrier on InP, as shown below. Unintentional surface oxidation is less problematic, however, with the absence of aluminum. Most importantly, phosphorus-based semiconductors typically exhibit much better surface electronic conditions than do arsenic-based semiconductors, as mentioned in Section 2.1. Given the surface effects discussed in Section 2.2, there is incentive to develop MSM photodetectors with InP cap layers.

The band offsets for InP/InGaAs are the subject of ongoing debate. Conduction band offsets ranging from 0.22 to 0.36 eV have been suggested [54],[77]. A mid-range value of 0.24 eV was assumed here, as in [78]. The corresponding valence band offset is approximately 0.35 eV. The Schottky barrier height on n-InP is approximately 0.45 to 0.55 eV, for most metals of interest [54],[77]. A representative band diagram for the InP/InGaAs MSM detector is shown in Figure 2.13.

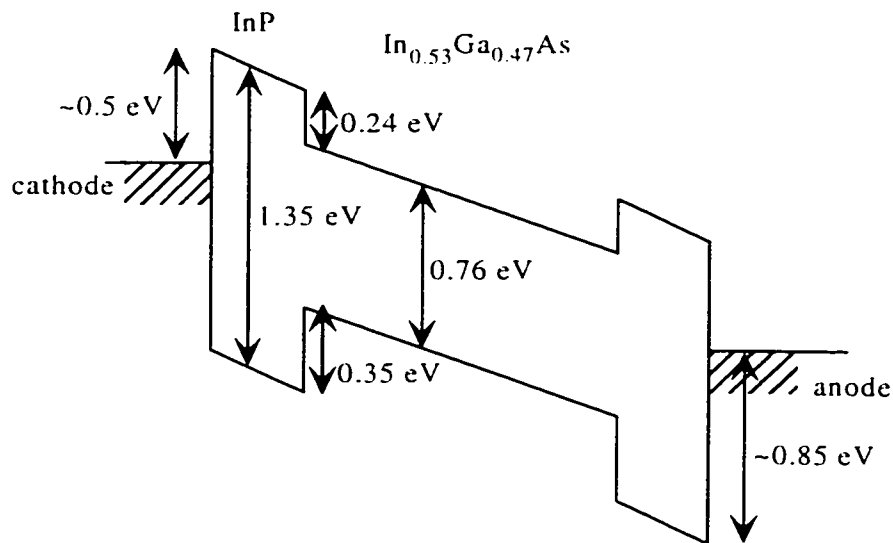


Figure 2.13. The one-dimensional band diagram for an InP/InGaAs MSM detector is shown. The band offset is apportioned primarily to the valence band. The electron barrier of a typical Schottky contact is relatively low, much lower than the corresponding hole barrier.

The relatively low electron barrier indicates that electron conduction should dominate the dark current characteristics. Also, dark current is typically higher than for the InAlAs/InGaAs devices discussed in the preceding sub-section. From the discussion in Section 2.7, the high valence band offset may limit the speed of an InP/InGaAs device at low bias.

2.4.3. $In_xGa_{1-x}P/InP/InGaAs$ Material System

Due to the relatively low electron barrier on InP, some researchers have grown a strained InGaP surface layer, to enhance Schottky barrier height [73],[79],[80]. With increasing Ga concentration, the lattice mismatch of InGaP increases, so the maximum thickness for pseudomorphic growth decreases.

For discussion, n- $In_{0.89}Ga_{0.11}P$ is considered here. That alloy has a band gap of 1.43 eV, and its critical thickness for pseudomorphic growth on InP is approximately 12 nm [77], although estimates vary upwards [73]. The authors of [77] found no improvement in Schottky barrier enhancement for a 60 nm $In_{0.89}Ga_{0.11}P/InP$ superlattice, when compared to an InP lattice matched layer of the same thickness. Similar results were obtained for Ti, Pt, and Al Schottky metals.

An InGaP surface layer produced significant barrier enhancement in [73], however, and others [79],[80] have reported very good dark current characteristics for $\text{In}_{0.9}\text{Ga}_{0.1}\text{P}/\text{InP}/\text{InGaAs}$ MSM detectors. Interestingly, Chyi et al. [80] compared InP/InGaAs and $\text{InGaP}/\text{InP}/\text{InGaAs}$ MSM detectors, and reported a reduction in low-frequency gain for the latter devices. This may point to an effective passivation of the InP surface by InGaP. The results reported in Chapter 3, for a similar material combination, support this hypothesis.

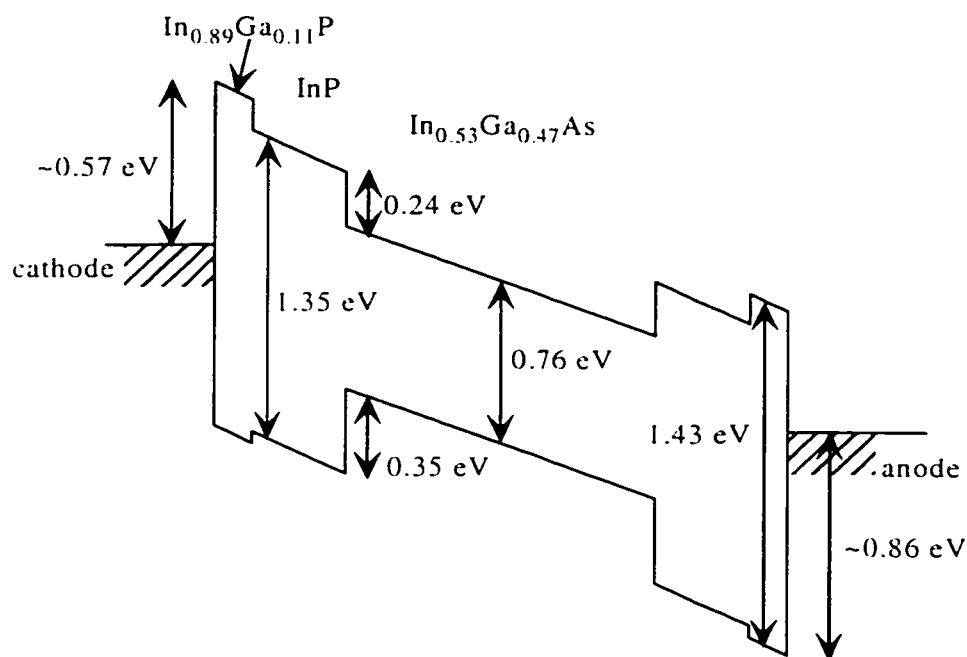


Figure 2.14. The one-dimensional band diagram for an $\text{InGaP}/\text{InP}/\text{InGaAs}$ MSM detector is shown. The inclusion of the strained InGaP layer results in a higher electron barrier at the Schottky contact, compared to an InP surface layer alone.

A simplified one-dimensional band diagram is shown in Figure 2.14. The band discontinuity at the InGaP/InP interface is accommodated primarily by the conduction band offset [73], but is not known precisely.

2.5. Alternative Epitaxial Materials For GaAs-based MSM detectors

MSM photodetector research has been conducted primarily in the $\text{InGaAsP}/\text{InP}$ and $\text{InAlGaAs}/\text{InP}$ material systems lately, as $\text{In}_{0.53}\text{Ga}_{0.47}\text{As}$ efficiently detects radiation at the long-haul communication wavelengths of 1.3

and 1.55 μm [16]. The earliest work reported was in the more mature AlGaAs/GaAs material system, with operation in the 800 nm range. The original concept of using an interdigitated, back-to-back Schottky configuration for high-speed detection can probably be attributed to Sugeta et al. [11], although interest in metal-semiconductor-metal structures predates that work [9]. The first demonstration of the advantages produced by heterostructure epitaxy, for MSM photodetectors, was by Figueroa and Slayman [15], and involved the AlGaAs/GaAs material system.

Although not suitable for long-haul fiber systems, GaAs-based optoelectronic integrated circuits (OEIC's) are expected to be very useful in the near term for short-distance optical interconnects between local area networks, processors, or boards [33],[81]. The maturity of transistor, laser, and integration technology on GaAs substrates is the primary reason.

For InGaAs-based MSM devices, a primary point of comparison is the dark current, as discussed in the preceding section. This is due to the low Schottky barrier generally achieved on InP, InAlAs, and InGaAs. For GaAs based devices, the dark current has typically been negligible for receiver applications, due to the high Schottky electron barrier of most metals on GaAs or AlGaAs [82]. In fact, unlike the InGaAs-based devices in Section 2.4, the GaAs-based devices generally have dark current characteristics that are dominated by hole transport. The more pertinent points of comparison for these devices are the responsivity, the bandwidth, and the amount of low-frequency gain present.

In a previous report [83], the best results from the literature were reviewed, and alternative epitaxy was identified. Presently, two material systems are of interest for GaAs-based double-heterostructure MSM detectors operating near a wavelength of 800 nm. In the following sub-sections, a brief synopsis is given.

2.5.1. AlGaAs/GaAs Material System

The AlGaAs/GaAs material system is very mature, owing to the high degree of lattice matching of $\text{Al}_x\text{Ga}_{1-x}\text{As}$, for all values of x . $\text{Al}_x\text{Ga}_{1-x}\text{As}$ is a direct

band-gap semiconductor for $x < 0.38$ [82]. Over the direct band-gap range, the change in band-gap from that of GaAs can be given by

$$\Delta E_g = 1.255x \quad , \quad (2.4)$$

and the discontinuity is apportioned primarily to the conduction band,

$$\Delta E_c = 0.65\Delta E_g \quad . \quad (2.5)$$

AlGaAs is prone to the incorporation of oxygen impurities during growth and when exposed to air (due to the Al content). This often results in the slow deterioration of device characteristics over weeks or months, if an AlGaAs surface is exposed to the environment [84]. A partial solution is to stabilize the AlGaAs surface, either with GaAs or with a dielectric passivant. Another problematic characteristic of $\text{Al}_x\text{Ga}_{1-x}\text{As}$ is the presence of DX centers; donor-related traps that lie in the band-gap for $x > 0.22$, and often dominate the photoconductive features of the semiconductor [85]. For MSM applications, nominally undoped layers are used, so the effect of DX centers should be minimized. However, by using layers with $x < 0.22$, the DX trap level lies in the conduction band, and slow transients in the photocurrent are avoided.

For double-heterostructure MSM detectors in the literature, a minimum Al concentration of $x=0.3$ has generally been used in the cap layer. This ensures that the band offsets are sufficiently high to isolate the surface, and that the band-gap of the surface layer is wide enough to make it wholly transparent in the 800 nm wavelength range. A surface layer of $\text{Al}_{0.2}\text{Ga}_{0.8}\text{As}$ should be sufficient for these purposes, however, having the characteristics identified in the band diagram of Figure 2.15. By keeping the Al concentration low, the added advantage is that a more stable free surface is expected.

The Schottky barrier heights in Figure 2.15 have been approximated using the known value for Ti on GaAs, along with the common anion rule [68]. The derived barrier height indicates that the dark current will be due to hole injection at the anode. The band-gap offset is apportioned primarily to the conduction band [78], which is advantageous for minimizing hole pileup (see Section 2.7).

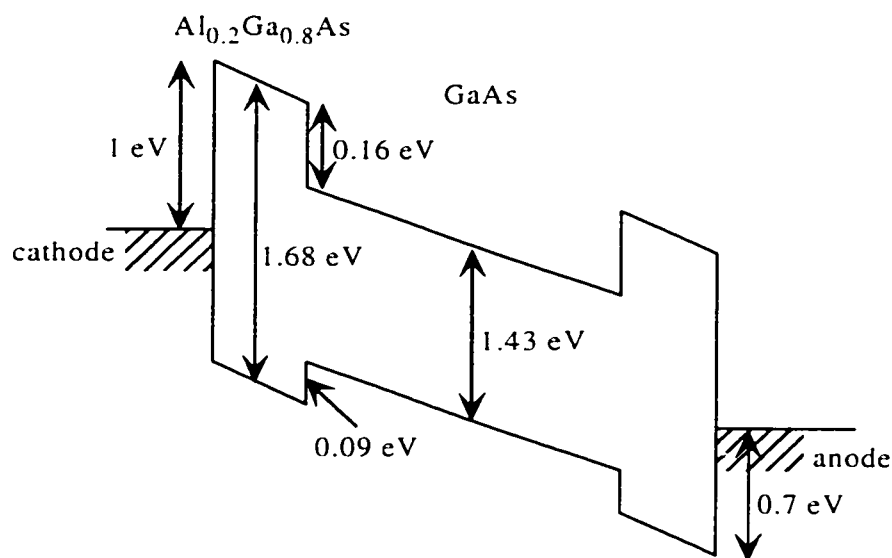


Figure 2.15. Simplified one-dimensional band diagram for an AlGaAs/GaAs MSM detector. The hole barrier at the Schottky junctions is much lower than the electron barrier, so hole transport is expected to dominate dark current.

For the substrate isolation layer, an AlGaAs alloy with higher aluminum concentration is necessary. Significant vertical field components might exist at that heterojunction, and larger band offsets are required to ensure carrier transport is confined to the absorption region. It may be advantageous to grow two consecutive AlGaAs layers, the first with high band offsets, to block carriers from the substrate, and the second with a small Al concentration, to isolate the absorption region from the effects of DX trapping centers.

2.5.2. $In_{0.49}Ga_{0.51}P/GaAs$ Material System

$In_{1-x}Ga_xP$ is a direct band-gap semiconductor for $x < 0.73$ [86]. For $x = 0.51$, it is lattice-matched to GaAs, with a band-gap of 1.9 eV, and can potentially replace AlGaAs in devices which have previously benefited from AlGaAs/GaAs heterostructures. The potential advantages are numerous. The interfacial and free surface recombination velocities (indicating the interface state density) for InGaP/GaAs are much lower than for AlGaAs/GaAs [52]. Also the crystalline quality of InGaP is higher, due to the absence of Al [87]. InGaP is essentially free of deep trapping states [88], and its environmental stability is superior.

Historically, a primary disadvantage has been the difficulty in growing phosphorus-containing compounds by solid-source MBE. However, this problem has been overcome in recent years, by the techniques of Gas Source MBE and solid source MBE using a valved phosphorus cracker [53].

A one-dimensional band diagram for an InGaP/GaAs MSM photodetector is shown in Figure 2.16.

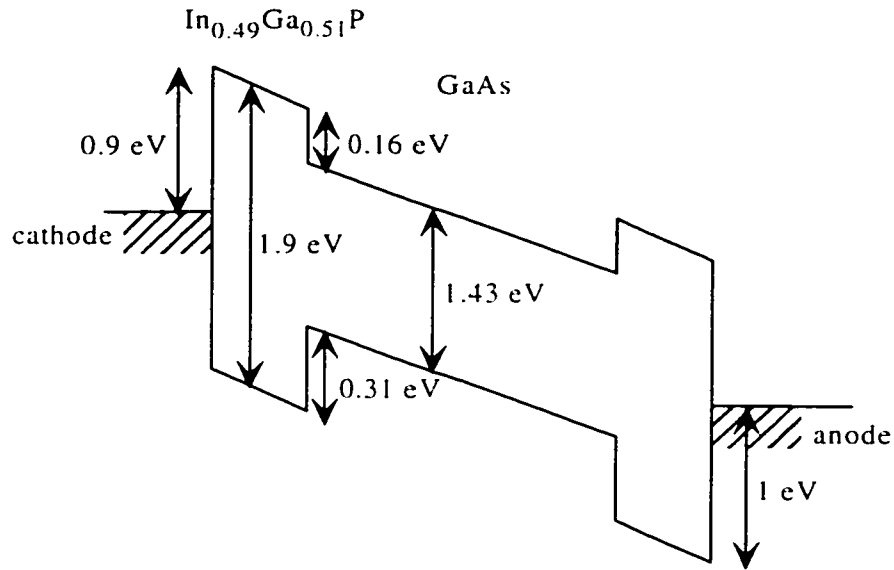


Figure 2.16. A simplified one-dimensional band diagram, for an InGaP/GaAs MSM detector, is shown. InGaP exhibits high Schottky barriers, and should produce a device with very low dark current. The high valence band offset may hinder efficient collection of photogenerated holes, as discussed in Section 2.7.

There is ongoing debate regarding the band offsets at InGaP/GaAs heterojunctions. The most recent literature [89],[90] suggests a conduction band offset of approximately 0.16 eV. The Fermi level for metals on InGaP has been observed to lie near mid-gap [91],[92] which is ideal for MSM applications (see Section 2.3.5). The valence band offset is quite high, and hole pileup might be a problem, as discussed in Section 2.7.

2.6. III-V Semiconductor Interfaces

2.6.1. Introduction

In the band theory of solids, derived from quantum-mechanical considerations, the electronic transport properties and other details of a complex three-dimensional solid are reduced to a simple but powerful one-dimensional model. Unfortunately, the required assumptions hold true only in the bulk of the solid, where the electrons are surrounded on all sides by an effectively infinite lattice of atomic sites. At the solid surface, the periodicity of the lattice is interrupted, and the surrounding environment for a representative electron is vastly different than in the bulk. Indeed, it has been said that if God created the perfect order of the semiconductor crystal, than the devil must be responsible for its surface (attributed to Linus Pauling [93]).

The overwhelming success of silicon in the microelectronics industry is attributable, in large part, to the electrical and optical stability of its free surfaces, and especially of its interfaces with its native oxides and nitrides [49]. The III-V semiconductors, which have superior bulk optical and electrical characteristics, have been plagued by technological problems, including the non-ideal nature of their free surfaces and interfaces. In electronic devices such as MODFET's, the high trap density at III-V interfaces contributes to non-ideal current-voltage characteristics and bandwidth reduction. In optoelectronic devices, such as photodetectors and lasers, the relatively high recombination velocities at III-V interfaces reduces quantum efficiency, and similar bandwidth reduction mechanisms are present. Interface states can also hinder characterization of devices, since they often produce slow transients in measurements. These are a result of trapping and detrapping processes, via the interface states.

Two interfaces are of primary importance in the design of modern semiconductor devices. The first is the metal-semiconductor interface, which, in rectifying or ohmic form, is central to essentially every important semiconductor device. The second is the semiconductor-insulator interface, which is central to the operation of capacitively coupled devices, such as MOS transistors. In

addition dielectric passivation of semiconductors is a general requirement, to improve the mechanical, thermodynamic, and electronic stability of the free surfaces.

2.6.2. Semiconductor Surfaces - General

An excellent discussion of the nature of solid surfaces has been provided by Rhoderick and Williams [68]. A surface or interface interrupts the perfect crystalline order we associate with a bulk semiconductor. The absence of neighbors for the surface atoms causes a shift in their equilibrium position, relative to the positions suggested by the bulk crystal lattice. A *relaxed* surface is one for which crystal symmetry is maintained in the plane of the surface, but which deviates from crystal symmetry in the direction perpendicular to the surface. A *reconstructed* surface displays deviations from crystal symmetry in the plane of the surface. The 'Selvedge' region is the depth, in atomic layers, over which reconstruction or relaxation occurs for a given surface.

In addition to the physical manifestations, the surface and bulk of a solid are also likely to differ chemically. Atomically clean surfaces can only be achieved and maintained under high-vacuum conditions. In the natural environment, an initially clean solid surface is covered with adsorbed environmental contaminants in a matter of seconds. Metal and semiconductor surfaces are typically covered with a few atomic layers of carbon, hydrocarbons, and oxygen, under atmospheric conditions.

Compared to its bulk, the surface of a solid also differs from a quantum mechanical perspective. The distribution of electron states, which is conveniently described by band theory for the bulk crystal, is considerably more complex at surfaces and interfaces. However, it is useful to describe the role of surface states, as they are understood, via the band model of the bulk. In this sense, the interface states are treated as a local perturbation of the perfect crystal. A typical band diagram, which integrates bulk and interfacial states, is illustrated in Figure 2.17. The surface states are represented as two-dimensional, continuous energy bands, which may or may not overlap the conduction and valence bands of the bulk

crystal. This is a reasonably accurate description of the surface-states observed in experiments.

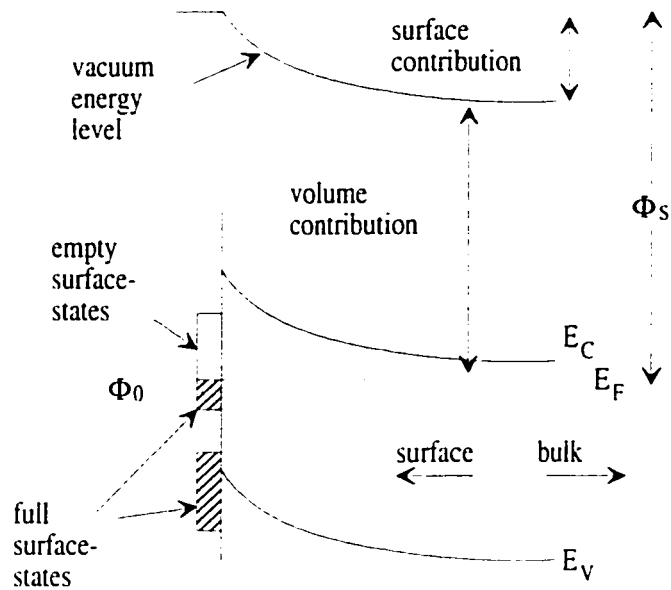


Figure 2.17. A band diagram is shown, at the surface of a semiconductor. Surface states are represented as two-dimensional bands, which may reside within or outside the band-gap of the semiconductor. Φ_S is the work function of the semiconductor. The work function includes a surface contribution, due to dipole-induced band bending at the surface. Φ_0 is the charge-neutrality level, a theoretical abstraction that allows the net charge at the surface to be inferred from the occupancy of the surface state bands. In the example shown, the surface contains a net-negative charge, so the bands bend upwards towards the surface. The excess electrons at the surface derive from the donor atoms in the n-type semiconductor shown.

The interface states differ from the bulk states in that they are localized. In other words, they have wave functions that decay away from the interface. The model of Figure 2.17 can accommodate both intrinsic surface states, which would result from cleaving a semiconductor in vacuum, and impurity-derived surface-states. Some portion of the surface-states will always be intrinsic, which is to say derived from the valence band and conduction band states near the surface. It follows that the densities of conduction and valence band states near the interface are reduced, and that charge neutrality of the combined bulk and surface requires partial occupation of the surface-states.

The free surface of a semiconductor is not generally charge neutral. This is due to the different free energies associated with the bulk and surface, and is represented by the band bending in Figure 2.17. The surface of Figure 2.17 has a negative charge. This implies that electrons were transferred from the bulk to the surface states, in order that the Fermi level is flat in equilibrium. Near the surface, the semiconductor is correspondingly depleted of free carriers.

Often, a charge neutrality level, Φ_0 , is defined for the surface. The position of the Fermi-level, relative to Φ_0 , indicates at a glance whether the surface contains a net-negative or positive charge. If a surface contains a net-positive charge, the bands bend downwards towards the surface. The surface is termed accumulated, in that case, since the semiconductor has excess electrons (carriers) in the near-surface region. The excess carriers derive from the surface-states.

The work function of a solid (Φ_S) is an extremely important concept in the analysis of interfaces. In a statistical sense, it is the mean energy required to raise an electron, from its ground state in the solid, to a state of rest outside the solid (the vacuum level). Φ_S , as illustrated in Figure 2.17, is the sum of two contributions. One is the volume contribution, which is due to the potential of the crystal lattice and its constituent free electrons. The other is a surface contribution, which is due to the existence of interface-states, and the resultant dipole layer at the surface. The dipole (surface) contribution to the work function is dependent on surface relaxation, reconstruction, and contamination, and is often different for the various crystallographic surfaces of the solid.

2.6.3. Metal-Semiconductor Interfaces – The Schottky Barrier

Schottky barriers are a key component for numerous semiconductor devices, including MSM photodetectors. For MSM photodetectors, it is important that the metal contacts exhibit good rectifying properties, over the operational range of bias voltage. This ensures low dark current and minimal secondary carrier injection. From the discussion in Section 1.1.1, the noise and speed

characteristics of the MSM detector are dependent on this. Deleterious surface effects in MSM detectors are often manifested by lowering of the Schottky barriers, as demonstrated in Chapter 3. For this reason, a brief discussion on the current understanding of Schottky barriers is included here.

The most technologically important (and common) metal-semiconductor interface is that between an n-type semiconductor and a metal, with the semiconductor having a smaller work function. Figure 2.18 illustrates a simple band diagram, useful for characterizing the interface.

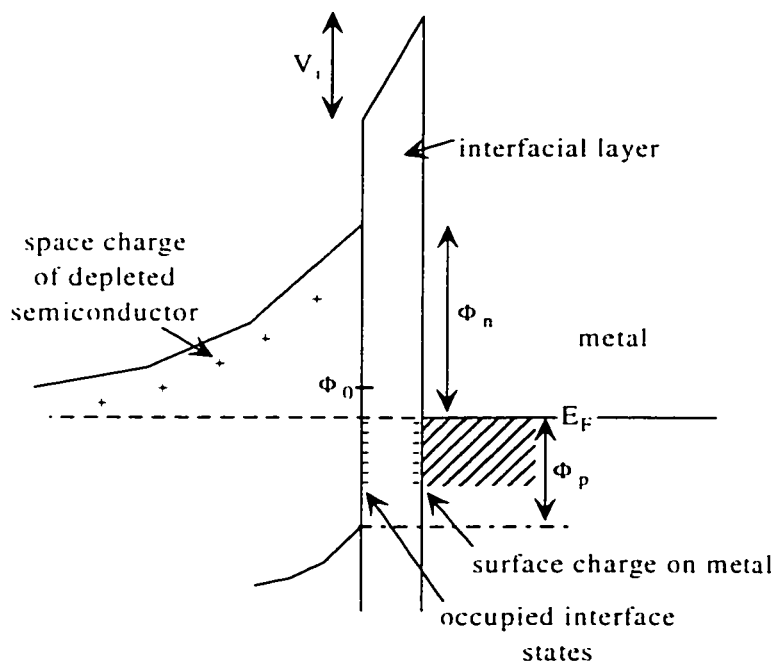


Figure 2.18. A band diagram is shown, for an interface between an n-type semiconductor and a metal, where the metal has a larger work function. Charge transfer establishes equilibrium (as indicated by the flat Fermi level), between the metal, the semiconductor surface states, and the semiconductor bulk. An idealized interfacial layer is assumed: it is insulating, thin enough that electrons can tunnel through unobstructed, but thick enough to withstand the applied field without breaking down. V_i is the voltage drop across the interfacial layer.

To establish thermodynamic equilibrium, electrons are transferred to the solid with larger work function, in this case the metal. Φ_n is the Schottky barrier for electrons, representing the mean potential barrier to electron emission from the metal to the semiconductor. The hole barrier (Φ_p) is somewhat less well defined, for the case illustrated in Figure 2.18. In basic terms, it represents the mean

potential barrier to hole emission from the metal to the semiconductor, under forward bias conditions. No barrier lowering mechanisms are included in Figure 2.18, so the sum of electron and hole barriers is equal to the semiconductor band-gap.

The negative charge on the surface of the metal lies within the Thomas-Fermi screening distance [68], which is less than an angstrom. In Figure 2.18, the surface states of the semiconductor hold a net-positive charge, since the Fermi-level lies below the charge neutrality level (Φ_0). As the following analysis will show, this assumption is not critical. It is mainly the density of surface states, and not whether they are effectively donors or acceptors, that affects the characteristics of the Schottky barrier. The net charge of the system, including space charge in the semiconductor and interfacial charges, is zero.

The interfacial layer is an ultra-thin insulator, and is a good approximation to the native contaminant layer that is always present, at least for contacts not formed in ultra-high vacuum. It is generally presumed that this insulating layer is only a few angstroms thick, and is therefore essentially transparent to charge flow, as electrons can tunnel easily through it. The interfacial layer, however, is thick enough to withstand intrinsic and applied fields at the interface.

Note that the presence of the interfacial layer implies a reduction or increase of the electron barrier, over that which would exist for the atomically clean interface. This is because the band bending required of the semiconductor, to align the Fermi levels, is altered by the potential drop (V_i) across the interfacial layer. In fact, even for contacts formed under vacuum conditions, a dipole layer exists at the intimate metal-semiconductor interface, arising from the distribution of electrons in the intrinsic interface states. This will be discussed in greater detail below.

The main features of the band diagram in Figure 2.18 were developed independently by Schottky and Mott [68]. They did not consider the presence of the interfacial layer, however, and in that case that the electron barrier is given by

$$\Phi_n = \Phi_m - \chi_s, \quad (2.6)$$

where Φ_m is the metal work function, and χ_s is the electron affinity of the semiconductor. This approximation of the Schottky barrier height is termed the Schottky-Mott limit. It neglects surface-dipole contributions to the solid work functions, which are always present, and which change upon formation of the contact. For this reason, (2.6) is a useful starting point only, and is not well obeyed in practice.

Bardeen [68] made the next major contribution to the understanding of Schottky barriers, in 1947. He correctly postulated that surface states were fundamental to the understanding of real metal-semiconductor interfaces. He also introduced the interfacial layer concept, and pointed out that surface states on the semiconductor make the electron barrier a weaker function of Φ_m and χ_s than predicted by (2.6). If an extremely high density of surface states is present near Φ_0 , the semiconductor surface states effectively screen the bulk of the semiconductor from the metal. That is, the semiconductor bulk has a pre-existing thermodynamic equilibrium with its surface states, and this equilibrium is not disturbed by the formation of the metal contact in the limit of extremely high interface state density.

In that case, a new equilibrium is established between the semiconductor surface states and the metal only, with the necessary built-in field dropping entirely across the interfacial layer. This model for Schottky barrier formation is termed the Bardeen limit, and is given by

$$\Phi_n = E_g - \Phi_0. \quad (2.7)$$

E_g is the band-gap of the semiconductor, and Φ_0 is the charge-neutrality level of its surface-states, measured from the valence band edge. In this limit, the Schottky barrier is not sensitive to the metal work function, as the barrier height is 'pinned' by the interface states.

Experimental studies show that semiconductors tend to exhibit intermediate behavior, between the limits suggested by (2.6) and (2.7). That is, the

barrier height shows some dependence on metal work function, but not the direct correlation suggested by (2.6). The limits of behavior, and an intermediate case, are illustrated schematically in Figure 2.19. D_s is defined as the energy-density of surface states on the semiconductor, and for simplicity is presumed to be constant throughout the band-gap.

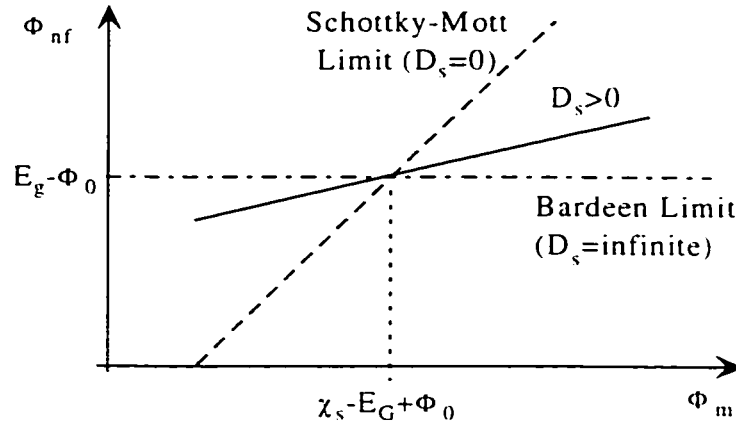


Figure 2.19. The variation of Schottky barrier height with metal work function (Φ_m) is illustrated schematically, for various limiting cases. D_s is the energy-density of surface-states, assumed for simplicity to be constant over the entire band-gap. Φ_{nf} is the flat-band barrier height, as defined in [68]. The curves intersect for a metal work function that is coincident with the charge neutrality level of the semiconductor surface states.

In practice, the assumption that surface states are evenly spread in energy across the band-gap is not realistic. Often, sub-bands of donor and acceptor states are observed experimentally, as illustrated in Figure 2.17. In that more realistic case, the slope of the graph in Figure 2.19 is not constant as shown, but rather varies in a more complex way. For example, if the lower and upper sub-bands in Figure 2.17 are exclusively donors and acceptors, respectively, the variation of barrier height with metal work function would be as illustrated in Figure 2.20.

From Figure 2.20, the essential point is as follows: acceptor-like surface-states, which can only hold negative charge or be neutral, will tend to increase the Schottky barrier height on n-type semiconductors, over that predicted by the Schottky-Mott theory. The opposite is true for the donor-like states. This can be understood with reference to the band diagram, in Figure 2.18, and recalling that the total charge in the system is neutral. The metal always has a negative surface

charge, for the case shown. Thus, negative charge in the semiconductor interface states implies greater band bending, and a higher barrier.

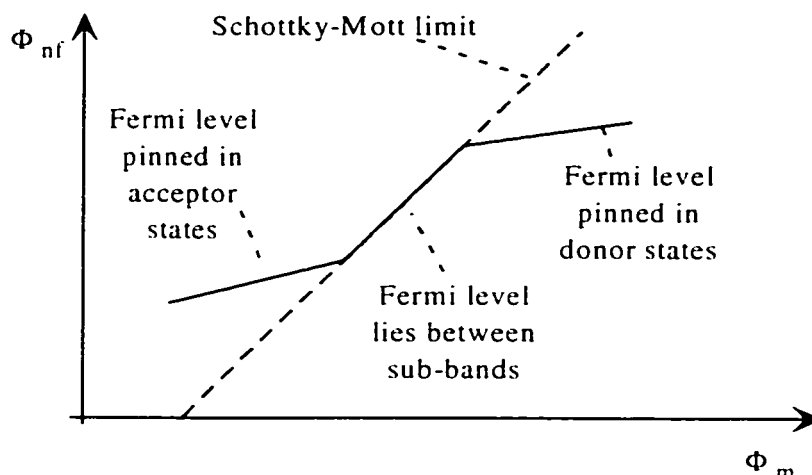


Figure 2.20. A typical relationship between Schottky barrier height and metal work function is illustrated schematically. The semiconductor surface states are distributed as sub-bands of acceptors and donors, as in Figure 2.17. Depending on the work function of the deposited metal, the surface Fermi level is pinned or not pinned.

The physical origin and nature of interface states at metal-semiconductor interfaces has been the subject of intense debate over the past twenty years [94-97]. In any event, a perfectly ordered and intimate metal-semiconductor contact is a theoretical abstraction. Metals deposited on semiconductors generally are polycrystalline, and the electronic details at the interface are dependent on the exact structure. In addition, even for metal deposited in high vacuum, the surface invariably becomes disordered, as metal atoms diffuse into the semiconductor and vice-versa. Also, new phases are formed, due to chemical reactions between the metal and semiconductor atoms.

From the point of view of the experimentalist, the origin of the interface states is not always important, as long as a good model is available to describe their influence. The Bardeen model of Figure 2.18 can accommodate interface states of any origin, and is therefore still the best available method for characterizing real metal-semiconductor contacts and interpreting experimental data.

Assuming a constant energy-density (number of surface states per surface area per energy interval) of surface states in the energy range near Φ_0 , and that the occupation of these states is determined by the metal Fermi level, an analytical expression for the flat-band barrier height can be obtained. The flat-band condition is a forward bias state, for which the semiconductor bands are flat adjacent to the contact. For this condition, the electric field is zero in the semiconductor region adjacent to the contact. The flat-band barrier height, derived from the Bardeen model, is given by

$$\Phi_{nf} = \gamma(\Phi_m - \chi_s) + (1 - \gamma)(E_g - \Phi_0);$$

$$\gamma = \frac{\epsilon_i}{\epsilon_i + q\delta D_s} \quad (2.8)$$

ϵ_i is the permittivity of the interfacial layer, δ is the thickness of the interfacial layer, and the other parameters were defined previously. As expected, as the surface state density tends to zero, the Schottky-Mott equation is recovered. As the surface state density tends to infinity, the Bardeen equation is recovered.

2.6.4. Bias-Dependent Barrier-Lowering Mechanisms

In the analysis of the rectifying behavior of a metal-semiconductor contact, it is necessary to consider physical mechanisms that result in a lowering of the Schottky barrier, relative to the simple cases outlined in the previous sub-section. This was observed experimentally for InAlGaAs/InP MSM photodetectors, described in Chapter 3.

Two such mechanisms are of primary importance, and are discussed here. First, the presence of the interfacial layer implies a potential drop V_i as shown in Figure 2.18. V_i will vary with bias, as bias shifts the occupation level of the interface states. If a constant energy density of surface states is assumed, and their occupation is determined by the metal Fermi-level, the field dependence of the barrier height (due to the interfacial layer) is given by [68]

$$\Phi_n = \Phi_{n0} - \alpha E_{\max};$$

$$\alpha = \frac{\delta \epsilon_s}{\epsilon_s + q \delta D_s} \quad (2.9)$$

ϵ_s is the permittivity of the semiconductor, and E_{\max} is the maximum field in the semiconductor, directly adjacent to the interface. E_{\max} is generally determined via the depletion approximation. The assumptions used to derive (2.9) are valid for reduction in barrier height less than approximately 0.1 eV. The corresponding bias dependence can be derived from (2.9), and is given by

$$\Phi_n(V) = \Phi_{n0} + \frac{\Phi_1}{2} - \left\{ \Phi_1 \left(\Phi_{n0} + \frac{\Phi_1}{4} - V - \xi - \frac{kT}{q} \right) \right\}^{1/2};$$

$$\Phi_1 = \frac{2\alpha^2 q N_d}{\epsilon_s} \quad (2.10)$$

ξ is the energy difference between the conduction band edge and the Fermi-level, in the bulk of the semiconductor, and N_d is the donor density. From equation (2.10), this barrier lowering mechanism is greater for high donor density, and increases with reverse bias. If reverse bias is much greater than kT/q , the interfacial barrier lowering mechanism is well approximated by [68]

$$\Delta\Phi_{int} \equiv \alpha \left[\frac{2qN_d V}{\epsilon_s} \right]^{1/2} \quad (2.11)$$

There is one other important, bias-dependent barrier-lowering mechanism. It is due to the image force that exists for a charge near a highly conducting plane, such as a metal contact. The bias-dependent barrier lowering due to the image force effect is given by

$$\Delta\Phi_{image} = \left\{ \frac{q^3 N_d}{8\pi^2 (\epsilon_{\infty})^2 \epsilon_s} \left(V_{bi} - V - \frac{kt}{q} \right) \right\}^{1/4}, \quad (2.12)$$

where ϵ_{∞} is the high frequency permittivity of the semiconductor, reflecting the thermal velocity of the charge carriers. V_{bi} is the built-in potential of the junction. The interfacial layer is neglected in deriving (2.12).

In analyzing current-voltage data for a real metal-semiconductor contact, it is necessary to consider both the interfacial layer and image-force barrier lowering mechanisms.

Practical contacts must meet the requirements of process compatibility, stability, and uniformity, and must accommodate bonding. As device dimensions shrink, it is becoming a greater challenge to produce integrated circuits which display uniform barrier height or contact resistance across the wafer. Ideally, the metal-semiconductor contact should be uniform on the nanometer scale, and stable throughout processing. A good summary of recent techniques aimed at producing low interface-state (therefore unpinned) metal-semiconductor contacts can be found in [95],[96].

2.6.5. Dielectric Layers on III-V Semiconductors

After the metal-semiconductor interface, the most critical interface for the optimization of semiconductor devices is the semiconductor-insulator interface. Interfaces in this category include intentionally deposited passivants and dielectrics, as well as native oxides. These interfaces affect the performance of essentially all modern semiconductor devices, including HBT's and pin detectors [98], MODFET's [99], and lasers. The success of silicon MOS devices is a result of the ability to control and engineer the properties of the silicon-oxide interface, so that charge storage in the near-surface semiconductor can be controlled by application of an electric field perpendicular to the interface. The recombination velocity for carriers at the Si/SiO₂ interface is as low as 10 cm/s, and the density of interface states capable of storing charge is on the order of 10¹⁰/ cm². This corresponds to less than one charge site per 10⁵ interfacial atoms [49].

The situation for the III-V semiconductors is not nearly as ideal. Attempts to develop a GaAs-based metal-insulator-semiconductor (MIS) integrated circuit technology have failed. This is due to the relatively poor chemical stability, and high interfacial-state density, between GaAs and its homomorphic oxides and nitrides [100]. The GaAs/AlGaAs semiconductor family exhibits especially high

surface recombination velocities, on the order of 10^6 cm/s [49]. This is partly due to the high affinity of atmospheric oxygen for aluminum, and also to the tendency of elemental arsenic to aggregate at the interface between arsenides and their natural oxides [101]. The other major III-V semiconductor family, InGaAsP/InP, exhibits surface recombination velocities on the order of 10^3 cm/s [49], a great improvement over AlGaAs, but not competitive with silicon.

Several techniques are available to improve the interface characteristics of III-V devices. First, lattice-matched heteroepitaxy allows the growth of highly ordered interfaces between an active region and a wider band-gap semiconductor alloy. The wide band-gap layer plays the role of the oxide in silicon technology, by isolating the active region of a device from defects at the free surface. Interface state densities can be quite low, between alloys such as AlGaAs and GaAs, or InGaAsP and InGaAs. In this sense, the cap layer described in Section 2.3 acts as a passivant for the underlying absorption region. However, there is a limit to the degree of isolation in such an approach. In lateral high-speed devices, carriers may be heated to the point that the band-offsets of a lattice-matched alloy are not confining, and the free surface is not effectively isolated. Still, heteroepitaxy is critical to the success of many devices, including MODFET's and double-heterojunction semiconductor lasers.

A second approach to improving III-V interface characteristics is the deposition of heteromorphic insulating layers, such as silicon dioxide, silicon nitride, or polymers. The aim is to eliminate and prevent the growth of the natural oxide layer. The combination of heteroepitaxy and heteromorphic passivation has proven especially successful. Care is required to deposit the heteromorphic insulator in intimate contact with the semiconductor. Often a thin (~5 nm) interfacial oxide layer remains [101], and can completely dominate the characteristics of the semiconductor surface, irrespective of the heteromorphic overlayer. To that end, it is required that the native oxide layer be removed by a suitable etchant, prior to deposition of the dielectric passivation layer. The etchant and the passivant must be developed in concert, as their effects are interrelated.

Recently, chemical pre-treatments of III-V surfaces, to alter the surface stoichiometry, have been investigated. Greatest success has resulted from treatment with sulfur-based compounds or antimony [100]. These methods are thought [102] to cause movement of the Fermi level at the surface (unpinning), and to reduce surface-recombination velocity. Both issues are somewhat contentious [100]. The improvement in surface conditions has generally been short-lived (hours), which limits the usefulness of many such surface treatments on their own. It is likely that the combination of a suitable chemical pre-treatment, followed by the deposition of a heteromorphic insulator, will ultimately be the technology of choice for stabilizing III-V semiconductor surfaces.

It is worth mentioning that a good theoretical discussion of surface-recombination can be found in [88]. The surface recombination velocity can be defined as [49]

$$S = \frac{J}{q(n_s - n_0)} , \quad (2.13)$$

where J is the current density due to recombination at the surface, and n_s and n_0 are the surface and bulk electron (volume) concentrations, respectively. Explicit expressions for S , derived from the physical models of surface states discussed in Section 2.6.3, can be found in [88]. S depends on the density and nature of the interface states, the doping density of the semiconductor, the density of photon-generated or electrically injected carriers, and the thermal velocity of carriers, among other things. It is also important to note that interfacial state densities, for a given surface, depend on the temperature and method of epitaxial growth [86].

2.6.6. Passivation of III-V Semiconductors

According to Green and Spicer [100], the ideal passivant should prevent reactions between the semiconductor and its atmosphere (chemical passivation), eliminate and prevent formation of a high density of band-gap interface states (electrical passivation), and present sufficient barriers to electrons and holes, such that carriers are confined to the semiconductor. A fourth requirement might be

added, in that the dielectric should shield against physical damage (mechanical passivation). This can be important in laser and photodetector applications, where the semiconductor device is coupled to an optical guide such as a fiber. A fifth role for the passivant, also for lasers and photodetectors, is as an anti-reflection coating.

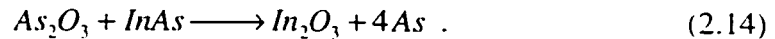
For passivation of III-V semiconductors, nitride- and oxide-based heteromorphic insulators have generally been used. Oxides tend to exhibit wider band-gaps, which is often deemed the most important characteristic of the insulator [103], but nitrides have the advantage of being much less reactive, and therefore do not promote the formation of mixed phases and interdiffusion at the semiconductor-insulator interface. On III-V semiconductors, deposited insulators such as SiO_2 and Si_3N_4 are generally amorphous and homogeneous [102]. The quality of a particular heteromorphic insulator is determined in part by its own bulk characteristics, but generally the physical and chemical reactions between the insulator and the III-V semiconductor are of greater importance.

2.6.6.1. Passivation of Arsenides

The most studied III-V semiconductor surface is the (100) face of GaAs. The natural oxide layer is generally amorphous, with constituent phases of Ga_2O_3 , As_2O_3 , and elemental As [104], amongst other Ga and As oxides, and adsorbed oxygen. In thermodynamic equilibrium, only Ga_2O_3 and As are stable phases, as discussed below, but As_2O_3 is often present in situations for which the oxide film growth has been governed by kinetic, rather than thermodynamic, factors. The total oxide film thickness is generally less than 5 nm, and tends to be striated, with Ga_2O_3 being the dominant species near the free-surface, and elemental As tending to accumulate near the semiconductor-oxide interface. A region of almost pure As near the interface may comprise up to 20% of the total oxide thickness [102].

Ternary arsenides such as InAlAs exhibit similar characteristics. The natural oxide layer on InAlAs is a mixture of phases, mainly In_2O_3 , As_2O_3 , Al_2O_3 , and As [104], [105]. Al_2O_3 and Ga_2O_3 are wide band-gap insulators, In_2O_3 is a fairly conductive semiconductor, and As is a metalloid.

The presence of free As at the interfaces of arsenides implies poor dielectric isolation perpendicular to the interface, in an MIS structure [103]. Also, it provides a path for leakage conduction parallel to the interface [101], which is a problem for lateral devices such as MODFETs and MSM detectors. Elemental As is also commonly thought [101] to be the primary source of band-gap interface states for the arsenides, and therefore the cause of Fermi-level pinning and excessive interface recombination. If not present initially, As may accumulate at the interface over time, due to substrate-oxide reactions such as [101]



For these reasons, passivation of arsenides usually requires that the interfacial As and arsenic-oxides be removed, prior to deposition of the heteromorphic insulator. In addition, for the InAlAs surface, passivation ideally involves the removal of the conductive In_2O_3 from the interface. Exposure to atomic hydrogen has been proposed [101] as a method to remove these species, but wet etchants are more typically used. The etchant contains an oxidant to tie up the free As, and an acid which will subsequently dissolve all of the arsenic and indium oxides. A dilute $NH_4OH:H_2O$ etchant was used to remove the surface oxide on InAlAs/InGaAs MSM photodetectors, as reported in Chapter 3.

Since elemental As is a product of oxidation, Si_3N_4 has generally been preferred as a passivant on the arsenides, rather than SiO_2 [102]. Even for Si_3N_4 , it is important that all sources of oxygen are removed from the deposition chamber. Further, it is beneficial to deposit with low substrate temperature, to minimize reactions between contaminant water and the arsenide surface. The low temperature PECVD method is particularly well suited to these requirements, and Si_3N_4 layers with extremely low oxygen content are attainable [103]. Within PECVD methods, many deposition parameters can influence the properties of the film, including substrate temperature, flow rates and chemical compositions of the reacting gases, chamber pressure, and plasma power and frequency [103]. Particle bombardment of the semiconductor surface can introduce interfacial defects [57], counter to the goals of the dielectric passivation.

2.7. Hole Pile-Up in Double-Heterostructure MSM Photodetectors

In modern heterojunction devices, a large band offset for one or both carrier species is often desirable; examples are electron confinement in the 2D channel of a MODFET, and confinement of both electrons and holes in the active region of double heterostructure and quantum well lasers. In other cases, large band offsets hinder transport of carriers, such as at the base-collector junction of a high-power HBT [53]. In double-heterostructure MSM detectors, the wide band-gap surface layer is a potential barrier to the collection of photogenerated carriers, as discussed briefly in Section 2.3.

A graded layer can essentially eliminate carrier pileup [106], but in some cases will not be feasible. It adds to the complexity of the MSM, while one of the primary advantages of the device is its simplicity, and it reduces the integration compatibility [107]. In addition, compositional grades are not generally achievable with InGaAsP, so superlattice grades are often substituted, with less desirable results.

Sano [108] studied electron pileup in an $\text{In}_{0.52}\text{Al}_{0.48}\text{As}/\text{In}_{0.53}\text{Ga}_{0.47}\text{As}$ MSM detector, and his Monte-Carlo results indicated it was only a concern at very low bias. This is not surprising, since for fields as low as 1-2 V/ μm in GaAs or InGaAs, a majority of electrons reside in the upper satellite valleys of the conduction band, with excess kinetic energy [84]. A more likely problem is hole pileup, as is found in other high-speed detectors [109],[110], and in quantum well spatial modulators [111].

In this section, a simplified model for hole transport in an MSM detector is developed. Based on this model, an estimate for the bias required to efficiently collect holes, in various material systems, is discussed. In the following, an MSM detector with 1 μm finger spacing and width, and a 0.5 μm absorption layer, is assumed. This allows direct comparison with the experimental results discussed in Section 3.4.

2.7.1. Bias Requirements for Saturation Bandwidth, in the Absence of Carrier Pileup

As discussed in Section 1.1, fast MSM detectors are gain-free devices: their photoresponse saturates at some low bias and is bias-independent thereafter. Also, the bandwidth of a gain-free MSM saturates at a slightly larger bias, one sufficient to drive all photocarriers at saturation velocity throughout the absorption volume. The bias at which saturated bandwidth is obtained depends on the finger spacing and width, the absorption region thickness, background doping in the layers, and secondary processes which delay carrier collection. These secondary processes include trapping in the bulk or at semiconductor interfaces, and free-carrier pileup at heterojunctions.

The transport properties of micron-size MSM detectors are generally well described by steady-state velocity-field relations [16]. For electrons, saturation velocity in GaAs or InGaAs is obtained for fields on the order of 0.1 V/ μm . Hole velocity in GaAs and InGaAs is nearly saturated at about 0.5 and 1 V/ μm , respectively [49]. Clearly, hole velocity determines the bias required for bandwidth saturation.

A one-dimensional MSM structure is fully depleted and has a unidirectional field for biases beyond the flat-band voltage [9], $V_{fb} = eN_d L^2 / 2\epsilon$, where e is the electron charge, N_d is the dopant concentration of the semiconductor, L is the finger spacing, and ϵ is the semiconductor permittivity. For an n-type semiconductor, the minimum field is near the anode, and beyond V_{fb} is given by $(V - V_{fb})/L$. For a nominally undoped carrier concentration of $5 \times 10^{14} \text{ cm}^{-3}$, a 1 μm MSM detector, on a III-V semiconductor, should exhibit a flat-band voltage of approximately 0.35 V. For InGaAs, the bias required to saturate hole velocity near the anode is then approximately 1.35 V.

A correction is necessary for two-dimensional effects [112],[113]. The field at the bottom of the absorption region (0.5 μm below the surface, in the '1x1' MSM) is uniformly about half the nominal one-dimensional value (bias/finger space). This is demonstrated in Appendix A. Thus, adding a correction factor of 2

to the result above, it is reasonable to expect that the ('1x1') InGaAs-based MSM could exhibit saturated bandwidth for a bias voltage as low as 3 V, in the absence of carrier pileup or similar mechanisms. The corresponding value for the GaAs device is approximately 2 V.

2.7.2. Hole Transport

Figure 2.21 illustrates the situation for holes approaching their collecting electrode in the DH-MSM. At low bias, the holes are insufficiently heated by the field near the cathode and do not emit efficiently over the valence band offset, which limits device bandwidth. Generally speaking, hot carrier effects in micron-size devices can be accurately treated using a hydrodynamic model [114]. A one-dimensional energy balance equation for holes is

$$\frac{\partial W}{\partial t} = -\frac{\partial}{\partial z} [(5/2)pkT_h)v_d] + J_h\xi - \frac{3/2pk(T_h - T)}{\tau_E}, \quad (2.14)$$

where W is the mean energy density of the holes, p is hole density, T_h is the mean hole temperature, T is the lattice temperature, J_h is the hole current density, v_d is the hole drift velocity, ξ is the electric field, k is Boltzmann's constant, and τ_E is an ensemble relaxation time, representative of energy exchange between holes and the lattice. A Maxwellian hole distribution is implicit in deriving (2.14), for the unambiguous definition of a hole temperature. Also, drift kinetic energy is assumed negligible relative to thermal energy.

An estimate of the bias required for negligible hole pileup, and thus saturated bandwidth, is sought. For low bias, holes pileup, and under modulated illumination a space charge builds up and decays near the valence band offset [109]. In this situation, a dynamical model would be useful in estimating the cut-off bandwidth due to hole pileup. If it is assumed a priori that hole pileup is negligible, however, a spatially uniform, steady-state approximation is reasonable, as follows.

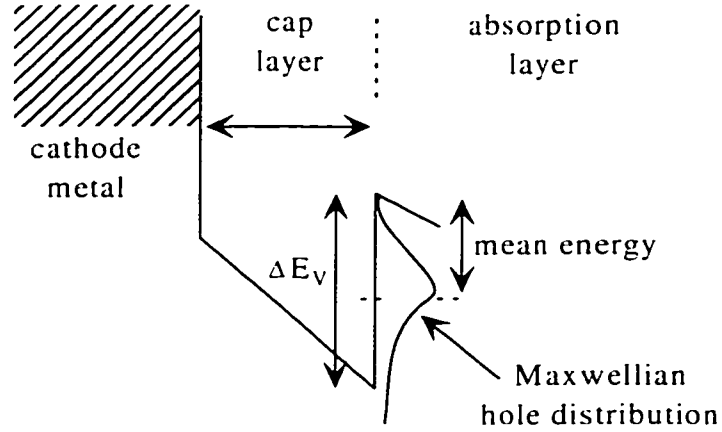


Figure 2.21. A Maxwellian hole distribution is shown schematically, incident on the valence band offset near the cathode. The holes are heated by the applied field, and have a characteristic mean energy. By comparing this mean energy to the valence band offset, as a function of bias voltage, an estimate of hole pileup can be obtained. The Maxwellian carrier distribution is never strictly valid, but is a commonly used approximation [114].

First, in most applications, the modulated signal illuminating the MSM is far below the level required to perturb the applied field, so the carriers travel along quasi-static field lines [16]. Second, the energy relaxation time in GaAs or InGaAs is on the order of 0.4 ps [110],[115], corresponding to an energy relaxation distance of 28 nm for holes drifting at saturation velocity. On this scale, the applied field in the micron-size MSM is very nearly uniform, so no large gradients in hole temperature or velocity are present. Also, even at 20 GHz modulation, hole density will be quite uniform. Thus, a very good first-order approximation to (2.14) is

$$ev_d \xi_c = \frac{3/2k(T_{hc} - T)}{\tau_E} \quad (2.15)$$

where ξ_c and T_{hc} are the quasi-static field and hole temperature near the cathode, respectively. Equation (2.15) sets an upper-limit on hole temperature, corresponding to negligible space-charge in the cathode region.

Using the one-dimensional field approximation [9] near the cathode $((V+V_{fb})/L)$ in (2.15), the hole energy $(3/2kT_h)$ as a function of bias was plotted in Figure 2.22. The one-dimensional field approximation at the cathode is quite valid in the real device [112], except near the corners of the fingers where the field is

enhanced (see Appendix A). The parameters used were 0.4 ps for the energy relaxation time [110], a lattice temperature of 300 K, and a saturation drift velocity for holes of 7×10^6 /cm [49]. This last assumption limited the validity of the model to biases greater than 2-3 V. The dashed line in Figure 2.22 was extrapolated from the model of Scholz [116] for stationary hole transport in GaAs. The data shown represent his estimate of heavy-hole heating as a function of static electric field, and were obtained with a more sophisticated treatment of energy relaxation by phonon scattering.

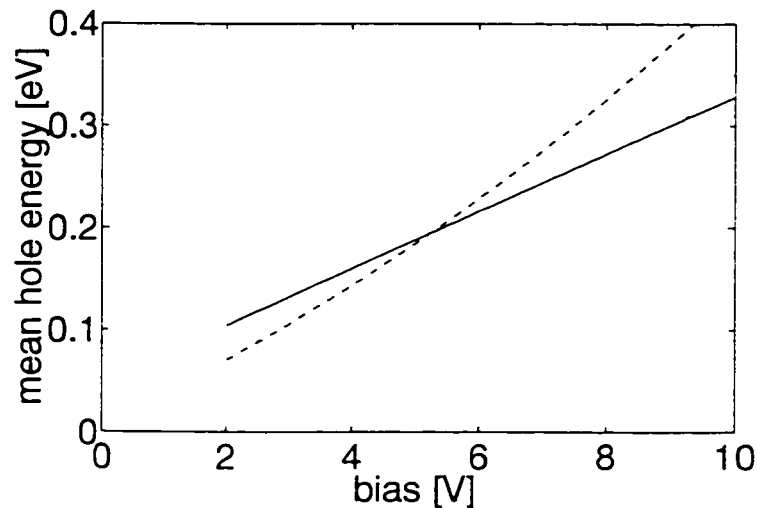


Figure 2.22. Mean hole energy near the cathode vs. bias is shown, per the model described in the text (solid) and extrapolated from data in reference [116] (dash). Dotted lines show band offsets for $\text{Al}_{0.2}\text{Ga}_{0.8}\text{As}/\text{GaAs}$ (0.09 eV), $\text{InAlAs}/\text{InGaAs}$ (0.2 eV), InP/InGaAs (0.35 eV), and InGaP/GaAs (0.31 eV). It is predicted that the phosphorus-based material systems will require higher bias for saturated speed.

Also shown in Figure 2.22 are the accepted valence band offsets [78] for the lattice-matched cap/absorbing layer combinations discussed in Sections 2.4 and 2.5. These values are compared to the hole energy curves, to estimate the bias voltage at which the assumption of negligible pileup becomes valid. The results of 2 to 3 V for $\text{Al}_{0.2}\text{Ga}_{0.8}\text{As}/\text{GaAs}$ and 5 to 6 V for $\text{InAlAs}/\text{InGaAs}$ are in general agreement with the experimental results described in Section 3.4, given the simplified nature of the model. It is predicted that the higher valence band offsets in the InGaP/GaAs and InP/InGaAs material systems will result in higher bias requirements for saturated speed. An accurate treatment of these effects would

consider time-dependent thermionic emission and tunneling of holes, out of the triangular quantum well in Figure 2.21 [109]. This is left for future work.

2.8. Design of an MSM Mask Set and Development of a Fabrication Process

As mentioned in Chapter 1, research involving MSM photodetectors is ongoing at TRILabs. It is expected that MSM photodetectors will be of central importance to various projects of current and future interest. Of primary interest for systems applications is the MSM detector array, discussed in Chapter 5. As a result of previous work on photodetector arrays at TRILabs, several novel array layouts were suggested [20]. The mask set developed here incorporated those novel arrays, and initial experimental results are presented in Chapter 5.

The mask set was also designed to facilitate MSM device research at TRILabs. As such, individual devices were included, properly configured for on-wafer probing, and varying in terms of relevant geometrical parameters. Finally, process control features were included for the first time, so that TRILabs can analyze the quality of semiconductor epitaxy and post-growth fabrication. The mask set was described in detail elsewhere [117], so only a brief outline is given here.

The mask set was developed using Cadence Design Framework II software, and consists of four separate layers. They were written on 4 in. x 4 in. soda-lime glass, 0.09 in. thick. The mask layout was divided into reticules of either 4.3 mm x 4.3 mm or 2 mm x 4.3 mm, with inter-reticule spacing of 500 μm , to accommodate scribe channels for wafer dicing. The unit cell of the mask comprises 15 of the larger chips and 20 of the smaller, and is repeated nine times on the glass plates. A legend describing the contents of the unit cell is shown in Figure 2.23. Figure 2.24 is a plot of the unit cell, shown schematically in Figure 2.23. Crosses were used to delineate the chips (and thus the scribe channels). Like the labels, these features were defined on the interconnect-metal layer.

8 detector 'goalpost' array 2x2_75 MSM	Large individual detectors	8 detector 'rake' array 2x2_75 MSM	8 detector 'goalpost' array 2x2_75 MSM	8 detector 'rake' array 2x2_75 MSM
8 detector 'goalpost' array 2x2_75 MSM	16 detector 'rake' array 1x3_75 MSM	8 detector 'rake' array 2x2_75 MSM	8 detector 'goalpost' array 2x2_75 MSM	8 detector 'rake' array 2x2_75 MSM
process control features	individual detectors	16 detector 'fat squid' array 2x2_75 MSM	individual detectors	16 detector 'fat squid' array 2x2_75 MSM
8 detector 'goalpost' array 2x2_75 MSM	Large individual detectors	8 detector 'rake' array 2x2_75 MSM	8 detector 'goalpost' array 2x2_75 MSM	8 detector 'rake' array 2x2_75 MSM
8 detector 'goalpost' array 2x2_75 MSM	16 detector 'rake' array 1x3_75 MSM	8 detector 'rake' array 2x2_75 MSM	8 detector 'goalpost' array 2x2_75 MSM	8 detector 'rake' array 2x2_75 MSM
individual detectors	16 detector 'skinny squid' array 2x2_75 MSM	individual detectors	16 detector 'skinny squid' array 1x4_75 MSM	individual detectors
16 detector 'skinny squid' array 2x2_75 MSM	individual detectors	individual detectors	16 detector 'fat squid' array 1x4_75 MSM	spectrometer detector

Figure 2.23. The figure provides a legend for the mask set designed as part of this research. The arrays of photodetectors were named for their physical appearance, as shown in Figure 2.24. The size of the MSM detectors in each array is also indicated. The labeling corresponds to 'finger width x finger spacing _ active region side length'. Each photodetector on the mask has an adjacent label, following the same convention.

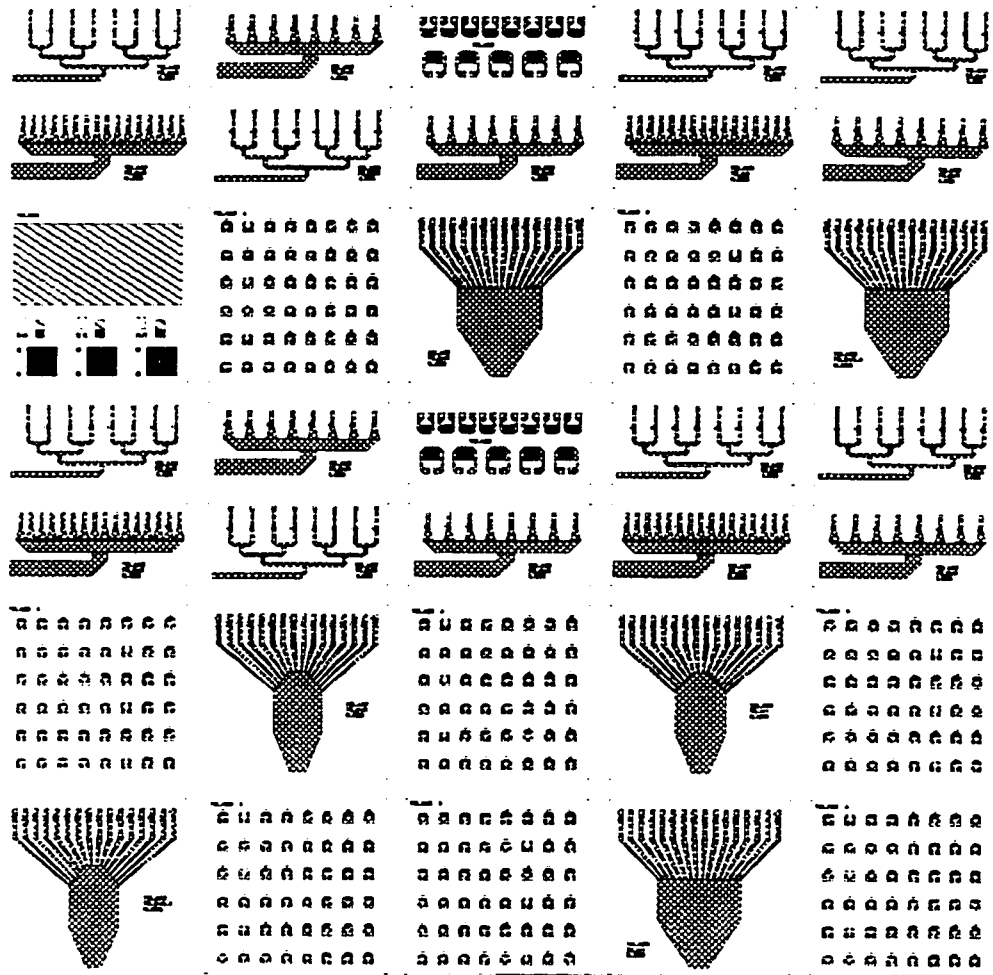


Figure 2.24. A unit cell of the mask set is shown. The features are described by the legend in Figure 2.23.

As mentioned, four mask layers were necessary to fabricate the devices required by TRILabs. The metal1 layer defines the fingers (electrodes) of the MSM only. This allows the designer freedom in terms of choosing an appropriate Schottky metal, including the use of semi-transparent or transparent materials. The metal2 layer defines the interconnect patterns amongst detectors, and from the detector to the point of signal extraction. Metal deposited using the metal2 mask generally lies on top of an insulating oxide or nitride layer, so adherence should be given some consideration. Also, bond wires will attach directly to this layer, so the deposited metal must be sufficiently thick and adherent to accommodate this.

A mesa mask was included for inter-device isolation in arrays. The fourth layer is a window mask, used to open windows in an insulating layer, for the active

detector regions. This allows the isolation of interconnect metal from the semiconductor, eliminating leakage current via these paths. The basic fabrication process, neglecting details such as wafer cleaning at various stages, is outlined in Figure 2.25.

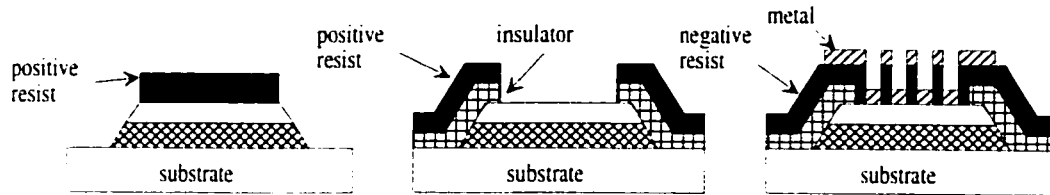


Figure 2.25. The process for fabrication of MSM photodetectors is shown schematically. The mesa mask is light field, and requires a positive resist. Following mesa formation, an insulator is deposited, and the window mask is used to open active regions. The window mask is dark field, and also requires a positive resist. Both metal layers are light field masks, and liftoff is performed with a negative resist. As an option, an anti-reflection or passivation layer can be deposited last, and defined with either the mesa or metal2 mask.

Finally, etchants were developed for the InP-based material systems described in Chapter 3. The fabrication work was performed at the Communications Research Centre in Ottawa, and expertise on etching GaAs-based materials was pre-existing. Both selective and non-selective wet etchant recipes were specified, for InAlGaAs/InP and InGaAsP/InP material systems. The details of these recipes were reported elsewhere [118],[119] and some were employed successfully, in fabrication of the devices reported in Chapter 3.

2.9. Summary of Technology Issues

MSM photodetector performance is dependent on the quality of two key interfaces: The metal-semiconductor interface must provide a high-quality Schottky barrier, and the free or passivated surface of the semiconductor epitaxy must not introduce deleterious effects. By comparison, the particular details of the epitaxy, such as band offsets, are probably of secondary importance.

The basic epitaxial structure of a double-heterostructure MSM detector, required for dependable performance, was described in Section 2.3. Based on that,

alternative epitaxial material systems, on both InP and GaAs, were discussed in Sections 2.4 and 2.5. A key advantage of phosphorus-based materials, as opposed to arsenic-based materials, is their inherently superior surface characteristics. On the other hand, the arsenic-based materials discussed exhibit slightly favorable band offsets.

The basic theory of semiconductor interfaces, including Schottky barriers and semiconductor-dielectric interfaces, was reviewed in Section 2.6. Passivation of arsenic-based semiconductors was given greater attention, due to the inferior surface-properties of those materials.

In Section 2.7, the transport of holes in the MSM photodetector was addressed theoretically. Hole pileup at heterojunctions is a common problem in bipolar devices such as photodetectors. It was demonstrated that a small valence band offset, at the cap layer of an MSM detector, allows higher speed operation at low bias. In this sense, the arsenic-based semiconductors discussed have an advantage.

In Section 2.8, the mask set and fabrication process for MSM photodetectors was described. This process was used successfully, and experimental results for high-performance MSM photodetectors are presented in Chapter 3.

3. Experimental Results For Double-Heterostructure MSM Photodetectors

3.1. Introduction

Based on the proposals outlined in Chapter 2, epitaxy was obtained in three different material systems, and MSM photodetectors were fabricated. Two alternative material systems were studied for InP-based detectors, operating at a wavelength of 1300 or 1550 nm. Those devices employed an $\text{In}_{0.53}\text{Ga}_{0.47}\text{As}$ absorption region. Also, double-heterostructure detectors were fabricated on a GaAs substrate, for operation at a wavelength near 800 nm.

As noted in Chapter 2, Schottky barrier heights on GaAs-based materials are generally quite high, and dark current is usually negligible. On the other hand, dark current is a key comparison point for InP-based MSM photodetectors. Therefore, detailed dark current studies were conducted for the InP-based devices. The dark current observed for the GaAs-based wafer was below the minimum range of the available test equipment (<100 nA), so a dark current study was not conducted.

DC photocurrent characteristics were studied for all of the wafers, to determine if low-frequency gain was present. The InGaAsP/InP material system, described in Section 3.2, was inherently free of low-frequency gain. That material system is presented first, since it produced devices that were very nearly ideal. This provided a standard of comparison, for the material systems described in later sections.

The InAlGaAs/InP material system exhibited low-frequency gain in initial testing. In section 3.3, those initial tests are described, and the results are contrasted with those for the InGaAsP/InP devices. A silicon nitride passivation layer reduced low-frequency gain in the InAlGaAs/InP devices. The details of that passivation technique are also described in Section 3.3.

Finally, for devices fabricated in the AlGaAs/GaAs material system, results are presented in Section 3.4. On that wafer, Approximately 80 % of the devices

were free of low-frequency gain, while the remainder exhibited substantial gain. This illustrated the degree to which local surface conditions can affect the performance of MSM photodetectors.

Nearly transit-time-limited bandwidth was observed, for each of the material systems investigated. For the InP-based MSM photodetectors, these were some of the fastest results reported in the literature at the time of writing [59],[120]. Extremely fast response was obtained for the gain-free AlGaAs/GaAs devices, at very low bias [121]. This was attributed to minimal hole pileup, for the optimized epitaxial structure used. Section 3.5 contains a summary of the results obtained, for basic double-heterostructure MSM photodetectors.

3.2. InGaP/InP/InGaAs/InP Material System – Experimental Results

As discussed in Chapter 2, the phosphorus-based semiconductors generally have superior surface characteristics, as compared to the arsenic-based semiconductors. MSM photodetectors are sensitive to surface conditions, so there is incentive to employ a phosphorus alloy as the cap layer on an InGaAs-based device. Unfortunately, InP does not exhibit satisfactory Schottky barrier heights, so dark current is often high [57] if InP is used as a cap layer. To improve this situation, several researchers have incorporated a pseudomorphically-grown, $\text{In}_x\text{Ga}_{1-x}\text{P}$ surface layer [73],[79],[80]. This reportedly increases the Schottky barrier height, over that for InP alone.

A review of the available literature (Section 2.4) seemed to indicate that a further benefit was associated with the InGaP surface layer: low-frequency gain had been less prevalent for the devices that incorporated the pseudomorphic layer. The InGaP surface layer may act as an electronic passivant for the InP cap layer. The results obtained here were consistent with this hypothesis: negligible low-frequency gain was present, while the wafer surface received no special treatment or passivation after device fabrication. This is discussed in detail below.

The wafer was grown by Nortel Technologies, and the layer structure is illustrated schematically in Figure 3.1. For reference, Nortel labeled the growth as R2-1053. The composition of the pseudomorphic surface layer was $\text{In}_{0.8}\text{Ga}_{0.2}\text{P}$, which can be grown defect-free on InP, up to a layer thickness of approximately 14 nm [73].

10 nm $\text{In}_{0.8}\text{Ga}_{0.2}\text{P}$
40 nm InP
1 μm $\text{In}_{0.53}\text{Ga}_{0.47}\text{As}$
50 nm InP
S.I. InP substrate

Figure 3.1. The epitaxial layer structure is shown, for the devices discussed in the present section. All layers were grown nominally undoped, by MOVPE, on a Fe doped (semi-insulating) InP substrate. The surface layer is slightly mismatched, but was thin enough to avoid dislocations.

The devices were grown on an Fe doped InP substrate, by low pressure MOVPE. The nominally undoped layer structure consisted of a 50 nm InP buffer layer, a 1 μm $\text{In}_{0.53}\text{Ga}_{0.47}\text{As}$ absorption region, and a Schottky barrier enhancement layer of 40 nm of InP, followed by 10 nm of pseudomorphically grown $\text{In}_{0.8}\text{Ga}_{0.2}\text{P}$. A similar Schottky enhancement layer was previously shown to result in extremely low dark current [79]. The active areas were defined by opening windows in a 150 nm silicon nitride layer. The interdigitated electrodes were formed by metal evaporation, followed by a liftoff procedure. The metals used were Ti/Pt/Au, with thickness of 100/150/400 nm. The Schottky metal was not annealed. Bond pads were subsequently defined using a Ti/Au liftoff procedure. No mesa definition was included, and the devices were not passivated or anti-reflection coated. A photograph of a fabricated device is shown in Figure 3.2.

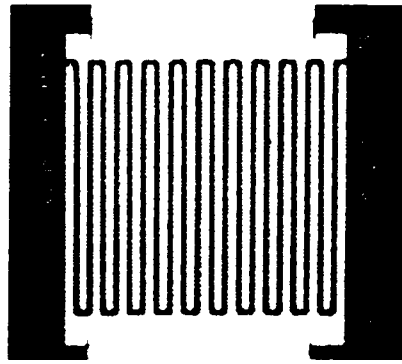


Figure 3.2. A microscope photograph is shown, of a 3x2 InGaAsP/InP MSM photodetector. The active region was defined by opening a window in a silicon nitride dielectric layer, and appears light grey. The area of the active region is $(100 \mu\text{m})^2$.

It should be noted that the devices were not fabricated with the mask set described in Chapter 2, but rather with an older mask set, referred to as TRILabs OTM-8. The relevant devices on this mask are illustrated schematically in Figure 3.3. Most of the results presented below were obtained for the devices with $3 \mu\text{m}$ finger width and $2 \mu\text{m}$ finger spacing ($'3 \times 2'$). The devices with $1 \mu\text{m}$ finger spacing were not successfully defined by the photolithography, so the $2 \mu\text{m}$ detectors were the fastest working devices on the wafer.

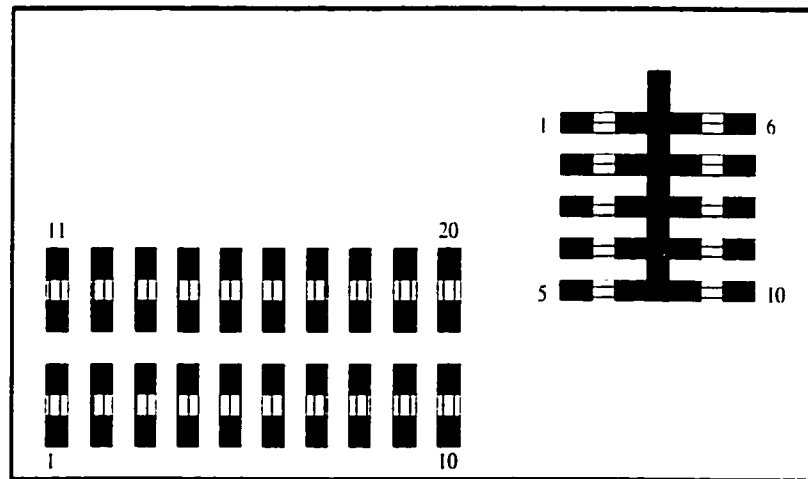


Figure 3.3. The relevant features of the OTM-8 mask set, used to fabricate the devices discussed in this section. The discrete photodetectors are labeled 1 to 20. Each has $3 \mu\text{m}$ finger width, and an active region area of $(100 \mu\text{m})^2$. The finger spacing ranges from $1 \mu\text{m}$ to $20 \mu\text{m}$. Most of the results were obtained for devices with $2 \mu\text{m}$ finger spacing. An array of ten detectors is also shown, but was not studied in detail here.

DC measurements were obtained first. A typical DC characteristic is shown in Figure 3.4, for a device with 3 μm finger width and 2 μm finger spacing. The devices display dark current of approximately 1 μA at moderate bias. This was attributed to a low Schottky barrier for electrons, of approximately 0.45 eV. The estimate was obtained from a temperature study, via the standard thermionic emission expression (see Section 2.3.5).

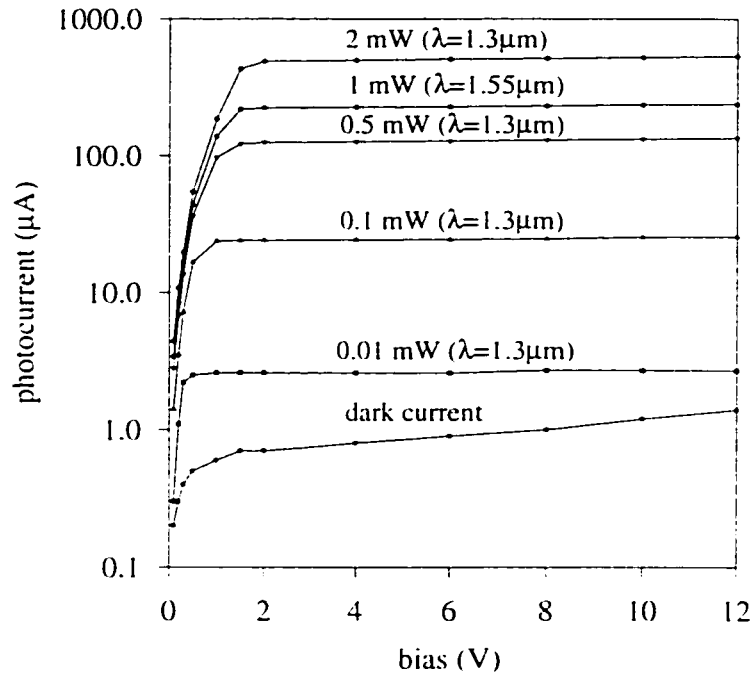


Figure 3.4. A typical photocurrent characteristic is shown, for a '3x2' MSM photodetector, fabricated in the InGaAsP/InP material system. The DC response is nearly ideal: The photocurrent saturates at a very low bias, and shows little bias-dependence thereafter. This is characteristic of a device for which low-frequency gain is negligible. The curves are labeled, to indicate the optical power and wavelength (λ) for each measurement.

The results of the temperature study are shown in Figure 3.5. It was established that electron transport dominated dark current, by a study of asymmetric metal patterns on the wafer. By reversing the polarity of bias, for detectors in the array of Figure 3.3, it was determined that the negative contact was injecting a greater number of carriers.

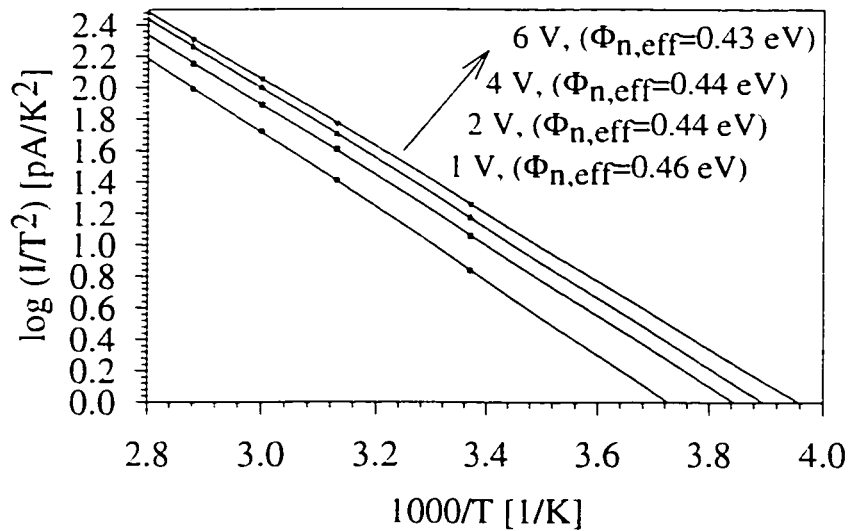


Figure 3.5. An activation energy plot is shown, for a '3x2', InGaAsP/InP device. The plot format is described in Section 2.3.5. The slope of the plots indicates the effective Schottky barrier height ($\Phi_{n,eff}$) of the MSM electrodes, at various bias voltages. As shown, Schottky barrier lowering effects were minimal.

The non-passivated $\text{In}_{0.8}\text{Ga}_{0.2}\text{P}$ surface exhibited good electronic characteristics. Minimal bias-dependent barrier lowering was observed. Also, the dark current characteristic was not dominated by carrier injection at the electrode peripheries. This was estimated by using a typical value for the modified Richardson constant ($7 \text{ A cm}^{-2} \text{ K}^{-2}$) in the standard thermionic emission expression (see Section 2.3.5). For a typical dark current value measured at 2 V and 24 C ($1 \mu\text{A}$), and the measured barrier height (0.44 eV), an electrically active area of $4500 \mu\text{m}^2$ was derived. This agreed well with the physical contact area for the devices, which was $3000 \mu\text{m}^2$. A more detailed discussion of the dark current results is contained in Section 3.3.1.

In spite of the low Schottky barrier for electrons, the devices exhibited negligible low-frequency gain. The I-V characteristic was flat beyond a saturation voltage of approximately 1 V, and responsivity was independent of optical power, over a range of optical powers from 0.01 to 2 mW. From Figure 3.4, the saturation responsivity was approximately 0.20 A/W at $1.3 \mu\text{m}$. This was in good agreement

with the theoretical estimate, taking into account surface reflection and shadowing by the opaque fingers.

The high-frequency characteristic of the 3x2 device is shown in Figure 3.6, measured at a wavelength of 1320 nm. The device of Figure 3.6 was typical, with a -3 dB bandwidth greater than 12 GHz, in good agreement with transit-time-limited estimates (see Section 1.6). Device bandwidths were nearly saturated at 7 to 8 V for all optical powers tested, up to 1.2 mW. The same device exhibited a -3 dB bandwidth greater than 9.5 GHz when tested at 1535 nm. The lower speed is expected, due to the greater absorption length for InGaAs at 1535 nm. This implies that more carriers are photogenerated deep in the absorption region, and transit-times are greater, on average.

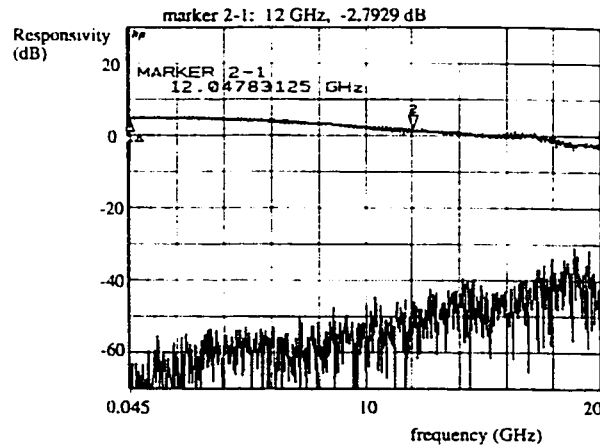


Figure 3.6. A frequency response is shown, for a typical 3x2 InGaAsP device. The upper trace was for a bias of 12 V, the lower trace was for a bias of 0 V. The wavelength of the incident light was 1320 nm, the average power was 1 mW. The on/off isolation was greater than 40 dB, across the entire 20 GHz measurement band. The vertical scale is in dB, relative to the photodetector used to calibrate the test system. 0 dB corresponded to approximately 0.1 A/W.

At 1 mW average illumination, the on/off isolation is shown for 12 V (upper trace) and 0 V (lower trace) bias conditions. The on-state response exhibited a -6 dB bandwidth of 18.5 GHz. The off-state response was the known noise floor of the measurement system. However, an on/off isolation of greater than 40 dB was established over the entire range of frequency. This level of

isolation suggests that these devices can be used as crosspoints, in the optoelectronic switching and signal processing elements discussed in Chapter 1.

The bandwidth as a function of bias is plotted in Figure 3.7, for an optical power of 0.4 mW at a wavelength of 1320 nm. Significant bandwidth was exhibited at bias voltages as low as 3 V. This is crucial for integration compatibility with electronic logic and amplifier devices, as discussed in Section 3.4.

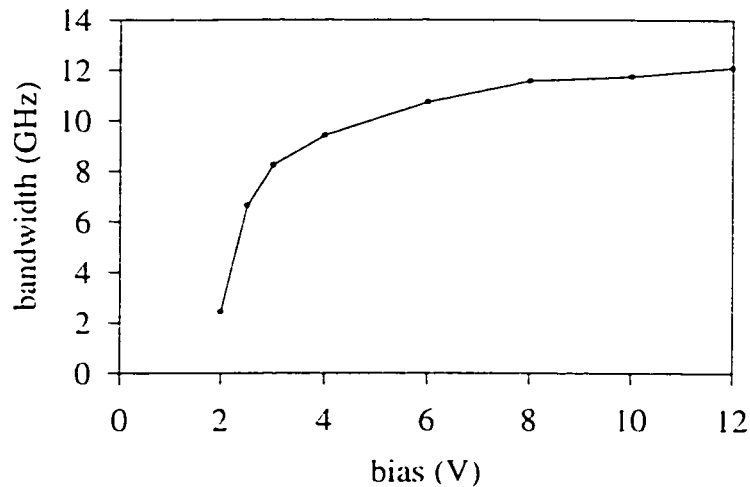


Figure 3.7. -3 dB Bandwidth as a function of bias is shown, for a typical 3x2 device on the InGaAsP/InP wafer. The device bandwidth was nearly saturated for bias as low as 7 to 8 V. The saturation bandwidth indicated (12 GHz) is in good agreement with the transit-time limited estimates discussed in Chapter 1.

Given the surface-oriented nature of the lateral MSM detector, and the ongoing search for suitable passivation methods on III-V semiconductors, it was significant that the InGaP interfaces exhibited inherently good electronic characteristics. It is also noted that no degradation in device characteristics occurred over a period of several months.

Previously, GaP has been identified [104] as the III-V semiconductor having the most thermodynamically stable surface. The natural oxide is essentially a single phase of quasi-insulating GaPO_4 , and elemental P is not present as it is on the free surface of InP. The results here, and in [79], suggest that InGaP surfaces may have superior characteristics to those of pure InP [57].

The low Schottky barrier height observed is typical for non-annealed metals on InGaP or InP [122]. A much higher barrier height was achieved in [79], for a similar pseudomorphic surface layer. This discrepancy presumably reflects differences in processing and surface treatment, as similar electrode metal was used in each case. In any case, dark current below approximately 1 μA is generally negligible relative to other sources of receiver noise [37], and often for MSM detectors the more critical issue is the elimination of low frequency gain [16]. From that perspective, the InGaAsP/InP detectors were more than acceptable.

In summary, transit-time-limited bandwidth was demonstrated (using frequency-domain measurement techniques) for large-area InGaAsP/InP MSM photodetectors. These devices have large active regions, which can be critical in many applications [23], and abrupt heterojunctions, which is important in maintaining integration compatibility with electron devices for receiver applications [107]. The excellent characteristics of the devices are attributed to the high-quality nature of the InGaP free surface.

For future work, it would be useful to develop a dielectric passivation technique that does not disturb the inherently good characteristics of the $\text{In}_{0.8}\text{Ga}_{0.2}\text{P}$ surface. The dielectric coating is important for improving the mechanical and environmental stability of the detector, and as an anti-reflection coating. These points were discussed in Chapter 2.

3.3. InAlAs/InGaAs/InP Material System – Experimental Results

The devices discussed in the preceding section provided a good example of nearly ideal characteristics, for a high-speed MSM photodetector. The InAlGaAs/InP devices did not exhibit ideal characteristics, however. In this section, the results for the two material systems are contrasted, to illustrate the deleterious effects of low-frequency gain and Schottky-barrier lowering. Also, techniques for assessing the origin of the low-frequency gain are presented. It is

demonstrated that, for the devices here, gain is due to traps at the semiconductor surface.

The epitaxy for the InAlGaAs/InP detectors was grown at the Advanced Materials and Process Engineering Lab (AMPEL), at the University of British Columbia. The epitaxial structure is illustrated schematically in Figure 3.8.

4 nm $\text{In}_{0.53}\text{Ga}_{0.47}\text{As}$
30 nm $\text{In}_{0.52}\text{Al}_{0.48}\text{As}$
0.54 μm $\text{In}_{0.53}\text{Ga}_{0.47}\text{As}$
10 nm $\text{In}_{0.52}\text{Al}_{0.48}\text{As}$
S.I. InP substrate

Figure 3.8. The epitaxial structure is shown, for the devices discussed in the present section. All layers were nominally undoped and nominally lattice-matched. The thin surface layer of InGaAs was grown to protect the aluminum-rich cap layer. InAlAs has a high affinity for atmospheric oxygen, which generally degrades the electronic characteristics of its free surface. Prior to deposition of the MSM electrodes, the surface InGaAs layer was selectively etched to expose the underlying InAlAs.

The devices were grown on a semi-insulating Fe-doped InP substrate, in a solid-source VG-V80H molecular beam epitaxy machine (base pressure 10^{-10} mbar). Growth was carried out at $1.1 \mu\text{m/hr}$, at a substrate temperature of 510 C and a V-III ratio of 20. The samples were grown under rotation, and showed a uniformity of $\pm 0.1\%$ in composition, as characterized by high-resolution x-ray diffraction (HRXRD) mapping. The layers were not intentionally doped, and were nominally lattice-matched. They consisted of a 10 nm InAlAs substrate buffer layer, followed by a $0.6 \mu\text{m}$ InGaAs absorption region, and capped with 30 nm of InAlAs. A thin (4 nm) InGaAs overlayer was grown at the surface, to protect the Al-rich cap layer from severe oxidation. The composition of the absorption layer was determined from HRXRD to be $\text{In}_{0.516}\text{Ga}_{0.484}\text{As}$, corresponding to slight tensile strain. No peak attributable to InAlAs could be found, but from the calibration it was expected to be nearly lattice-matched.

MSM photodetectors were fabricated on the wafer, at the Communications Research Centre in Ottawa. It began with standard cleaning, followed by PECVD deposition of 150 nm of silicon nitride. Windows were opened in the silicon nitride isolation layer to form active regions, followed by the removal of the surface InGaAs layer using a citric acid-based selective etchant [118]. The interdigitated electrodes were formed by liftoff of Pt/Au, and bond pads were subsequently defined by liftoff of Ti/Au. The mask set described in Section 3.2 was also used to fabricate the devices discussed in the present section.

3.3.1. Dark-Current Study of InP-based MSM Photodetectors

As discussed in Chapter 2, MSM photodetector performance is dependent on the quality of the Schottky contacts, and on the electronic surface conditions of the semiconductor epitaxy. Similar sets of MSM photodetectors were fabricated in two InP-based material systems, as described above. This provided an opportunity to make direct comparison of alternative epitaxy. The InGaAsP epitaxy exhibited nearly ideal Schottky contacts and surface electronic conditions, as discussed in Section 3.2. The InAlGaAs devices did not, however. In the present section, the effects of sub-optimal interface characteristics are illuminated, by comparing dark current characteristics for the two sets of devices.

Typical dark current characteristics for the InAlGaAs and InGaAsP devices (3x2) are shown in Figure 3.9. While the devices exhibited similar dark current values at moderate bias, the shape of the dark current characteristic was different. With reference to Figure 2.11, the InGaAsP dark current was apparently due to thermionic emission of electrons over a relatively low electron barrier. This was in fact proven to be the case, in the following.

The I-V curve for the InAlGaAs devices suggested a dark current characteristic dominated by hole conduction, with a reach through voltage near 2 V (again, see Figure 2.11). Fortunately, the mask set used to fabricate these devices contained a few highly asymmetric metal structures. By studying these structures, it was established that electron injection at the cathode was the

dominant process, in keeping with the expected situation for Schottky contacts on both n-InGaP/InP and n-InAlAs. The predicted electron barrier for most metals on n-InP is in the range of 0.45 to 0.55 eV, and on n-InAlAs is in the range of 0.6 to 0.7 eV, as discussed in Chapter 2. In each case the predicted hole barrier (see Figure 2.5) is much higher.

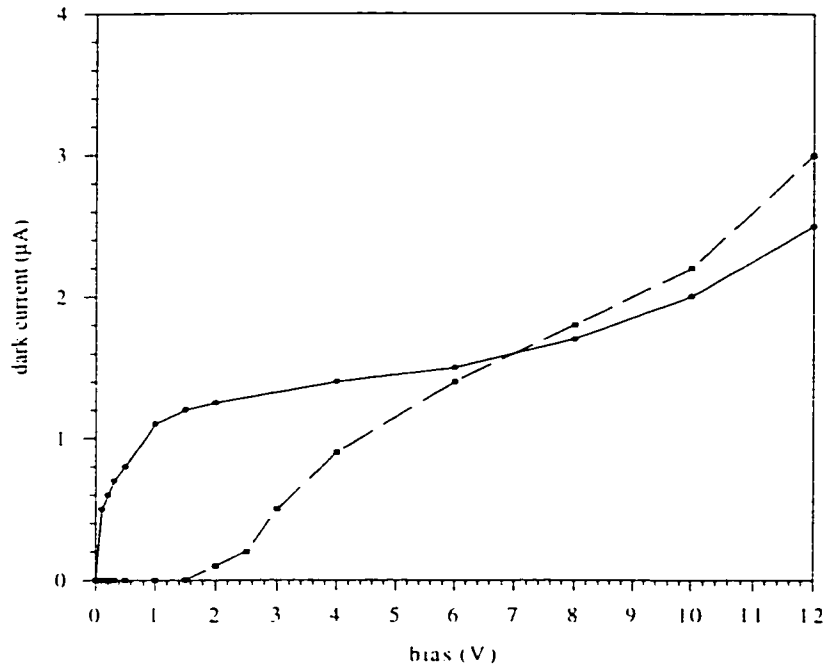


Figure 3.9. Typical dark current characteristics of '3x2' devices are shown; for the InAlGaAs/InP (dashed) and the InGaAsP/InP (solid) material systems. The magnitude of the dark current was similar, at moderate bias, but the curve shapes were different. The InGaAsP/InP characteristic is representative of an ideal Schottky contact, under reverse bias, as discussed in the text.

Once electron conduction was established as the dominant mechanism, an explanation was sought for the discrepancy between the two characteristics shown in Figure 3.9. The 'soft' breakdown characteristics (at approximately 8 V) reflect the onset of tunneling [68], especially near the edges of the metal fingers where the applied field is strongest. For the InGaAsP device, the low bias portion of the I-V curve was as expected for a Schottky contact: current saturation at relatively low voltage, followed by a gradual increase. This is characteristic of a high quality barrier, well described by the thermionic emission model.

The InAlGaAs device, by contrast, exhibited very low dark current at low bias, followed by a breakdown at only 2 V bias, and a rather kinked shape. This type of characteristic had been observed previously for MSM detectors [123], and surface effects were believed to be the primary cause. The kink in the I-V characteristic was attributed [123] to a transition in the dominant barrier lowering mechanism, from image force lowering to field emission (tunneling).

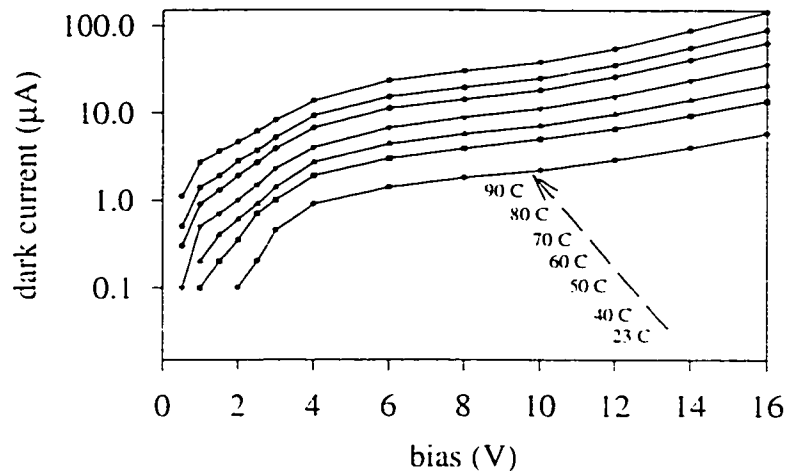


Figure 3.10. Dark current of an InAlGaAs '3x2' device is shown, as measured at various temperatures. Heating the device facilitated a better determination of the dark current characteristic, at low bias. At least three separate dark current regimes were observed: a rapid increase at low bias, followed by quasi-saturation, followed by soft breakdown at high bias.

The dark current of the InAlGaAs devices, at low bias and room temperature, was below the range of the measuring equipment available. Thus, results for a '3x2' device were obtained at elevated temperature, and are plotted in Figure 3.10. As many as three distinct regimes were apparent in the I-V characteristic.

Figure 3.11 is an ideality factor plot for an InGaAsP/InP, '3x2' device, as described in Section 2.3.5. The solid line is a linear regression of the data. The good linearity of the data points, and the near-unity ideality factor (1.04), provided further evidence that a good Schottky contact was achieved for those devices. The zero-bias barrier was estimated from the vertical intercept of the graph, and using an approximate value for the modified Richardson constant ($7 \text{ A cm}^{-2} \text{ K}^{-2}$).

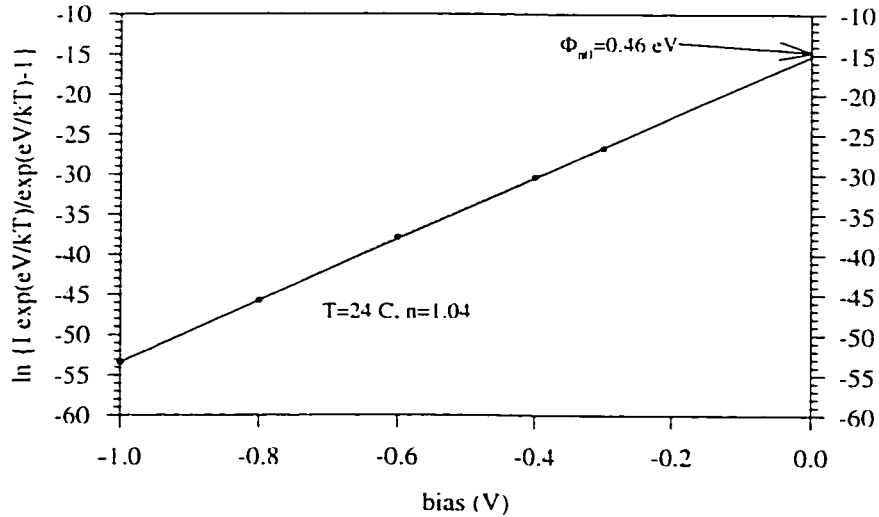


Figure 3.11. An ideality factor plot (see Chapter 2) for an InGaAsP/InP detector is shown. The data were taken at room temperature. The zero bias intercept indicated a Schottky barrier for electrons (Φ_{ni}) of 0.46 eV, with a typical value assumed for the modified Richardson constant. The reverse-bias ideality factor (n), determined from the slope of the plot, was approximately 1.04.

The device of Figure 3.11 was typical. For similar devices, the zero-bias barrier varied between 0.42 eV and 0.46 eV, while the ideality factor was consistently in the range of 1.02 to 1.04. The ideality factor, as determined, is not necessarily a reliable indicator of contact quality. Schottky contacts are more correctly characterized by forward bias measurements, which are not possible with the MSM structure. Note that these estimates for the Schottky barrier height are in excellent agreement with the activation energy plot for the same devices, in Figure 3.5.

From similar plots for the InAlGaAs devices, lower quality Schottky contacts were indicated. Figure 3.12 was a typical ideality factor plot for an InAlGaAs '3x2' device. The zero-bias barrier height was estimated as above, and was approximately 0.59 eV. Results from many plots of this type were consistently in the range of 0.58 to 0.62 eV. These are typical values for Pt on n-InAlAs [76].

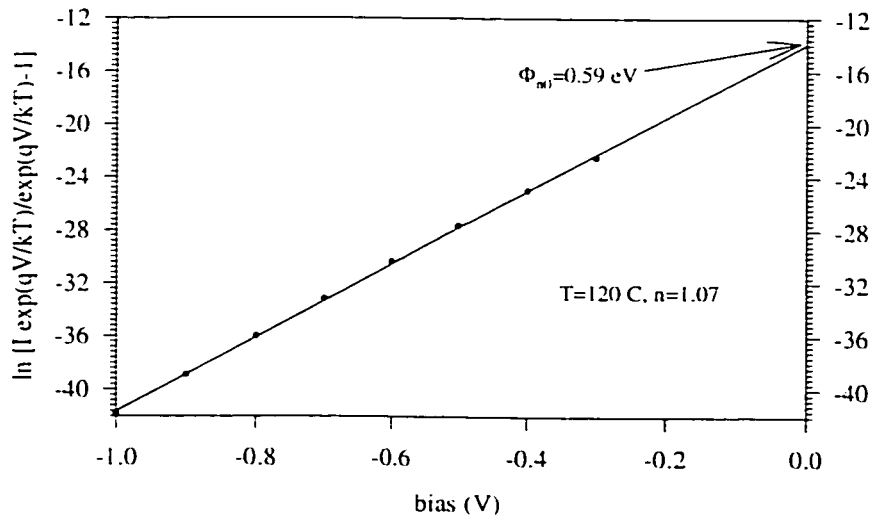


Figure 3.12. An ideality factor plot for an InAlGaAs '3x2' device is shown. The data were obtained at a temperature of 120 C. The zero-bias barrier height (Φ_{n0}) was estimated as 0.59 eV. From the slope of the curve, a reverse-bias ideality factor of 1.07 was estimated.

The activation energy plot for an InAlGaAs device is shown in Figure 3.13. Unlike the results for the InGaAsP/InP device above, the plot revealed that rapid and continuous barrier lowering was present, over the range of 1 to 3 V. This was followed by gradual barrier reduction above 3 V. The barrier height for 1 V bias was in good agreement with the zero-bias barrier height, estimated in Figure 3.12.

The observed barrier reduction suggested that edge effects might be contributing to the results. This was confirmed by plugging the data for 3 V, 23 C (0.5 μ A, 0.34 eV) into the thermionic emission equation, as described in Section 3.2. An electrically active area of only 50 μm^2 was estimated, which is a small fraction of the physical contact area of 3000 μm^2 . Thus, dark current was mainly due to emission over reduced barriers at the peripheries of the MSM fingers. The effective barrier height did not change significantly between 3 and 10 V, while the current showed a fairly dramatic increase (see Figure 3.10). This can be attributed in part to an increase in tunneling through a barrier of constant height. However, it probably reflects an increase in the electrically active area. In other words, the portion of the fingers exhibiting a saturated barrier height of 0.33 eV grows inward from the peripheries, with increasing bias.

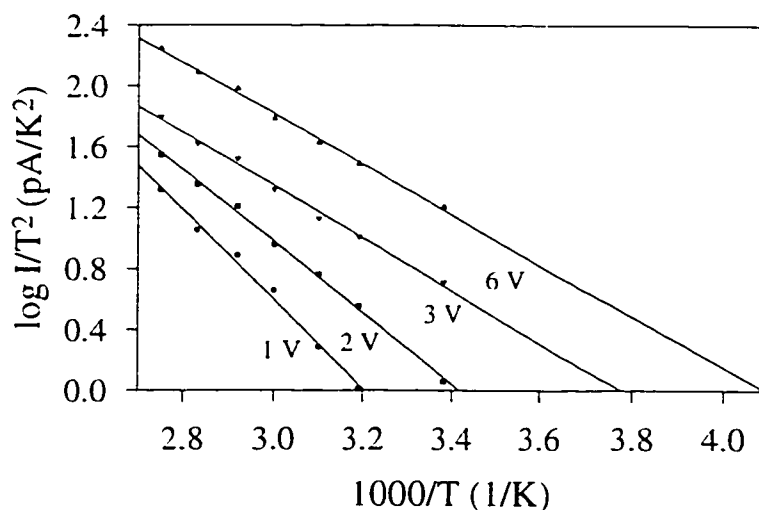


Figure 3.13. An activation energy plot for an InAlGaAs/InP '3x2' device is shown. From the slope of the curves, Schottky barrier lowering was observed in the 0 to 3 V bias range. The effective Schottky barrier at 1, 2, 3, and 6 V was estimated as 0.58 eV, 0.47 eV, 0.34 eV, and 0.33 eV, respectively.

The initially rapid decrease in barrier height can be attributed to a layer of high positive charge density, near the cathode contacts. The predominance of edge effects, evinced by the small electrically active area, suggested that surface effects were the cause. As mentioned, the InAlAs layer was etched by a selective citric-acid solution, designed to remove a thin surface InGaAs layer. From the results, it was speculated that an abundance of donor states were formed on the InAlAs surface. With bias applied to the MSM fingers, a very strong field exists between the peripheries of the cathode and these positively charged surface states. This greatly reduces the effective barrier height in these regions. Figure 2.3 illustrates the situation.

Similar results had been attributed to surface states by others ([123], and references therein). The InGaP/InP barrier enhancement layer apparently provided an extremely stable and trap-free surface. Conversely, the InAlAs surface may have been left with a high trap density, following MSM fabrication. These ideas were speculative, as more extensive experimental techniques would be required to determine the electronic conditions at these surfaces. Based on the discussion above, however, a portion of the InAlGaAs/InP wafer was passivated. The

passivation technique, and the corresponding improvement in device characteristics, is described in the following sub-section.

3.3.2. Reduction of Low-Frequency Gain by Silicon Nitride Passivation

The results in the preceding section favored the InGaAsP/InP material system. However, InAlGaAs/InP is an attractive alternative to InGaAsP/InP, for optoelectronic applications at the wavelengths of 1.3 and 1.55 μm [56]. Many devices of interest for the InAlAs/InGaAs material system are of a planar nature, including MODFETs and MSM detectors, and are sensitive to surface conditions, since typically only a narrow InAlAs barrier layer isolates the InGaAs active region from the environment. Since the combination of such planar devices holds great promise for optoelectronic integrated circuits (OEICs) [40], reliable passivation methods for $\text{In}_{0.52}\text{Al}_{0.48}\text{As}$ could have a major impact in this area.

Silicon nitride is a high quality dielectric, with good mechanical characteristics. It is hard and strong, has outstanding thermal-shock resistance and good thermal conductivity, is resistant to corrosion, and has a refractive index which makes it an excellent AR coating on most semiconductors [124]. It is traditionally the passivant of choice on arsenic-rich semiconductors, since it can be grown with low oxygen content [103], which prevents the oxidation-related aggregation of the metalloid As at the semiconductor surface [101]. It had been used as an anti-reflection coating on InAlAs/InGaAs MSM photodetectors previously [125], but few details of its passivating effects had been given [46]. More information was available [57] on the passivation of InP/InGaAs MSM detectors.

Low temperature PECVD is the preferred deposition technique for silicon nitride passivation of arsenic alloys [103], to minimize in situ oxygen and water incorporation. Silicon nitride films deposited by chemical vapor deposition (CVD) are generally amorphous (SiN_x), but the stoichiometry is typically well described by the crystalline form Si_3N_4 [124].

Passivation was attempted after it became clear, from the results in the preceding sub-section, that the InAlAs surface conditions were sub-optimal. The wafer was cleaved, and one half received no further treatment. The second half was etched for 20 seconds in an $\text{NH}_4\text{OH}:\text{H}_2\text{O}$ (1:10) solution, to remove the native oxide from the exposed InAlAs between the interdigitated fingers. It was then rinsed in D.I. water, blown dry with nitrogen, and immediately deposited with a passivating layer of 170 nm of SiN_x , by PECVD. The passivating layer was designed to be a first order anti-reflection (AR) coating at 1300 nm. It was deposited at a substrate temperature of 200 C, and the reacting gases were silane, nitrogen, and ammonia. The chamber pressure was 750 mTorr, and the plasma power and frequency were 20 W and 13.56 MHz, respectively.

All results were for MSM detectors with 3 μm finger width and 2 μm finger spacing ('3x2'), and an active region area of $(100 \mu\text{m})^2$. Results from several devices, at various locations on the wafer, were consistent. Dark current (discussed in Section 3.3.1) was relatively unaffected by silicon nitride passivation, showing only a slight reduction in soft breakdown at high bias.

Though dark current was unaffected, the deposition of silicon nitride essentially eliminated low frequency gain, which was apparent in the DC photocurrent characteristics of the non-passivated devices. This is shown in Figures 3.14 and 3.15.

Note that the theoretical responsivity for the AR-coated devices was approximately 0.2 A/W, while for non-AR-coated devices it was 0.14 A/W. For high bias and low optical power, the non-passivated devices exhibited quantum efficiency greater than 1. These are the accepted signs of the deleterious low-frequency gain often exhibited by MSM detectors, discussed in Chapter 1.

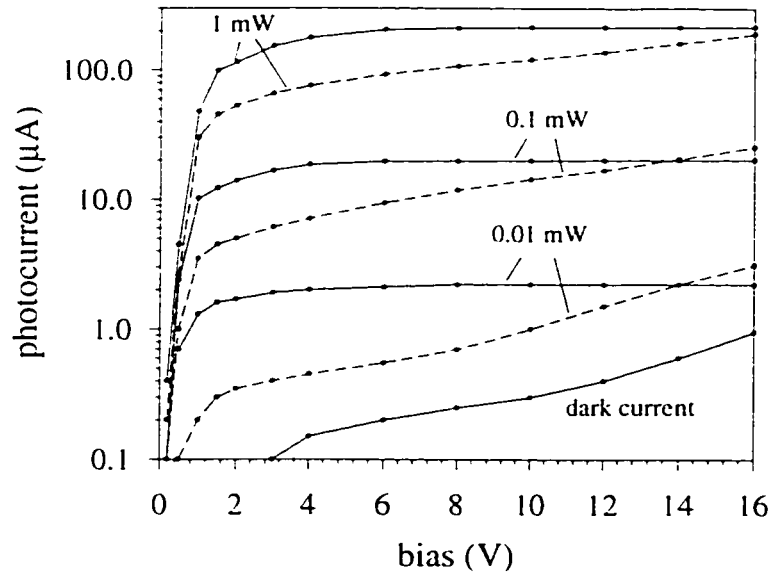


Figure 3.14. Photocurrent characteristics for a 3x2 InAlGaAs/InP MSM detector are shown: before passivation (dashed line), and after passivation (solid line). The photocurrent curves revealed much less recombination and low-frequency gain for the passivated device. The dark current was nearly identical before and after passivation. The photocurrent was measured for several optical powers, at 1320 nm wavelength, as indicated by the labels.

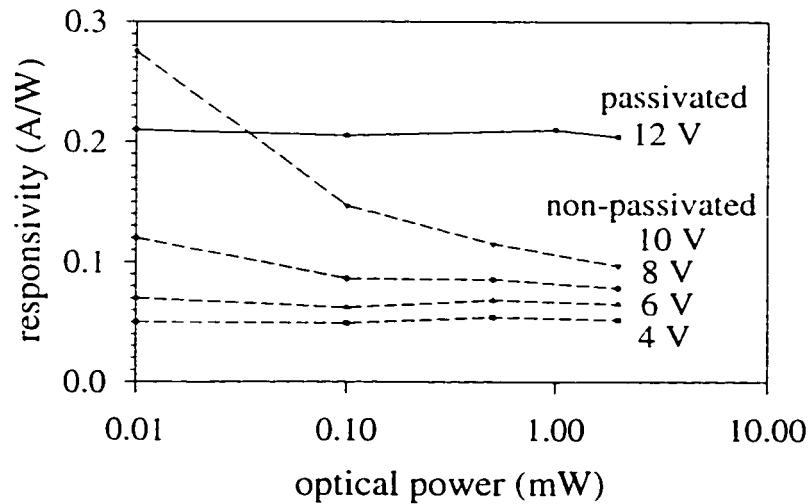


Figure 3.15. Plots of responsivity as a function of optical power are shown, for the passivated (solid line) and non-passivated (dashed lines) InAlGaAs/InP detectors. A responsivity that is independent of optical power indicates a gain-free MSM detector, as explained in the text. The plots were obtained at various bias voltages, as indicated by the labels.

The plot given in Figure 3.15 is generally interpreted [107] as follows. Gain is believed to be due to long-lifetime trapping of photogenerated electrons or

holes, field enhancement at the anode or cathode, and subsequent secondary injection of holes or electrons, respectively. Low optical power is sufficient to saturate the traps, so their contribution to photoresponse becomes negligible at higher powers. Thus, gain is most apparent at high bias and low optical power, as observed in Figure 3.15.

Note that at low bias and high optical power, for the non-passivated devices, the responsivity was below the theoretical estimate. This indicated that photogenerated carriers were recombining at the surface in those devices. After passivation, the photoresponse curves saturated at the theoretically expected responsivity, and responsivity was insensitive to optical power over the range measured. Presumably, the recombination and gain were mediated by band-gap surface states, whose characteristics were modified by the dielectric deposition.

Figures 3.14 and 3.15 also indicate that the dielectric overlayer was effective as an anti-reflection coating. This provided evidence that a nearly stoichiometric silicon nitride layer was deposited, with a refractive index near 2 as expected [124].

Figure 3.16 shows a frequency-domain measurement of bandwidth, and compares a passivated and non-passivated device for identical bias and optical power conditions. Low frequency gain for the non-passivated device, indicated by a peaked response at low frequency, was clearly visible. The non-passivated device also exhibited much lower AC responsivity. The passivated devices showed complete absence of low frequency gain under high-speed measurement, in agreement with the DC results.

The variation of bandwidth with bias is shown in Figure 3.17. The saturation bandwidth for the passivated devices was 10 to 11 GHz, and was obtained for bias voltage greater than 12 V. This compared well to transit-time-limited estimates discussed in Chapter 1.

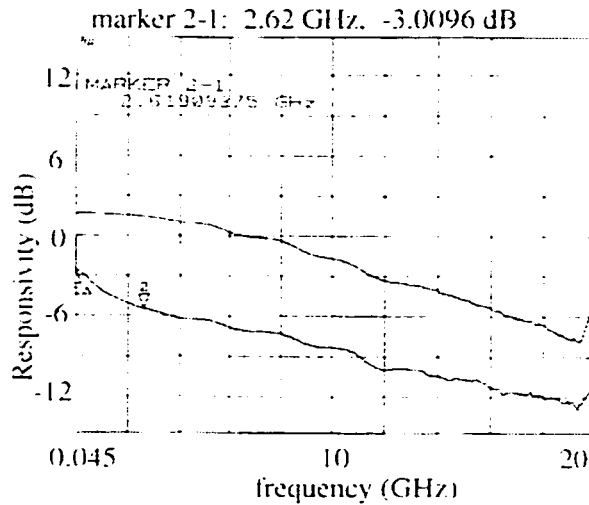


Figure 3.16. High-frequency measurements for the passivated (upper scan) and non-passivated (lower scan) InAlGaAs/InP MSM detectors are shown. The devices had finger width of $3 \mu\text{m}$, finger spacing of $2 \mu\text{m}$, and an active region area of $(100 \mu\text{m})^2$. Results were obtained with an optical power of 0.3 mW , at a wavelength of 1320 nm , and for a bias voltage of 12 V . Marker 2 indicates the bandwidth of the non-passivated device, 2.6 GHz . For the passivated device, the bandwidth exceeded 10 GHz . This was due to the absence of a peaked response at low frequency. The vertical scale is relative to the responsivity of the photodetector used to calibrate the system. 0 dB corresponds to approximately 0.15 A/W .

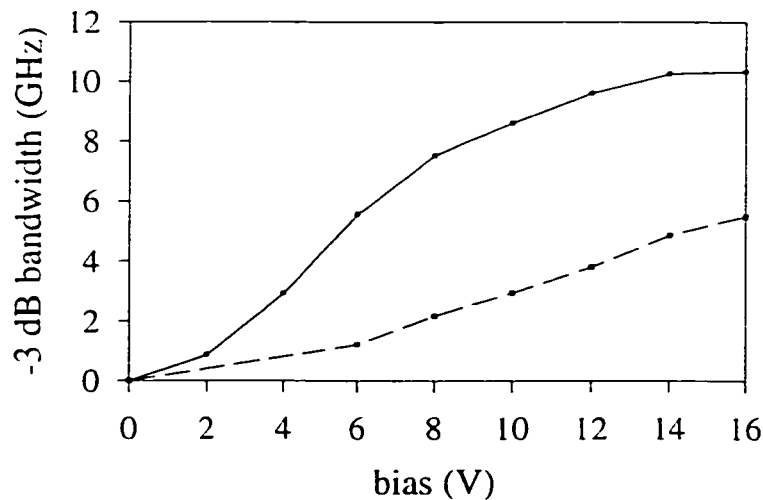


Figure 3.17. The bandwidth as a function of bias is shown, for the passivated (solid line) and non-passivated (dashed line) InAlGaAs/InP MSM detectors. The devices had finger width of $3 \mu\text{m}$, finger spacing of $2 \mu\text{m}$, and an active region area of $(100 \mu\text{m})^2$. The bandwidth of the non-passivated devices was limited by low-frequency gain, as shown in Figure 3.16.

Two primary conclusions could be drawn from the results. First, dark current was dominated by thermionic emission of electrons, over reduced barriers at the peripheries of the cathode fingers, both before and after SiN_x passivation. This indicated that a high density of fixed positive charge lowered the Schottky barrier in these regions. Second, low-frequency gain and excessive recombination were essentially eliminated by the passivation. This indicated that both were caused, in the non-passivated case, by the electronic nature of the free, oxidized InAlAs surface.

Previously, electron and/or hole trapping have been cited as the cause of low frequency gain in MSM detectors [65], and both dark current soft-breakdown characteristics (barrier lowering) and photocurrent gain have been attributed [57] to surface states. It was interesting that passivation eliminated low frequency gain here, but did not significantly alter the dark current. Similar results had been reported by others [57], but a satisfactory explanation was not available in the literature.

If both the barrier lowering and photocurrent gain were caused by charge storage at the surface, traps of opposite polarity must be responsible. Otherwise, the passivation should have had similar effects on each. Two distinct sub-bands of surface states might mediate the two observables, allowing passivation to affect (or not) each independently. The anti-site defect model (ADM) [95],[126] is compatible. In that model, the n-InAlAs surface Fermi level is pinned in mid-gap donor states.

With bias, in the dark, the InAlAs layer is depleted of carriers and a portion of these mid-gap donor states would empty, giving the surface a net positive charge and accounting for barrier lowering at the cathode. Under illumination, these empty donor states would be efficient electron traps, and the surface might revert to a negative charge condition, especially near the anode. This would produce secondary injection of holes, accounting for the gain. Also, photogenerated holes might be attracted towards the surface, where they would recombine via these mid-gap states.

Per Spicer [95], changes in stoichiometry at a surface correlate directly with the densities of donor and acceptor interface states. NH_4OH -based pre-etchants, as used here, reportedly leave an As-rich surface [127]. On the other hand, deposition of SiN_x by PECVD, using silane and ammonia, is associated [38],[103] with the conversion of free-surface As to arsine gas, and its subsequent removal. Thus, the overall change in stoichiometry is not clear. It is speculated that passivation reduced the density of III_{As} -related acceptor states, thereby reducing the negative charge stored at the InAlAs surface. This could minimize the proposed gain and recombination mechanisms, while not affecting dark current barrier lowering at the cathode significantly. A similar model has been proposed for sulfur passivation of III-V semiconductors, by Spicer [95].

Alternatively, dark current might not have been mediated by surface states, but rather by charged defects formed at the time of metal evaporation [58]. Also, a portion of the dark current might have been due to quasi-ohmic conduction, via metalloid arsenic and semi-conducting oxide phases (such as In_2O_3) at the interface [101].

3.4. AlGaAs/GaAs Material System – Experimental Results

Based on the recommendations in Section 2.5, a double-heterostructure wafer was obtained for operation in the 800 nm wavelength region. The wafer was grown by MOCVD, by the Communications Research Centre in Ottawa. For reference, the wafer was labeled as 97D25, and the fabrication run as CRC-96-072. The epitaxial structure is illustrated in Figure 3.18.

The epitaxial design of this wafer was described briefly in Section 2.5.1. A low aluminum concentration was used in the cap layer to reduce carrier pileup, as discussed below. Also, $\text{Al}_x\text{Ga}_{1-x}\text{As}$ alloys with $x < 0.22$ do not suffer from the DX-center traps lying in the band gap [85]. Finally, reduced aluminum concentration correlates with higher quality growth and greater environmental stability. The substrate isolation layers were a 50 nm layer of $\text{Al}_{0.5}\text{Ga}_{0.5}\text{As}$, to ensure that carriers

generated in the substrate are blocked from slowing the device, followed by a 50 nm $\text{Al}_{0.2}\text{Ga}_{0.8}\text{As}$ layer which should be free of DX traps.

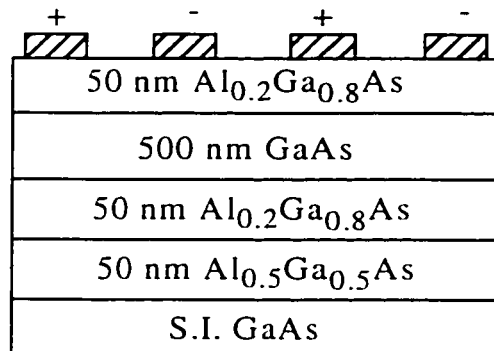


Figure 3.18. The epitaxial structure is shown, for the wafer discussed in the present section. The design of the epitaxy was described in Section 2.5.1. MSM fingers are shown schematically, at the top surface, in cross-section. The layers were grown on a semi-insulating (S.I.) GaAs substrate. Not shown is a 5 nm GaAs surface layer, grown to protect the AlGaAs cap layer from severe oxidation, and etched prior to metal deposition and passivation. The passivation layer (silicon nitride) is also not shown.

Following epitaxial growth, device active regions were formed, by etching mesas down to the semi-insulating GaAs substrate. Next, 200 nm of silicon nitride was deposited and windows were opened on top of the mesas. MSM fingers were formed by liftoff of Ti/Pt/Au, and bond/probe pads of Ti/Au were subsequently deposited. Finally, after a brief etch in dilute NH_4OH , a 105 nm passivation/anti-reflection layer of silicon nitride was deposited over the active regions. This passivation technique was identical to the one reported in section 3.3.2. Most of the results discussed here were obtained for devices with 1 μm finger spacing and width ('1x1'), and 2500 μm^2 active regions.

A photograph of one of the devices is shown in Figure 3.19. The mask set described in Section 2.8 was used to fabricate the devices.

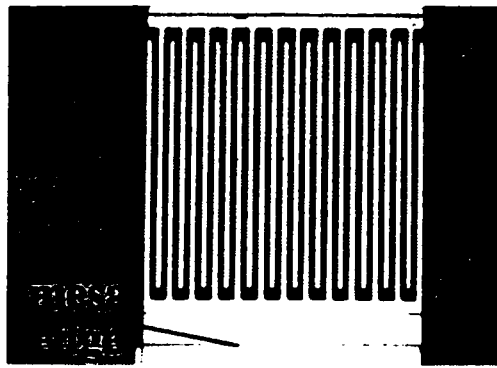


Figure 3.19. A microscope photograph of an AlGaAs/GaAs MSM detector is shown. The edge of the mesa is labeled. The device has 1 μm finger spacing and width (1x1), and an active region area of $(50 \mu\text{m})^2$.

The dark current of the devices was lower than could be measured with the available test equipment ($<100 \text{ nA}$ up to 10 V). Such a low dark current is typical for an AlGaAs MSM detector, as discussed in Chapter 2. The DC responsivity was measured, and a typical result is shown in Figure 3.20. The responsivity was in the 0.12-0.13 A/W range, limited by the thin absorption region, and reflection from the opaque metal electrodes. The DC photoresponse was gain-free to 5 V, but by 10 V there was a 10 to 20 % increase.

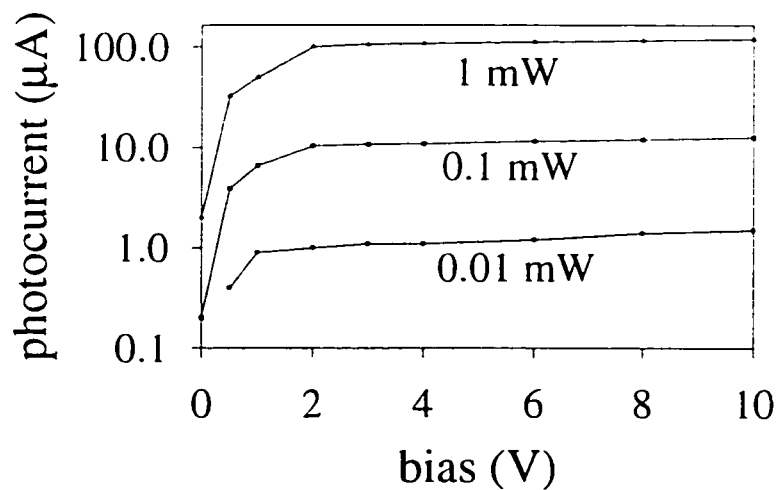


Figure 3.20. DC photoresponse characteristics are shown, for an AlGaAs/GaAs MSM detector, with 1 μm finger width and spacing. The curves were relatively flat up to 5 V, but show a gradual increase at higher bias. This is indicative of the onset of low-frequency gain. The photoresponse was measured for several different optical powers, at a wavelength of 830 nm, as indicated by the labels.

In keeping with the DC results, the high frequency measurements also revealed the onset of low-frequency gain, for bias voltage greater than approximately 7 V. The high-frequency response at lower bias was exceptional, however. Figure 3.21 shows the frequency response at 3 V bias, under 1 mW average illumination, at a wavelength of 830 nm. The -3 dB bandwidth exceeded 18 GHz. The initial roll-off followed by a plateau at higher frequency in Figure 3.21 is characteristic of transit-time-limited response, and is due to different average velocities for electrons and holes (see Section 1.6.2).

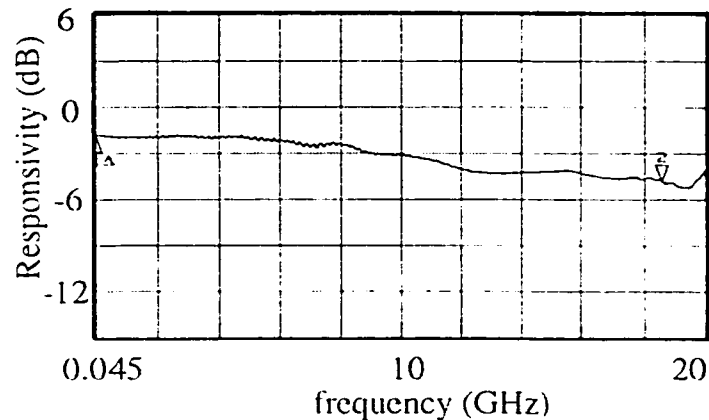


Figure 3.21. A frequency scan, for a 1x1 AlGaAs/GaAs device, is shown. The bias voltage for the measurement was 3 V, and the optical power was 1 mW, at 830 nm wavelength. Marker 2 indicates the -3 dB bandwidth, which was greater than 18 GHz. The vertical axis is relative to the photodetector used to calibrate the test system. 0 dB corresponds to approximately 0.15 A/W.

Figure 3.22 shows the variation of bandwidth with bias. Also shown are data reported by Wohlmuth et al. [128], for InAlAs/InGaAs devices of identical geometry ('1x1', 0.5 μm absorbing layer), measured at 1550 nm, 0.22 mW optical power. InGaAs at 1550 nm and GaAs at 830 nm have similar absorption coefficients (approximately $10^6/\text{m}$), so it was reasonable to compare the speed of the devices [16]. The devices reported here showed considerably enhanced speed at low bias, in spite of the fact they did not contain graded layers, as did the devices in reference [128]. The ultimate saturation bandwidth of the devices was not determined, due to the limitations of the test system. From measurements for '2x2' devices on the same wafer, it was estimated to be in the 21-22 GHz range, in good agreement with transit-time-limited estimates.

The detectors here and in reference [128] shared geometry, were nominally undoped, and exhibited nearly gain-free DC characteristics. The significant difference in bandwidth at low bias might be due to the different band offsets at the cap layers, and therefore different degrees of free-carrier pileup. Hole pileup was treated in Section 2.7. The bias required to saturate bandwidth, from Figure 3.22, was approximately 2 to 4 V for the $\text{Al}_{0.2}\text{Ga}_{0.8}\text{As}/\text{GaAs}$ devices, and 5 to 7 V for the $\text{InAlAs}/\text{InGaAs}$ devices in [128]. These estimates are in good agreement with the theoretical estimates, based on hole pileup, described in Section 2.7. Thus, these experimental results provided strong support for the previous theory.

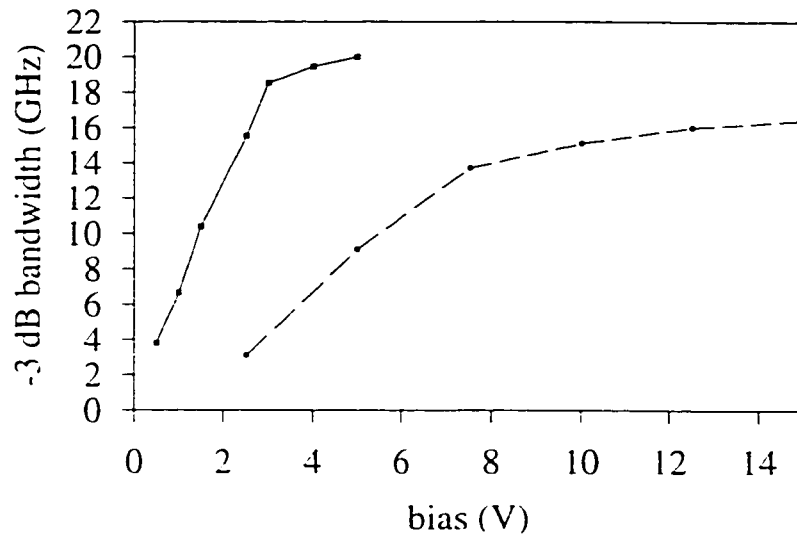


Figure 3.22. The -3dB bandwidth as a function of bias is shown, for the devices described in the present section (solid curve) and for the $\text{InAlAs}/\text{InGaAs}$ devices described in [128] (dashed curve). The $\text{AlGaAs}/\text{GaAs}$ devices reported here exhibited exceptional bandwidth at low bias. This was attributed to reduced hole pileup, as described in Section 2.7.

The low bias required for ultra-high bandwidth in these devices is important for OEIC applications, discussed in Section 1.4. In those cases, the integrated photodetector must be compatible with state-of-the-art transistors, which typically operate with a bias voltage on the order of 5 V or less. These results indicate that highly optimized MSM photodetectors were produced in the $\text{AlGaAs}/\text{GaAs}$ material system. Device bandwidth is not reduced by secondary mechanisms, such as trapping or pileup of photogenerated carriers.

3.5. Summary and Conclusions

In this chapter, attempts to optimize the technology of MSM photodetectors have been described. Devices were designed, fabricated, and tested, using both InP- and GaAs-based material systems.

As discussed in Chapter 2, MSM photodetectors are quite sensitive to the electronic properties of the semiconductor surface. The results of this chapter are entirely consistent. Significant evidence for the deleterious effects of surface states was obtained, from numerous measurements. In measurements of dark current, barrier lowering was attributed to charge storage at the semiconductor surface, and resultant field enhancement at the peripheries of the interdigitated electrodes. In DC responsivity measurements, surface effects produced excessive recombination at low bias, and gain at higher bias. In high-frequency measurements, the same gain was visible as a peaked response at low frequency.

InGaP/InP/InGaAs double-heterostructure MSM detectors were demonstrated in Section 3.2. These devices exhibited excellent low and high frequency characteristics, without need for any special surface treatment or dielectric passivation. This was attributed to the passivating effects of the $\text{In}_{0.8}\text{Ga}_{0.2}\text{P}$ cap layer used. Phosphorus semiconductor alloys reportedly exhibit superior surface properties, relative to arsenic alloys, and this was supported by the results. Thus, there is significant incentive to develop MSM detectors on InGaAsP/InP. Devices on the InGaP/InP/InGaAs wafer exhibited transit-time limited bandwidths, as high as 12 GHz for a detector with 2 μm finger spacing. This was one of the fastest results reported in the literature [120] at the time of writing, for photolithographically-defined, InP-based MSM photodetectors.

InAlAs/InGaAs detectors were investigated in Section 3.3. The initial results were sub-optimal, and this was attributed to a high density of charged interface states at the InAlAs surface. Subsequent passivation greatly improved the device characteristics. The passivation technique included a brief oxide etch, with dilute NH_4OH , and subsequent deposition of silicon nitride. Low-frequency

gain was nearly eliminated, as observed in both DC and high-frequency measurements.

The same passivation technique was used in the fabrication of AlGaAs/GaAs MSM detectors, as described in Section 3.4. Those devices also exhibited transit-time limited performance. The bandwidth of the devices saturated at very low bias, compared to similar devices in the literature. This was attributed to a reduction in hole pileup, by careful design of the epitaxial layers. A device with 1 μm finger spacing and width, and an active region area of $(50 \mu\text{m})^2$, exhibited a bandwidth in excess of 18 GHz at 3 V bias [121].

The work reported here should assist in the design of high-performance MSM detectors, operating at 800 nm, 1300 nm, and 1550 nm. Deleterious effects common to MSM detectors were identified, and some techniques for minimizing these effects were demonstrated. It would be unwise to make general claims regarding the growth and fabrication methods used. The results reported in each section were obtained for a single wafer. A systematic study is required, with several wafers of each type, before the technology can be considered mature.

4. Resonant-Cavity-Enhanced MSM Photodetectors

4.1. Introduction – Improving the Responsivity of MSM photodetectors

With modern epitaxial growth techniques, vertical resonant cavities can be used to enhance the performance of optoelectronic devices. The most established example of this is the class of vertical cavity, surface-emitting lasers (VCSEL's). Other examples are resonance-enhanced photodetectors, optical modulators and amplifiers, and light-emitting diodes [129]. These devices rely on or benefit from the wavelength selectivity and/or optical field resonance introduced by the cavity. For photodetectors, the enhanced field absorption made possible by resonance allows the use of narrow active regions. This reduces carrier transit-times, enabling ultra-high speed operation. In addition, narrower absorption regions are potentially more compatible for integration with state-of-the-art electronic devices, since those devices rarely rely on thick layers of narrow band-gap materials. This must be weighed against the overall increase in epitaxial complexity required for the resonant device.

For MSM detectors, the drawback most often cited is a lack of responsivity, due to shadowing by opaque fingers. Thus, the enhancement of quantum efficiency by resonant-cavity techniques is especially attractive. Other potential methods for improving responsivity include: using semi-transparent electrodes [130],[131] using narrower fingers [132], illuminating the detector from the substrate side [125], forming the detector on a semiconductor optical waveguide [22], and using an integrated phase grating [133]. The integrated phase grating creates a near-field diffraction pattern, such that normally incident light is focused to the areas between opaque fingers. Each of these techniques compromises the simplicity of the MSM detector somewhat, and some of them affect other aspects of device performance.

Semi-transparent electrodes require an increase in process complexity (due to the non-standard materials used), and produce an increase in the series resistance of the fingers. Also, electron-hole pairs are created in relatively weak

field regions, beneath the transparent electrodes. These last two complications tend to slow the device [131], due to RC and transit-time effects, respectively.

The rear-illumination and waveguide approaches each suffer from an increase in the complexity of efficiently coupling light to the device, such that the intended benefit (responsivity enhancement) may be nullified. Rear-illumination requires either a transparent substrate or substrate removal, and makes alignment of fibers or free-space beams more technologically challenging. It also reduces device speed [125], generally speaking, since most of the photo-generated carriers are produced at the bottom of the absorbing layer, far from the collecting electrodes at the surface. This problem can be alleviated if rear-illumination is combined with resonant-cavity techniques [134], enabling use of a narrow absorption region. Waveguide detectors suffer from a reduction in speed, for similar reasons. In addition, the challenge of coupling fibers to small semiconductor waveguides remains formidable, making it likely that no real gain in responsivity is achieved by such an approach.

The use of an integrated diffraction grating is promising [133]. The literature on this technique is of a theoretical nature to date, but reduction in finger shadowing by 70-80 % seems quite feasible. The lack of experimental evidence may be related to the fact that surface effects in MSM detectors are the subject of on-going research (see Chapters 2, 3). The phase grating is etched in a dielectric layer(s), lying on top of the active region, so the effects of the dielectric layer on the electronic properties of the surface must be understood.

Finally, extremely narrow fingers require the use of advanced UV or E-beam lithographic techniques. Also, with narrow fingers the series resistance increases, such that RC effects can limit device speed.

Unlike the other techniques, the resonant-cavity approach does not imply a tradeoff, between responsivity and some other operational attribute of the device, such as its bandwidth. In fact, responsivity and speed may be simultaneously enhanced, as nearly 100 % absorption (in non-shadowed regions) is possible, with

extremely narrow absorbing layers. The cost is an increase in epitaxial complexity, which may be a significant cost in OEICs, depending on the nature of the other devices on the same wafer. A less critical cost to bear in mind is the reduction in spectral bandwidth, since the resonant-cavity absorbs efficiently within a limited spectral region only. As the designs in the following sections reveal, this spectral bandwidth can be quite large, up to approximately 50 nm. While some of the experimental results reveal the effects of missed layer thickness targets, it is expected that this error could be minimized after one or two growth iterations. Modern epitaxial techniques, such as molecular-beam-epitaxy (MBE) and metal-organic chemical vapor deposition (MOCVD), routinely achieve growth errors of 1-2 %, once a system is calibrated for a specific composition of layers. These capabilities are continually being refined, and improved growth accuracy will be available in the future, due to new in-situ characterization tools [135].

For all of the photodetectors discussed in this thesis, the immediate application is to optoelectronic switching and signal-processing techniques, as discussed in Chapter 1. Research on these systems is currently being conducted at a hybrid level of integration [20],[23]. Thus, the MSM photodetectors, and arrays of MSM photodetectors, can generally be optimized separate from other system requirements. However, top-illuminated detectors are definitely preferred in these systems at present, as they enable efficient coupling of free-space, optical fiber, and polymer waveguide light signals, and reduce the cost and technological challenge of system alignment.

The resonant-cavity devices discussed in the following sections are well suited to the requirements of hybrid optoelectronic systems. They allow simultaneous optimization of detector responsivity and bandwidth, and introduce no complications at the systems level. In addition, the resonant-cavity approach is central to the realization of the novel devices discussed in appendix A.

In Section 4.2, reflective quarter-wave-stacks, fabricated from semiconductor materials, are discussed in general terms. In Section 4.3, some

background theory for resonant-cavity absorption is introduced. In Section 4.4, the design criteria for a top-illuminated, resonant-cavity-enhanced MSM photodetector are outlined. In Section 4.5, recommendations are made for resonance-enhanced MSM detectors operating at various wavelengths. In addition, experimental results are given in Section 4.5, for two types of resonant MSM detectors operating near 800 nm wavelength. Finally, Section 4.6 contains conclusions and a summary of experimental results for resonant-cavity-enhanced MSM photodetectors.

4.2. Semiconductor Quarter-Wave-Stacks as Distributed Bragg Reflectors

Vertical resonant cavities use distributed Bragg reflectors (DBR), to provide reflection at one or both ends of the cavity. The DBR is composed of alternating semiconductor layers of higher and lower refractive index, which are usually designed to be a quarter wavelength thick at the desired center wavelength. Such quarter-wave-stacks (QWS) are commonly employed in the manufacture of highly reflecting dielectric mirrors, a modern example being the manufacture of reflective masks and lenses for x-ray lithography [136]. For photodetector applications, it is often adequate to use the air-semiconductor interface as the top mirror of the resonant structure. As will be discussed later, the optimized resonant-cavity-enhanced photodetector (RCEPD) typically has a highly reflecting bottom mirror and a much less strongly reflecting top mirror.

The development of semiconductor quarter-wave-stacks began in the mature AlGaAs/GaAs material system [137], and has recently shifted to the InAlGaAs [138-140] and InGaAsP [140-142] material systems. Lattice-matched to InP substrates, these latter systems have band-gaps that can be tuned to the fiber communication wavelengths of 1.3 and 1.55 μm . Unfortunately, InP and its lattice-matched alloys do not exhibit the relatively high refractive index offsets that are available with AlGaAs/GaAs. The ramifications of this are discussed in the following sections.

The reflectivity of a quarter-wave-stack is determined by the refractive index step at each interface, the number of pairs in the mirror, the angle of incidence, and, for off-normal incidence, the polarization of the incident light. In most of what follows, we consider normal-incidence conditions only. Aside from the simplification that this affords, it is demonstrable that the reflective properties of quarter-wave-stacks are degraded very little for incident angles that deviate up to 30 degrees from normal [143]. This leaves component materials and number of periods as the two factors that determine mirror performance. The quarter-wave-stack is illustrated schematically in Figure 4.1. As shown, two scenarios are possible, in that the stack may have an even or odd number of layers (N or $N/2$ periods).

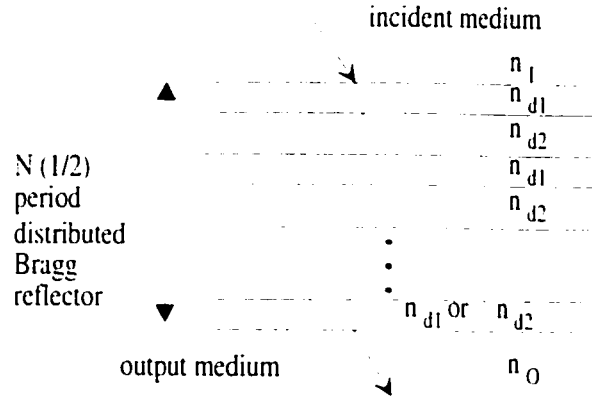


Figure 4.1. A quarter-wave-stack distributed Bragg reflector, with alternating refractive indices, n_{d1} and n_{d2} . The stack is embedded in semi-infinite media, with refractive index n_i at the input, n_o at the output. The stack may have an even number of layers (starting with layer n_{d1} , ending with layer n_{d2}) or an odd number of layers (starting and ending with layer n_{d1}). N is the number of periods, each consisting of one n_{d1} and one n_{d2} layer.

The overall reflection coefficient for the N period stack is given by [144]

$$r_N = \frac{1 - \frac{n_o}{n_i} \left(\frac{n_{d1}}{n_{d2}} \right)^{2N}}{1 + \frac{n_o}{n_i} \left(\frac{n_{d1}}{n_{d2}} \right)^{2N}}, \quad (4.1)$$

and that for the $N/2$ period stack is

$$r_{N+1/2} = \frac{1 - \frac{n_{d1}}{n_i} \frac{n_{d1}}{n_o} \left(\frac{n_{d1}}{n_{d2}} \right)^{2N}}{1 + \frac{n_{d1}}{n_i} \frac{n_{d1}}{n_o} \left(\frac{n_{d1}}{n_{d2}} \right)^{2N}} \quad (4.2)$$

In the cases of interest below, the quarter-wave-stack lies beneath an absorbing layer, and on top of a substrate, both semiconductors. Thus, $n_i \sim n_o$, and the term $(n_{d1}/n_{d2})^{2N}$ dominates in both (4.1) and (4.2). For a high reflectivity mirror, both a large index offset and a large number of layers are beneficial. Whether the mirror has an even or odd number of layers is relatively unimportant in terms of the mirror reflectivity. Aside from its amplitude, the phase of the stack's reflection coefficient is critical in the design of the resonant cavity, as discussed in Section 4.4. From (4.1) and (4.2), it is apparent that the ratio n_{d1}/n_{d2} determines the phase of the reflection coefficient, irrespective of an odd or even number of layers. For a lossless mirror, as assumed here, the reflected field is in phase with the incident field when $n_{d1} < n_{d2}$. If $n_{d1} > n_{d2}$, the reflected and incident fields are completely out of phase (have a phase offset of π).

Figure 4.2 illustrates the effects of varying the number of half-wave periods, and of different refractive index steps between the alternating materials comprising the mirror. Figure 4.2 was taken from reference [145]. It is clear that a superior mirror is obtained for a higher refractive index step and/or a higher number of periods in the mirror. This is true not only in terms of reflectivity at the design wavelength, but also in terms of broadening the spectral bandwidth.

For the photodetector applications addressed here, the resonant cavity is intended solely as a means of increasing responsivity, and not as a method of discriminating wavelengths. As such, a mirror with broader spectral bandwidth allows for greater deviation from design parameters in fabrication, while still maintaining a high reflectivity at the design wavelength. In fact, mirrors with broad spectral bandwidth are desirable even for wavelength selective devices, as the wavelength discrimination is achieved by forming a high Q cavity between two

highly reflecting mirrors. The cavity, not the mirrors, determines the wavelength of peak response.

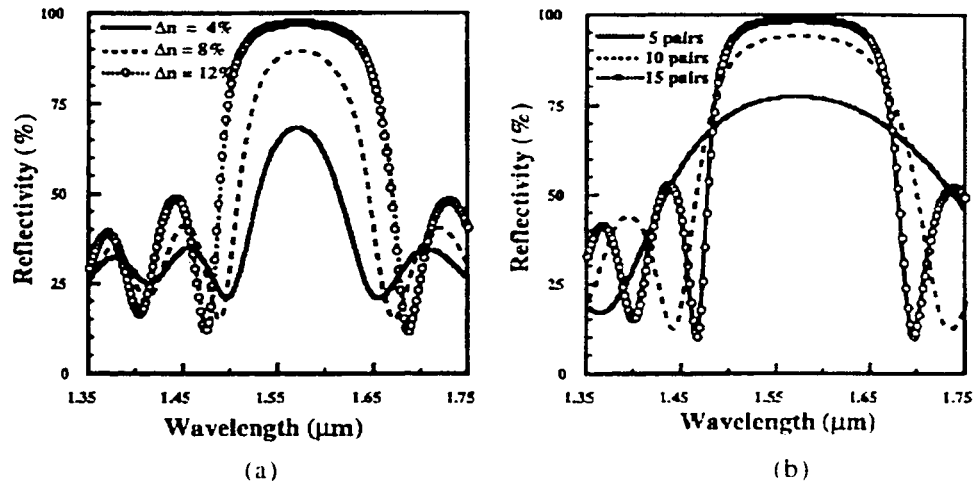


Figure 4.2. The effect on reflectivity of varying refractive index (a) and of varying number of periods in a GaAs/AlGaAs stack (b). The data are from reference [145].

It should also be noted that a further requirement for efficient reflection is the use of non-absorbing materials, and this is a primary criterion in the designs that follow. Strictly speaking, any amount of refractive index dispersion, however small, is necessarily accompanied by a finite amount of absorption [60]. However, for photon energies below the band-gap in the semiconductors of interest, it is generally quite reasonable to ignore the small loss terms of the complex refractive index. Strachan et al. [137] have investigated the slight perturbations caused by finite loss in the layers of a quarter-wave-stack. In the following, lossless mirror layers are assumed, except in Section 4.5.2, where an inherently lossy mirror is used.

Given the fact that one is generally restricted to a few choices for non-absorbing material combinations at a specific wavelength, the primary variable left for the designer is the number of periods in the mirror(s). Naturally, there is a tradeoff associated with using mirrors of many periods. The compromise derives from the limited thickness of defect-free and accurate growth that can be achieved, by any one of the epitaxial techniques available. This is a greater problem at the

longer wavelengths, where the thickness of quarter-wavelength semiconductor layers is on the order of $0.1 \mu\text{m}$. As the number of periods in a mirror is increased, a point of diminishing returns is reached, due to growth fluctuations that start to degrade the performance of the stack. Several demonstrations of high-quality mirrors that are several μm thick, grown by various methods, have been reported in the literature. Based on these, and with bias for caution, the following targets were used as a guide in the designs that follow:

1. At the design wavelength, a minimum of 90% of the incident power (in non-shadowed regions, between MSM fingers) should be absorbed.
2. Total epitaxy, including mirrors, absorption layer, and others, should not exceed a thickness of approximately $4 \mu\text{m}$.

4.3. Resonant-Cavity-Enhancement of Absorption - Theory

The design of resonant-cavity-enhanced photodetectors has been addressed in detail by Unlu et al. [129], and by Chin et al. [146]. Unlu et al. derived an approximate solution, by treating the photodetector active region as part of a simple Fabry-Perot cavity, with fixed mirrors. This approach provides certain unique insights, and can be used to derive analytical expressions, for quantities such as quantum efficiency and cavity finesse. However, it does not directly take into account the wavelength dependence of optical constants (dispersion), or the effect of standing waves in the cavity. As a result, it can be misleading, requiring the inclusion of correction factors. This is especially true in the case of narrow absorption regions. Nevertheless, we discuss some of the results from that approach in section 4.3.1, for the insight it affords.

Chin et al. used an exact field and impedance approach [146], which proceeds by analyzing the reflections associated with each interface in a multi-layer structure. The mathematics can be simplified by using a well established transfer-matrix method [143]. The parameters in the transfer-matrix model are the

wavelength dependent, complex indices of refraction for all layers. This approach, while requiring slightly more numerical manipulation, is still highly analytical, and leads to an exact determination of the spectral response of the entire RCEPD. This latter approach was used here. An even more rigorous approach is to combine the transfer-matrix theory with perturbation theory [147], to account for the variation of refractive index in each layer, arising from thin-film effects and local electric field conditions. It might be argued that such rigor is justified in the case of the resonant cavity, since the local field intensity due to standing waves could cause refractive index variation (nonlinear effects). However, the precision afforded by such an approach is probably excessive for photodetector design. Consider a typical incident power density of 10^4 W m^{-2} , and an absorption region 200 nm thick, absorbing 100 % of the incident power. The average power (volume) density is then approximately 10^{10} W m^{-3} , well below that required to produce optical non-linearity in a typical semiconductor [148].

The transfer-matrix of a dielectric layer relates the electric and magnetic field quantities at its interfaces, as illustrated in Figure 4.3. It is important to note that the field quantities shown in Figure 4.3 represent total fields, traveling in either direction, and that the summation of reflected and incident quantities is built in to the transfer-matrix method. The field quantities are related as

$$\begin{bmatrix} E_{\perp} \\ H_{\perp} \end{bmatrix} = M_2 \begin{bmatrix} E_{\parallel} \\ H_{\parallel} \end{bmatrix}. \quad (4.3)$$

M_2 is the transfer-matrix corresponding to medium 2, and, for normal incidence, is given by

$$M_2 = \begin{bmatrix} \cos(k_2 d) & i \sin(k_2 d) / Y_2 \\ i \sin(k_2 d) Y_2 & \cos(k_2 d) \end{bmatrix}, \quad (4.4)$$

where k_2 is the wave vector in medium 2 and Y_2 is the admittance of medium 2.

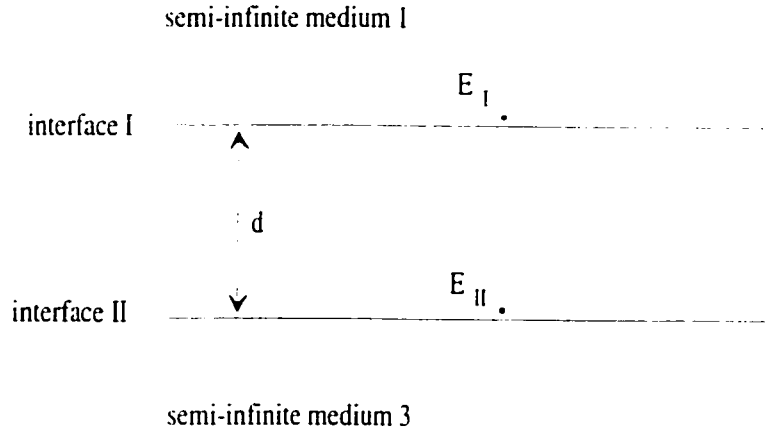


Figure 4.3. Total field quantities in adjacent dielectric media. E_I and E_{II} (and the corresponding magnetic fields) are related by a transfer-matrix, based on the boundary conditions for material interfaces.

The elegance of the transfer-matrix method derives from the fact that, for multiple layers between two semi-infinite media, the total transfer-matrix is simply the product of the transfer-matrices for each layer in turn. It is interesting to note that this technique is mathematically equivalent to that used to calculate energy levels in multiple quantum wells, appendix A. A similar method is also used to describe wave propagation on periodically loaded transmission lines, in Chapter 5. Thus, for n layers,

$$M_{TOTAL} = M_1 M_2 \cdots M_n, \quad (4.5)$$

where layer 1 is closest to the incident medium. Once the complete transfer-matrix is determined, the reflection and transmission coefficients for the entire system of layers can be calculated, using the elements of the matrix:

$$r = \frac{E_{tr}}{E_i} = \frac{Y_i M_{11} + Y_i Y_s M_{12} - M_{21} - Y_s M_{22}}{Y_i M_{11} + Y_i Y_s M_{12} + M_{21} + Y_s M_{22}}, \quad (4.6)$$

$$t = \frac{E_t}{E_i} = \frac{2Y_i}{Y_i M_{11} + Y_i Y_s M_{12} + M_{21} + Y_s M_{22}}$$

where Y_i is the admittance of the input medium, and Y_s is the admittance of the output (substrate) medium. E_i is the incident field intensity, E_{tr} is reflected field intensity at the first interface, and E_t is the field intensity transmitted into the output medium. In terms of calculating reflection and transmission, there is no

loss in generality if all Y 's in (4.4) to (4.6) are replaced by the complex refractive index of each respective medium.

A numerical simulation was implemented using Matlab. A complete Matlab script file is contained in appendix B. The models used for optical constants are discussed in the following sections. Inputs to the simulation are the thickness of each layer, the number of periods in a buried quarter-wave-stack, and the wavelength range of interest. Also, the simulation allows for off-normal incidence.

4.3.1. Analytical Formulae for Resonant-Cavity Photodetectors

Analytical expressions for resonant-cavity-enhanced photodetectors have been derived [129], by modeling the detector as a simple cavity embedded within a pair of 'hard' mirrors. This model is illustrated in Figure 4.4.

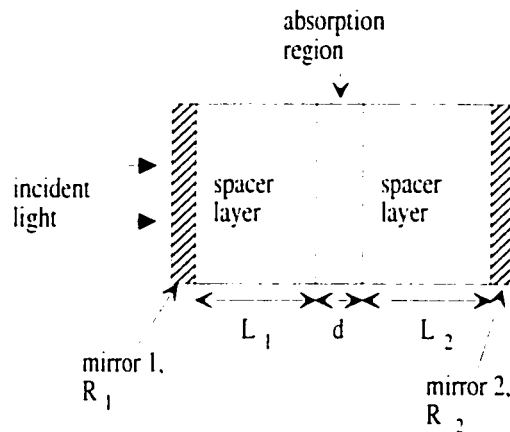


Figure 4.4. Simplified model of a resonant-cavity photodetector, used to obtain analytical design formulae. R_1 and R_2 are the reflectivity of the top and bottom mirrors, respectively. The reflectors are treated as 'hard' mirrors, not penetrated by the internal field in the cavity. Correction factors, including the phase of each mirror, are required for wavelengths other than the center wavelength of the quarter-wave-stacks.

The absorption region is surrounded by non-absorbing spacer layers, which are tuned to produce the desired resonance wavelength. The weakness of this model is that it does not inherently take account of the refractive index dispersion within each layer, or the effect of refractive index offsets at the spacer/absorbing

layer interfaces. Also, for very narrow absorbing regions, a correction factor is necessary to account for the position of the absorbing material, relative to the standing wave in the cavity. However, for reasonably thick absorbing layers, standing wave effects may be neglected, and a reasonable approximation of detector quantum efficiency, η , (not accounting for finger shadowing) is

$$\eta = \left[\frac{(1 + R_2 e^{-\alpha l})}{1 - 2\sqrt{R_1 R_2} e^{-\alpha l} \cos(2\beta L + \psi_1 + \psi_2) + R_1 R_2 e^{-2\alpha l}} \right] (1 - R_1)(1 - e^{-\alpha l}). \quad (4.7)$$

R_1 and R_2 are the reflectivity of the top and bottom mirrors, respectively, and ψ_1 and ψ_2 are their associated phase shifts. Wavelength dispersion is neglected, so $\beta = 2n\pi/\lambda_0$, where n is a constant refractive index and λ_0 is the free-space wavelength. In the designs that follow, the top mirror is the air-semiconductor interface, and its associated phase shift is approximately zero, independent of wavelength. The bottom mirror is a quarter-wave-stack, however, which has zero phase shift only at its center wavelength. The effective phase-shift at off-center wavelengths is not easily determined without resorting to numerical techniques [129].

The peak quantum efficiency, η_0 , occurs at the resonant wavelength of the cavity, where the quarter-wave-stack introduces zero phase shift. In that case, (4.7) reduces to

$$\eta_0 = \left[\frac{(1 + R_2 e^{-\alpha l})}{(1 - \sqrt{R_1 R_2} e^{-\alpha l})^2} \right] (1 - R_1)(1 - e^{-\alpha l}) \quad (4.8)$$

Similar expressions may be derived for free spectral range and cavity finesse [129]. In the simulations that follow, the analytical results of this section were used as a guide only. Exact solutions, from the transfer-matrix theory described above, were used to develop the structures recommended in Section 4.5.

4.4. Top-Illuminated Resonant-Cavity Enhanced MSM photodetectors - Design Criterion

Resonant enhancement of top-illuminated MSM photodetectors has been addressed previously, by Li et al. [149]. They considered an AlGaAs/GaAs structure with a buried DBR, a substrate buffer layer, a GaAs absorption region, and a silicon nitride AR coating. Their approach was to arbitrarily set the absorption region thickness, and subsequently tune the entire structure to the desired resonance wavelength, by adjusting the thickness of the substrate buffer layer and AR coating. This is essentially the approach taken in the experimental reports of top-illuminated [150] and rear-illuminated [134], resonance-enhanced MSM photodetectors. A slightly different approach is taken here, in the interest of designing a double-heterostructure MSM (DH-MSM) device. The absorption region is isolated from both the top surface and the substrate, by wider band-gap layers.

The advantages of the double-heterostructure are addressed in Chapters 2 and 3. Generally, the layers below and above the absorption region are restricted to lie within a certain range, for reasons discussed in Chapter 2. It then becomes necessary to tune the absorption region thickness for resonance at the desired wavelength. The basic structure used in the following designs is illustrated in Figure 4.5.

Figure 4.5 illustrates some of the problems associated with using the simple Fabry-Perot cavity analysis, discussed in Section 4.3.1. The location of R_1 and R_2 (the mirrors) is dependent on the refractive index profile of the entire structure. In addition, the absorption region is only a portion (in some cases a fraction) of the resonant cavity, so standing wave effects cannot be ignored. That is, if the absorption region happens to lie at the position of a standing-wave node inside the cavity, quantum efficiency is degraded rather than enhanced.

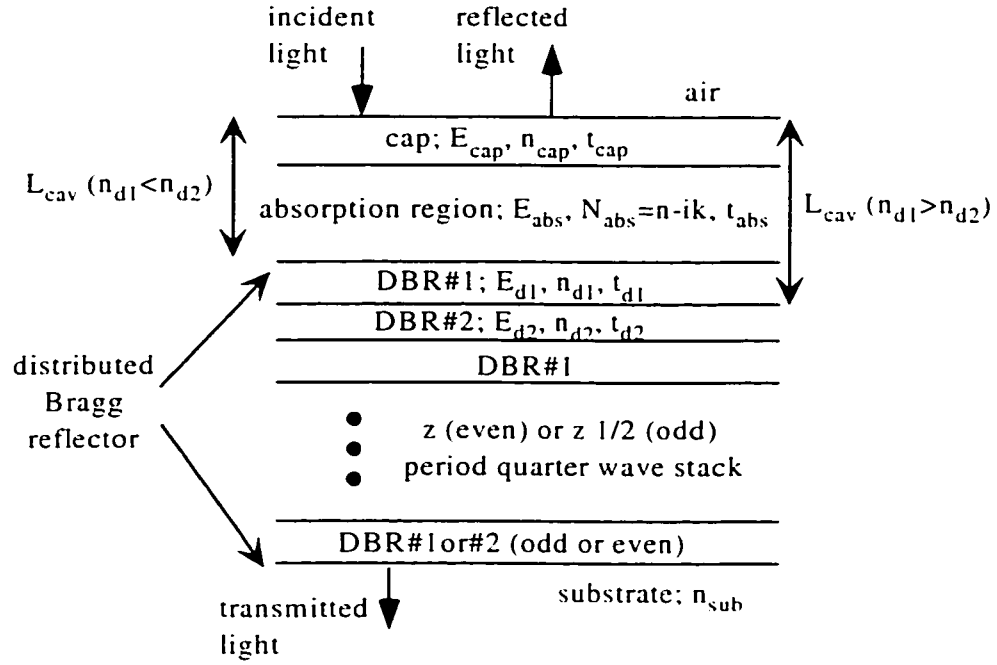


Figure 4.5. Model structure used for design of top-illuminated resonance-enhanced MSM photodetectors. E's are band-gaps, n's are refractive indices, and t's are layer thickness'. L_{cav} is the effective cavity length, which must satisfy the resonance condition. It is dependent on the ratio of refractive indices for the first and second layers of the quarter-wave-stack. This is to satisfy the phase condition for the resonant-cavity, as discussed in the text.

The resonance condition is slightly altered by the refractive index offsets between different layers in the cavity. However, this generally produces only a small perturbation, and the resonance condition is well approximated by

$$\begin{aligned}
 n_{cap}t_{cap} + n_{abs}t_{abs} &= \frac{m_{even}\lambda_0}{4}; \quad m_{even} = 2,4,\dots; \quad \text{for } n_{d1} < n_{d2}, \\
 n_{cap}t_{cap} + n_{abs}t_{abs} &= \frac{m_{odd}\lambda_0}{4}; \quad m_{odd} = 1,3,\dots; \quad \text{for } n_{d1} > n_{d2}.
 \end{aligned}
 \tag{4.9}$$

These conditions can be understood from the discussion in Section 4.2. For the buried mirror, the phase of the reflection coefficient depends on the ratio n_{d1}/n_{d2} . Thus, the cavity boundary is located at the first interface of the lower refractive index material. If $n_{d1} > n_{d2}$, the top layer of the mirror is equivalent to the spacer layer discussed in Section 4.3, Figure 4.4.

Another concern is the quality (Q) factor of the resonant cavity. The Q factor is given by

$$Q \equiv 2\pi\nu \frac{\text{energy stored by resonator}}{\text{power dissipated per cycle by resonator}} = \frac{\nu}{\delta\nu} = 2\pi\nu t_c \quad (4.10)$$

where ν and $\delta\nu$ are the center frequency and bandwidth of the cavity, respectively, and t_c is the photon lifetime in the cavity [151]. As mentioned, for the photodetectors of interest here, it is desirable to maintain a reasonably broad spectral bandwidth, to compensate for fabrication tolerances. There are two mechanisms that produce a finite photon lifetime in the resonant-cavity photodetector: finite reflectivity of the mirrors, and absorption in the cavity. Since high quantum efficiency depends on a highly reflecting bottom mirror (as discussed below), it is not generally desirable to broaden the spectral bandwidth by reducing reflectivity. Thus, Q is affected only by variations in the absorption coefficient of the cavity material, or by variations in the thickness of the absorption layer (relative to the length of the entire cavity). A high absorption coefficient, or a thick absorption layer, reduces the photon lifetime in the cavity. From (4.10), a broader spectral bandwidth results.

In practice, for the devices recommended here, minimal spectral broadening results from an increase in absorption coefficient, or from a thicker absorption layer. The Q factor is already low, because the top mirror (the air-semiconductor interface) generally has only 30% reflectivity. This is illustrated in Figure 4.9, below.

In any case, resonant cavity photodetectors have unique requirements, as concerns the quality factor that optimizes quantum efficiency. For a VCSEL, the optical energy originates in the cavity. A high Q factor is required, so that the optical energy density in the cavity is maximized, and the threshold current is minimized. For a RCEPD, the optical energy must enter from outside and then resonate. The optimized device has a highly reflective bottom mirror, in concert with a less reflective incident-side mirror. For zero reflection at the input interface [146],

$$\begin{aligned}
r_{front} &\approx r_{back} \exp(-\alpha_{abs} t_{abs}), \\
R_{front} &\approx R_{back} \exp(-2\alpha_{abs} t_{abs}),
\end{aligned}
\tag{4.11}$$

where r is reflection coefficient, R is the power reflectivity, and α_{abs} is the absorption coefficient of the active region.

To maximize quantum efficiency, the back mirror should have 100 % reflectivity, and the front mirror is subsequently tuned according to equation (7). Alternatively, if the front mirror has fixed reflectivity, as is the case here ($R_{front} \sim 0.3$ for an air-semiconductor interface), then the absorption region thickness can be tuned for zero reflection. Since the target for back mirror reflectivity is 0.9 (Section 4.2), and given a typical absorption coefficient of $1.2 \times 10^6 \text{ m}^{-1}$ for GaAs or InGaAs, quantum efficiency is optimized for an absorption region thickness of approximately 450 nm. This is an important result. There is a reduction in quantum efficiency for thicker absorption regions, as the Q factor of the cavity is reduced. This produces the criterion given by

$$t_{abs} = \frac{\ln\left(\frac{R_{back}}{R_{front}}\right)}{2\alpha_{abs}}.
\tag{4.12}$$

Equation (4.12) always holds as a criterion for zero reflection from the front surface. If the back mirror has a reflectivity near 1, then equation (4.12) also specifies the absorption region thickness for which quantum efficiency is maximized. Generally, in reducing absorption region thickness, responsivity is sacrificed in favor of speed. However, an absorption region thicker than specified by (4.12) causes a reduction in both speed and responsivity, at the design wavelength. The only reason a thicker absorption region might be used is to broaden the spectral bandwidth, as discussed in relation to (4.10). Note also that, as both mirrors' reflectivity tends to 1, the optimal absorption region thickness tends to zero. This is consistent with the requirements of a high Q factor cavity, as mentioned above.

MSM detectors are often passivated to improve the electronic conditions at the surface, as discussed in Chapter 2. A single passivation layer may be useful for

tuning the resonance condition in certain cases [149], but will always reduce the peak quantum efficiency of the detector. This is because the dielectric layer will typically have a refractive index that is intermediate to those of air and the semiconductor (as required for an anti-reflection coating). This implies equal or lower reflectivity at the top surface, compared to the bare semiconductor. Thus, the passivation layer is neglected in the following sections. In practice, it can be made one half wavelength thick, so that it is a 'vanishing' layer at the center wavelength of the cavity.

Others [134] have used a multiple-layer dielectric stack to passivate resonant-cavity photodetectors, which can result in an enhancement of top-mirror reflectivity at the design wavelength. In some designs [152], both top and bottom mirrors are epitaxially grown QWS. One of these techniques is necessary if a wavelength-selective device is sought, in order to enhance the Q factor of the cavity.

A relatively minor design criterion is the use of an odd or even period QWS as the back mirror. The carrier confinement requirements of the double-heterostructure MSM detector (see Chapter 2) were given primary consideration in the designs. Thus, the higher band-gap (lower refractive index) material from the QWS was placed adjacent to the absorption region. As a result, if the substrate is a lower refractive index material (as in the case of InP), an even period mirror is a slightly better choice, and if the substrate is a higher refractive index material (as with GaAs), an odd period mirror is a slightly better choice.

4.5. Recommended Structures

Optoelectronic systems are presently being developed for operation both at 800 nm and at the fiber communication wavelengths of 1300 and 1550 nm. The designs which follow are tailored to the 800 nm range (GaAs/AlGaAs or GaAs/InGaP), the 1300 nm range (InP/InGaAsP or InP/InAlGaAs), and the 1550 nm range (InP/InGaAs).

At the time of writing, epitaxial material had been acquired in the GaAs/AlGaAs and GaAs/InGaP material systems only. Of these, MSM device fabrication was complete for the GaAs/AlGaAs material system only. Preliminary device results are presented for GaAs/AlGaAs, along with experimental reflectivity spectra. Results for the GaAs/InGaP wafer were limited to verification of spectral characteristics on reflection.

4.5.1. GaAs/AlGaAs Resonant-Cavity Detector Operating Near 800 nm

4.5.1.1. Epitaxial Design

The recommended structure for the AlGaAs material system is shown in Figure 4.6. The targeted center-wavelength was 800 nm. The wavelength-dependent refractive indices used were least-square-error, polynomial fits to the best available data from the literature. In the case of $\text{Al}_x\text{Ga}_{1-x}\text{As}$, this data has been summarized in [82]. The resulting polynomials are checked for accuracy at the design wavelength, which is most critical, both against the data in [82] and against recently reported values, in [153],[154].

The polynomial fit used for the refractive index of GaAs, over the wavelength range of interest, is given by

$$\begin{aligned}
 N_{\text{GaAs}} &= n_{\text{GaAs}} - i\kappa_{\text{GaAs}}; \\
 n_{\text{GaAs}}(\lambda) &= 1.599\lambda^2 - 3.4289\lambda + 5.3907, \\
 \kappa_{\text{GaAs}}(\lambda) &= -40.8032\lambda^3 + 95.6687\lambda^2 - 75.0627\lambda + 19.799,
 \end{aligned} \tag{4.13}$$

where n is the refractive index, κ is the extinction coefficient, and λ is wavelength, in units of μm . This predicts a complex refractive index, at the center wavelength, of $N_{\text{GaAs}}=3.67-i0.0856$, which corresponds to an absorption coefficient of $1.34 \times 10^6 \text{ m}^{-1}$.

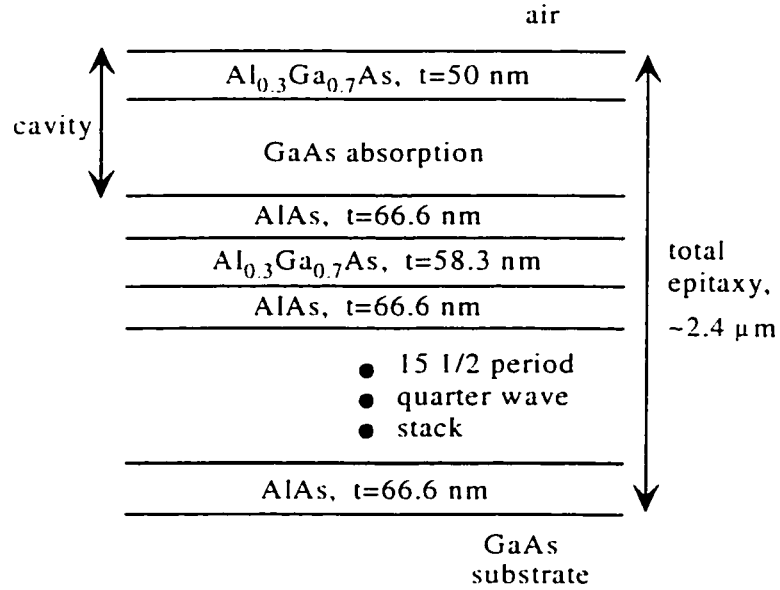


Figure 4.6. Recommended epitaxial structure for an AlGaAs/GaAs resonant-cavity-enhanced MSM detector, with a center wavelength of 800 nm. All layers are nominally undoped.

The alloy Al_{0.3}Ga_{0.7}As has a direct band-gap energy of 1.87 eV (which corresponds to a wavelength of 665 nm), and is therefore totally transparent at the wavelengths of interest. The refractive index is very nearly real over the wavelength range considered and is modeled as

$$n_{AlGaAs}(\lambda) = 3.5817\lambda^2 - 6.6919\lambda + 6.4945, \quad (4.14)$$

which predicts a value of 3.43 at 800 nm wavelength.

For AlAs, the refractive index is similarly modeled as

$$n_{AlAs} = 0.8528\lambda^2 - 1.7972\lambda + 3.8969, \quad (4.15)$$

which predicts a value of 3.005 at 800 nm wavelength. As mentioned, all of these polynomial expressions were obtained by fitting data from [82] and confirming the numbers at 800 nm with those in [153] and [154].

The 15 1/2 period mirror shown in Figure 4 will produce a reflectivity of over 95% when embedded in GaAs, due to the large refractive index step ($\Delta n=0.43$) between the component semiconductors. With a front mirror reflectivity of 30%, and the absorption coefficient stated above, equation (4.11)

indicates that optimal quantum efficiency will occur for an absorption region thickness of approximately 430 nm.

The reflected, transmitted, and absorbed power spectra for the device in Figure 4.6, with an absorption region thickness of 389 nm, are shown in Figure 4.7. Note that, even with a modest amount of epitaxy dedicated to the bottom mirror, the power absorption at the design wavelength exceeds 95%. The broad spectral bandwidth of the bottom mirror is apparent in the transmitted power characteristic. The absorption characteristic is much narrower, and determined by the Q factor of the entire cavity, as discussed previously.

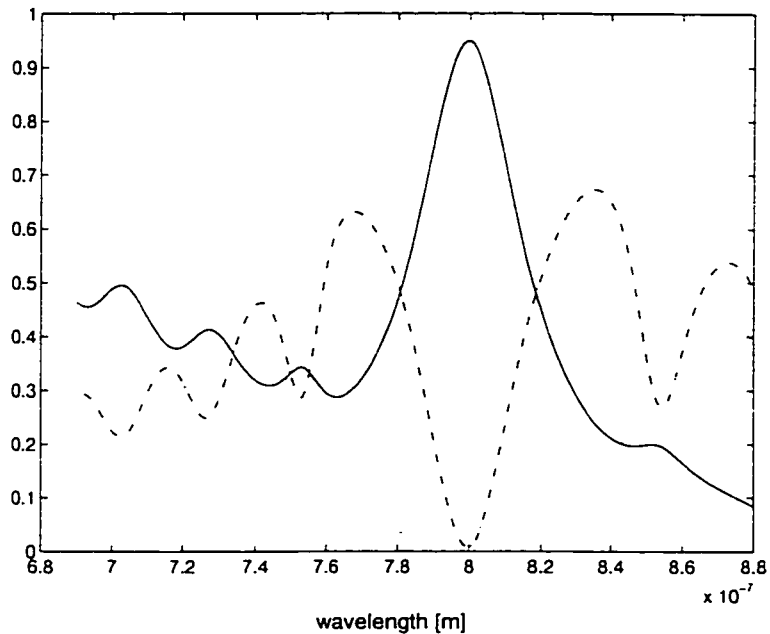


Figure 4.7. The simulated spectral characteristic of the resonant cavity structure illustrated in Figure 4.6, with an absorption region thickness of $t_{\text{abs}}=389$ nm. The horizontal scale is fraction of power absorbed (solid), transmitted (dot), and reflected (dash-dot). This absorption region thickness is near the optimal value, as given by (4.12).

Figure 4.8 illustrates the variation of absorbed power for different absorption regions, each of which is tuned to satisfy the resonance condition given by equation (4.9). Note that the optimal quantum efficiency is obtained for an absorption region thickness between 389 nm and 498 nm, as predicted by equation (4.12), and that for thicker absorption regions the quantum efficiency is degraded. Also note that the quality factor of the resonance condition is essentially

unchanged for various absorption region thicknesses. This is due to the low reflectivity of the top mirror, as discussed in Section 4.4.

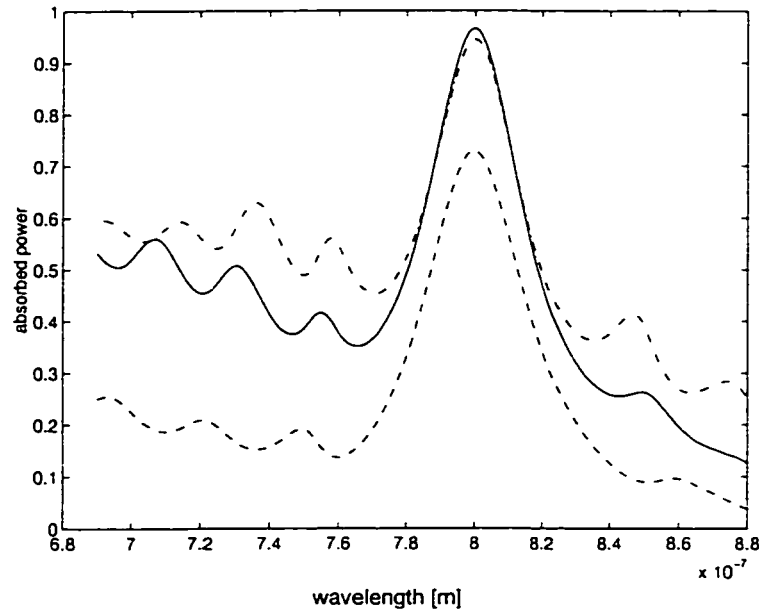


Figure 4.8. Variation of absorbed power for the structure of Figure 4.6, with different absorption region thickness. $t_{\text{abs}}=171$ nm (dash), 280 nm (dot), 498 nm (solid), and 716 nm (dash-dot). In keeping with the theory in Section 4.4, the peak absorption is maximized by a layer thickness of approximately 400 nm. A reduction or increase in this thickness reduces peak absorption.

Figure 4.9 illustrates the effect of adding a silicon nitride passivation layer, to the previously optimized epitaxial structure of Figure 4.6. As mentioned in Section 4.4, the top mirror reflectivity cannot be enhanced by the addition of a single layer of intermediate refractive index, so peak quantum efficiency can only be degraded or unchanged (in the case of a $\lambda/2$ passivation layer). The passivation layer can be used to tune the resonant wavelength slightly, always at the expense of some absorption. Also, silicon nitride (or another passivant) can be used to establish a resonance condition for an arbitrarily thick absorption region, as in [149].

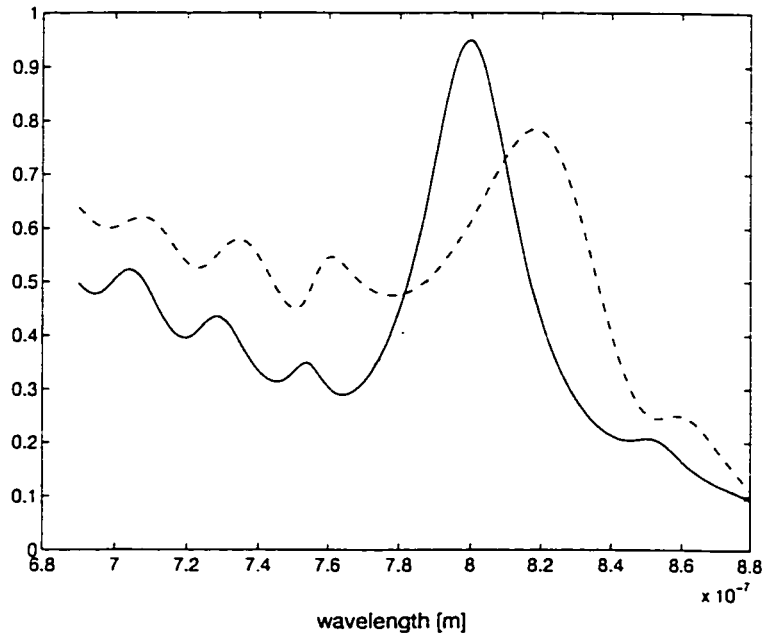


Figure 4.9. Effect of a silicon nitride passivation layer on the absorption characteristics of the device of Figure 4.6, with $t_{\text{abs}}=389$ nm. $t_{\text{SiN}}=205$ nm (solid), 40 nm (dot), 75 nm (dash). Note that the passivation layer, having an intermediate refractive index, cannot improve the reflectivity of the front mirror. Thus, a passivation layer should be made 'vanishing' by restricting its thickness to a multiple of a half wavelength at the design frequency. This is the case for the 205 nm layer.

The peak absorption of these AlGaAs devices could be increased to nearly 100%, by using a greater number of periods in the bottom mirror. The design of Figure 4.6 was intentionally modest in terms of total epitaxy, to improve the probability of obtaining high quality, working devices. A peak absorption of 95% (Figure 4.7) corresponds to a responsivity of 0.41 A/W, for an MSM device with 1 μm finger width and 2 μm finger spacing (1x2). This is an improvement of 3.5 times, over the responsivity of a device with the same absorption region thickness, but no resonant enhancement. If the finger spacing is increased to 3 μm , which should not affect bandwidth too greatly for such a narrow absorption region, the predicted responsivity is 0.46 A/W. Maximum responsivity for a gain-free photodetector at 800 nm is 0.65 A/W.

4.5.1.2. Fabrication and Experimental Results

Based on the design in the preceding sub-section, the epitaxy of Figure 4.6 was obtained from the Communications Research Centre, Ottawa. The layers were grown by MOCVD, on a semi-insulating GaAs substrate. For reference, the wafer was specified as CRC-97D47, and the fabrication run was specified as CRC-97-001. The mask set described in Chapter 2 was used for post-growth processing.

Device fabrication proceeded by deposition of a 150 nm layer of silicon nitride, in which windows were opened to define MSM active regions. To simplify the processing, mesa isolation was not included. Interdigitated electrodes were formed by liftoff of Ti/Pt/Au. Bond pads were formed by lift-off of Ti/Au. The active regions were not passivated, to simplify interpretation of the spectral characteristics. A microscope photograph of a fabricated device is shown in Figure 4.10.



Figure 4.10. Photograph of a fabricated MSM device, on the GaAs/AlGaAs resonant-cavity wafer. The finger spacing and width are 2 and 1 μm , respectively, for the device shown. The active region appears light gray, and was defined by opening a window in a silicon nitride layer.

Most of the devices exhibited fairly severe low-frequency gain, both in their DC characteristics and in high frequency measurements. Low-frequency gain is discussed in detail in Chapters 2 and 3. It is generally attributable to non-optimal electronic conditions at the surface. In the case of the resonant-cavity structure, it is also possible that the crystalline quality of the semiconductor is

degraded towards the surface. This can result from the relatively long growth times, and the thickness of the total epitaxy.

For future work, it would be worthwhile to passivate this wafer, in an attempt to improve the surface electronic conditions. A passivation technique for arsenic-based MSM detectors was demonstrated in Section 3.3.2, and may be applicable here. Some of the devices (roughly 25 %) exhibited relatively little low-frequency gain, but enough to reduce speed below transit-time estimates. An example frequency scan, for a $(50 \mu\text{m})^2$ detector with $1 \mu\text{m}$ finger width and $2 \mu\text{m}$ finger spacing, is shown in Figure 4.11.

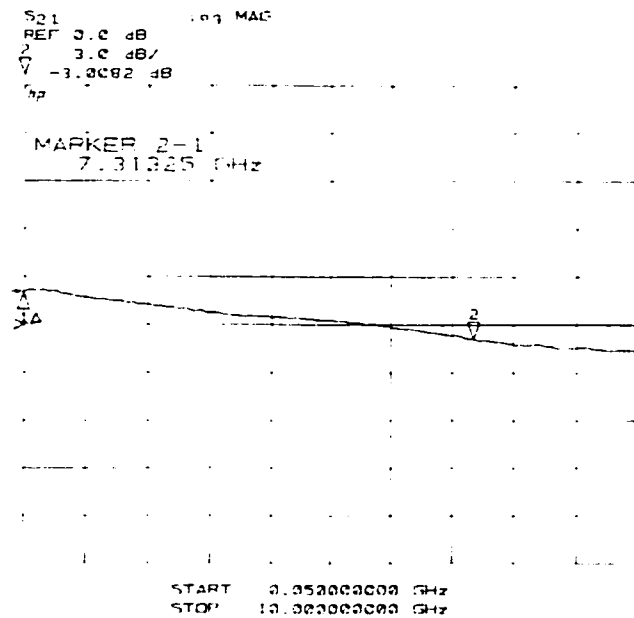


Figure 4.11. Frequency response for a resonant-cavity-enhanced MSM detector, with $(50 \mu\text{m})^2$ active regions, $1 \mu\text{m}$ finger width, and $2 \mu\text{m}$ finger spacing. Comparing to the results in Chapter 3, the detectors on this wafer did not exhibit transit-time-limited bandwidth. Rather, the bandwidth is limited by low frequency gain. The scan was obtained for 0.4 mW of modulated light, at 830 nm wavelength. The device was biased at 5 V. The plot is the screen output of a network analyzer. The horizontal scale is linear in frequency, starting at 50 MHz and ending at 10 GHz. The vertical scale is logarithmic, 3 dB per division. The 0 dB reference line is marked by the 'greater-than' symbol at the left, and represents approximately 0.1 A/W.

While the device results were sub-optimal, of more immediate interest to the discussion in this chapter were the spectral characteristics of the wafer. The

reflectivity spectrum of the wafer was investigated, using a white halogen light source and a monochromator. For this experiment, a region of bare semiconductor was required. The mask set incorporated several 'process control' cells, as described in Section 2.8. These cells contain a region of bare semiconductor, approximately 2 mm by 4 mm, after wafer processing. Light from a monochromator was focused to these regions, to obtain the required reflectivity spectra, due only to the epitaxy.

Several reflectivity scans were obtained, at various locations on the wafer. The observed wafer uniformity was quite good. Figure 4.12 shows a typical experimental result, and a theoretical fit to the data. The best fit to the experimental data was obtained by assuming that all AlAs and AlGaAs layers were under-grown by approximately 4 %, while the GaAs absorption region was grown as specified. This is a reasonable hypothesis, since often a growth system is very well calibrated for the binary GaAs, and less well calibrated for AlGaAs or AlAs.

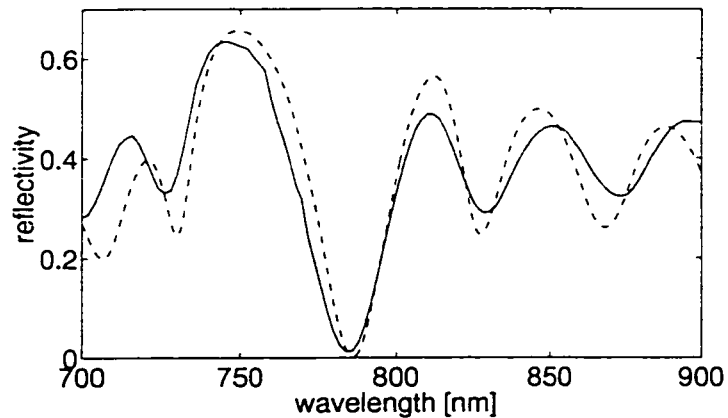


Figure 4.12. An experimental reflectivity scan is shown, for the AlGaAs/GaAs resonant cavity structure (solid line). Also shown is a theoretical fit to the data (dashed line). The theoretical fit was obtained by assuming the GaAs absorption region to be grown as specified, and all AlGaAs layers to be under-grown by 4 %. The observed resonant peak was typically at 785 nm wavelength, compared to the design target of 800 nm.

Several small discrepancies are present between the experimental and theoretical reflectivity, Figure 4.12. A detailed discussion of the origin of these discrepancies is contained in Section 4.5.2.5. It should be noted, however, that it

was not possible to focus the incident light completely within the patch of bare semiconductor available on these wafers. This resulted in a reduced depth-of-modulation for the secondary features, exhibited by the experimental curve in Figure 4.12. Some peripheral light was reflected from dielectric-covered semiconductor, reducing the accuracy of the experiment.

4.5.2. GaAs/InGaP Resonant-Cavity Detector Operating Near 800 nm

4.5.2.1. Introduction

The results in Chapter 3, and in the preceding sub-section, illustrate that surface conditions can greatly effect the attributes of an MSM detector. Phosphorus-based alloys tend to exhibit better surface properties than arsenic-based alloys [49]. This is certainly supported by the experimental results in Chapter 3, for example by comparing the devices in Sections 3.2 and 3.3. For that reason, a novel resonant-cavity device operating near 800 nm was investigated. The design of the device, and some preliminary experimental results, are presented in this section.

Recently, the InGaAsP/GaAs lattice-matched material system has been investigated as an alternative to AlGaAs/GaAs [53],[131],[155]. It has superior interface and surface characteristics, indicated by a low surface recombination velocity [52]. As an Al-free system, it has greater environmental stability, and growth-related problems such as alloy clustering are reduced [87]. In addition, the band offsets are apportioned primarily to the valence band for InGaAsP/GaAs [90], which is advantageous for certain devices such as high power Npn HBTs [53]. Higher n-type dopant concentrations have been achieved for InGaAsP than AlGaAs, and the availability of selective etchants for InGaP/GaAs is important for the precision etching required in modern HEMT and HBT fabrication [87]. Finally, InGaP apparently does not have the large concentration of donor-related DX traps associated with AlGaAs [85], which makes it attractive as a replacement for AlGaAs in HEMT technology [156].

One drawback of InGaAsP/GaAs is the low refractive index offset between its lattice-matched alloys, compared to AlGaAs/GaAs. This is disadvantageous for guided wave and mirror-based devices, limiting the viability of completely Al-free structures. While the advantages of AlGaAs mirrors and InGaP interfaces can be combined [89], this generally complicates growth. The maximum index offset of InGaAsP occurs for $\text{In}_{0.49}\text{Ga}_{0.51}\text{P}/\text{GaAs}$. These materials have been used to design distributed Bragg reflector (DBR) devices operating in the 980 nm wavelength range [157],[158], with strained InGaAs active layers. Since GaAs becomes absorptive for wavelengths less than approximately 900 nm, the use of intrinsic InGaP/GaAs is precluded in the design of highly efficient DBRs in the 800 nm wavelength region, where GaAs-based devices traditionally operate.

InGaAsP/InP also has the disadvantage of relatively small index offsets (compared to InAlGaAs/InP, for example), as discussed in Section 4.5.3. It has been reported [140] that efficient mirrors centered at 1550 nm can be constructed of alternate layers of $\text{In}_{0.53}\text{Ga}_{0.47}\text{As}$ and InP or InAlAs, in spite of the fact that $\text{In}_{0.53}\text{Ga}_{0.47}\text{As}$ is normally strongly absorbing at 1550 nm. These mirrors are attractive because they maximize the refractive index offset available in InGaAsP/InP. Also, the absence of a quaternary [140] simplifies growth and enhances growth accuracy. The high efficiency is achieved by heavily n-doping the mirror layers, to shift the InGaAs absorption edge to shorter wavelengths and increase transparency at 1550 nm. The primary mechanism responsible for the band-edge shift is band filling by donor electrons [159], which has traditionally been called the Burstein-Moss effect [148]. Section 4.5.5 contains a recommendation for a resonant-cavity detector operating near 1550 nm, based on this concept.

Band filling effects are largest in narrow band-gap semiconductors with small effective electron mass, and therefore low density of conduction-band states near the band edge. Thus, InGaAs is a particularly good candidate. The goal here was to investigate similar effects in n-GaAs, to determine the feasibility of efficient $\text{In}_{0.49}\text{Ga}_{0.51}\text{P}/\text{GaAs}$ DBR mirrors operating in the 800 nm wavelength

range, where the cheapest and most commercially ubiquitous solid-state sources are available.

In Section 4.5.2.2, the primary effects on optical constants caused by heavy doping are reviewed. In Section 4.5.2.3, an epitaxial proposal is outlined. In section 4.5.2.4, growth and fabrication are described. In Section 4.5.2.5, experimental results are detailed, for a resonant-cavity epitaxial structure with a buried InGaP/GaAs DBR mirror, operating near 800 nm.

4.5.2.2. Doping-Induced Changes in Optical Constants

The effects of high free-carrier concentration, on the optical constants of III/V semiconductors near their band edge, have been treated recently by Bennett et al. [159]. Three physical mechanisms contribute to changes in the complex refractive index, relative to the case of the intrinsic, non-injected semiconductor. They are band filling (Burstein-Moss effect), band-gap shrinkage, and free-carrier absorption.

As mentioned, band filling is most pronounced in semiconductors with small effective masses and a small energy gap. This is understood from the facts that the effective density of states in the bands is proportional to $(m^*)^{3/2}$, and that degenerate doping is more readily achieved in narrow band-gap semiconductors. In fact, narrow band-gap semiconductors also tend to have small effective masses [49]. Band filling is illustrated schematically in Figure 4.13.

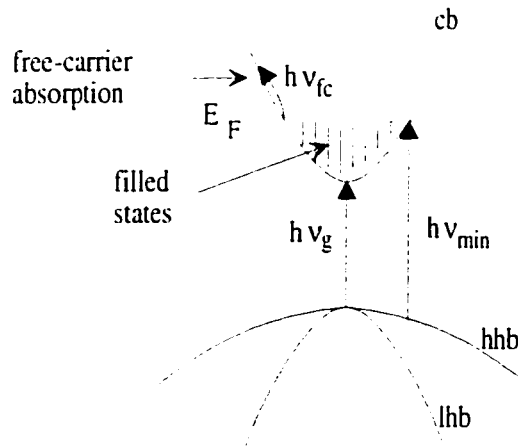


Figure 4.13. Band-filling in a degenerately n-doped, direct band-gap semiconductor. E_F is the Fermi-level, $h\nu_g$ is the band-gap energy, and $h\nu_{min}$ is the minimum photon energy for absorption. $h\nu_{fc}$ is a typical free-carrier transition, and hhb, lhb, and cb are the heavy-hole, light-hole and conduction bands, respectively.

In Figure 4.13, heavy n-type doping has produced a degenerate semiconductor. Since few states are empty near the conduction band edge, optical transitions involving those states are unlikely, and the band-edge for optical absorption is shifted to shorter wavelength ($h\nu_{min} > h\nu_g$). A similar effect occurs for p-type doping. It is typically much smaller, since the heavy-hole mass is much larger than the electron mass, and the density of states near the valence band edge is correspondingly greater.

The effect of band filling is often modeled as a rigid shift of the absorption edge. In actuality, the band edge remains relatively fixed, while the absorption is only decreased (not eliminated) in the vicinity of the band edge. This is illustrated schematically in Figure 4.14. Note that an abrupt band edge is assumed, with no residual absorption below the band edge due to phonon, impurity, and exciton effects [148].

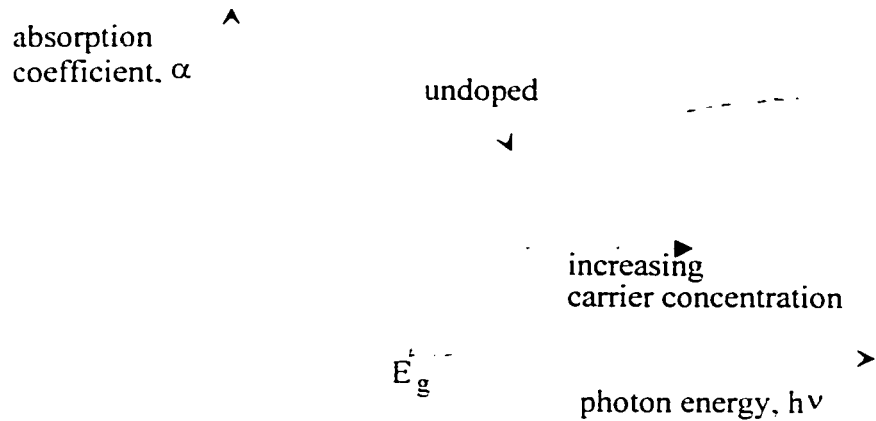


Figure 4.14. The shift of the absorption band-edge due to band filling in a heavily doped semiconductor. Transparency is increased for photon energy slightly greater than the nominal band gap.

The change in absorption illustrated in Figure 4.14 implies a change in refractive index near the band-gap wavelength, via the Kramers-Kronig relations [148]. For band filling, the refractive index decreases for photon energies near and below the band-gap energy, and increases at energies above E_g (see Figure 4.16).

Band-gap shrinkage occurs for high free-carrier concentration, and is essentially a plasma effect. In simple terms, the free carriers screen each other from the background potential of the crystal lattice, and have reduced potential energy. Solution of the Schrodinger equation for carriers in the doped crystal predicts a smaller band-gap, and this is borne out by experiment [160]. The result is a shift of the absorption band edge to lower photon energy (longer wavelength), so band-gap shrinkage offsets the effect of band filling on optical constants. The shift in the absorption edge due to band-gap shrinkage is illustrated in Figure 4.15.

Free-carrier absorption for electrons is illustrated in Figure 4.13. At optical frequencies in semiconductors, a classical (Drude) model for the electrons predicts a free-carrier absorption coefficient that is proportional to the carrier concentration and the square of wavelength [60].

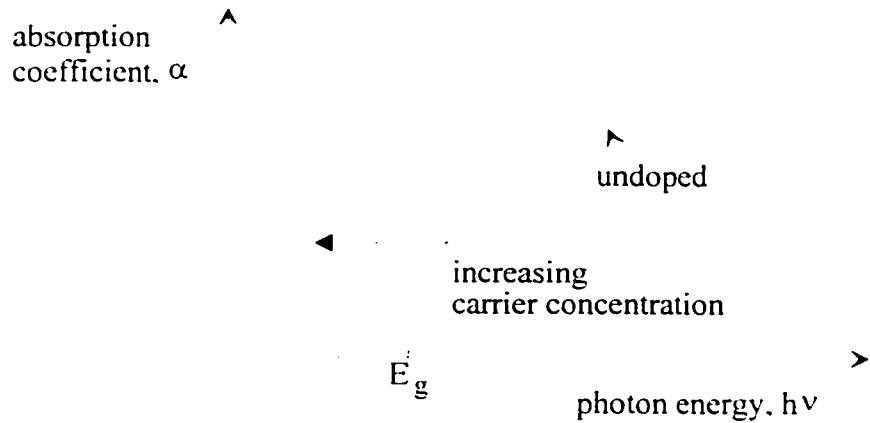


Figure 4.15. The shift of the absorption edge in a degenerately doped semiconductor due to band-gap shrinkage. The nominal band gap is shifted, due to potential energy screening by free carriers in the crystal lattice.

When the three effects are combined, it is found that one or more may dominate, for a given carrier concentration in a particular semiconductor. Figure 4.16 schematically illustrates the change in refractive index due to each mechanism, near the band-edge of a degenerately n-doped semiconductor.

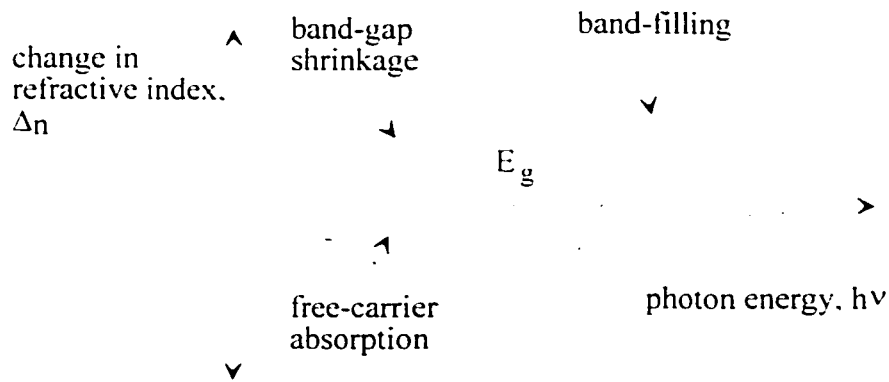


Figure 4.16. Changes in refractive index (relative to undoped case) for a degenerately n-doped semiconductor, due to band filling, band-gap shrinkage, and free-carrier absorption. Depending on the particular semiconductor, and the doping level, one or more of the three effects can dominate.

It is apparent that band filling and band-gap shrinkage are competitive physical mechanisms, in terms of their effect on optical constants near the band-edge wavelength. The major concern for the devices reported here was the overall shift in the effective absorption band-edge. The goal was to dope GaAs heavily, so that band-filling effects were much larger than the competing effects. This

increases its transparency at wavelengths slightly longer than its nominal band-edge wavelength, approximately 870 nm.

Bennett et al. [159] predict that for carrier concentrations greater than approximately 10^{18} cm^{-3} , in both InP and GaAs, band-filling effects dominate changes in the optical constants near the band edge. Thus, for sufficiently high n-type doping, a reduction in absorption near the nominal band edge is expected for GaAs, as is the case for $\text{In}_{0.53}\text{Ga}_{0.47}\text{As}$ [140]. To model the optical constants of n-GaAs, with a dopant concentration of approximately $7 \times 10^{18} \text{ cm}^{-3}$, the experimental data of Hwang [161] and Sell et al. [162],[163] were used. The effective band-edge shift, with this level of doping, is illustrated in Figure 4.17.

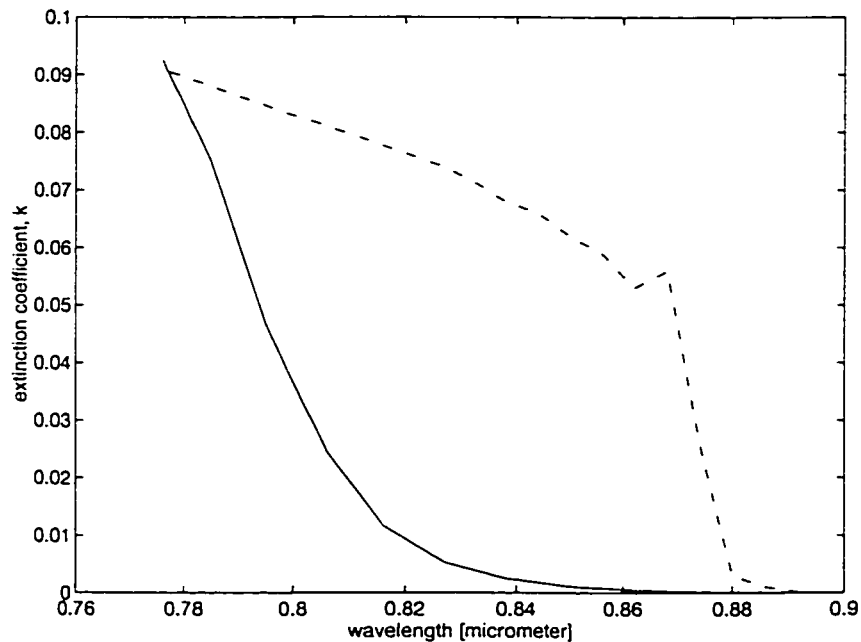


Figure 4.17. Absorption edge of intrinsic (dash-dot line) and heavily doped ($n \sim 7 \times 10^{18} \text{ cm}^{-3}$) (solid line) GaAs. The band edge is effectively shifted, due to band-filling by donor electrons.

From the data in Figure 4.17, heavy n-type doping can significantly increase the transparency of GaAs for wavelengths in the 825 to 875 nm range. In the following section we discuss the design of a device intended to exploit this effect, for operation near 830 nm wavelength.

4.5.2.3. Epitaxial Design

Based on the available data and the discussion in the preceding section, a resonant-cavity epitaxial structure was designed using a heavily n-doped InGaP/GaAs DBR mirror, with a target center wavelength of 830 nm. The structure is illustrated in Figure 4.18. The top mirror of the resonant cavity is provided by the large refractive index step at the air-semiconductor interface.

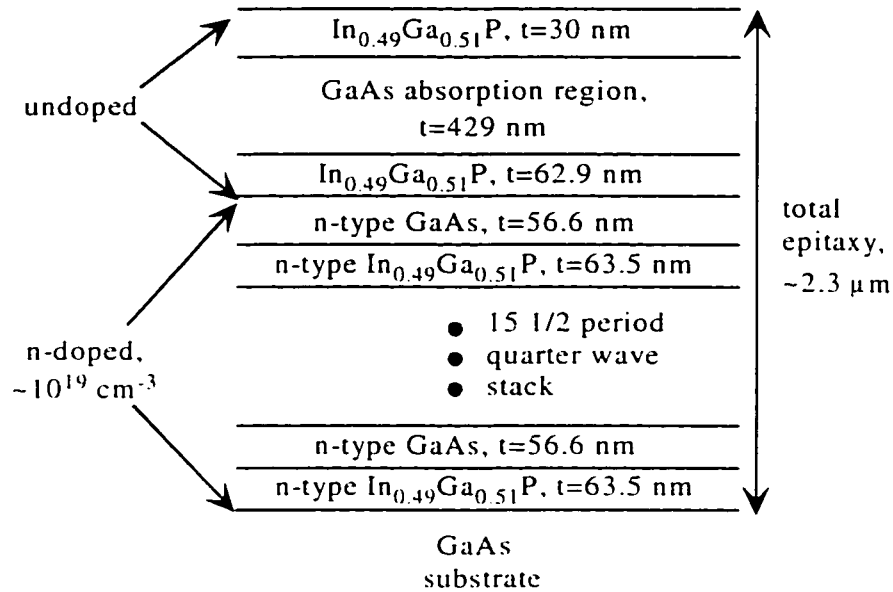


Figure 4.18. Resonant-cavity epitaxial structure, using a buried n-type InGaP/GaAs DBR mirror, with a target center wavelength of 830 nm. Doping the GaAs layers in the mirror makes them effectively transparent at 830 nm.

The epitaxy in Figure 4.18 is designed for fabrication of a double-heterostructure MSM photodetector. The top layers, including the InGaP cap layer, the GaAs absorption region, and an InGaP buffer layer, are not intentionally doped. This is critical to obtain a low operating bias, low capacitance MSM device, and ensures efficient absorption in the undoped GaAs layer at 830 nm. The DBR mirror is heavily doped, ideally such that the GaAs layers in the mirror have an n-dopant concentration greater than $5 \times 10^{18} \text{ cm}^{-3}$.

The reflection, transmission, and absorption properties of the entire structure are simulated using the transfer-matrix formalism described in Section

4.3 (see the Matlab file in appendix B). The dispersion relations for the complex refractive indices were taken from experimental data in the literature, mentioned above. For undoped GaAs, the data were from [82]. For undoped InGaP, the data of Schubert et al [164] were used. For doped GaAs, the data of Hwang ($n \sim 6.5 \times 10^{18} \text{ cm}^{-3}$) [161] were used for the extinction coefficient, and the data of Sell et al. ($n \sim 6.7 \times 10^{18} \text{ cm}^{-3}$) [162] were used for the real part of the refractive index. It was assumed that the wide band-gap InGaP layer would also be doped to a level of greater than 10^{18} cm^{-3} in the mirror. Based on the work of Bennett et al. [159] for InP, InGaAsP, and GaAs, in the near band-edge transparent region, a fixed reduction in refractive index ($\Delta n = -0.02$) for doped InGaP, relative to the intrinsic case, was used. The real parts of the refractive indices for various layers were thus modeled as illustrated in Figure 4.19.

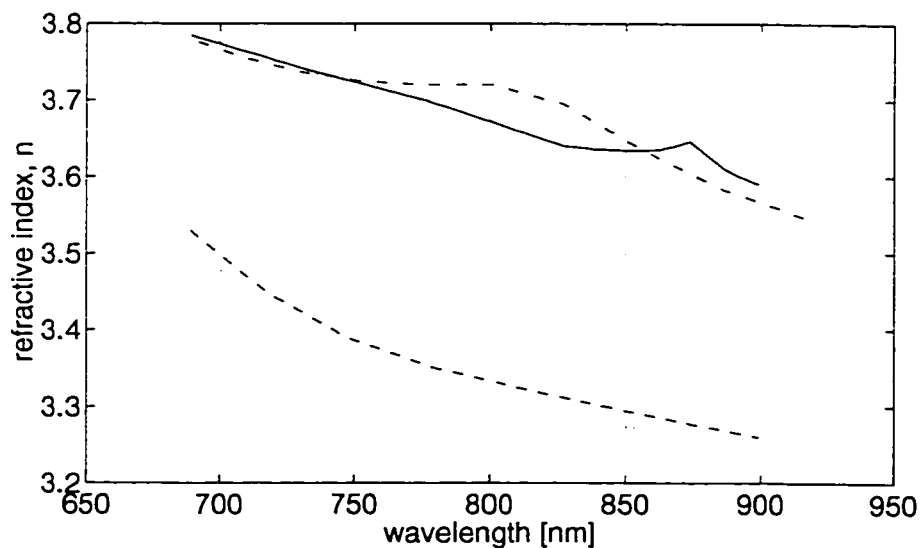


Figure 4.19. Modeled real parts of the refractive indices for the various layers in Figure 4.18. The indices shown are for undoped GaAs (solid line), doped GaAs (dash-dot line), undoped InGaP (dash line), and doped InGaP (dot line).

Note that a secondary benefit is predicted for the heavily doped mirror: there is an increase in the refractive index of GaAs and a decrease in the refractive index of InGaP at 830 nm, for the doped layers. This results in a superior refractive index offset for the DBR layers, and therefore higher reflectivity, to go

along with the increased transparency of the mirror. In fact, the offset of 0.4 at 830 nm approaches the offset of 0.45 for the transparent AlGaAs/GaAs combination discussed in the previous section.

The reflected, transmitted, and absorbed power spectra were simulated for the layer structure of Figure 4.18. The result, for normally incident illumination, is shown in Figure 4.20.

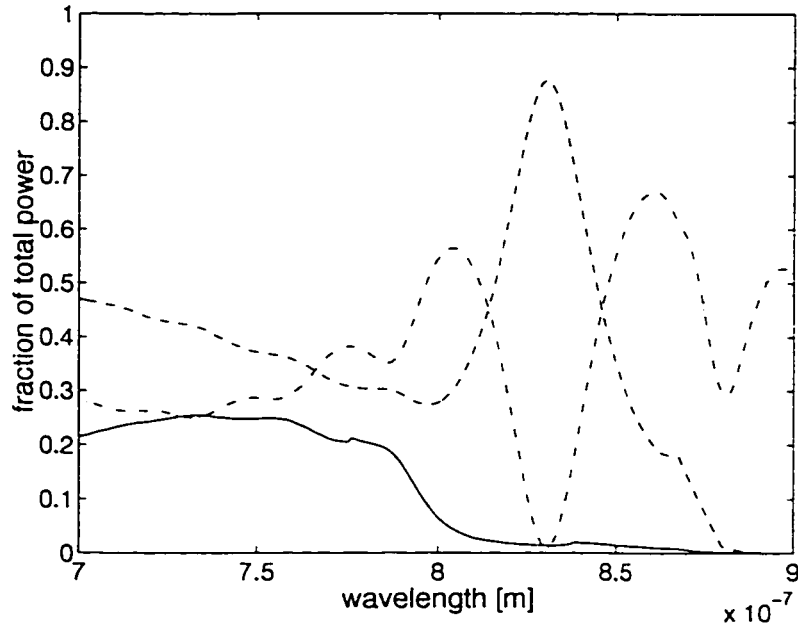


Figure 4.20. For the structure of Figure 4.18: the percentage of incident power absorbed in the absorption layer (dash line), absorbed in the mirror (solid line), reflected from the surface (dash-dot line), and transmitted into the substrate (dot line). Peak absorption of 88 % is predicted at 830 nm. This is limited primarily by the reflectivity of the bottom mirror (90 %). Less than 2 % of the power is absorbed in the mirror, for wavelengths of 810 nm and above.

Peak absorption of approximately 88 % is predicted at 830 nm. This is limited in part by the reflectivity of the 15 1/2 period mirror (~90 %), and in part by residual absorption (~2 %) in the doped GaAs layers of the mirror. Note that over a wide range of wavelengths, as low as approximately 810 nm, the predicted loss in the doped mirror is less than 2 %. This level of residual absorption compares well to previous results [142] for a Burstein-Moss shifted InGaAs/InP mirror of similar reflectivity, operating near 1550 nm. As illustrated in Figure

4.21, peak efficiency of greater than 96 % would be possible, if a buried mirror having a greater number of layers was employed.

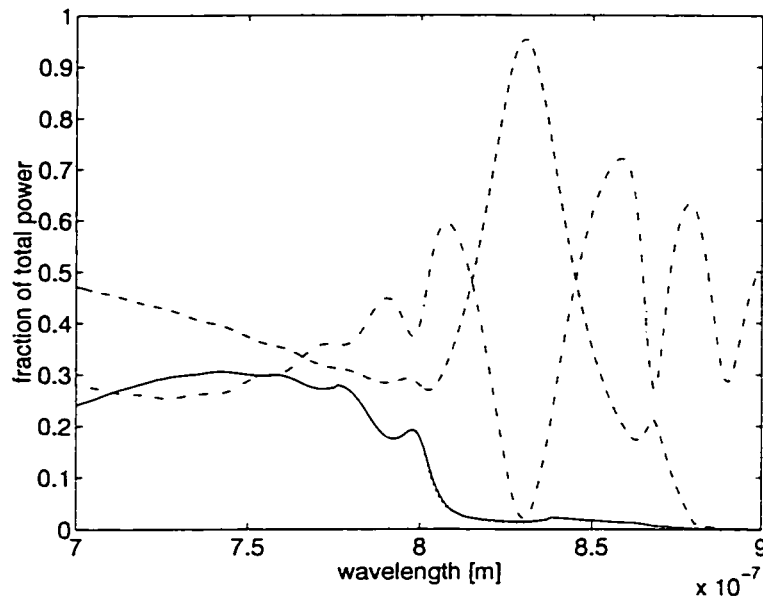


Figure 4.21. Spectral response for the structure of Figure 4.18, with a 25 period buried mirror. The legend is the same as in Figure 4.20. Peak absorption greater than 96 % is predicted.

4.5.2.4. Fabrication

The structure in Figure 4.18 was grown for TRILabs by Nortel Technologies in Ottawa. It was grown by low-pressure, metal-organic-vapor-phase-epitaxy (LP-MOVPE). For reference, Nortel labeled the job as growth T-1522, on wafer U2267-057. The substrate was a semi-insulating GaAs wafer, four inches in diameter. Si was employed as the dopant for the mirror layers. From standard calibration information for the MOVPE system, the doping levels were estimated as $8 \times 10^{18} \text{ cm}^{-3}$ for n-GaAs and $4 \times 10^{18} \text{ cm}^{-3}$ for n-InGaP. That n-dopant density is nearly the maximum achievable for GaAs, by MOVPE [82]. The data of Hwang [161] and Sell et al. [162] were for a dopant density of $6.5\text{-}6.7 \times 10^{18} \text{ cm}^{-3}$, and were obtained from Te-doped, melt-grown GaAs samples. In spite of these discrepancies, those sources represent the best available data regarding the optical constants of heavily doped GaAs.

4.5.2.5. Experimental Results and Discussion

After epitaxial growth, Nortel conducted a preliminary characterization of the wafer. Reflectivity and differential photoluminescence measurements indicated a resonant center wavelength of approximately 787 nm, for data collected near the center of the wafer. The wafer was forwarded to TRILabs, and the surface reflectivity was mapped using a Varian spectrophotometer, at the University of Alberta. Those data indicated good wafer uniformity. Data taken near the wafer edges showed a resonance wavelength slightly closer to the target wavelength of 830 nm. A representative reflectivity scan is shown in Figure 4.22. Unfortunately, the spectrophotometer switches its internal photodetector at 800 nm wavelength, so a spurious discontinuity was present in some of the plots at this wavelength.

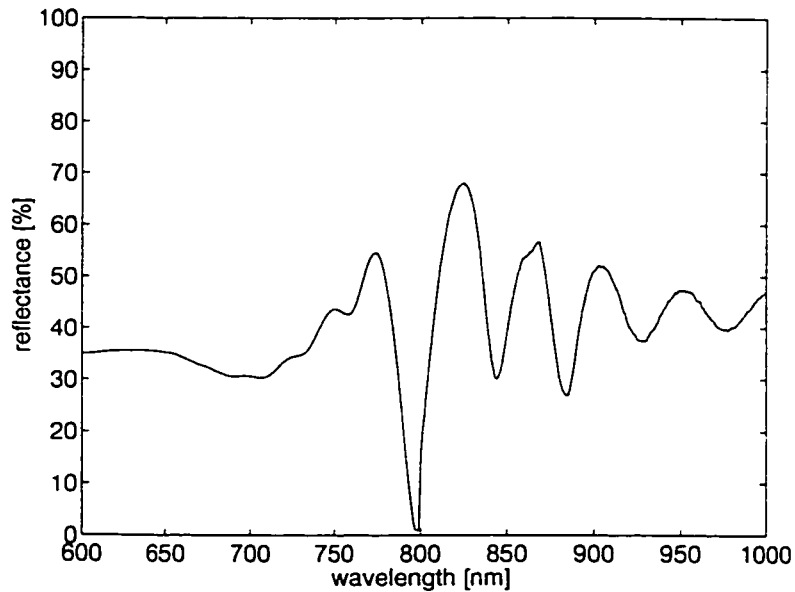


Figure 4.22. An experimental power reflectivity scan is shown, for the epitaxial structure illustrated in Figure 4.18. The spectrum was obtained with a Varian spectrophotometer. Away from the center of the wafer, the resonant wavelength of the structure was typically 796 nm \pm 2 nm.

Several factors might contribute to the discrepancy in the simulated (Figure 4.20) and measured spectra. Layer composition and thickness inaccuracies were potential growth-related errors, while uncertainty in the optical constants was the primary source for error in the simulation.

X-ray diffraction analysis at Nortel indicated that a highly lattice-matched structure was achieved ($\Delta a/a < 10^{-3}$, where a is the lattice constant). Thus, it was likely that composition targets for $\text{In}_{0.49}\text{Ga}_{0.51}\text{P}$ were met within a fraction of a percent, and compositional error did not contribute significantly to the missed targets. This implied that either layer thickness error or uncertainty in optical constants was responsible for the discrepancy.

The resonance condition for the cavity is given by (4.9). The discrepancy in center wavelength (796 nm compared to 830 nm) represents an error of approximately 5 %, which may be attributed to uncertainty in the refractive indices and/or the thickness of layers forming the cavity. In the structure of Figure 4.18, the layers in the cavity are nominally doped GaAs and InGaP.

From an analysis of the available refractive index data, an uncertainty of much less than ± 5 % was estimated. Especially for intrinsic GaAs, which forms the bulk of the cavity for this structure, the data are known within much less than ± 1 %. This is supported by the agreement between various sources and by the stated uncertainties in experimental reports [82]. For InGaP, the data available from various sources [164],[165] agrees quite closely, suggesting an uncertainty less than 1 or 2 %. Therefore, it seemed likely that the as-grown layers were 4 to 5 % thinner than specified.

From the X-ray diffraction analysis provided by Nortel, the combined thickness of the high and low refractive index layers in the mirror was estimated as 116.4 nm. Comparing to Figure 4.18, this corresponded to a 3 % growth error, and supported the hypothesis above.

As discussed by Murtaza et al. [166], various types of layer thickness errors can occur in the long growth times required for multi-layer DBR structures. They investigated the effects of several types of errors: random variations around target thickness, fixed error in all layers due to inaccurate system calibration, and gradual drift in growth rate over the period of the growth. Some alternative growth-related

errors of these types were simulated, in an attempt to reproduce the experimental data of Figure 4.22.

First, it was assumed that a majority of the growth thickness error was attributable to the InGaP layers, since that material is less well characterized and less commonly used than GaAs. Figure 4.23 illustrates that a -17% growth error (which is highly unlikely) must be assumed for the InGaP layers, in order to account for the observed discrepancy in center wavelength. At this level of error, the secondary features of the theoretical spectrum do not match well with the experimental spectrum.

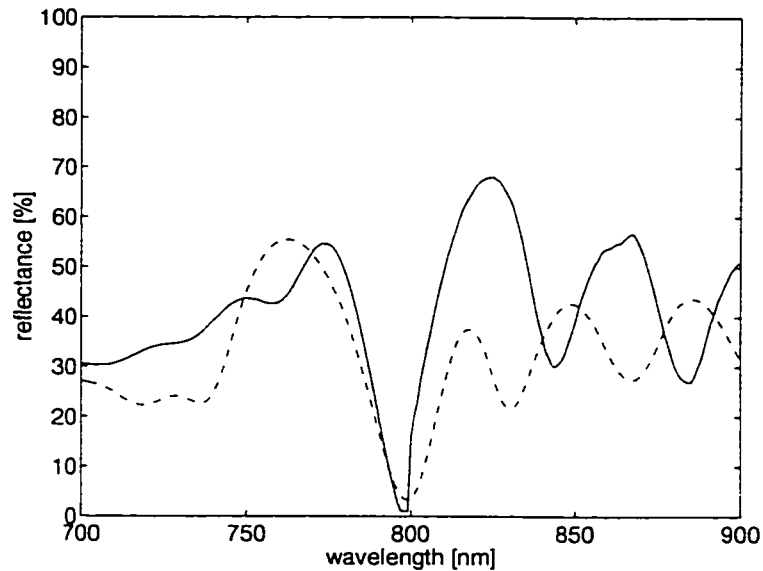


Figure 4.23. A comparison of experimental (solid line) and theoretical (dashed line) reflectivity spectra is shown. For the theoretical spectra, a -17 % growth error was assumed for the InGaP layers, while the GaAs layers were assumed to be as specified. This assumption did not produce a good match to the secondary features of the experimental spectrum.

Much better agreement was obtained by presuming a fixed growth error for all layers. Figure 4.24 compares the experimental and theoretical reflectivity spectra, when a fixed thickness error of -4.8 % is assumed, for all of the layers in Figure 4.18. In that case, the observed and simulated spectra are in excellent agreement, with even the excitonic discontinuity reproduced by the theoretical plot. The excitonic feature is not well resolved in the theoretical plot, however.

This might reflect the refractive index data that were used for the simulation, as mentioned in Section 4.5.2.2. The data date back to 1975, and were obtained for melt-grown GaAs samples. In any case, the quality of agreement here is comparable to a similar study performed on an AlGaAs/GaAs resonant cavity device [150], in spite of the fact that the optical constants are known with greater accuracy in that case.

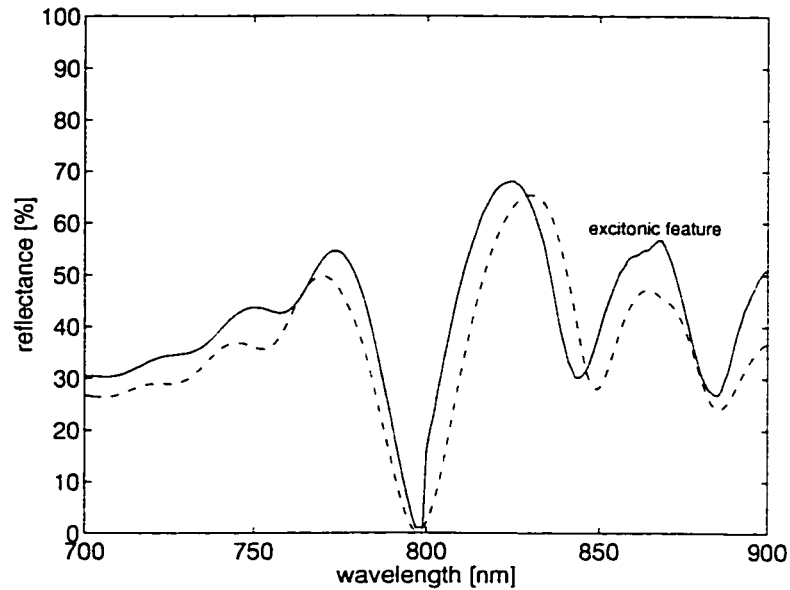


Figure 4.24. A comparison of experimental (solid line) and theoretical (dashed line) spectra is shown. For the theoretical spectra, a fixed growth thickness error of -4.8% was assumed, for all of the layers in Figure 4.18. The excitonic feature at the GaAs band edge is labeled on the experimental spectrum. It is present, but less resolved in the theoretical plot. This might reflect the fact that the refractive index data for the simulation correspond to melt-grown GaAs samples, as discussed in the text.

Some discrepancies remain in Figure 4.24. The experimental scan exhibits secondary minima of slightly higher reflectivity. This reflects the fact that an infinite substrate was assumed in the simulation. For example, at long wavelengths, where the entire structure is non-absorbing, a minimum of approximately 30% of the incident power is reflected at the bottom of the finite GaAs substrate [157]. The mismatches in the positions of secondary extrema reflect random thickness errors in the DBR stack [137].

The excellent match in Figure 4.24 provided strong evidence for a relatively fixed thickness calibration error. Modern epitaxial techniques can often obtain growth accuracy of 1-2 % [158], but errors of up to 5 % are typical, and might be expected for the relatively large amount of epitaxy here (2.4 μm). Also, the InGaP/GaAs material system has not been used extensively. At the time of growth, Nortel had not fully calibrated their systems for that material combination.

In order to confirm the results of Figure 4.24, a small chunk of the wafer was cleaved off and mounted for scanning electron microscope (SEM) analysis. The SEM analysis was performed at the University of Alberta, by the Geophysical Sciences department. The epitaxial layers were magnified in cross-section, to obtain layer thickness estimates. Because the cleaved edge was not selectively etched to differentiate the InGaP and GaAs layers, the resolving capabilities of the SEM were challenged, and it was not possible to produce high quality images and accurate layer thickness estimates.

However, the SEM results generally supported the assumption of a growth thickness error on the order of 4 to 5 %. Figure 4.25 is a SEM image of the entire layer structure. The alternating layers of the DBR mirror are clearly visible. The cap layer appeared as a bright band, near the top of the image. As shown, an estimate of approximately 410 nm was obtained for the absorption region thickness. This is equivalent to a -4.5 % growth error, which supported the data in Figure 4.24. Similar results were obtained for higher magnification images (not shown), of the quarter-wave-stack layers only.

While the under-grown wafer can operate as a resonant cavity structure at 800 nm, it is apparent from Figure 4.20 that this is outside the range for which the buried mirror has high transparency. As a result, the peak quantum efficiency at 800 nm is about 77 %, as illustrated by the simulation in Figure 4.26. The mirror layers absorb approximately 15 % of incident power in that case.

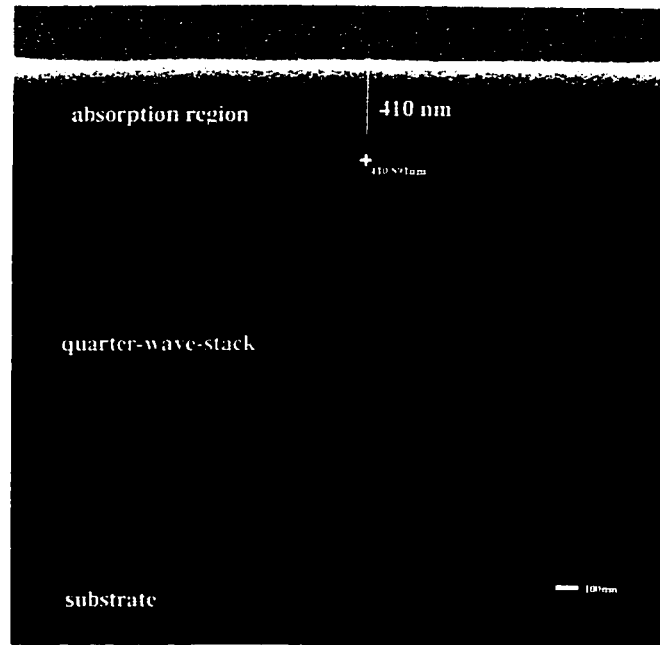


Figure 4.25. A scanning electron microscope (SEM) image is shown, of the grown epitaxial structure in cross-section. The structure is illustrated schematically in Figure 4.18. As indicated by the label, the absorption region thickness was estimated as 410 nm, from the SEM image. This represents a -4.5% growth error, which supports the simulation of Figure 4.24.

Given the experimental nature of the epitaxy, the results were encouraging. It is expected that the growth error would be reduced in future iterations. The peak absorption (77 %), predicted by Figure 4.26, corresponds to a responsivity of 0.5 A/W at 800 nm. An MSM detector with 1 μm finger width and 2 μm finger spacing should exhibit responsivity (with finger shadowing) of 0.34 A/W. This is double the responsivity attainable, for the same absorption region thickness, without the resonant cavity. Based on the results in Chapter 3, such a device will exhibit a -3 dB bandwidth of approximately 15 GHz. The corresponding gain-bandwidth coefficient is nearly 8 GHz.

Based on these results, the wafer was forwarded to the Communications Research Centre in Ottawa, for device fabrication. Experimental results for the devices will be reported elsewhere. It will be important to investigate any secondary effects on device performance, caused by the introduction of doped layers. For example, a built-in field will exist at the interface of the doped layers. It might drive holes to the surface, while attracting electrons toward the substrate.

This will impact speed in an undetermined way. Also, the depletion capacitance of the device (see Chapter 1) may increase, due to the highly doped layers beneath the active region.

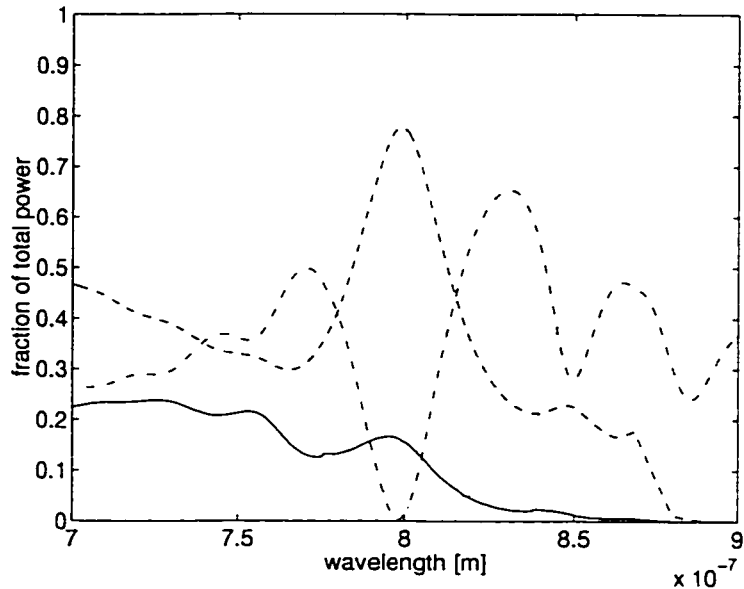


Figure 4.26. Simulated power spectra for the layer structure of Figure 4.18, with all layers undergrown by 4.8 %. The legend is as given in Figure 4.20. The mirror layers absorb about 15 % of the incident power, and only 77 % is absorbed in the intended absorption region. This corresponds to responsivity (neglecting finger shadowing) of 0.5 A/W, for a photodetector operating at approximately 800 nm wavelength.

4.5.3. InP/InGaAsP Resonant-Cavity Detector Operating Near 1300 nm

The InGaAsP material system, lattice matched to InP, exhibits relatively small refractive index offsets, much like the materials discussed in Section 4.5.2. For this reason, InGaAsP/InP has rarely been used for the fabrication of resonance-enhanced photodetectors [140]. It is considered here since it has the inherent value of being an aluminum-free system, which is generally associated with superior growth, reduced oxidation, and greater electrical stability of interfaces and surfaces. This is supported by the results for basic double-heterostructure MSM detectors, in Chapter 3. The performance attainable for a resonant-cavity MSM using InGaAsP/InP, and with a reasonable amount of epitaxy, is demonstrated in

this section. The recommended structure for this material system is illustrated in Figure 4.27. The target center-wavelength is 1320 nm. A device operating at 1550 nm would require considerably more epitaxy than specified in Section 4.4.

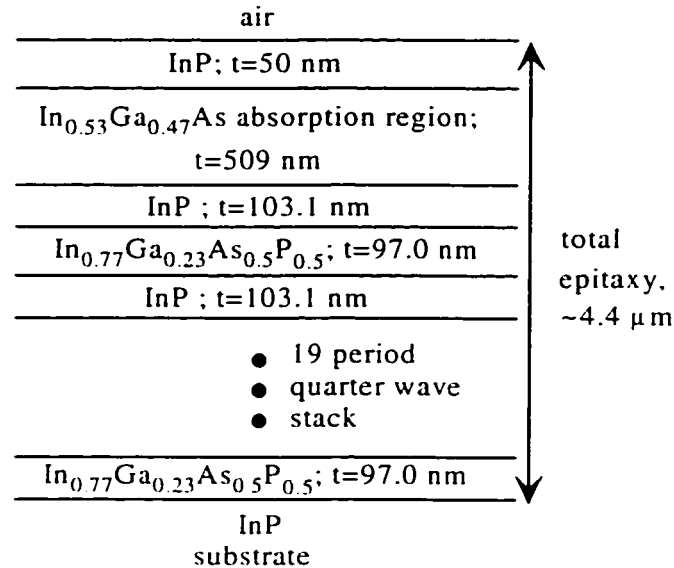


Figure 4.27. Recommended epitaxial structure of an InGaAsP/InP resonant-cavity-enhanced MSM detector, with a center wavelength of 1320 nm. All layers nominally undoped. The total epitaxy exceeds the specifications in Section 4.4, but is the minimum required for an efficient device.

The wavelength-dependent refractive index of InP is modeled using a fit to the data summarized in reference [54], p. 133. The fit over the wavelength range of interest here is given by

$$n_{InP}(\lambda) = 0.1849\lambda^2 - 0.6885\lambda + 3.7888 . \quad (4.16)$$

This predicts a refractive index at the chosen center-wavelength (1320 nm) of 3.20, which is verified repeatedly in the literature, for example in [167].

The second component material for the DBR mirror is chosen as In_{0.77}Ga_{0.23}As_{0.5}P_{0.5}, which has a band-gap energy of 1 eV. This quaternary has maximum refractive index offset, relative to InP, while maintaining transparency at the design wavelength. The refractive index data is taken from p. 420 of reference [54], and is modeled as

$$n_{InGaAsP}(\lambda) = 0.8906\lambda^2 - 2.8021\lambda + 5.5493 , \quad (4.17)$$

which predicts a refractive index of 3.40 at the design wavelength. Note that the refractive index step between the component materials of the InGaAsP mirror is less than half that for the AlGaAs system, Section 4.5.1.

For the absorbing InGaAs, the refractive index was modeled using the data of Pan et al. [168], and confirming the results with the data of Nojima et al. [169]. The fit is given by

$$\begin{aligned} N_{InGaAs} &= n_{InGaAs} - i\kappa_{InGaAs} ; \\ n_{InGaAs} &= -0.1518\lambda^2 + 0.2502\lambda + 3.54, \\ \kappa_{InGaAs} &= -0.7870\lambda^3 + 2.6825\lambda^2 - 3.0354\lambda + 1.2739 , \end{aligned} \quad (4.18)$$

which predicts a complex refractive index of 3.61-i0.13 at the design wavelength. This value of extinction coefficient corresponds to an absorption coefficient of $1.25 \times 10^6 \text{ m}^{-1}$. The 19 period mirror buried, sandwiched by InGaAs and InP, has a reflectivity of only 70%. This implies that the reflectivity of the entire structure will approach zero for an absorption region thickness of approximately 340 nm, per equation (4.12). With such a poor back reflector, the zero reflectivity condition will not correspond to maximum quantum efficiency, as is shown in the following simulation. Figure 4.28 shows the absorption, reflection, and transmission spectra, simulated for the device of Figure 4.27.

A relatively thick absorption region is required for good efficiency, due to the poor Q factor of the cavity. A thickness of 509 nm is a good compromise, since it produces nearly maximum power absorption of 79%, while being narrow enough to benefit device bandwidth. Power absorption of 79 % corresponds to responsivity of 0.56 A/W at 1320 nm, for an MSM detector with 1 μm finger width and 2 μm finger spacing.

It should be noted that the power absorption of 79% for the 509 nm thick InGaAs layer, while not outstanding, is still 2 to 3 times that which would occur without the buried QWS. However, the design criteria of Section 4.4, 90%

absorption and less than 4 μm of epitaxy, are necessarily compromised in this material system.

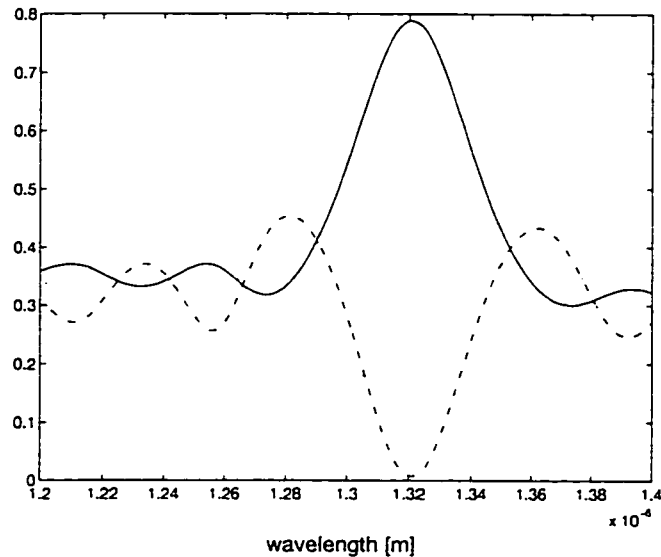


Figure 4.28. The reflected (dot), transmitted (dash-dot), and absorbed (solid) power as a fraction of incident power, for the device illustrated in Figure 4.27.

4.5.4. InP/InAlGaAs Resonant-Cavity Detector Operating Near 1300 nm

The InAlGaAs material system, as an alternative to InGaAsP, has several inherent advantages, as mentioned in Section 3.3.2. These include simpler growth by MBE, owing to the absence of phosphorus, greater ease of quaternary growth, owing to the near-unity sticking coefficient of the group III elements, and superior band characteristics, for devices that require electron confinement. The InAlGaAs system also has some disadvantages. The disadvantages include the difficulty of obtaining high quality epitaxy, due to the tendency of Al compounds to form clusters of distinct alloys during growth, the greater tendency to oxidize, and the somewhat higher density of interface and surface states typically exhibited (see Chapters 2 and 3).

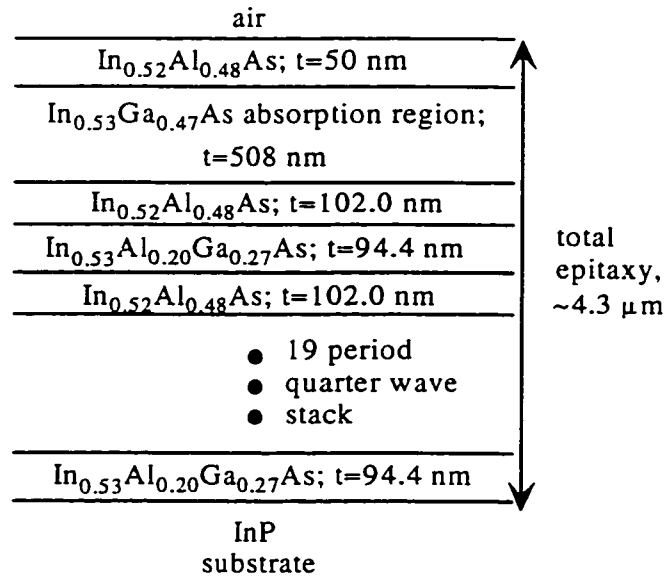


Figure 4.29. Recommended structure for a resonant-cavity MSM photodetector, using the InAlGaAs material system. The target center-wavelength is 1320 nm. All layers are nominally undoped.

InAlGaAs is superior in one other sense, however: slightly larger refractive index steps are available for the lattice-matched quaternaries, while maintaining transparency at the fiber communication wavelengths. The endpoints of the system are $\text{In}_{0.53}\text{Ga}_{0.47}\text{As}$ and $\text{In}_{0.52}\text{Al}_{0.48}\text{As}$, with band-gaps of 0.75 eV and 1.47 eV, respectively, and refractive indices in the 3.6 and 3.2 range, respectively. InAlGaAs has been used previously for resonant-cavity photodetector applications, with operation at 1550 nm [146] and 1300 nm [134]. The structure recommended here is designed for operation at 1320 nm and is illustrated in Figure 4.29.

The refractive index data for $\text{In}_{0.52}\text{Al}_{0.48}\text{As}$ are taken from [168], and confirmed with [169],[170]. The polynomial fit over the wavelength range considered in the simulation is

$$n_{\text{InAlAs}}(\lambda) = 0.1607\lambda^2 - 0.6032\lambda + 3.7521, \quad (4.19)$$

which predicts a refractive index of 3.24 at the design wavelength. The quaternary component of the DBR mirror is chosen as $\text{In}_{0.53}\text{Al}_{0.20}\text{Ga}_{0.27}\text{As}$, which has a band-gap energy of approximately 1.0 eV [55], and should be essentially transparent at 1320 nm. This is contradicted somewhat by the data in [168], where a similar

quaternary showed absorption at wavelengths up to 1400 nm. It is presumed that the absorption in that case related to the crystalline quality of the InAlGaAs measured, and represents band-tail absorption. The refractive index of the chosen quaternary is predominantly real, over the wavelength range of interest, and given by

$$n_{\text{InAlGaAs}} = 0.8214\lambda^2 - 2.7564\lambda + 5.7041 . \quad (4.20)$$

This fit is a linear interpolation of available data, for the quaternaries reported in references [168-170], and [138]. The predicted refractive index, for the quaternary at 1320 nm, is 3.50.

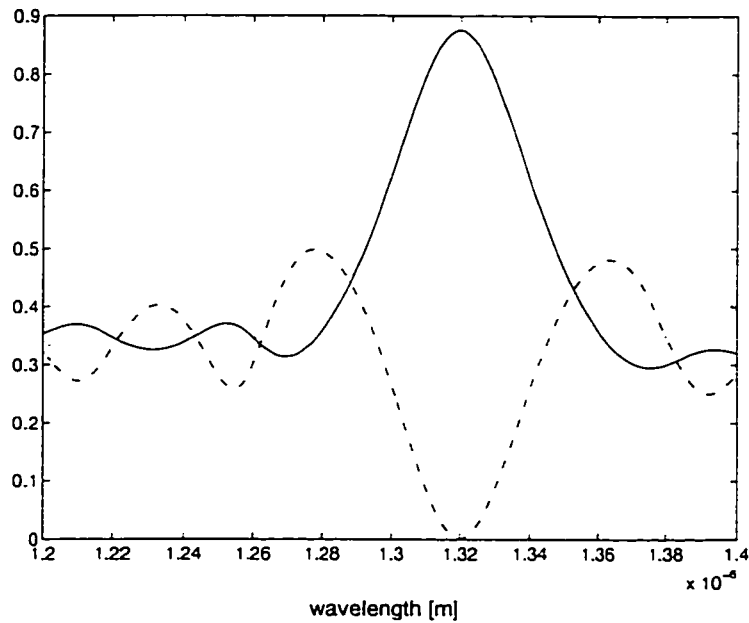


Figure 4.30. The predicted spectral response for the device of Figure 4.29 is shown. The traces are for absorbed (solid), reflected (dash-dot), and transmitted (dot) percentages of incident optical power.

Figure 4.30 shows the simulated spectra for the device of Figure 4.29. The structure exhibits peak absorption of 88%, which is a 9% improvement over the similar InGaAsP device discussed in the preceding subsection. This would correspond to a responsivity of 0.63 A/W, for an MSM detector with 1 μm finger width and 2 μm finger spacing. The buried DBR mirror has a reflectivity of approximately 83% in this case.

4.5.5. InP/InGaAs Resonant-Cavity Detector Operating Near 1550 nm

At 1300 nm, both the InAlGaAs and InGaAsP material systems fail to satisfy the design criteria, outlined in Section 4.4. With the traditional approach, discussed to this point, the situation is worse at 1550 nm. In spite of the fact that larger refractive index offsets are available for transparent materials at 1550 nm, the increase in thickness of each quarter wavelength layer results in greater total epitaxy. A different approach has been reported recently [140]. This involves heavy n-type doping of $\text{In}_{0.53}\text{Ga}_{0.47}\text{As}$ layers, in order to make them effectively transparent at 1550 nm. The GaAs/InGaP structure described in detail in Section 4.5.2 is based on the same effect, in GaAs at 830 nm.

This approach allows the use of InGaAs/InP DBR mirrors, which exhibit the maximum refractive index offset for the InGaAsP/InP material system. The blue shift of the optical band-gap with heavy doping is termed the Burstein-Moss effect, and has been described in detail in Section 4.5.2.2. Guy et al. [140] have demonstrated high quality, MBE-grown mirrors using this technique. Murtaza et al. [142] fabricated a resonant-cavity p-i-n photodetector with a buried InGaAs/InP DBR mirror, by MOCVD.

To make InGaAs nearly transparent at 1550 nm wavelength, free-electron concentrations greater than $5 \times 10^{18} \text{ cm}^{-3}$ are necessary. The recommended structure, for a top-illuminated resonant-cavity-enhanced MSM detector, is illustrated in Figure 4.31. The target center-wavelength is 1535 nm. Note that quaternary materials are not required. This is advantageous, since quaternaries are more difficult to grow, and more sensitive to growth fluctuations over the long run-times required for a quarter-wave-stack at 1550 nm. Ternary $\text{In}_{0.52}\text{Al}_{0.48}\text{As}$ layers may replace InP layers, in the device illustrated, and similar performance is predicted.

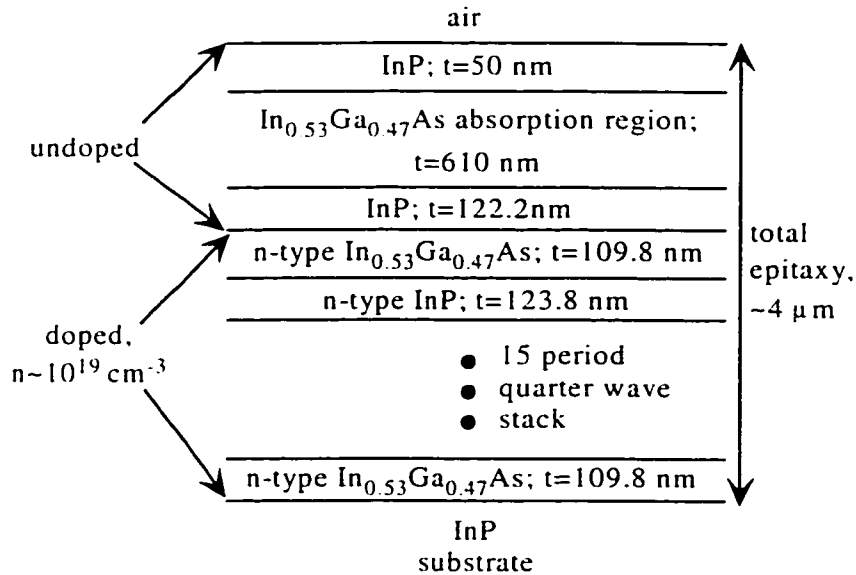


Figure 4.31. A recommended structure for operation in the 1550 nm wavelength region. A Burstein-Moss shifted InGaAs/InP DBR mirror is used. The relevant theory is contained in Section 4.5.2. The target center-wavelength is 1535 nm.

Note that the last half-layer of the QWS, prior to the absorption region, is not doped. This is to isolate the absorption region from the heavily doped layers, so that it does not become unintentionally doped by diffusion. For the simulation, heavily doped InGaAs is assumed to exhibit a fixed refractive index offset of -0.05 [159]. From (4.18), the refractive indices of undoped and doped InGaAs are predicted to be 3.57 and 3.52, respectively. The absorption coefficient of the undoped InGaAs at 1535 nm is approximately $7.25 \times 10^5 \text{ m}^{-1}$. Because of the relatively weak absorption, the required layer thickness for maximizing quantum efficiency, per equation (4.12), is somewhat greater than in previous examples.

Equation (4.16) predicts a refractive index of 3.17 for the undoped cap layer, at 1535 nm. For the heavily doped InP layers, in the quarter-wave-stack, a fixed refractive index offset of -0.04 is assumed [159]. The resultant spectra for the structure of Figure 4.34 are shown in Figure 4.32.

Approximately 88% power absorption is predicted for a 15 period mirror. A slightly thicker absorption region is required at 1550 nm, as mentioned. 88%

power absorption corresponds to a responsivity of 0.73 A/W at 1535 nm, for a (1x2) MSM detector.

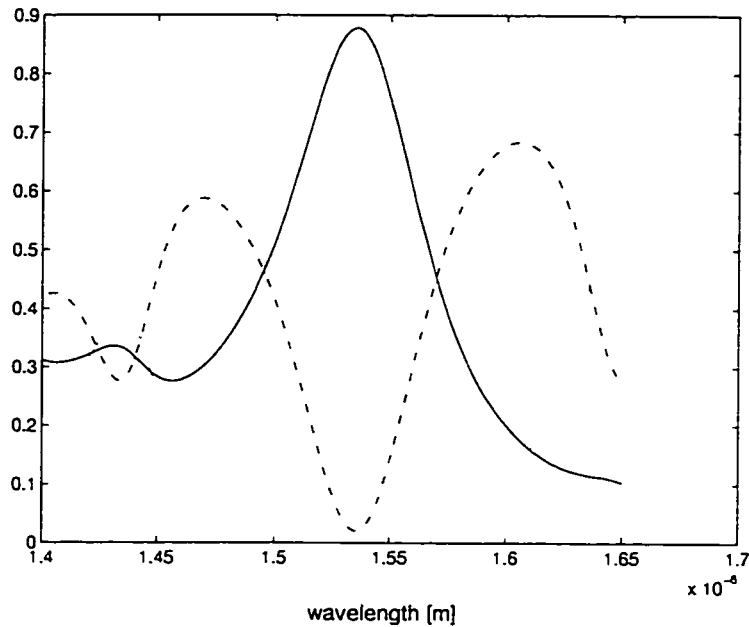


Figure 4.32. Simulated power spectra for the device of Figure 4.31: Absorption (solid), reflection (dash-dot), and transmission into the substrate (dot).

The introduction of doped layers beneath the active region of the MSM detector could influence device performance in other ways, as discussed in Section 4.5.2.5.

4.6. Summary and Conclusions

Epitaxial structures have been proposed, for resonant-cavity-enhanced, top-illuminated MSM photodetectors operating at 800 nm, 1300 nm, and 1550 nm. Experimental verification has been obtained for devices operating near a wavelength of 800 nm, in two different material systems.

AlGaAs/GaAs is the most-mature material system available, and was investigated first. A resonant-cavity structure was grown and demonstrated, operating near 800 nm. The MOCVD system used was not under computer control at the time, so the growth times were monitored manually. In spite of this,

relatively accurate layer thickness was achieved. The reflectivity scans for the wafer showed a resonant peak at 785 nm. The spectrum was in good agreement with theory, if a -4% growth error was assumed for the AlGaAs and AlAs layers in the quarter-wave-stack. It is expected that growth accuracy could be greatly improved in future iterations.

Unfortunately, the devices fabricated on the AlGaAs/GaAs wafer revealed problematic low-frequency gain. This is typical for arsenic-based semiconductors, as discussed in Chapters 2 and 3. For future work, dielectric passivation of this wafer should be investigated, using the techniques described in Chapter 3. If low-frequency gain could be minimized, by altering the surface conditions, the devices are potentially attractive for operation at 785 nm wavelength. Absorption in the 389 nm thick GaAs layer should exceed 90 % at the center wavelength, enabling very fast and efficient MSM detectors. To verify this, the individual photodetectors should be studied using a photocurrent spectroscopy technique, once low-frequency gain is reduced. This would augment the information obtained using reflectance spectroscopy, reported here.

InGaP/GaAs was investigated as an alternative material system for operation near 800 nm wavelength. The primary motivation is that InGaP has superior surface properties, as discussed in Chapter 2. Unfortunately, these materials exhibit reduced refractive index offsets, compared to AlGaAs/GaAs. To partially compensate, a novel resonant-cavity structure was investigated, using a heavily doped InGaP/GaAs quarter-wave-stack. A high free-electron concentration in the GaAs layers is predicted to increase their transparency at wavelengths of 810 to 870 nm. InGaP/GaAs exhibits the highest refractive index offset for the material system, and produces a high reflectivity mirror, with relatively few layers. A Further advantage is that quaternary layers are not required, simplifying growth.

An InGaP/GaAs wafer was grown, but device fabrication was pending. For experimental verification, data were obtained from reflectance spectroscopy on the

bare wafer. A slightly greater growth error was observed, compared to the AlGaAs/GaAs wafer. This is attributed to the relative immaturity of the InGaP/GaAs material system. Good agreement with theory was obtained by assuming a -4.8% growth error in all layers. This reproduced the observed resonant peak at approximately 795 nm, compared to the target center wavelength of 835 nm. The doped GaAs layers of the mirror will not be fully transparent at 795 nm, so it is predicted that only 75-80 % of incident light will be converted to photocurrent in this structure. Experimental device results were left for future work.

At 800 nm, good performance is possible with minimal epitaxy, owing to the large refractive index steps in the available material systems. At the longer wavelengths, performance is limited by the lower refractive index steps of the appropriate material systems, and it is not possible to simultaneously meet the design guidelines presented in Section 4.4 ($>90\%$ absorption, $<4\ \mu\text{m}$ of epitaxy). Two structures were recommended for operation near 1300 nm, in Sections 4.5.3 and 4.5.4. $\text{In}_{0.53}\text{Ga}_{0.47}\text{As}$ can be doped, to increase its transparency near 1550 nm wavelength, similar to the GaAs device discussed above. A structure based on this concept was recommended in Section 4.5.5. At the time of writing, a wafer was on order, based on the recommendation at 1535 nm wavelength.

The enhancement of responsivity afforded by resonant-cavity techniques has good long-term potential, for MSM photodetectors used in hybrid optoelectronic systems. The results reported here indicate that controlling growth errors will be the main challenge in implementing these techniques. With the continuing development of growth methods, including in-situ monitors, these errors will become less problematic in the near future [135].

5. MSM Photodetector Arrays

5.1. Introduction

As discussed in Section 1.3, optoelectronic switching and signal processing techniques rely on some method of combining the electrical signals from several photodetectors, in a broadband manner. Broadband photodetector arrays represent a major engineering challenge. This can be understood from the fact that photodetectors are essentially current sources, and to first-order are represented by an open-circuit impedance. Most commercial suppliers of broadband, discrete photodetectors use a fairly unsophisticated technique to match the detector output to a $50\ \Omega$ system: the photodetector is mounted in parallel with a $50\ \Omega$ termination resistor, so that spurious reflections with the external load are minimized over the frequency range of interest. Half of the photocurrent is dissipated internally.

Broadband photodetector arrays in common-bus configuration are essentially unavailable from commercial suppliers, at present. At the time of writing, the author was aware of a preliminary product offering from Mitsubishi, which is an array of ten p-i-n photodetectors with 1 GHz bandwidth (Mitsubishi part # PD7XX9). The immediate goal for optoelectronic switching is an OC-192-compatible channel bandwidth (10 Gb/s). An array of photodetectors with a bandwidth of at least 8 GHz is required.

In Section 5.2, some general issues relevant to the design of broadband photodetector arrays are outlined. In Section 5.3, an experimental study of several novel photodetector array layouts is detailed. These layouts were proposed previously [20], and the goal was uniform operation beyond 10 GHz for an 8 or 16 detector array. The initial experimental results are not in agreement with simulations in [20]. The experimental results are discussed in the context of identifying parasitic circuit elements that may have been neglected in the simulations, and may be contributing to the sub-optimal results.

In section 5.4, an alternative approach to achieving broadband operation in a photodetector array is proposed. The technique is based on treating the

photodetector array as an artificial transmission line, and matching its impedance to the external system. These are termed impedance-matched-MSM-photodetector-arrays (IMMPA), and the theoretical requirements are outlined in detail. In section 5.5, experimental results for the IMMPA are presented, and they show good agreement with the theoretical treatment in Section 5.4.

In Section 5.6, the maximum length of an IMMPA is explored. In Section 5.7, the IMMPA approach is compared to alternative techniques. Finally, conclusions are presented in Section 5.8.

5.2. Photodetector Arrays - General

Photodetector arrays for telecommunications fall into two broad categories. The first category describes arrays of discrete photodetectors on a single semiconductor chip [171], aimed primarily at high fiber density, parallel receiver applications. The goals in that case are to improve detector uniformity, reduce system size, and reduce cost. The second category of photodetector arrays includes devices that have been termed common-cathode arrays [172], common-bus arrays [173], traveling-wave photodetector arrays (TWPA) [174], and velocity-matched photodetector arrays (VMPA) [175].

The terminology used here is common-bus array. Common-bus arrays are designed such that an electrical and/or function is achieved, ideally with a broadband response. This type of array was first conceived in connection with optoelectronic switching techniques [18]. Recently, progress in analogue fiber-optics has produced new potential requirements for such photodetector arrays, since it is difficult to design single detectors which operate at microwave frequencies and have high power-handling capability [174],[175]. These applications define two further sub-categories, since arrays for optoelectronic switching require bias control of individual detectors, while arrays for microwave power combining do not. The need for individual bias control is a complicating factor in the design of broadband arrays.

In this chapter, we address common-bus MSM photodetector arrays, designed for optoelectronic switching and signal processing. Progress on these arrays has been relatively slow, as the challenge of combining the signals of several current sources, in a broadband manner, is formidable [20]. These arrays are typically on the order of a few mm in length, so distributed parasitic effects became problematic when multiple GHz operation became a requirement. Position-dependent response for MSM photodetectors tied to a simple bus was identified experimentally in 1994 [20],[176]. Subsequent modeling by Liu [173] and Sharma [20] showed that the capacitance of the detectors in the array combines with the effective inductance of the common bus to produce a complex parasitic load, unique for each detector in the array. As a result of that work, alternative layouts were proposed [20], inspired by broadband power-combining techniques within the microwave community. Those arrays were incorporated in the mask set described in Chapter 2. Initial experimental results are discussed in the following section.

Figure 5.1 illustrates the issues involved in the packaging of a generic MSM array. Several discrete devices are tied to a common bus, and the entire length of the array is quite comparable to the microwave wavelengths involved in operation. At least one end of the common bus must interface to a $50\ \Omega$ system, usually a microwave pre-amplifier. The second contact of each MSM provides a means of bias control. It is important that proper bias-decoupling occur very close to this contact [185], so that the external bias circuitry does not introduce additional parasitic effects.

As mentioned, two primary issues were identified with respect to these arrays, in previous work [4],[20],[173]. First, at wavelengths much longer than the length of the bus, the capacitance of each photodetector, and all other sources of capacitance (see Section 1.6), essentially add in parallel. Thus, while an individual detector ($C \sim 100$ fF) may have negligible RC-related speed limitations, 16 detectors in parallel limit $50\ \Omega$ system bandwidth to 1-3 GHz. Second, at shorter wavelengths, the bus and its attached photodetectors must be treated using a fully

distributed model. From such a treatment, a position-dependent response is predicted [173], and this has been verified experimentally [4].

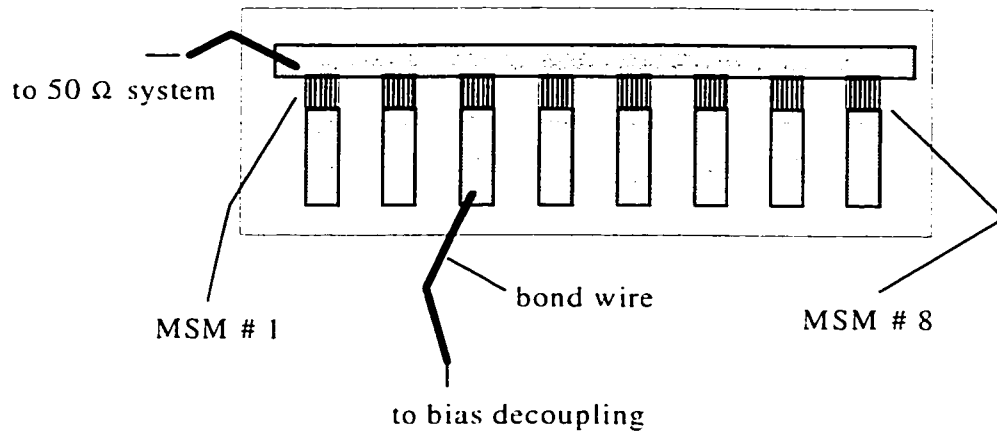


Figure 5.1. A generic MSM photodetector array. Several photodetectors are interconnected, by a common bus. This accommodates an electrical and/or summation of their signals. The opposite side of each MSM detector is selectively biased, providing a control function, useful for switching or weight-setting. The bus must interface to an external system, generally a 50 Ω load.

Results for p-i-n photodetector arrays in common-cathode configuration have also been reported in the literature. Liu [172] reported 5 GHz bandwidth for a 4 detector p-i-n array, which to our knowledge represented the previous speed record. However, they did not report on uniformity of response in that case.

5.3. Experimental Results for Single-Output Arrays

The mask set described in Section 2.8 incorporated several novel photodetector array layouts, as mentioned above. In this section, experimental results for those arrays are discussed. The results were obtained for arrays fabricated on the wafers discussed in Section 3.4: CRC-97D11 is simply 2 μm of GaAs epitaxy deposited on a semi-insulating GaAs substrate and CRC-97D25 is an AlGaAs/GaAs double-heterostructure, on a semi-insulating GaAs substrate. Both wafers received full processing: the active regions were mesa isolated, and silicon nitride was deposited prior to deposition of interconnect and pad metal.

While the results for discrete devices on these wafers were generally quite good, especially for CRC-97D25 [121], the results for the arrays were not in

agreement with previous simulations [20]. Those simulations were performed using HP-Microwave Design Systems software. The metal patterns of the array were modeled as variable impedance microstrip lines, and a simple equivalent circuit model was used for the MSM photodetectors. The data discussed below indicate that the simulations may not have properly accounted for coupled-line effects, and may have underestimated the parasitic capacitance in the arrays. The origin of the excess capacitance is not clear. The metal interconnects lie on a dielectric, which in turn lies on a semi-insulating semiconductor layer. This arrangement produces minimal depletion capacitance, as discussed in Section 1.6. Thus, it is probable that the excess capacitance is inherent to the large metal patterns in these arrays. In other words, the interconnected-microstrip model may have been an oversimplification. This is discussed in more depth in Section 5.3.4.

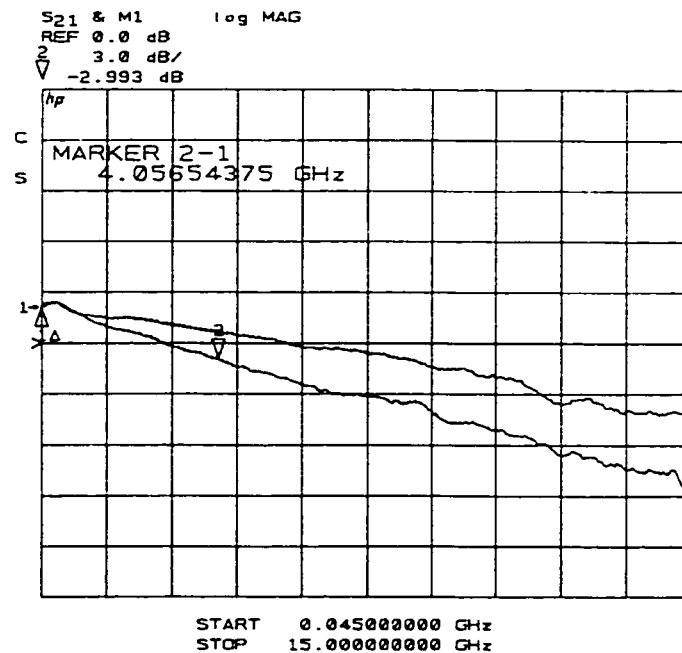


Figure 5.2. Frequency scans for a single $(75 \mu\text{m})^2$ MSM detector, with $2 \mu\text{m}$ finger spacing and width. The top scan is for a device with $(100 \mu\text{m})^2$ bond pads, as for the device results in Chapter 3. The lower scan is for the same detector in a 'skinny squid' detector array (see Section 5.3.1). Each scan was obtained with a ground-signal RF probe, making contact across the detector. The plot is the screen output of a HP-8510B network analyzer. The horizontal scale is linear in frequency, starting at 45 MHz and ending at 15 GHz. The vertical scale is logarithmic, 3 dB per division. The 0 dB reference represents 0.15 A/W responsivity.

If similar arrays are designed in the future, they should be characterized using a three-dimensional electromagnetic simulation package. This would produce a better estimate of parasitic elements. Those estimates could then be incorporated into an electrical model [20].

Before mounting the arrays on test substrates, the effect of the large metal interconnect patterns, on the performance of a single device in the array, was investigated. Single devices were contacted with a ground-signal RF probe. The chip in this case was mounted on an insulating test jig, with no bond wires. Figure 5.2 shows a typical result, and indicates that a considerable amount of excess capacitance is associated with the metal attached to each side of the MSM detector. The device in the array shows a much greater RC roll-off. Nearly identical results were observed for all of the single-output detector arrays discussed in this section.

The arrays were mounted on various RF substrates, with appropriate bias-decoupling circuitry, for testing purposes. Several photographs are shown in the following sub-sections.

5.3.1. 16 detector arrays – (*'squid' arrays*)

Two of the arrays illustrated in Figure 2.24 were termed the 'fat' and 'skinny' 'squid' layouts. A photograph of a mounted 'skinny squid' array is shown in Figure 5.3. The arrows and labels are used to illustrate some of the potential sources of parasitic effects, identified from the experimental results, below. As shown, the long metal strips, connecting each detector to the low-impedance output section, may potentially couple with each other. This effect was not considered in the simulation [20].

Figure 5.4 shows a typical result obtained for either of the 'fat' or 'skinny' 'squid' layouts. It is obvious from these results that the arrays did not behave well from a RF perspective. The frequency response is not flat and is not uniform for different devices in the array.



Figure 5.3. A photograph of a packaged 'skinny squid' array. The array contains 16 MSM detectors, each with $(75 \mu\text{m})^2$ active regions. The arrows identify the numbering of the MSM detectors, for discussion purposes. Also indicated are the adjacent metal strips relevant to the discussion of coupled-line effects in the text.

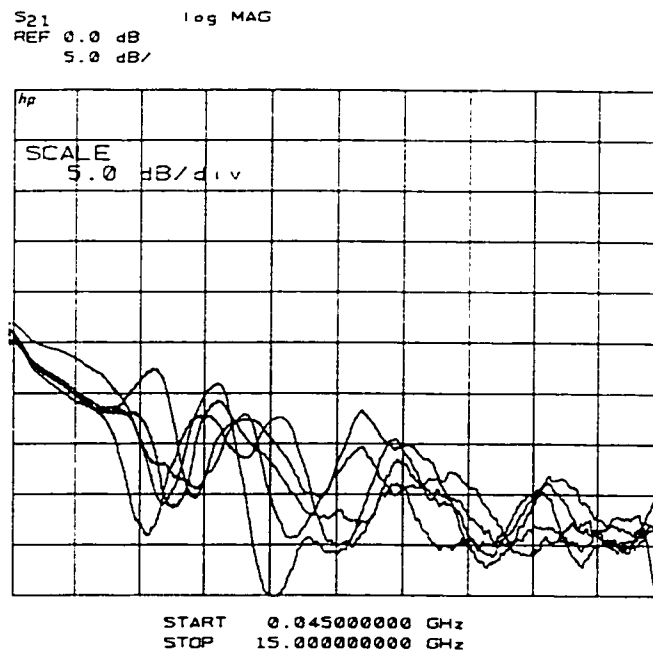


Figure 5.4. The scans show the typical frequency response for detectors in the 'fat' or 'skinny' 'squid' arrays. This particular plot was for a 'skinny squid' array, and shows the response of detectors 1,4,6,11, and 16 in the array. The frequency responses exhibit a strong RC roll-off, and position-dependent spurious features above 2 GHz. The plot is the screen output of a HP-8510B network analyzer, see Figure 5.2.

Strong evidence of coupled-line parasitic effects was observed for these devices, such as in Figure 5.5. Figure 5.5 is the response of an end detector (MSM #1) in a 'skinny squid' array, with the adjacent MSM bonded to AC ground. Testing the end detector allowed coupled-line effects to be studied, for the simple case of one nearest neighbor.

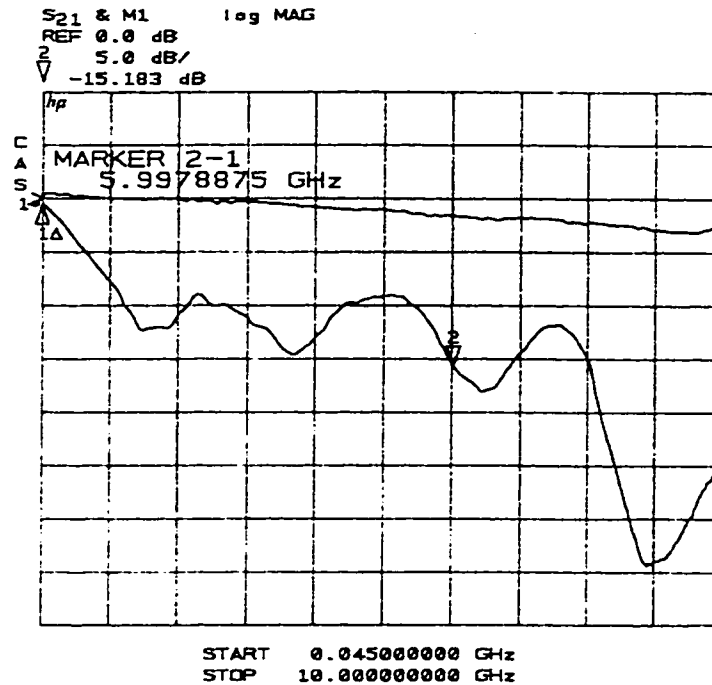


Figure 5.5. A typical frequency response for an MSM detector in one of the 16 detector 'squid' arrays. The upper trace was a frequency scan for a discrete detector of identical geometry, on the same wafer, for reference. The lower scan was for MSM #1 in a 'skinny squid' array, with the adjacent detector bonded to ground. The bias voltage was 8 V, and the optical power was 1 mW, at 830 nm wavelength. See Figure 5.2 for a description of the plot format.

The theory of coupled microstrip lines is well-established [177], and can be modeled as shown in Figure 5.6.

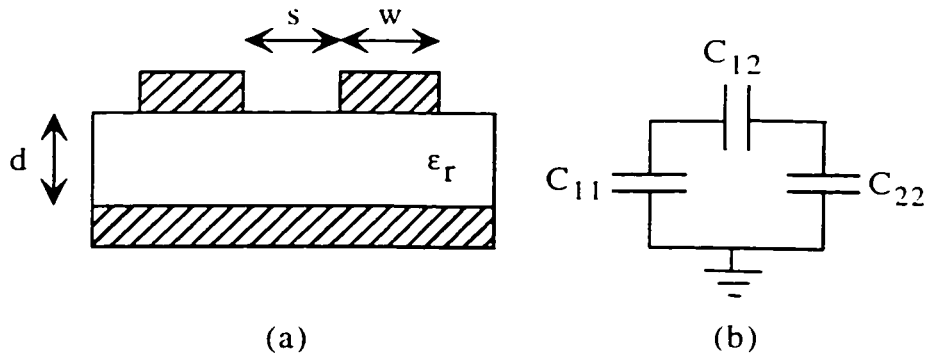


Figure 5.6. A schematic illustration of coupled microstrip lines (a), and a simple equivalent circuit (b). The lines have width w , spacing s , and are a distance d from the ground plane. They lie on a dielectric with relative permittivity, ϵ_r . C_{11} and C_{22} are the capacitances (per unit length) between each strip and the ground plane, in the absence of the other strip. C_{12} is the coupling capacitance between the adjacent strips, in the absence of the ground plane.

The adjacent lines of detectors 1 and 2 in the squid arrays (see Figure 5.3) resemble a coupled-line filter section [177]. This is illustrated schematically in Figure 5.7.

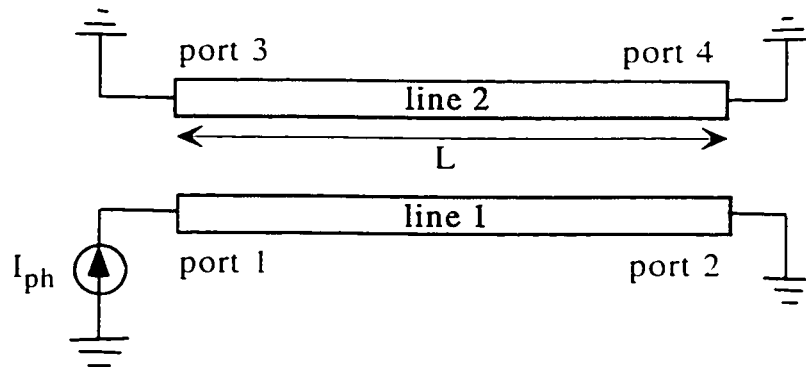


Figure 5.7. A coupled-line directional coupler model for the adjacent lines indicated in Figure 5.3. The length of the adjacent sections is L . The bias pads are connected to AC ground. The opposite end of each microstrip line is terminated by the low-impedance output section of the array.

The coupled-lines in Figure 5.7 essentially form a directional coupler [177], with a portion of the RF energy, originating in MSM #1, being coupled to each of the ports. The efficiency of coupling to the through port (Port 2) is a periodic function of frequency, as illustrated in Figure 5.8.

A coupling factor, C_C , is defined as

$$C_c = (Z_{0e} - Z_{0o}) / (Z_{0e} + Z_{0o}), \quad (5.1)$$

where Z_{0e} and Z_{0o} are the even and odd mode characteristic impedance of the coupled-line pair [177]. The magnitude of C_c is large for large values of coupling capacitance (C_{12}) between the adjacent strips. The transfer function in Figure 5.8 is periodic in the frequency domain, with periodicity determined by the electrical length. The minima occur at frequencies given by

$$f_{\min} \approx mv_{ph} / 4L, \quad (5.2)$$

where m is an integer, v_{ph} is phase velocity on the coupled-lines, and L is the length of the coupled section.

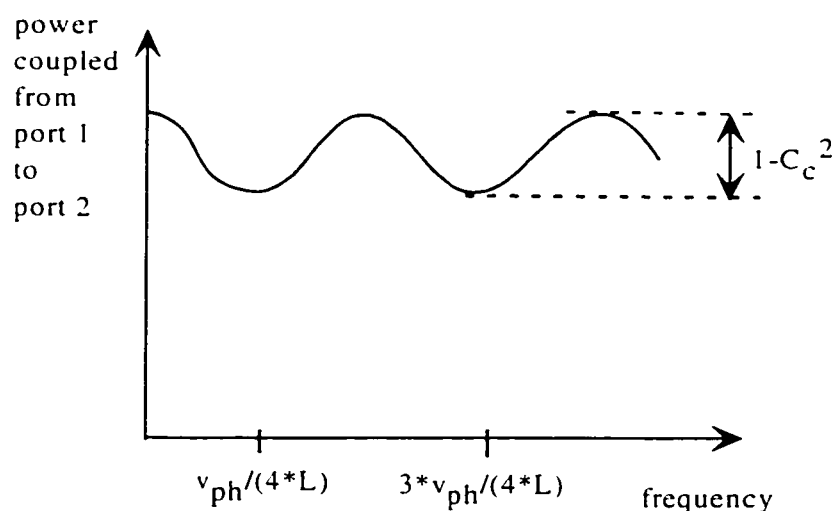


Figure 5.8. Schematic illustration of the periodic nature of power transfer in a coupled-line directional coupler. The minima occur at the frequencies shown, and are determined by the adjacent length (L) of the coupled-lines, and the phase velocity (v_{ph}).

A quantitative analysis has not been attempted, due to the approximate relationship between the coupled line model and the actual device. However, it is noted that in order to obtain reasonable agreement between Figure 5.8 and the experimental result in Figure 5.5, a very low phase velocity must be assumed for the coupled lines. Also, the level of capacitive coupling (via C_c) indicated by the result in Figure 5.5 is quite high. A low phase velocity is a characteristic of capacitively loaded lines, as discussed in Section 5.4.

These results are of a qualitative nature only, but do suggest that the long, adjacent access lines in the squid structures might result in problematic coupling effects. The complex and position-dependent characteristics observed in Figure 5.4 may reflect coupling of a particular device with both its nearest neighbors and those further removed in the array.

5.3.2. 8 detector arrays – type 1 ('goalpost' arrays)

Capacitive coupling between adjacent detectors was not evident in the results for the 8-detector arrays, contrary to the results in the preceding section. This is presumably due to the greater inter-detector spacing ($500\ \mu\text{m}$) and the shorter adjacent line sections. Still, excess capacitance does seem to be hindering the performance of these arrays. A packaged 'goalpost' array is shown in Figure 5.9.

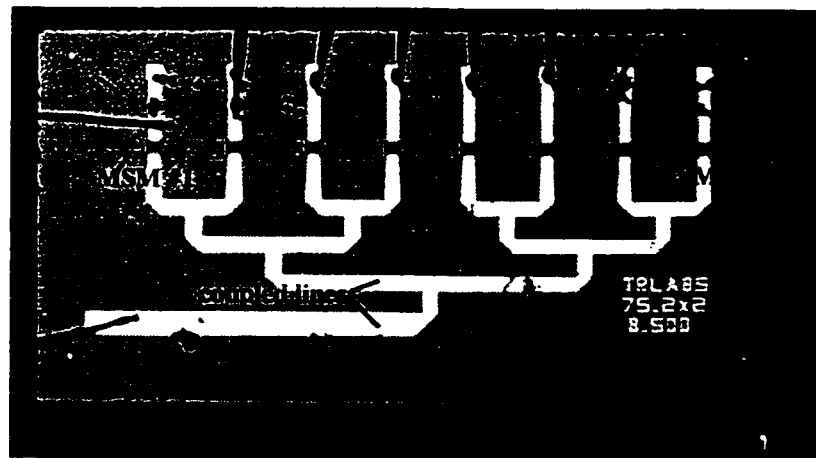


Figure 5.9. Photograph of a packaged 'goalpost' array. The bond wires appear black in the image. The MSM detectors are numbered for discussion purposes. The array contains eight MSM photodetectors, with $(75\ \mu\text{m})^2$ active regions, and a finger spacing and width of $2\ \mu\text{m}$. The inter-detector spacing is $500\ \mu\text{m}$. Asymmetric frequency responses for detectors on either side of center suggested that coupled-line effects were present at the location indicated.

As with the 'rake' array discussed in the following section, the 'goalpost' array is symmetric except for the output line. The coupling of this output line with the adjacent conductor was observed to produce a unique frequency response for detectors 1 to 4 as compared to detectors 2 to 8. Note that the output line is much

narrower than that for the 'rake' array, and it is adjacent to the neighboring metal over a shorter distance. In spite of this, the responses for 'goalpost' and 'rake' arrays exhibited similar asymmetry. This is shown in Figure 5.10.

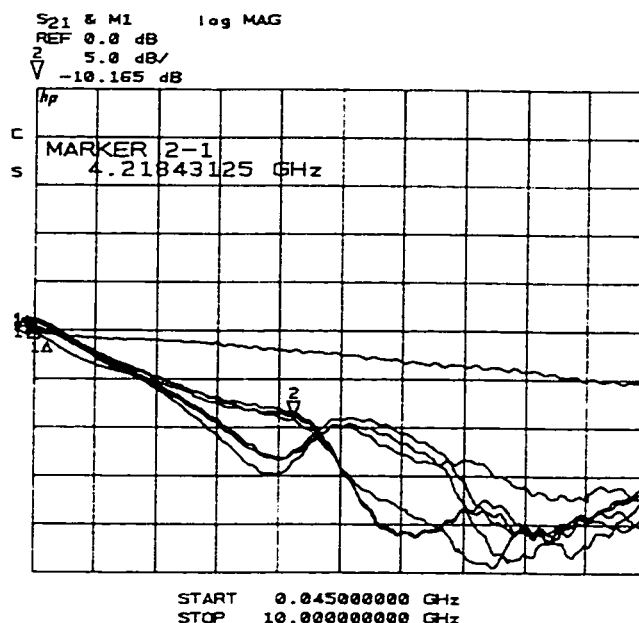


Figure 5.10. Frequency responses for several detectors in the packaged 'goalpost' array. The upper scan was for a discrete MSM detector of the same size, for reference. The lower scans revealed unique characteristics for detectors on either side of the line of symmetry, in the 'goalpost' array. The scans that are indicated by marker 2 were for detectors 2,3, and 4. The others were for detectors 5,7, and 8. The optical power was 0.8 mW, at 830 nm wavelength. The bias voltage was 10 V. See Figure 5.2 for a description of the plot format.

Note that the general trend of the frequency response provided evidence that RC effects were dominant. This was indicated by the 20 dB/decade roll-off from 1 to 10 GHz. Subsequently, the frequency response of a single detector was investigated, by successively removing the bond wires of neighboring detectors. Removing bond wires has the effect of removing the capacitance contribution of the corresponding photodetectors. The results are shown in Figure 5.11.

As with the 'rake' array below, the results generally indicate that capacitive parasitic effects dominate the frequency response of the 'goalpost' array.

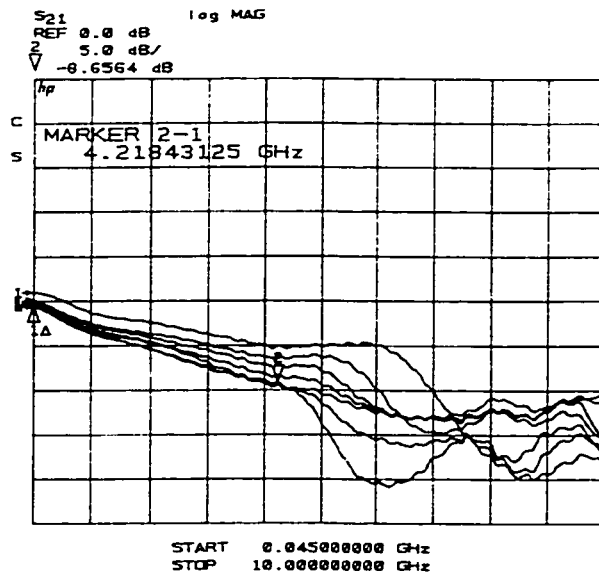


Figure 5.11. The frequency response of MSM #8 in the 'goalpost' array. The traces show decreasing roll-off in the response of MSM #8, as bond wires of the neighboring detectors (starting with MSM #7) were successively removed. The optical power was 0.8 mW, at 830 nm wavelength. MSM #8 was biased at 10 V. See Figure 5.2 for a description of the plot format.

5.3.3. 8 detector arrays –type 2 ('rake' arrays)

The results for the 'rake' arrays were very similar to those for the 'goalpost' arrays, discussed in the preceding section. Thus, the results are presented with little discussion. Figure 5.12. is a photograph of a packaged 'rake' array.

Figure 5.13 shows the frequency response for MSM #8, as bond wires are removed from the neighboring detectors. The results are similar to those observed for the 'goalpost' array.

As bond wires were removed, the RC roll-off in the response of MSM #8 decreased. With all bond wires but that of MSM #8 removed, the response is very similar to that in Figure 5.2, except for some inductive peaking near 8 GHz. This indicated that the sub-optimal results were not a result of parasitic packaging effects, but rather were inherent to the array.

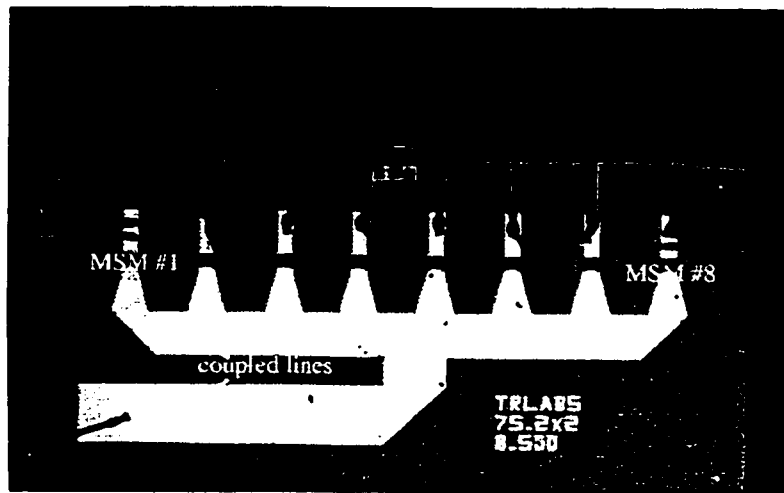


Figure 5.12. Photograph of a packaged 'rake' array. The array contains 8 MSM photodetectors, each with a $(75 \mu\text{m})^2$ active region. The detectors are numbered for discussion purposes. The location of coupled-line effects, revealed by experiment, is also indicated.

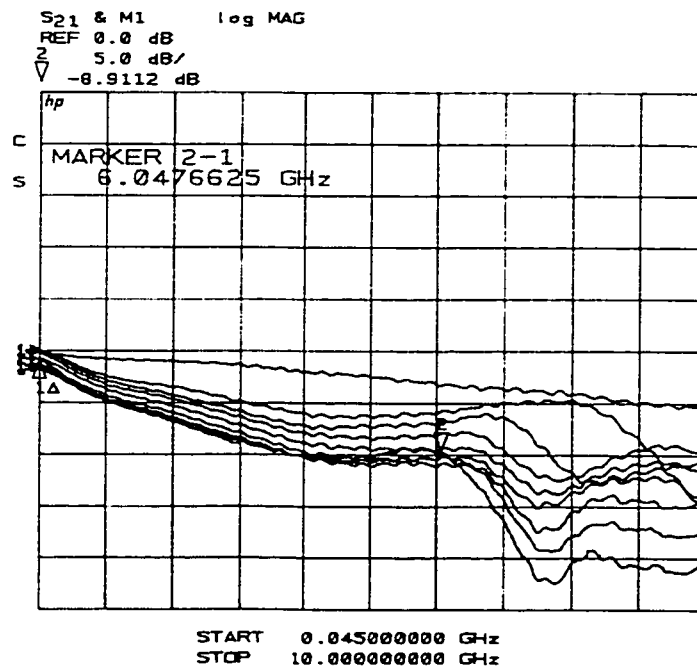


Figure 5.13. The frequency response of MSM #8 in the 'rake' array. The upper trace is the frequency response of a single isolated detector, for reference. The lower traces show decreasing roll-off in the response of MSM #8, as bond wires of the neighboring detectors (starting with MSM #7) were successively removed. The optical power was 0.8 mW, at 830 nm wavelength. MSM #8 was biased at 10 V. The plot is a screen output from a HP-8510B network analyzer. The horizontal scale is linear in frequency, starting at 45 MHz and ending at 10 GHz. The vertical scale is logarithmic, 5 dB/division.

5.3.4. Summary of results for single-output arrays

The experimental results for the single-output arrays provided consistent evidence that excess parasitic capacitance was present. Unfortunately, it is difficult to make definitive statements based on these experimental results. The arrays were fabricated on a semi-insulating surface, which is expected to reduce the effects of depletion capacitance (see Section 5.5). However, it is not clear whether the large coupling capacitance observed above is consistent with an absence of depletion capacitance. The task of obtaining a more accurate electrical model for these arrays is left for future work.

Some possible shortcomings of the model used to design these arrays [20] are as follows:

1. In the arrays, narrow access lines connect each photodetector to a large common-output section (see Figure 5.3). The access lines and the output sections were treated as microstrip sections, on an equal footing. In reality, the interface between these sections represents a huge impedance discontinuity, which probably necessitates a three-dimensional electromagnetic solution. Further, in the model the access lines from each photodetector are assumed to converge to a single point prior to interfacing the low impedance output section. In reality, this interface has a large lateral extent, with access lines distributed along the interface. Again, the electromagnetic behavior may be too complex to treat as an interface between microstrip line sections.
2. The effective capacitance between anode and cathode of an MSM is quite dependent on the attached pad or interconnect metal, as discussed in Chapter 1. In these arrays, a very large metal pad is attached to one side of each detector. This might produce a much higher parasitic capacitance than was assumed in the electrical model for the MSM detector.
3. Coupled-line effects were neglected in the model.

Broadband, planar power-combiners are of great interest generally. A fairly intensive research effort has been ongoing within the microwave devices community [178-180]. It is interesting to note that the goals of that research have generally been modest compared to what has been attempted with the photodetector arrays discussed above. For example, Maurin et al. [179] recently reported a 3-way power combiner using microstrip, operating over the 1.7 to 2.1 GHz range. In addition, the models for these devices typically incorporate a three-dimensional electromagnetic solution [178].

The long-term feasibility of such an approach for broadband photodetector arrays is not clear. It can be stated with certainty that further optimization is required. As discussed in Section 5.7, the potential advantages of using these single-output arrays, as compared to the impedance-matched detector arrays introduced in Section 5.4, may be minimal.

5.4. Impedance-Matched MSM Photodetector Arrays (IMMPA)

5.4.1. Introduction

A fundamental tradeoff exists between bandwidth and responsivity for most high-speed photodetectors, including pin and MSM detectors [16]. Around 1990, researchers began investigating novel traveling-wave photodetectors [181], to circumvent this limitation. These traveling-wave photodetectors (TWPDs) have taken various forms since, but most have been optical waveguide devices. That is, a single distributed photodetector [182] or several embedded discrete detectors [175] have been designed as part of a microwave transmission line, matched to the impedance of the external circuit, lying on a semiconductor optical waveguide. The bandwidth-responsivity tradeoff is potentially eliminated, as device speed in that case is limited only by the mismatch between optical group velocity in the waveguide and the electrical phase velocity on the transmission line. In effect, a distributed architecture is used to overcome the traditional RC bandwidth limitation in thin, large-area devices. With proper design, electrical and optical

velocities can be matched [175], potentially allowing device bandwidths of several hundred GHz.

Recently, Goldsmith et al. [174] proposed and demonstrated a similar concept, only using top-illuminated, discrete pin photodetectors. In that case, either bond wires or microstrip lines on alumina were used to provide compensating inductance for the capacitive photodetectors.

The goal of most of this previous work was to increase the power handling capability of receivers in high-power, analog fiber links. This has importance for cable TV distribution, wireless systems with fiber backbones, antenna remoting, and wide-band optical processing of microwave signals. The challenge is to coherently sum the photocurrent from several simultaneously illuminated detectors, over a multi-GHz bandwidth. Similar techniques have been employed in the design of low-voltage, high-bandwidth electro-optic modulators on III-V semiconductors [183].

These goals are entirely compatible with the requirements of photodetector arrays for optoelectronic switching and signal processing, discussed in Section 1.3. In fact, the requirements for optoelectronic switching are somewhat relaxed, as coherent summation of the signals from different photodetectors in the array is not needed. Rather, it is only required that the detectors exhibit a broad and uniform bandwidth, as they drive the output load in turns, not concurrently. In signal processing applications (Section 1.3.2) the electrical delay between detectors can be compensated, by proper tuning of the optical delay lines feeding the array [174].

In the following sections, the concept of an impedance-matched detector array is introduced. In Section 5.4.2, a lumped-element model is studied. At high frequencies, interconnect lines are not well modeled as lumped elements. Thus, in Section 5.4.3, a more accurate treatment of the photodetector array is presented, which treats the interconnecting metal as sections of high impedance transmission line (microstrip on GaAs in the cases studied here).

5.4.2. Lumped-element treatment of a photodetector array

The lumped-element approximation of an impedance-matched photodetector array is schematically illustrated in Figure 5.14. A simple RC circuit represents capacitance and high-frequency loss in the semiconductor device (MSM photodetector), while a lossy inductor represents some method of interconnection, such as bond-wires, or an on-wafer bus. If the photodetectors and bus lie on a multi-layer semiconductor, the loss terms derive mainly from the finite conductivity of the epitaxial layers. Other sources of loss at high frequency are radiation loss, and conductive loss in the metal interconnects. For frequencies well below the dielectric relaxation frequencies of the semiconductor layers ($\omega\rho_s\epsilon_s \ll 1$, where ρ_s is resistivity and ϵ_s is permittivity [184]), the reactive terms in Figure 5.14 will derive almost entirely from the particular geometry of the metal contacts and interconnect patterns. Thus, the circuit design is greatly aided by highly resistive semiconductor layers, as this minimizes spurious losses and facilitates the accurate prediction of imaginary impedance components.

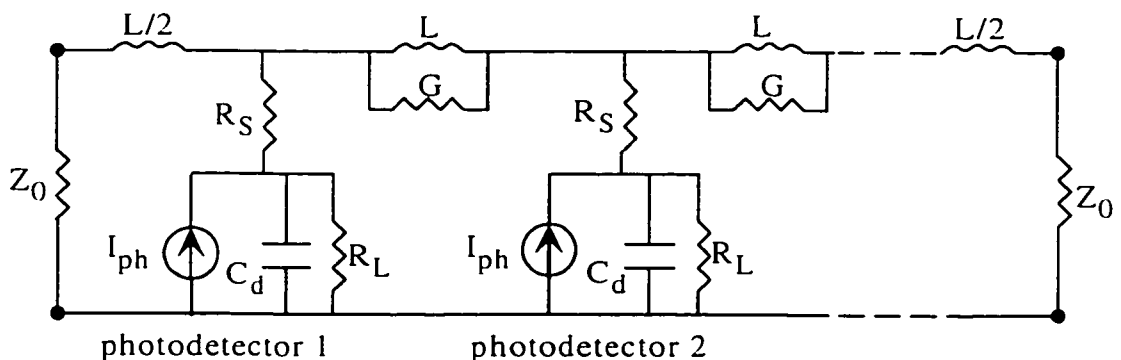


Figure 5.14. A lumped-element representation of an array of photodetectors, such as in Figure 5.1. A simple equivalent circuit is used for the photodetector, including the capacitance and resistive losses associated with the device. For MSM photodetectors, R_S is generally the series resistance associated with the thin metal fingers, and R_L is the conductive loss associated with free and interfacial charge in the epitaxial layers. C_d is the total capacitance associated with each photodetector. Adjacent photodetectors are interconnected by a conductive element with high AC impedance, modeled simply as an inductor with some associated loss. Each end of the array is terminated in the system impedance.

Of course, Figure 5.14 is very nearly the lumped-element representation of a lossy transmission line. Typical values are, as confirmed below, R_S of a few ohms, R_L in the $M\Omega$ range, C in the fF range, and L in the nH range. It is somewhat more difficult to predict the transverse conductance, G . It is quite dependent on the epitaxy, if the interconnect is a planar line on a semiconductor substrate. Generally speaking, G should be minimized, as discussed in Section 5.6. This may be accomplished by etching down to a semi-insulating substrate before depositing the metal interconnect layer of the array. Over a wide frequency range ($\omega \ll 1/RC$, $\omega \ll 1/GL$ [182]), the complex propagation constant of such a line is well approximated by [184]

$$\gamma = \alpha + j\beta \approx \frac{\omega^2}{2v_c} (R_S C_d + GL) + j \frac{\omega}{v_c} , \quad (5.3)$$

where v_c is the phase velocity, and R_L is assumed to be negligibly large. The characteristic impedance of the artificial line is then given by

$$Z_A \approx \sqrt{L/C_d} \{1 + j(\omega/2)(R_S C_d - GL)\} . \quad (5.4)$$

For the case of negligible loss components, the characteristic impedance reduces to the familiar result for a loss-free line,

$$Z_A = \sqrt{L/C_d} . \quad (5.5)$$

The line is termed artificial since the dominant capacitive and inductive contributions are not truly distributed, but are instead spatially periodic. Each section in the artificial line, consisting of two inductive elements sandwiching a single detector capacitance, resembles a constant- k filter section [177]. The cutoff frequency for such a network (neglecting loss terms) is

$$f_c = \frac{1}{\pi \sqrt{LC_d}} . \quad (5.6)$$

For frequencies well below cutoff, the electrical propagation delay, τ_c , of a single filter section, is given nominally by

$$\tau_c = \sqrt{LC_d} . \quad (5.7)$$

This theory is most valid for a fully distributed traveling-wave photodetector [182], where the circuit components in Figure 5.14 represent values per unit length. In the periodic traveling-wave photodetector array [174],[175], where several discrete photodetectors are embedded in an electrical transmission line, care must be taken to ensure that at the frequencies of interest, the lumped-element approximation is valid. For example, for inter-detector spacing of 250 μm (see Figure 5.19), the strip-line interconnecting devices has length comparable to millimeter-wavelength signals, and is not necessarily well modeled as a lumped-element inductor. This can lead to non-physical estimates for some of the parameters above, such as an electrical delay that suggests propagation faster than the speed of light.

5.4.3. Semi-distributed treatment of a photodetector array

5.4.3.1. Periodic structures

At very high frequencies, the photodetector array is more accurately treated using a semi-distributed model. The individual photodetectors, which have dimensions on the order of tens of μm , are still treated using a lumped-element approximation. Lumped-element models are very accurate for typical MSM photodetectors, up to at least 100 GHz [42]. However, the common-bus of the array is typically several hundred μm in length between adjacent detectors, and is not accurately treated as a lumped-element inductor for frequencies greater than a few GHz. Also, the common-bus will typically have both distributed inductance and capacitance, characteristic of a high-impedance transmission line. This is certainly true of the arrays discussed in the following, for which the common bus is essentially a microstrip line on a semiconductor.

A transmission line periodically loaded with reactive elements is commonly termed a periodic structure [177]. Given the discussion in the previous paragraph, the photodetector array is essentially a periodically loaded, high-impedance transmission line. The reactive loads are photodetectors, which to first

order may be modeled as capacitors. Thus, the theory of periodic structures is applicable to understanding the broadband characteristics of a common-bus photodetector array.

A portion of an MSM photodetector array is shown schematically in Figure 5.15. (a). Figure 5.15. (b) illustrates the relevant loaded-line equivalent circuit. Note that losses are neglected initially, to simplify the analysis.

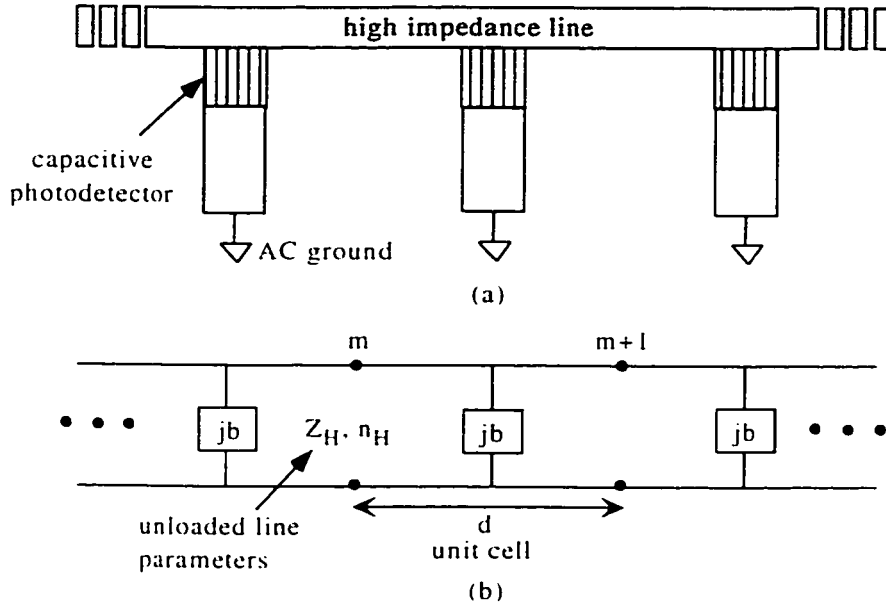


Figure 5.15. (a). A portion of a common-bus MSM photodetector array. The bus is equivalent to a high impedance microstrip line. The MSM detectors, to first order, are capacitive loads, periodically spaced along the line. (b). An equivalent circuit for the periodically loaded line. The unloaded microstrip line has impedance Z_H , and effective propagation index n_H . The susceptance of the photodetector loads is b .

The loaded line can be treated as a cascaded series of identical two-port networks. Each unit cell is comprised of a transmission line section, of length $d/2$, followed by a shunt susceptance, jb , followed by another transmission line section of length $d/2$. The ABCD matrix relates the voltage and current on either side of the unit cell as

$$\begin{bmatrix} V_m \\ I_m \end{bmatrix} = \begin{bmatrix} A & B \\ C & D \end{bmatrix} \begin{bmatrix} V_{m+1} \\ I_{m+1} \end{bmatrix}. \quad (5.8)$$

For the unit cell in Figure 5.15, the ABCD matrix is [184],

$$\begin{bmatrix} \cos \theta - \left(\frac{jbZ_H}{2} \right) \sin \theta & jZ_H \left(\sin \theta + \left(\frac{bZ_H}{2} \right) (\cos \theta - 1) \right) \\ \frac{j}{Z_H} \left(\sin \theta + \left(\frac{bZ_H}{2} \right) (\cos \theta + 1) \right) & \cos \theta - \left(\frac{jbZ_H}{2} \right) \sin \theta \end{bmatrix}. \quad (5.9)$$

In (5.9), $\theta = k_H d$ is the electrical length of an unloaded unit cell. For wave propagation on the loaded line, general solutions are given as

$$\begin{aligned} V(z) &= V(0) \exp(-\gamma z) \\ I(z) &= I(0) \exp(-\gamma z) \end{aligned} \quad (5.10)$$

where γ is a propagation constant for the loaded line. If the line is infinite in length, periodic boundary conditions can be used to obtain a solution. This is identical to the Bloch-theorem treatment of electron wave propagation in solid crystals. The periodic boundary conditions are

$$\begin{aligned} V_{m+1} &= V_m \exp(-\gamma d) \\ I_{m+1} &= I_m \exp(-\gamma d) \end{aligned} \quad (5.11)$$

Equation (5.11) is the mathematical statement of the fact that two points, m and $m+1$, are indistinguishable in the infinite periodic structure. In other words, any wave solution on the loaded line will reflect its periodic nature.

Inserting (5.11) into (5.9) yields, with some manipulation [177],

$$\cosh(\gamma d) = \cos \theta - (bZ_H / 2) \sin \theta. \quad (5.12)$$

Generally, $\gamma = \alpha + j\beta$. However, since a lossless high impedance line is assumed (θ is real), the right hand side of (5.12) is real. Thus, for (5.12) to be satisfied requires either $\alpha = 0$ or $\beta = 0$. Clearly, the case of $\beta = 0$ describes a non-propagating wave, and therefore defines the stop bands of the loaded line. In those cases, the attenuation (α) is due to constructively interfering reflections at each unit cell. It cannot represent power dissipation, since lossless elements have been assumed. This is exactly analogous to the stop bands of the quarter wave stack reflectors discussed in Chapter 4. It is also analogous to the formation of energy band gaps in solid crystals, as mentioned above. The band gap is a range of electron energy (frequency) for which propagation in the crystal is not possible.

Of more relevance to the photodetector array are the pass bands of the loaded line structure. In this case, $\alpha=0$, and (5.12) reduces to

$$\cos(\beta d) = \cos\theta - (bZ_H/2)\sin\theta, \quad (5.13)$$

which is the dispersion relation for wave propagation on the loaded line.

A characteristic impedance (often termed the Bloch impedance) can be defined for the loaded line, as [184]

$$Z_B = V_m/I_m = (B/C)^{1/2}, \quad (5.14)$$

where B and C are taken from the ABCD matrix, (5.9). For pass band frequencies, Z_B is a real quantity. In the following section, matched termination of the periodic structure is discussed.

5.4.3.2. Termination of periodic structures

In the previous sub-section, an analogy was drawn between a photodetector array and a periodically loaded transmission line. The theory for infinite periodic structures was discussed. Clearly, a real photodetector array will not be infinite in length, but must interface to an external system, as shown in Figure 5.1. In this sub-section, the matching conditions for the periodic structure are developed. These specify the conditions for zero reflection at the terminated ends of the photodetector array, which is the main requirement for broadband operation.

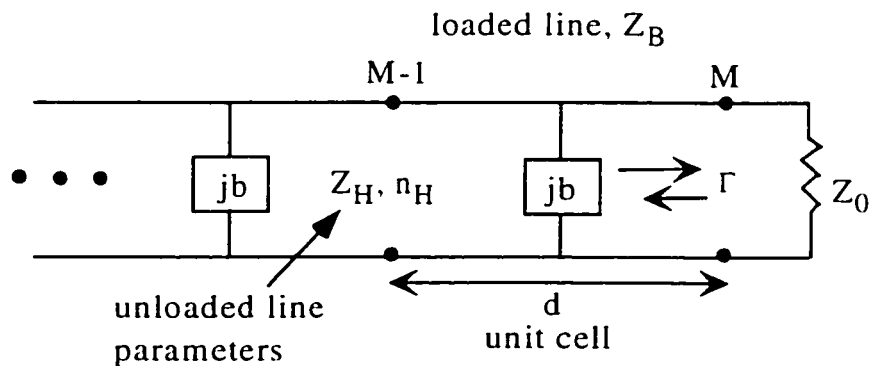


Figure 5.16. A periodically loaded transmission line, terminated by an external system impedance, Z_0 . Γ is the reflection coefficient at the load.

The situation at one end of the photodetector array is illustrated schematically in Figure 5.16. As it turns out, the matching conditions for the loaded line are identical to those of an unloaded line, but with the characteristic impedance given by (5.14). Thus, for zero reflection at the load

$$Z_0 = \left(\frac{B}{C}\right)^{1/2}, \quad (5.15)$$

where B and C are from the ABCD matrix, (5.9). Since B and C are functions of electrical length, and therefore frequency, it is not possible to match the loaded line over an arbitrary range of frequency. However, as demonstrated in Section 5.4.4, the periodic structure is very nearly dispersionless up to its nominal cutoff frequency, given by (5.6).

Generally, $\lambda \gg d$ on the common bus, where λ is wavelength and d is the inter-detector spacing. This can be verified from the experimental numbers discussed in the following sections. In this case, $\cos(\theta) \sim 1$, and $\sin(\theta) \sim \theta$, and (5.15) simplifies to

$$\frac{Z_0^2}{Z_H^2} \approx \frac{\theta}{bZ_L + \theta}. \quad (5.16)$$

Several useful expressions can be derived from (5.16). If photodetector capacitance and the impedance properties of the interconnecting bus are fixed, the inter-detector spacing required for matching to an external system, Z_0 , is given by

$$d_H = \frac{cZ_H C_d}{\left[\frac{Z_H^2}{Z_0^2} - 1\right]n_H}. \quad (5.17)$$

Equation (5.17) was derived previously by Goldsmith et al. [174], by replacing the high impedance transmission line sections between detectors with a pi-equivalent circuit. Thus, in the simplifications used to obtain (5.17), a return to a lumped-element model is implicit. However, it is more accurate than the lumped element model described in Section 5.4.2, since now both the capacitive and inductive contributions of the high-impedance line are included.

Assuming the matching condition is satisfied, the effective propagation index on the terminated periodic structure is

$$n_{eff} = \frac{Z_H n_H}{Z_0} . \quad (5.18)$$

Also, the electrical propagation delay between adjacent detectors is given by

$$\tau_e = \frac{Z_H^2 C_d}{\left[\frac{Z_H^2}{Z_0^2} - 1 \right] Z_0} , \quad (5.19)$$

and the cutoff frequency for propagating waves is

$$f_c = \frac{1}{Z_0 \pi C_d} \left[1 - \frac{Z_0^2}{Z_H^2} \right] = \frac{1}{\pi \tau_e} . \quad (5.20)$$

These results indicate that maximizing Z_H increases the cutoff frequency of the artificial line, but also produces a lower phase velocity on the structure. Some of the implications of this are discussed in the following sections. From (5.18), it is obvious that the photodetector array will tend to be a slow-wave structure, with phase velocity much less than the speed of light in vacuum.

5.4.4. Properties of microstrip transmission lines on III-V semiconductors

The common bus of an MSM photodetector array has generally been a planar conducting strip [4],[20], as in Figure 5.1. This type of array was used here to experimentally verify traveling-wave concepts, as discussed in the following sections. The common bus is most conveniently modeled as a microstrip line, assuming that the array chip is mounted on a ground plane. In this section, some basic properties of microstrip are reviewed.

Microstrip is perhaps the most commonly used planar transmission line, although coplanar waveguide and others are increasingly popular [177]. The basic geometry of microstrip line is illustrated schematically in Figure 5.17.

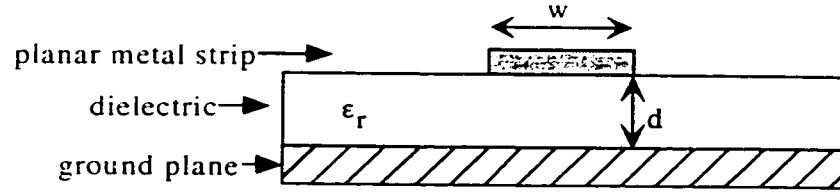


Figure 5.17. Microstrip transmission line in cross-section. In general, ϵ_r is complex, accounting for dielectric loss. If the 'dielectric' is a semiconductor, conductivity is the primary source of loss.

Purely TEM waves do not propagate on microstrip, due to the dielectric discontinuity at the surface. In most cases, however, the dielectric substrate is electrically thin ($d \ll \lambda$). This allows a quasi-TEM analysis, the results of which are available in many standard reference texts [177],[184]. The phase velocity and propagation constant are given by

$$v_H = \frac{c}{n_H} \quad , \quad (5.21)$$

$$k_H = k_0 n_H \quad .$$

where k_0 is the free-space propagation constant and n_H is the effective propagation index. The subscripts denote high impedance line, and are used for consistency with the discussion in Section 5.4.3.

The effective propagation index is the square root of the effective dielectric constant, which is approximated by

$$\epsilon_H = \frac{\epsilon_r + 1}{2} + \left(\frac{\epsilon_r - 1}{2} \right) \left(\frac{1}{\sqrt{1 + 12d/w}} \right) \quad . \quad (5.22)$$

The characteristic impedance of the non-loaded microstrip line can also be approximated empirically, as

$$Z_H = \frac{60}{n_H} \ln \left(\frac{8d}{w} + \frac{w}{4d} \right) \quad . \quad (5.23)$$

In the following section, the common bus is modeled as a dispersion-free microstrip line. The dispersive properties of microstrip are discussed in reference [184]. For the microstrip geometry discussed below, the assumption of zero dispersion is a very good one, even at the highest frequencies studied.

In Section 5.6, the maximum length of a traveling-wave detector array is considered. Essentially, the length of an array is limited by the maximum tolerable attenuation from one end to the other. Besides resistive losses in the photodetectors, the dominant sources of attenuation are the inherent microstrip losses along the common bus. Planar transmission lines generally exhibit three types of loss: dielectric loss related to bound and free charges in the substrate media, conductor loss due to finite conductivity of the metal guides, and radiation loss. Radiation loss is negligible at the frequencies of interest here, since wavelengths are longer than bus. The attenuation constant due to dielectric loss along the guide may be approximated by [177]

$$\alpha_d = \frac{k_0 \epsilon_r (\epsilon_{II} - 1) \tan \delta}{2 \sqrt{\epsilon_{II} (\epsilon_r - 1)}} [Np/m], \quad (5.24)$$

where k_0 is the free-space propagation constant, and $(\tan \delta)$ is the loss tangent of the dielectric. An approximation for conductor loss is

$$\alpha_c = \frac{R_s}{Z_{II} w} [Np/m], \quad (5.25)$$

where R_s is the surface resistivity of the conductor. Both dielectric and conductor losses can be significant for microstrip lines on a semiconductor.

For a general media, the loss tangent is given by

$$\tan \delta = \frac{\omega \epsilon'' + \sigma}{\omega \epsilon'} . \quad (5.26)$$

In a semiconductor, the conductive term dominates. Thus, a semiconductor is treated as a conductor at low frequencies, and as a low-loss dielectric for frequencies greater than σ/ϵ' . Low frequency (static) values for conductivity and permittivity are appropriate in the microwave region.

5.5. Experimental Results –Impedance-Matched Detector Arrays

5.5.1. *Selecting an appropriate array*

To verify the concepts discussed in the previous section, a preliminary study was conducted using existing MSM photodetector arrays, configured as 8 or 16 photodetectors attached to a simple microstrip line (common bus) on a GaAs chip. Preliminary results for these devices were reported previously [4],[20].

Initially, the capacitance of detectors in the various arrays was studied. The goal was to determine whether any available detectors exhibited appropriate capacitance to compensate the inductance of the interconnecting bus, and provide a reasonably close impedance match in a 50 ohm system. As discussed below, the interconnect inductance between adjacent detectors (L in Figure 5.14) is typically 0.1-0.12 nH. Thus, from the discussion in the previous section, a capacitance of approximately 50 fF is required for each detector in the array, in order to match the array to a 50 Ω system.

From the discussion in Section 1.6, the capacitance of devices in the array is dependent on several factors, including the attached interconnect and pad metal, and the particular details of the underlying epitaxy. Many of the available arrays contained MSM detectors with $(76 \mu\text{m})^2$ or $(100 \mu\text{m})^2$ active regions. The simple, geometric capacitance estimates [44] for the active region of these devices is in the 50-100 fF range. However, keeping in mind the sources of excess capacitance, these values were expected to represent only a half to a third of the real capacitance. This was verified experimentally by probing individual devices in these arrays and measuring their S_{22} parameters. Figure 5.18 is a simplified equivalent circuit for the MSM detector in this instance. By measuring capacitance at relatively low frequencies (<5 GHz), it is ensured that any inductive impedance associated with the attached array is negligible.

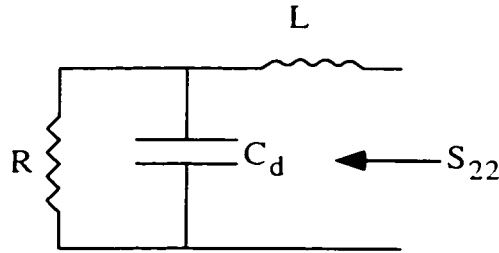


Figure 5.18. Simplified equivalent circuit for an individual detector in an array. The devices are probed between the common bus and their bias pad. The measured capacitance is approximately the entire amount attributable to that detector. In a wire-bonded array, there may be an additional small component due to adjacent bias pads. The inductance is due primarily to the extended metal patterns attached to each side of a detector, see Figure 5.19.

If the epitaxial layers are highly insulating, the resistive losses due to free charge motions in the semiconductor will be small, and the S_{22} parameter will be that of a reasonably ideal capacitor, revealing the sum capacitance of the MSM fingers and the pad and interconnect metal.

Using these techniques the measured capacitance for the $(72 \mu\text{m})^2$ and $(100 \mu\text{m})^2$ detectors was consistently in the 100-200 fF range, consistent with previous reports [20]. Apparently, the arrays are characterized by bond pad and interconnect capacitance that is much greater than the geometrical capacitance associated with the MSM active region. Thus, to properly design an impedance-matched photodetector array in the future, a numerical solution of the capacitance associated with all metal patterns will be required. It is also recommended that these arrays lie on highly insulating layers, to negate the effects of excess depletion capacitance, which can be difficult to predict in advance.

By good fortune, arrays of smaller MSM photodetectors, with similar interconnect patterns, were also available. Figure 5.19 illustrates the layout of the arrays used to obtain the results discussed in the following sub-section. They were fabricated on a nominally doped GaAs epitaxial layer by the Communications Research Center in Ottawa (CRC fabrication run # 94R14, on Sumitomo S.I. GaAs substrate, # 2984-1B). The epitaxial material was guaranteed by the manufacturer to have free electron concentration less than 10^{14} cm^{-3} .

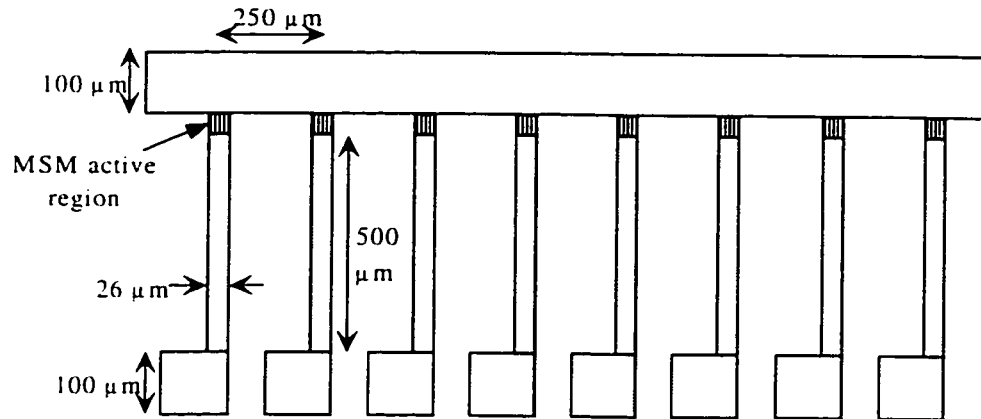


Figure 5.19. Layout of the photodetector array used to demonstrate impedance-matched photodetector concepts. The MSM detectors have active regions of $(26 \mu\text{m})^2$, finger width and spacing of $2 \mu\text{m}$. The arrays lie on a semi-insulating GaAs substrate. Arrays of eight and sixteen photodetectors were studied.

As shown, the devices have active regions of $(26 \mu\text{m})^2$. The finger spacing and width is $2 \mu\text{m}$, and the individual detectors are attached to a $100 \mu\text{m}$ wide bus, with an inter-detector spacing of $250 \mu\text{m}$. Note that the metal trace connecting each MSM to its bias pad is only $26 \mu\text{m}$ wide. The small device active area and the narrow interconnect are both believed to contribute to the required reduction in capacitance, over that for the larger devices. For a $(26 \mu\text{m})^2$ device with $2 \mu\text{m}$ finger spacing, the geometrical capacitance associated with the active region is estimated as 10 fF . Figure 5.20 shows a measured S_{22} characteristic for one of the $(26 \mu\text{m})^2$ devices, in the array. The advantage of resistive layers was apparent in these measurements. The S_{22} characteristic followed the outer circle (nearly lossless) of the Smith Chart, which allowed easy derivation of capacitance from the equivalent circuit.

The derived capacitance estimate was 49 fF , and was found to be independent of bias and frequency. Thus, the capacitance was believed to derive primarily from interconnect metal. Measurements on several similar devices consistently produced estimates in the $40\text{-}60 \text{ fF}$ range. Unfortunately, on-wafer calibration standards were not available for the ground-signal microwave probe used to obtain the results. Rather, the system was calibrated with a similar ground-signal-ground probe, and an assumption of equal electrical length for the two

probes was necessary. This is reflected in the scatter in measured capacitance. Appropriate calibration standards are critical for accurate determination of equivalent circuit component values, especially when the impedance values are small.

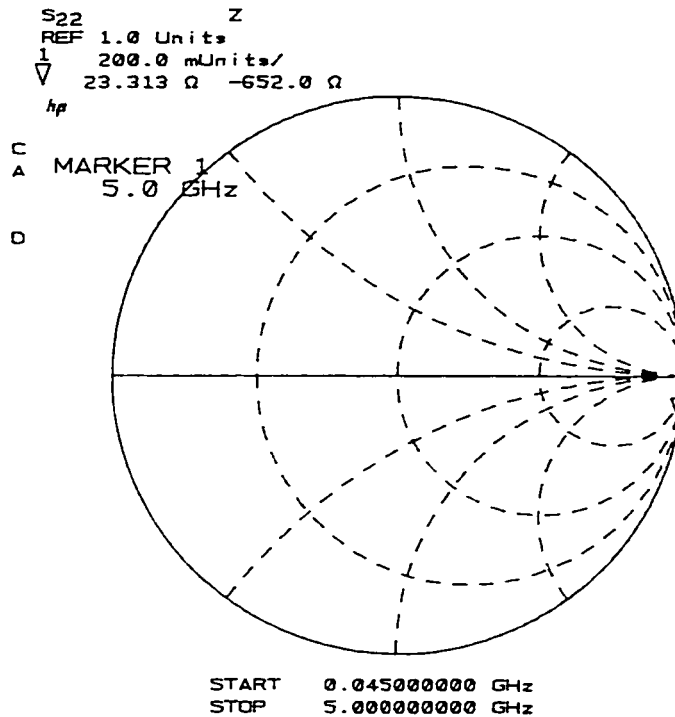


Figure 5.20. Experimental S_{22} characteristic for one of the detectors in the array of Figure 5.19. The trace lies very close to the open-circuit point on the Smith-chart, indicating the device has very low capacitance and negligible resistive loss. Reflection measurements were made over the frequency range 45 MHz to 5 GHz. The marker indicates that the device impedance at 5 GHz ($23.3-j652 \Omega$) is almost completely reactive, and corresponds to a capacitance of approximately 49 fF. The measured capacitance was not bias-dependent.

The common bus in Figure 5.19 is essentially a high-impedance transmission line, as discussed in Section 5.4. The characteristics of the bus are dependent on the presence or absence of a ground plane beneath the GaAs chip. If the ground plane is present, the bus is modeled as a microstrip line, using the theory in Section 5.4.3. The line is 100 μm wide, and the GaAs chips are approximately 500 μm thick. From (5.21) to (5.23), with a dielectric constant of 12.9, the impedance of this microstrip line is estimated as 80 Ω and the effective propagation index is 2.78. With these high-impedance line parameters, and

recalling the inter-detector spacing of 250 μm , (5.17) indicates that a detector capacitance of 45 fF is required for matching to a 50 Ω external system. This is very close to the measured capacitance, Figure 5.20.

If the chip is mounted on insulating material, so that no ground plane is present, then the bus is more accurately treated as an inductive element. For a flat-wire inductor [10], the inductance at high frequency is given empirically by

$$L = 0.002 \cdot l \cdot \left[\ln\left(\frac{2l}{W+t}\right) + 0.5 + 0.2235\left(\frac{W+t}{l}\right) \right] , \quad (5.27)$$

where l , W , and t are the length, width and thickness of the flat conductor in cm, L is in μH , and non-magnetic media are assumed. For the metal trace here, t is negligible ($<1 \mu\text{m}$) relative to W and l , and (5.27) produces an estimate of 0.11 nH, for the effective inductance between adjacent photodetectors. From (5.5), this implies that the required detector capacitance for a 50 Ω match is 44 fF. The agreement between this value and the one derived above is somewhat coincidental, and not a general rule. Still, the conclusion is that, for these particular arrays, a reasonably good match is expected with or without a ground plane beneath the chip.

Assuming perfect matching ($C_d=45$ fF), the loaded-line characteristics of the detector array can be estimated using the theory described in Section 5.4.3. From (5.18), the effective propagation index is 4.45, which corresponds to a slow-wave velocity of $0.22c$, where c is the speed of light in vacuum. Further, (5.19) and (5.20) predict that the propagation delay between adjacent devices will be 3.7 ps, and that the fundamental pass-band of the loaded-line will exhibit a cutoff frequency of 86 GHz.

These approximations can be verified by direct numerical solution of the dispersion relation, (5.13). Figure 5.21 is a k - β diagram for the loaded line, given the high-impedance line and photodetector parameters discussed above.

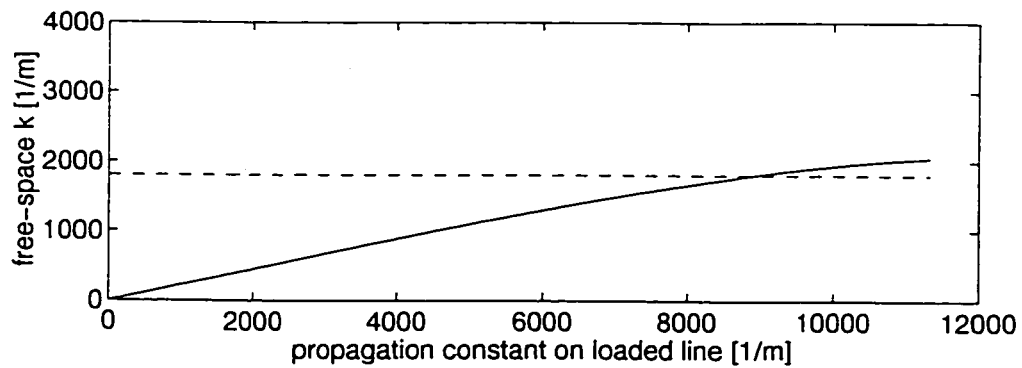


Figure 5.21. The solid line shows free-space propagation constant vs. loaded-line propagation constant (k - β relationship), predicted for the detector array described in this section. The dashed line is the nominal cutoff propagation constant, as determined from (5.20). The dotted line is for propagation at the speed of light, for reference.

Figure 5.21 illustrates the slow-wave property of the photodetector array, and the phase velocity is in good agreement with the estimate above. Propagation on the structure is very nearly dispersionless, up to the nominal cutoff frequency. To further illustrate, phase velocity on the loaded-line is plotted as a function of frequency in Figure 5.22.

Given this analysis, it was expected that broadband performance might be achieved with the array in Figure 5.19, if properly terminated in 50Ω at both ends of the common bus. The results of these experiments are described in the following sections.

It is important to note that several physical mechanisms will contribute to the ultimate speed attainable for an array of photodetectors. Most fundamental is the transit-time limitation for each device, as discussed in Chapters 1 to 3. The cutoff frequency discussed above does not imply an expected bandwidth, but rather is an estimate of the maximum frequency which can be supported by the artificial line without distortion.

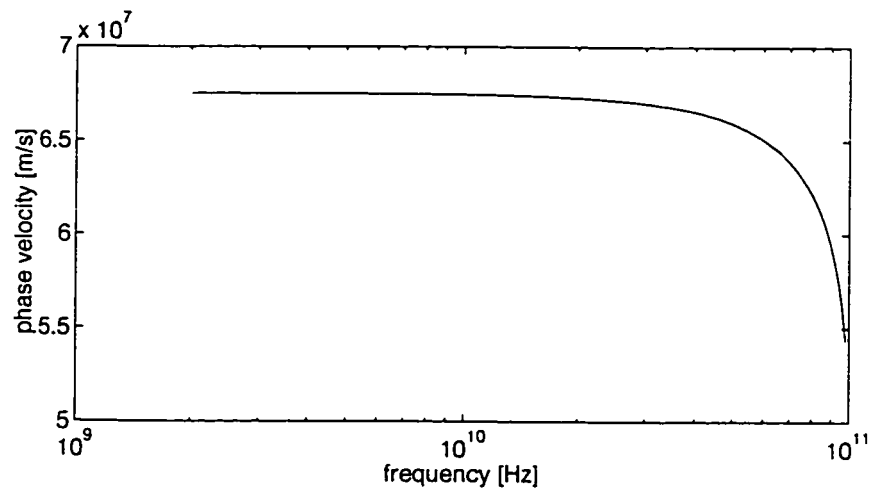


Figure 5.22. The predicted phase velocity on the detector array, as a function of frequency. The loaded-line is very nearly free of dispersion up to the nominal cutoff frequency, 86 GHz.

5.5.2. Experimental results – 16 detector array

To verify the analysis in 5.5.1, several 16-detector arrays were mounted on glass RF substrates [185], with coplanar waveguide access lines at each end of the array bus. A photograph of a mounted array is shown in Figure 5.23.

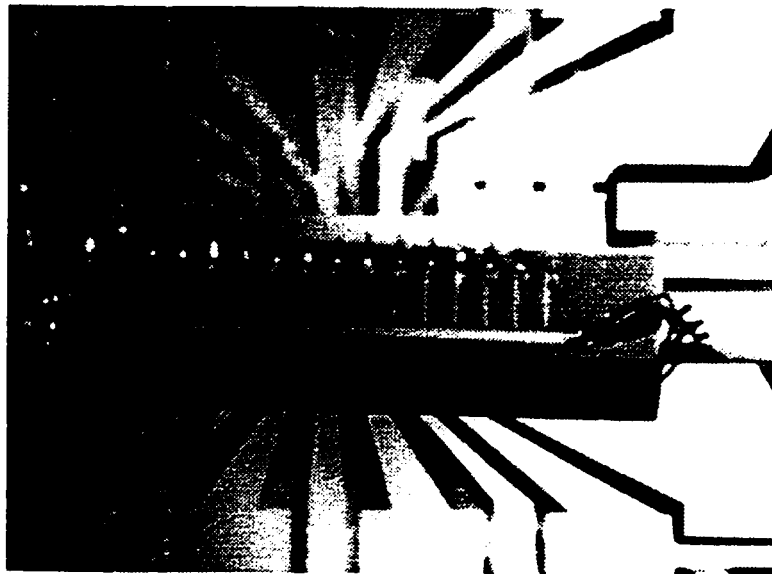


Figure 5.23. A photograph of a packaged, 16-detector array is shown. A 47Ω chip resistor (not visible) terminated one end of the common bus, while the other end interfaced to a 50Ω system. Multiple bond wires were used to connect each end of the bus to coplanar waveguide lines on the RF substrate. A single bond wire connected each detector's bias pad to the ground plane on the RF substrate.

These substrates allowed each end of the bus to be terminated, as required. One end was terminated by a 47Ω chip resistor on the glass substrate. Unfortunately, the coplanar waveguide housing the termination resistor was not designed to be 50Ω [185]. Experiments with a similar 8-detector array, Section 5.5.3, indicated that it is very important that each end of the bus be properly terminated, to reduce spurious features in the 6 to 16 GHz range. Also, the chip lay on a discontinuous ground plane, as the chip carrier was designed for a different application [185]. This may have affected the impedance match.

Each end of the bus was connected to the coplanar waveguide on the RF substrate using multiple bond wires, in an effort to approximate the required inductance ($L/2 \sim 0.05 \text{ nH}$) at the ends of the artificial transmission line. The bond wires were approximately 1 mm in length, implying an inductance of approximately 0.6 nH [10]. Unfortunately, it was not possible to fit 12 parallel bond wires at each end of the bus, due to pad size limitations, so the required matching inductance could not be achieved. Typically, 3 bond wires were placed at each end, implying 0.2 nH inductance. It is likely that the high inductance associated with these bond wires contributed to the lower than expected return loss measured, below. It should also be noted that it is not generally reliable to use bond wires as inductive elements in networks operating beyond a few GHz [174]. In future designs, it is recommended that bond wires be minimized or eliminated. An extremely short and wide bond-ribbon at each end of the bus would be superior, as would flip-chip bonding techniques [185].

As shown in figure 5.23, the bias pads of all detectors were wire-bonded directly to the ground plane on the RF substrate, to simplify the testing procedure. This required that all detectors were biased simultaneously through an internal bias-tee in the test equipment. From the discussion in Section 1.6, this has implications in terms of device capacitance. However, as mentioned above, measured capacitance was bias-independent for detectors on the wafer in question. This reflected the highly resistive nature of the epitaxial material.

In practice, each detector would be connected to a bias-decoupling network. The design of this decoupling network is separate from the problem addressed here, which is the matching of the array of photodetectors to a 50 Ω system at each end of the bus.

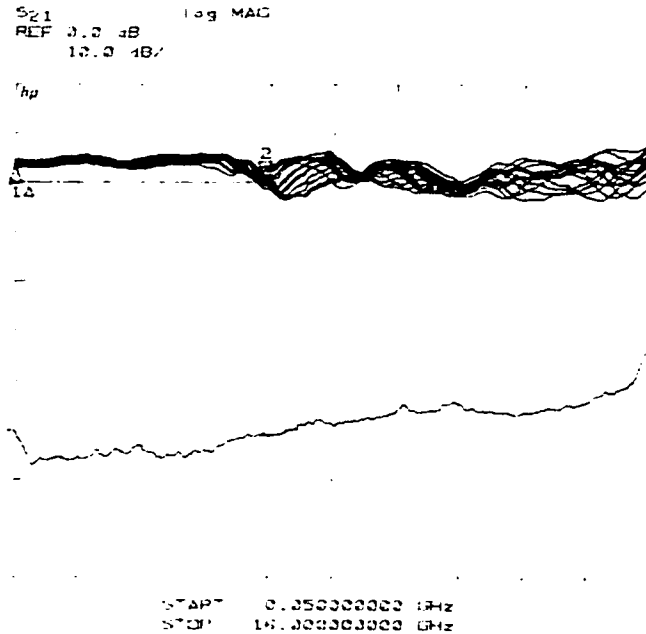


Figure 5.24. The upper scans are the frequency response of all 16 detectors, for the array in Figure 5.23. The lower scan indicates the noise floor of the test system. Good response uniformity was observed up to the measured 3 dB bandwidth, 6.5 GHz, which is indicated by the markers. Pass-band ripple and position-dependence were observed in the 6 to 16 GHz range. The plot is the screen output of a HP-8510B network analyzer (see Figure 5.2).

Figure 5.24 shows the frequency response of all 16 detectors in an array. The single lower trace is the noise floor of the measurement system, for reference. Excellent response uniformity was obtained up to approximately 6.5 GHz, which also represents the -3 dB bandwidth. Even beyond 6.5 GHz, the amplitude of the ripple in device response was less than approximately 5-6 dB, indicating that minimal RC roll-off was present. Rather, an imperfect impedance match, and non-optimized terminations (as discussed above), are responsible for the spurious features above 6 GHz. A consistent positional dependence was observed for several arrays, with detectors closest to the 50 Ω load exhibiting a slight rise in response at the highest frequencies. This was probably consistent with the high

inductance of the output bond wires, which for the close detectors is not mediated by a long length of matched artificial line. Also, detectors furthest from the load were attenuated by propagation along the bus, as discussed in Section 5.6.

This result compared well to the best previous report for a common-bus photodetector array, with individual bias pads. Liu et al. [172] reported 5 GHz bandwidth for an array of four p-i-n photodetectors, but did not provide details on response uniformity.

Still, from the analysis in Section 5.5.1, it was expected that a flatter, more uniform response might be possible in the frequency range above 6 GHz. As mentioned, the coplanar waveguide at the terminated end of the array was not designed to be $50\ \Omega$, for the substrates used here. While the distance between the array chip and the termination resistor was quite short, it seemed likely that this imperfect termination could produce spurious features at the higher frequencies. Also, at the time of testing, $50\ \Omega$ chip resistors were not available and $47\ \Omega$ resistors were used instead. Finally, the available broadband probes were not compatible with the waveguide at the terminated end of the array. As a result, a calibrated $50\ \Omega$ load could not be attached in place of the chip resistor.

The results for the eight detector arrays, discussed in the following section, were superior. This was thought to reflect the improved termination of the array in that case, and not its reduced length.

5.5.3. Experimental results – 8-detector arrays

Based on the promising results in the preceding section, similar arrays of 8 photodetectors were mounted on an alumina substrate for testing. Unlike the glass substrate used for the devices in the preceding section, the alumina substrates contained a pair of identical, $50\ \Omega$ coplanar waveguide access lines. These lines were spaced at an ideal distance to accommodate the 8-detector array, allowing short bond wire lengths at each end of the common bus. A photograph of one of these arrays is shown in Figure 5.25.

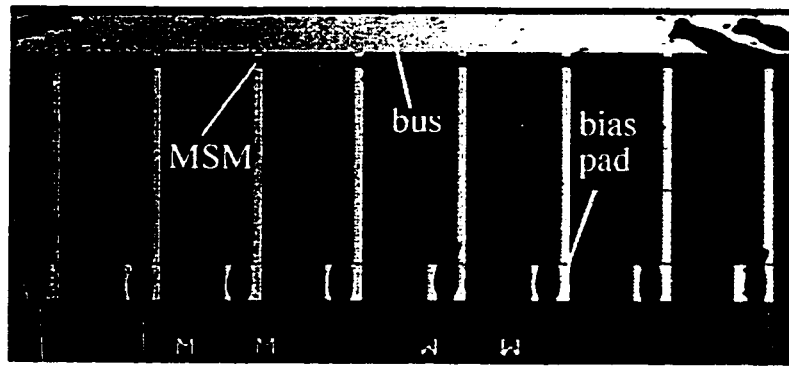


Figure 5.25. A microscope photograph of an 8-detector array, as discussed in the present section. Each MSM photodetector has an active region of $(26\ \mu\text{m})^2$, and finger spacing and width of $2\ \mu\text{m}$. The chip was mounted on a gold-deposited alumina substrate, with $50\ \Omega$ coplanar waveguide access lines. Each end of the bus was bonded to an identical coplanar line on the RF substrate, with a pair of wire bonds approximately $0.5\ \text{mm}$ in length.

To ensure a high-quality termination, the coplanar waveguides were each terminated by broadband RF probes. At one end, the probe was attached to a calibrated $50\ \Omega$ load, from the HP-8510B 3.5 mm calibration kit. At the other end, the microwave signal was extracted for characterization, by a HP-8510B network analyzer.

Bias was applied via the common bus, and the detectors were illuminated sequentially with modulated light, at $830\ \text{nm}$ wavelength. The frequency response of each detector was measured in turn, and the results are plotted in Figure 5.26.

The devices exhibited extremely good response uniformity up to $10\ \text{GHz}$. Excellent matching of the array to the $50\ \Omega$ system is apparent. The response up to $6\ \text{GHz}$ was extremely smooth, while in the 6 to $10\ \text{GHz}$ region, some small spurious features were present. Since these were present in the response for all detectors, it is believed they represented slight mismatch between the array and the external system.

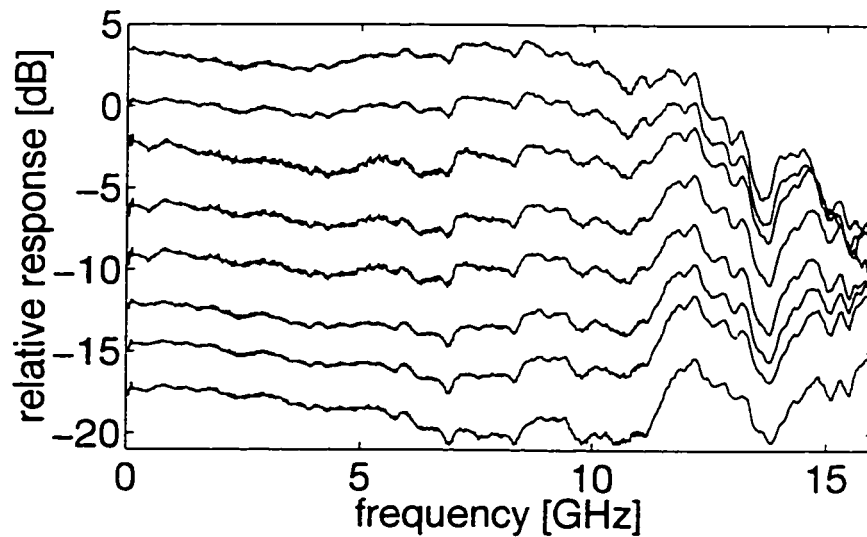


Figure 5.26. Frequency response of all detectors in an 8-detector array, measured sequentially. The traces are arranged (top to bottom) in order of increasing distance from the load, and are offset for clarity. The top trace is not offset, and 0 dB represents approximately 0.1 A/W, determined by the detector used to calibrate the measurement system. The frequency response varies by less than 3 dB up to 12 GHz, for each photodetector. The wavelength of measurement was 830 nm, and the detectors were illuminated with 0.4 mW average optical power. The bias voltage was 5 V.

It should be noted that the transit-time limited bandwidth of MSM detectors with 2 μm finger spacing is on the order of 10 to 15 GHz. Thus, the results of Figure 5.26 represent transit-time limited performance for 8 MSM photodetectors attached to a common bus. In order to reach speeds beyond 20 GHz in the array, MSM detectors with smaller finger spacing will be required. In Chapter 3, greater than 20 GHz bandwidth was demonstrated for discrete devices with 1 μm finger spacing. Others [132] have reported devices with sub-micron finger spacing, and bandwidth in excess of 40 GHz.

In Figure 5.26, it is apparent that the detectors furthest from the load displayed a slightly increased roll-off in the 0 to 10 GHz range. This was most likely due to microwave losses along the common bus, as discussed in Section 5.6. These arrays were formed on a single layer of epitaxial material, without mesa isolation of the active regions. This loss could be essentially eliminated in the future, by etching mesas down to a semi-insulating substrate, prior to deposition of the common-bus and interconnect metal.

To further investigate the quality of the achieved impedance match, return loss measurements were obtained. Figure 5.27 is a typical S_{22} return loss characteristic for the packaged 8-detector array.

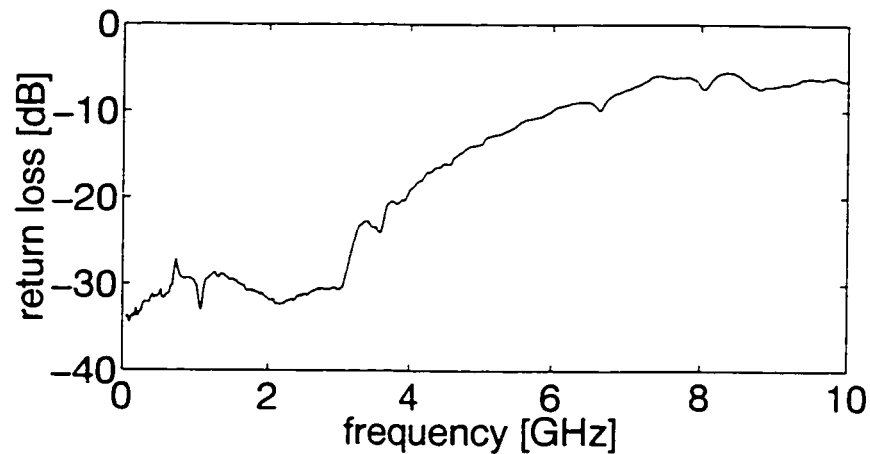


Figure 5.27. The measured return loss characteristic is shown, for the packaged 8-detector array. The return loss was measured at the point of contact to the RF substrate. As such, it represents the total mismatch for the packaged array, including that due to the bond wires at each end of the common bus. In the low frequency range, where the bond wires have relatively negligible impedance, the return loss is due to the impedance of the detector array alone.

The result of Figure 5.27 indicated the packaged array was well matched in the 0 to 4 GHz range. A return loss of 30 dB indicates that only 0.1 % of the energy incident at one end of the array is reflected back. As noted in the previous section, the bond wires at each end of the bus are the only non-matched element in the circuit. For the 8-detector arrays, two bond wires, 0.5 mm long, were attached at each end of the bus. This produces an inductance of approximately 0.2 nH at each end. This represents significant impedance at 5 GHz and above, which is reflected in the degraded return loss. Also, it is quite likely that the spurious features in the frequency response above 12 GHz (Figure 5.26) are partially caused by this excess inductance. This portion of the packaged array should be optimized in future designs.

Finally, a third experiment was conducted, to investigate signal propagation along the detector array, and verify the theory presented in Section 5.4. The details of the experiment are illustrated schematically in Figure 5.28.

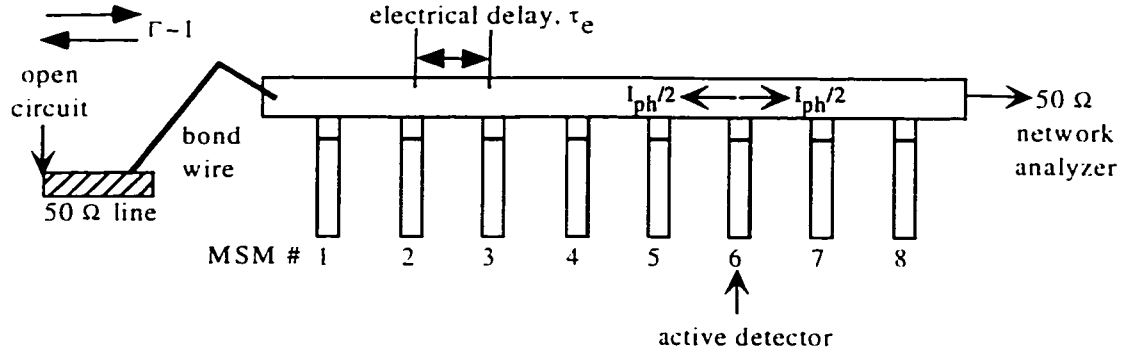


Figure 5.28. A schematic illustration of an experiment conducted to investigate electrical propagation along the photodetector array. As shown, the termination was removed from one end of the array, producing an open-circuit condition. The photocurrent from an active detector splits approximately equally in each direction. The photocurrent wave incident at the open circuit is reflected back towards the load end of the device. At the load, the total photocurrent is the sum of two signals of equal frequency, but unequal phase, which interfere.

As shown in Figure 5.28, it was possible to construct an experiment to investigate interference of photocurrent waves, emanating in either direction from an active device. Neglecting loss along the detector array, it is expected that the frequency response at the load will exhibit an infinite notch. The notch occurs at the frequency for which the two photocurrent waves are completely out of phase. This frequency is given by

$$f_n = \frac{1}{2\Delta\tau} \quad (5.27)$$

where $\Delta\tau$ is the difference in time-delay between the two signal paths.

The total signal path for the reflected signal in Figure 5.28 includes propagation on the alumina substrate. By measuring the notch frequency for two detectors in the array, on wafer propagation can be isolated. For two detectors, m and n , $\Delta\tau$ differs by a fixed amount, given by

$$\Delta\tau_m - \Delta\tau_n = 2(m-n)\tau_e \quad (5.28)$$

τ_e is the inter-detector propagation delay, as calculated theoretically in Section 5.4, and shown in Figure 5.28. Thus, an experimental verification of τ_e is possible, by measuring the notch frequency of two detectors. The value is obtained from

$$\tau_c = \frac{1}{4(m-n)} \left(\frac{1}{f_{nm}} - \frac{1}{f_{nn}} \right). \quad (5.29)$$

An experimental result of this kind is shown in Figure 5.29.

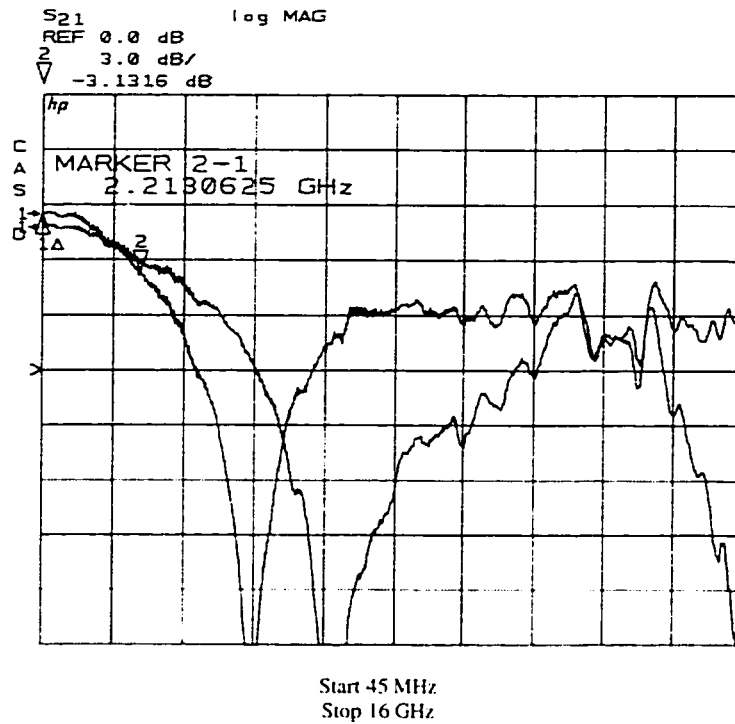


Figure 5.29. A result for the experiment described by Figure 5.28. The detectors are in an 8-detector array. The trace indicated by marker 2 is for detector 6, the other is for detector 2. The notch frequencies are approximately 4.7 GHz and 6.6 GHz, respectively. The bottom of the notches is off the display, but is about 30 dB below the DC response. The plot is the screen output of a HP-8510B network analyzer, see Figure 5.2 for details of the plot format.

Note that very distinct notches were observed, indicating that a large portion of the signal reflected at the open circuit is transferred back to the load end. The depth of the notch is a good measure of unwanted reflections along the array. A deep notch requires that two signal paths, characterized by unique time delays, are dominant. Typically, the bottom of the notch was more than 30 dB below the DC signal level. This indicated that spurious reflections along the array were minimal. For -30 dB of destructive interference, the two main contributions to the signal at the load must have current magnitudes that differ by less than 3 %.

From the data in Figure 5.29, and using equation (5.29), an inter-detector delay along the common bus of 3.8 ps is derived. This is in good agreement with the theoretical estimate of Section 5.5.1, 3.7 ps.

In summary, the 8-detector arrays discussed in this section represent a significant step forward in the development of optoelectronic switching techniques. Both the size and bandwidth of the array represent considerable improvements over the best previously reported devices [186]. The experimental results are in good agreement with the theory discussed in Section 5.4. Faster individual detectors, and improvements in matching characteristics of the array, should enable even faster operation for future designs.

5.6. Limits on Array Length – Microwave Loss

For most of the analysis in Section 5.4, the effects of loss were neglected. If this were valid, photodetector arrays of infinite length would be possible, assuming perfect impedance matching. In reality, the cumulative effects of the loss terms in Figure 5.14 place a practical limitation on array length. Goldsmith [174] has discussed this in some detail. An exact numerical solution should be pursued in the future, using the equivalent circuit of Figure 5.14, and realistic loss-terms for the photodetectors and interconnects of interest.

In this section, some limiting cases are discussed, to illuminate the issues. First, a reasonable first-order approximation, for the arrays discussed in Section 5.5, is to neglect the loss terms of the individual detector elements. This is because the lengths of the detector elements are much less than the length of the interconnecting microstrip lines ($26\ \mu\text{m} \ll 250\ \mu\text{m}$). Thus, microstrip losses, as discussed in Section 5.4.4, will dominate in many cases. If the microstrip is deposited on a semi-insulating semiconductor, those losses might be reduced enough that losses in the photodetectors determine maximum array length.

Microstrip losses are extremely sensitive to the net carrier concentration of the underlying semiconductor. As an example, losses were calculated using (5.24)

and (5.25), and assuming an electron concentration of $3 \times 10^{13} \text{ cm}^{-3}$. This is representative of the wafers used in the previous section: the manufacturer guaranteed a carrier concentration less than 10^{14} cm^{-3} , for the GaAs epitaxial layer. Figure 5.30 is a plot of dielectric and conductor loss per unit length. The geometrical parameters of the microstrip line were those for the common bus in the previous section. From the discussion in Section 5.4.4, the semiconductor can only be treated as a dielectric under certain conditions, $\omega > \sigma/\epsilon$. Since the empirical relations used to approximate microstrip loss were derived for dielectrics, the analysis was restricted to frequencies greater than 10 GHz.

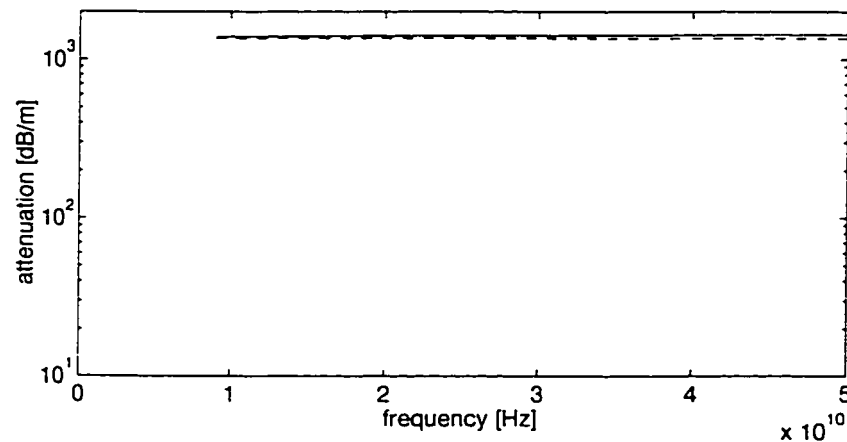


Figure 5.30. Losses for a microstrip line on GaAs, with an electron concentration of $3 \times 10^{13} \text{ cm}^{-3}$. The conductor loss is not sensitive to the underlying material, and is shown by the dotted line. The dielectric loss dominates, and is shown by the dashed line. The total loss is shown by the solid line, and is approximately 1.5 dB/mm, independent of frequency.

The data in Figure 5.30 represent a first-order approximation. The empirical relation used to calculate dielectric loss is not rigorously applicable to the case of a conducting material. However, it is clear that, on lightly doped epitaxial material, dielectric losses are dominant and will severely limit the length of an array.

On the other hand, for carrier concentrations less than approximately 10^{11} cm^{-3} , the dielectric loss drops to negligible levels, and total loss is given by the

conductor loss curve in Figure 5.30. Such low carrier concentrations are routinely available, with semi-insulating material [82]. To further illustrate the effect of reducing free carrier concentration, data were plotted in the format of Figure 5.31. Based on the arrays in the previous section (inter-detector spacing of $250\ \mu\text{m}$), the maximum number of detectors in an array was plotted as a function of the required cutoff frequency.

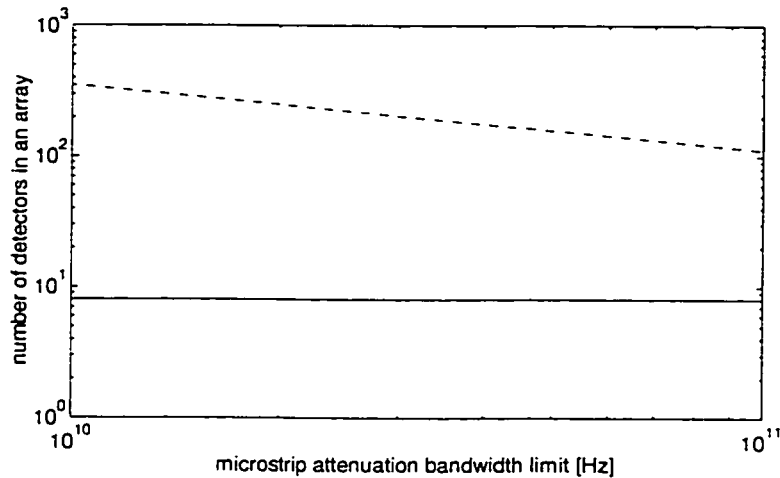


Figure 5.31. The maximum number of detectors in an array is plotted against the cutoff frequency, as determined by microstrip attenuation alone. Two limiting cases are considered. The first assumes a carrier concentration of $3 \times 10^{13}\ \text{cm}^{-3}$ in the semiconductor underlying the microstrip (solid line). This is representative of the wafers discussed in Section 5.5. The second case assumes the microstrip lies on a semi-insulating semiconductor, so that dielectric losses are negligible (dashed line).

It should be reiterated that the transit-time limited bandwidth of individual detectors is neglected in the analysis. The bandwidth limit due solely to microstrip attenuation is defined as the frequency at which the signal is attenuated by 3 dB in traveling from one end of the array to the other. This should represent a worst-case scenario, for the detector furthest from the load.

Clearly, if microstrip losses alone limited array size, it would be possible to construct arrays of several hundred photodetectors, operating at bandwidths greater than 10 GHz. In reality, the loss terms due to individual detectors (R_s and R_L in Figure 5.14) will further limit the length. Also, the cumulative effects of slight mismatches will cause greater problems in long arrays. Thus, extremely

careful design and highly resistive semiconductor layers are requirements for extending array length.

Figure 5.31 illustrates that depositing the common-bus on a nominally doped, epitaxial layer, is not generally acceptable. The simple model predicts that microstrip loss limits the array size to 8 detectors in that case. Since the dielectric loss, predicted in Figure 5.30, is not frequency dependent, the limit does not derive from a frequency roll-off. Rather, it is a measure of the maximum length for which the detector furthest from the load delivers 3 dB less power than that closest to the load.

In a more accurate treatment, the loss is expected to show some frequency dependence [182]. Keeping this in mind, the results in Section 5.5.3 are in qualitative agreement with the analysis here. For the 8-detector array studied experimentally, Figure 5.26 shows that the detector furthest from the load exhibits a 3 dB roll-off at approximately 10 GHz. Thus, it is quite likely that the array length is limited to approximately 8 detectors in that case, in agreement with the results in Figure 5.31. It should be possible to eliminate the roll-off, by forming the array on a semi-insulating substrate. In that case, the maximum array length will lie between the limits shown in Figure 5.31. More accurate modeling is required, but arrays of 50 to 100 detectors seem feasible with careful design.

5.7. Comparison of Impedance-Matched and Single-Output Arrays

In previous work [4], the benefits of terminating both ends of an MSM photodetector array were noted. At the time, this was an experimental observation only. The obvious drawback of going to this type of approach is that only half the photocurrent is delivered to the intended load, with the other half being dissipated in the termination resistor. This implies a 6 dB power penalty. Because of this, efforts were focused on single-output arrays [20],[173]. In this section, the impedance-matched array approach is compared to alternative single-output approaches.

First, it should be noted that it is possible to combine the signals from each end of the impedance-matched array, and deliver the sum to an external load. This technique is limited by the delay difference between the two signal paths. The half-power bandwidth is given by

$$f_{sum} = \frac{1}{4\Delta\tau} , \quad (5.30)$$

where $\Delta\tau$ is the difference in propagation delay for the two paths. The worst-case scenario is for a detector at the end of an array, for which $\Delta\tau$ is equal to the propagation delay along the entire length of the array. As an example, for the 8-detector array demonstrated in Section 5.5.3, the total propagation delay along the common-bus was approximately 30 ps. Thus, signal summation as described is feasible up to approximately 8 GHz. The bandwidth could be increased by a reduction of the inter-detector spacing. However, this would increase crosstalk between devices and make optical alignment more difficult.

In the future, it is likely that longer arrays and wider bandwidths will be required. Thus, the technique of combining signals from either end of the array is not likely to remain feasible. It will be necessary to compensate for the 6 dB power penalty, in the pre-amplifier following the array.

Liu [173] previously described a technique to equalize the response of all detectors in a common-bus array, with the bus terminated at one end only. The arrays he considered were very similar to those in Section 5.5. Essentially, by tuning the inter-detector inductance in such an array, it would be possible to minimize the dependence of device bandwidth on position in the array. However, the bandwidth with this approach is limited by reflection at the open-circuit end of the common-bus. This is very similar to the experiment described in Figure 5.28, and the plots in Figure 5.29 are representative of the response possible with such an approach. The round-trip delay is double the single-pass value in (5.30), so the maximum bandwidth is further reduced. The predicted bandwidth for the 8-detector arrays described in Section 5.5.3 is 4 GHz, and this value is inversely proportional to the number of detectors in an array. It will not be possible to

achieve 10 GHz bandwidth with such an approach, unless array sizes or inter-detector spacings are greatly reduced. The simulations of Liu [173] predicted an equalized bandwidth of 1.5 GHz, for 8 detectors spaced at 250 μm .

The designs detailed in Section 5.3 represent an alternative approach to single-output arrays. From the discussion in Section 5.3.4, there is considerable work to be done in optimizing that approach. However, some generalizations regarding power-transfer are possible. It can be shown [177] that it is not possible to construct a microwave power combiner that is matched at all ports, and lossless. The interpretation of this is that in attempting to combine the signals of several sources, it is necessary that some residual loss be present, either due to resistive elements in the combiner, or due to reflections at mismatched ports.

Sharma's simulations [20], for the devices in Section 5.3, indicated that 4 dB of loss is introduced by the combining technique. This is a fairly typical value for Wilkinson power combiners in microstrip [180], which provided the inspiration for his approach. Thus, at best the designs will produce a 2 dB improvement in insertion loss over the impedance-matched photodetector array. This small improvement may not justify the effort required to optimize the techniques discussed in Section 5.3.

5.8. Conclusions and Summary

In this chapter, some significant advances in the construction of broadband MSM photodetector arrays were detailed. An 8-detector array has been impedance-matched to a 50 Ω external system. With this technique, the distributed nature of the common-bus array introduces negligible signal distortion up to 12 GHz. The theory for these impedance-matched-MSM-photodetector-arrays (IMMPA) has been developed, and generally shows good agreement with the experimental results.

The major drawback of the approach is that it requires the photodetector array to be terminated at each end of its common bus. This produces a 6 dB power

penalty, which will need to be compensated by amplification elsewhere in the system. Alternative single-output approaches were reviewed, and experimental results for some novel single-output arrays were presented. The single-output approaches introduce a comparable power penalty in one case, and cannot achieve the required bandwidths in the other case.

The impedance-matched arrays require further optimization in future work, as follows.

1. Numerical simulations should be pursued, of the inductive and capacitive reactances attributable to the metal patterns of the array. This would allow array layouts to be optimized, to achieve more precise impedance matching with the external system. This will be critical for extending the array to more than 8 or 16 photodetectors.
2. Arrays should be fabricated on highly insulating semiconductor material, to minimize microwave loss. A preliminary treatment in this Chapter suggests that arrays of up to 50 photodetectors might be feasible, if all sources of microwave loss are reduced.
3. Improved packaging is necessary, to reduce spurious features observed in the 10 to 20 GHz range. Bond-wires should be minimized, or replaced by alternative methods such as bond-ribbon or solder bump techniques. Also, RF substrates (chip carriers) should be designed with optimal contact points for the arrays of interest.

The results in Section 5.5.3 represent nearly transit-time limited performance for a common-bus array of eight MSM photodetectors. The fundamental limits of the impedance-matching technique were not approached by that demonstration. By using faster MSM detectors, bandwidths in the 40 to 50 GHz range are possible [175]. Such speeds will require a precisely optimized design, as detailed above.

6. Conclusions and Recommendations

The goals of this work were essentially threefold: to optimize the technology of basic MSM photodetectors, investigate methods to improve their responsivity, and develop methods of integrating several MSM photodetectors in a broadband array. The work was conducted with specific applications in mind, in particular broadband optoelectronic switching and signal processing systems. Significant progress was made with regards to each of the goals listed above.

The applications were reviewed in Chapter 1, along with the basic characteristics of MSM photodetectors. The strengths and weaknesses of the MSM photodetector, relative to the alternative p-i-n photodetector, were discussed. It was noted that surface effects are the primary cause of sub-optimal attributes for MSM photodetectors. As such, alternative surface layers and passivation techniques were given primary consideration in Chapters 2 and 3. In Chapter 4, responsivity enhancement using resonant-cavity techniques was investigated, both theoretically and experimentally. Based on this, a novel device with bias-dependent responsivity is analyzed in Appendix A. Finally, broadband MSM photodetector arrays were studied theoretically and experimentally in Chapter 5.

Detailed summaries and conclusions are contained at the end of each chapter. In the present chapter, only the most significant results are discussed. Also, suggestions are made for future work.

6.1. Overview of Significant Results

The discussion in Chapter 2, and in much of the literature, indicates that surface effects often dominate the performance of MSM photodetectors. This is due to the lateral (planar) structure of the detectors, and the existence of strong fields at the peripheries of the interdigitated electrodes. In addition, III-V semiconductors generally suffer from sub-optimal surface attributes, and techniques to improve this situation are the focus of much research. As such, reliable surface treatments and passivation techniques are the keys to realizing a mature MSM photodetector technology.

An optimized technology on InP was sought first, as MSM photodetectors operating at the fiber wavelengths (1300 and 1550 nm) are of greatest importance at present. Two material systems were investigated, and state-of-the-art performance was demonstrated in each case. A pseudomorphic InGaP surface layer was found to act as a high quality passivant on InP/InGaAs/InP MSM detectors. The DC and AC characteristics of those devices were very nearly ideal, and they exhibited transit-time-limited speed. Their 12 GHz saturation bandwidth (see Figure 3.6) was the highest reported in the literature [120], at the time of writing, for devices of such large size ($100 \mu\text{m}$)². It was speculated that the passivating effects of InGaP might derive from the superior thermodynamic stability of GaP, relative to most other III-V semiconductors.

Nearly transit-time-limited speed was also demonstrated for InAlAs/InGaAs/InAlAs/InP MSM detectors. In that case, a suitable surface etch and dielectric passivant were necessary, to eliminate problematic low-frequency gain. The work described in Section 3.3.2 clearly illuminates the dependence of MSM detector performance on the electronic conditions at the surface. InAlGaAs/InP is receiving much attention for high-speed electronics and optoelectronics, and the passivation technique described might have application to many devices [59].

Aside from surface effects, it was postulated in Section 1.7 that heterojunction band offsets can impact MSM photodetector performance, especially at low bias. A first-order model was developed, to approximate hole pileup effects in alternative material systems. It was speculated that arsenide-based cap layers, having smaller valence band offsets, might exhibit superior performance at low bias. Based on this, an optimized epitaxial structure was designed, in the AlGaAs/GaAs material system. 18 GHz bandwidth was demonstrated at 3 V bias (see Figure 3.21) [121], a significant improvement over the best previous results in the literature, for photolithographically-defined devices.

In Chapter 4, resonant-cavity epitaxial structures were designed for operation at 800, 1300, and 1550 nm wavelengths. The concepts were verified experimentally at 800 nm. In particular, a novel structure was designed and fabricated, using heavily-doped GaAs/InGaP layers to produce an efficient mirror in the 800 nm wavelength region. This approach is attractive for a number of reasons, especially since it requires only binary and ternary semiconductor layers. Initial experimental results were quite promising (see Figure 4.24), and full details will be reported elsewhere, after device fabrication is complete.

The results of Chapter 5 are perhaps of greatest significance. Broadband photodetector arrays have proven difficult to realize, but are expected to find extensive application in emerging optical networks. The impedance-matched MSM photodetector arrays (IMMPA) demonstrated were the first of their kind, although similar concepts had been employed in the microwave fiber optics community. A uniform bandwidth of 12 GHz was demonstrated, for 8 MSM photodetectors attached to a common bus (see Figure 5.26). This result represents a large step forward [186], for arrays of photodetectors with individual bias control.

6.2. Suggestions for Future Work

The results in Chapters 2 and 3 should be useful in choosing and realizing an optimized MSM photodetector technology, on both InP and GaAs substrates. However, the experimental results in Chapter 3 were necessarily limited to a few wafers. In order to obtain a mature technology, a systematic study is required, involving a larger number of wafers and devices. In particular, surface processing techniques on III-V semiconductors are notoriously difficult to reproduce with great accuracy. This lack of process refinement requires further study. Also, while the passivation techniques employed were successful, the explanations are speculative at present. A detailed study using surface diagnostic tools would be useful for obtaining a deeper understanding of the underlying physics.

The resonant-cavity techniques of Chapter 4 are very promising for hybrid optoelectronic systems. Unfortunately, the required growth accuracy was not

achieved in either of the experimental demonstrations. Efforts should be made to refine these techniques. In particular, resonant-cavity structures represent an excellent opportunity to test emerging in-situ growth monitoring methods.

Finally, the impedance-matched detector arrays demonstrated in Chapter 5 show outstanding potential. While the results are already significant, the limits of the technique have not been approached. Longer arrays, operating at higher speeds, should be possible in future work. Also, the technique should be demonstrated on InP substrates, as this would be of greater interest for fiber optic networks.

7. References

- [1] J. Iyer, "Photodetectors demystified", *IEEE Potentials*, pp. 5-10, December 1993.
- [2] J. Wilson, J.F.B. Hawkes, *Optoelectronics, An Introduction, second edition*, Prentice Hall International, London, 1989, Chapter 7.
- [3] S.J. Wojtczuk, J.M. Ballantyne, S. Wanuga, Y.K. Chen, "Comparative study of easily integrable photodetectors", *Journal of Lightwave Technology*, vol. LT-5, no. 10, pp. 1365-1370, October 1993.
- [4] R.G. DeCorby, "Frequency response characterization of GaAs MSM photodetector arrays: test facility and experimental results", M.Sc. Thesis, University of Saskatchewan, May 1995.
- [5] B.G. Streetman, *Solid State Electronic Devices, third edition*, Prentice-Hall Inc., New York, 1990, Chapter 4.
- [6] B.L. Kasper, J.C. Campbell, "Multigigabit-per-second avalanche photodiode lightwave receivers", *Journal of Lightwave Technology*, vol. LT-5, no. 10, pp. 1351-1364, October 1987.
- [7] S. Melle, A. MacGregor, "How to choose avalanche photodiodes", *Laser Focus World*, pp. 145-156, October 1995.
- [8] B.F. Levine, "Optimization of 10-20 GHz avalanche photodiodes", *IEEE Photonics Technology Letters*, vol. 8, no. 11, pp. 1528-1530, November 1996.
- [9] S.M. Sze, D.J. Coleman, A. Loya, "Current transport in metal-semiconductor-metal (MSM) structures", *Solid State Electronics*, vol. 14, pp. 1209-1218, 1971.
- [10] B.C. Wadell, *Transmission Line Design Handbook*, Artech House, Inc., Boston, 1991, Chapter 7.
- [11] T. Sugeta, T. Urisu, S. Sakata, Y. Mizushima, "Metal-semiconductor-metal photoconductor for high-speed optoelectronic circuits", *Japan J. Appl. Phys.*, vol. 19, supplement 19-1, pp. 459-464, 1980.
- [12] M. Ito, O. Wada, "Low dark current GaAs metal-semiconductor-metal (MSM) photodiodes using WSi_x contacts", *IEEE Journal of Quantum Electronics*, vol. QE-22, no. 7, pp. 1073-1077, July 1986.
- [13] D.K. Lam, R.I. MacDonald, J.P. Noad, B.A. Syrett, "Surface-depleted photoconductors", *IEEE Transactions on Electron Devices*, vol. ED-34, no. 5, pp.1057-1060, May 1987.
- [14] G. Keiser, *Optical Fiber Communications, second edition*, McGraw-Hill, inc., New York, 1991, Chapter 6.

- [15] L. Figueroa, C.W. Slayman, "A novel heterostructure interdigital photodetector (HIP) with picosecond optical response", *IEEE Electron Device Letters*, vol. EDL-2, no. 8, pp. 208-210, August 1981.
- [16] J.B.D. Soole, H. Schumacher, "InGaAs metal-semiconductor-metal photodetectors for long wavelength optical communications", *IEEE Journal of Quantum Electronics*, vol. 27, no. 3, p. 737-752, March 1991.
- [17] J.E. Bowers, "Ultrawide-band long-wavelength p-i-n photodetectors", *Journal of Lightwave Technology*, vol. LT-5, no. 10, pp. 1339-1350, October 1987.
- [18] R.I. MacDonald, "Optoelectronic hybrid switching", Chapter 7 in *Photonics in Switching, Volume 1*, J.E. Midwinter, ed., Academic Press, inc., New York, 1993, pp. 169-193.
- [19] R.I. MacDonald, E.H. Hara, "Optoelectronic broadband switching array", *Electronics Letters*, vol. 16, pp. 502-503, 1978.
- [20] R. Sharma, "Broadband optoelectronic switching and signal processing", Ph.D. Thesis, University of Alberta, Fall 1996.
- [21] M. Veilleux, R.I. MacDonald, "An optoelectronic switching matrix with high isolation", *Journal of Lightwave Technology*, vol. 10, no. 7, pp. 988-991, July 1992.
- [22] M. Ersoni, X. Wu, P.E. Jessop, J.P. Noad, "Optical signal distribution in waveguide-coupled metal-semiconductor-metal detector arrays", *Journal of Lightwave Technology*, vol. 15, no. 2, pp. 328-333, February 1997.
- [23] N. Rajkumar, J. McMullin, B. Keyworth, "Optoelectronic cross-bar switching using free-space optical distribution", *IEEE Photonics Technology Letters*, vol. 8, no. 11, pp. 1534-1536, Nov. 1996.
- [24] R.I. MacDonald, "Optoelectronic switching in digital networks", *IEEE Journal on Selected Areas in Communications*, vol. SAC-3, no. 2, pp. 336-344, March 1985.
- [25] H.S. Hinton, "Architectural considerations for photonic switching networks", *IEEE Journal on Selected Areas in Communications*, vol. 6, no. 7, pp. 1209-1226, August 1988.
- [26] A. Jajszczyk, H.T. Mouftah, "Photonic fast packet switching", *IEEE Communications Magazine*, pp. 58-65, February 1993.
- [27] R. Ramaswami, "Multiwavelength lightwave networks for computer communication", *IEEE Communications Magazine*, pp. 78-88, February 1993.
- [28] E.J. Lerner, "Multiple wavelengths exploit fiber capacity", *Laser Focus World*, pp. 119-125, July 1997.
- [29] R. Sharma, R.I. MacDonald, "A signal transparent 10x10 space-division optoelectronic switch core for virtual-transparent path-based

- multiwavelength networks”, *Journal of Lightwave Technology*, vol. 15, no. 8, pp. 1522-1529, August 1997.
- [30] B.P. Keyworth, “Optical and optoelectronic switching: approaches and limitations”, invited presentation, EdTel and TRILabs, Edmonton, April 1996.
- [31] B.E. Swekla, R.I. MacDonald, “Optoelectronic transversal filter”, *Electronics Letters*, vol. 27, no. 19, pp. 1769-1770, September 1991.
- [32] R.I. MacDonald, “Optoelectronic equalisation”, *IEEE Photonics Technology Letters*, vol. 6, no. 4, pp. 565-567, April 1994.
- [33] M. Dagenais, R. Leheny, H. Temkin, P. Bhattacharya, “Applications and challenges of OEIC technology: a report on the 1989 Hilton Head workshop”, *Journal of Lightwave Technology*, vol. 8, no. 6, pp. 846-861, June 1990.
- [34] E.J. Lerner, “Optoelectronic integrated circuits promise simplicity”, *Laser Focus World*, pp. 99-102, June 1997.
- [35] P.P. Bohn, M.J. Kania, J.M. Nemchik, R.C. Purkey, “Fiber in the loop”, *AT&T Technical Journal*, pp. 31-45, January/February 1992.
- [36] T.L. Koch, U. Koren, “Photonic integrated circuits”, *AT&T Technical Journal*, pp. 63-74, January/February 1992.
- [37] D.L. Rogers, “Integrated optical receivers using MSM detectors”, *Journal of Lightwave Technology*, vol. 9, no. 12, pp. 1635-1638, December 1991.
- [38] A.A. Ketterson, J. Seo, M.H. Tong, K.L. Nummila, J.J. Morikuni, K. Cheng, S. Kang, I. Adesida, “A MODFET-based optoelectronic integrated circuit receiver for optical interconnects”, *IEEE Transactions on Electron Devices*, vol. 40, no. 8, pp. 1406-1415, August 1993.
- [39] E. John, M. Das, “Design and performance analysis of InP-based high-speed and high-sensitivity optoelectronic integrated receivers”, *IEEE Transactions on Electron Devices*, vol. 41, no. 2, pp. 162-171, February 1994.
- [40] P. Fay, W. Wohlmuth, C. Caneau, I. Adesida, “18.5-GHz bandwidth monolithic MSM/MODFET photoreceiver for 1.55- μ m wavelength communication systems”, *IEEE Photonics Technology Letters*, vol. 8, no. 5, pp. 679-681, May 1996.
- [41] K. Takahata, Y. Muramoto, H. Fukano, K. Kato, A. Kozen, O. Nakajima, S. Kimura, Y. Imai, “20 Gbit/s monolithic photoreceiver consisting of a waveguide pin photodiode and HEMT distributed amplifier”, *Electronics Letters*, vol. 33, no. 18, pp. 1576-1577, August 1997.
- [42] E.H. Botcher, D. Kuhl, F. Heironymi, E. Droge, T. Wolf, D. Bimberg, “Ultrafast semiinsulating InP:Fe-InGaAs:Fe-InP:Fe MSM photodetectors: modeling and performance”, *IEEE Journal of Quantum Electronics*, vol. 28, no. 10, p. 2343-2357, October 1992.

- [43] J. Lu, R. Surridge, G. Pakulski, H. van Driel, J.M. Xu, "Studies of high-speed metal-semiconductor-metal photodetector with a GaAs/AlGaAs/GaAs heterostructure", *IEEE Transactions on Electron Devices*, vol. 40, no. 6, pp. 1087-1092, June 1993.
- [44] Y.C. Lim, R.A. Moore, "Properties of alternately charged coplanar parallel strips by conformal mappings", *IEEE Transactions on Electron Devices*, vol. ED-15, no. 3, pp. 173-180, March 1968.
- [45] S.E. Ralph, M.C. Hargis, G.D. Petit, "Large area, low voltage, transit time limited InGaAs metal semiconductor metal photodetectors", *Applied Physics Letters*, vol. 61, no. 18, pp. 2222-2224, November 1992.
- [46] A. Xiang, W. Wohlmuth, P. Fay, S. Kang, I. Adesida, "Modeling of InGaAs MSM photodetector for circuit-level simulation", *Journal of Lightwave Technology*, vol. 14, no. 5, pp. 716-723, May 1996.
- [47] W.C. Koscielniak, J. Pelouard, M.A. Littlejohn, "Intrinsic and extrinsic response of GaAs metal-semiconductor-metal photodetectors", *IEEE Photonics Technology Letters*, vol. 2, no. 2, pp. 125-127, February 1990.
- [48] S. Tiwari, M.A. Tischler, "On the role of mobility and saturated velocity in the dynamic operation of p-i-n and metal-semiconductor-metal photodetectors", *Applied Physics Letters*, vol. 60, no. 9, pp. 1135-1137, March 1992.
- [49] J.C. Bean, "Materials and technologies for high-speed devices", in *High-Speed Semiconductor Devices*, S.M. Sze, ed., Wiley-Interscience, New York, 1990, pp. 13-55.
- [50] Hewlett Packard product note 8510-15, "Lightwave measurements using the HP 8510", 1990.
- [51] R.A. Metzger, "Is silicon-germanium the new 'material of the future'", *Compound Semiconductor*, vol. 1, no. 3, November/December 1995.
- [52] J.M. Olson, R.K. Ahrenkiel, D.J. Dunlavy, B. Keyes, A.E. Kibbler, "Ultralow recombination velocity at Ga_{0.5}In_{0.5}P/GaAs heterointerfaces", *Applied Physics Letters*, vol. 55, no. 12, pp. 1208-1210, September 1989.
- [53] T.P. Chin, J.C.P. Chang, J.M. Woodall, W.L. Chen, G.I. Haddad, "InGaP/GaAs/InGaP double-heterojunction bipolar transistors grown by solid-source molecular-beam epitaxy with a valved phosphorous cracker", *Journal of Vacuum Science and Technology*, vol. 14, no. 3, pp. 2225-2228, May/June 1996.
- [54] *Properties of Indium Phosphide*, INSPEC, The Institution of Electrical Engineers, London, 1991.
- [55] *Indium Phosphide and Related Materials: Processing, Technology, and Devices*, Avishay Katz, ed., Artech House, Boston, 1992.
- [56] S.J. Chua, A. Ramam, "Molecular-beam epitaxy of high quality lattice matched In_{1-x-y}Ga_xAl_yAs epitaxial layers on InP Substrates", *Journal of*

- Vacuum Science and Technology*, vol. B14, no. 3, pp.1719-1724, May/June 1996.
- [57] St. Kollakowski, U. Schade, E. Bottcher, D. Kuhl, D. Bimberg, P. Ambree, K. Wandel, "Silicon dioxide passivation of InP/InGaAs metal-semiconductor-metal photodetectors", *Journal of Vacuum Science and Technology B*, vol. 14, no. 3, p. 1712-1718, May/June 1996.
- [58] D.C. Dumka, R. Riemenschneider, J. Miao, H.L. Hartnagel, B.R. Singh, "Electrochemically fabricated high-barrier Schottky contacts on n-InP and their application for metal-semiconductor-metal photodetectors", *Journal of the Electrochemical Society*, vol. 143, no. 6, pp. 1945-1948, June 1996.
- [59] R.G. DeCorby, R.I. MacDonald, M. Beaudoin, T. Pinnington, T. Tiedje, F. Gouin, "Elimination of low frequency gain in InAlAs/InGaAs metal-semiconductor-metal photodetectors by silicon nitride passivation", *Journal of Electronic Materials*, vol. 26, no. 12, pp. L25-L28, December 1997.
- [60] R. Bube, *Electrons in Solids, An Introductory Survey, Third Edition*, Academic Press Ltd., London, 1992.
- [61] C. Matthai, R.H. Williams, "Aspects of the physics of heterojunctions", in *Physics and Technology of Heterojunction Devices*, D.V. Morgan, R.H. Williams eds., Peter Peregrinus Ltd., London, 1991.
- [62] Z.I. Alferov, *Semiconductor Heterostructures*, MIR Publishers, Moscow, 1989.
- [63] B.J. Van Zeghbroeck, W. Patrick, J.M. Halbout, P. Vettiger, "105 GHz bandwidth metal-semiconductor-metal photodiode", *IEEE Electron Device Letters*, vol. 9, no. 10, pp. 527-529, October 1988.
- [64] J. Burm, K.I. Litvin, D.W. Woodard, W.J. Schaff, P. Mandeville, M.A. Jaspan, M.M. Gitin, L.F. Eastman, "High-frequency, high-efficiency MSM photodetectors", *IEEE Journal of Quantum Electronics*, vol. 31, no. 8, pp. 1504-1508, August 1995.
- [65] M. Klingenstein, J. Kuhl, J. Rosenzweig, C. Moglestue, A. Hulsmann, J. Schneider, K. Kohler, "Photocurrent Gain Mechanisms in metal-semiconductor-metal photodetectors", *Solid-State Electronics*, vol. 37, no. 2, p. 333-340, February 1994.
- [66] O. Wada, H. Nobuhara, H. Hamaguchi, T. Mikawa, A. Tackeuchi, T. Fujii, "Very high speed GaInAs metal-semiconductor-metal photodiode incorporating an AlInAs/GaInAs graded superlattice", *Applied Physics Letters*, vol. 54, no. 1, pp. 16-18, January 1989.
- [67] W. Wohlmuth, P. Fay, C. Caneau, I. Adesida, "Low dark current, long wavelength metal-semiconductor-metal photodetectors", *Electronics Letters*, vol. 32, no. 3, pp. 249-250, February 1996.

- [68] E.H. Rhoderick, R.H. Williams, *Metal-Semiconductor Contacts, second edition*, Oxford University Press, Oxford, 1988.
- [69] C. Moglestue, J. Rosenzweig, J. Kuhl, M. Klingenstein, M. Lambsdorff, A. Axmann, J. Schneider, A. Hulsmann, "Picosecond pulse response characteristics of GaAs metal-semiconductor-metal photodetectors", *Journal of Applied Physics*, vol. 70, no. 4, pp. 2435-2448, August 1991.
- [70] S. Tiwari, M.C. Hargis, Y. Wang, M.C. Teich, W.I. Wang, "1.3 μm GaSb metal-semiconductor-metal photodetectors", *IEEE Photonics Technology Letters*, vol. 4, no. 3, pp. 256-258, March 1992.
- [71] P.W. Leech, E. Stumpf, N. Petkovic, L.W. Cahill, " $\text{Hg}_{1-x}\text{Cd}_x\text{Te}$ metal-semiconductor-metal (MSM) photodetectors", *IEEE Transactions on Electron Devices*, vol. 40, no. 8, pp. 1364-1369, August 1993.
- [72] R.G. DeCorby, "Design and fabrication issues for InGaAs based long wavelength MSM photodetectors", TR Labs Internal Report, TR-96-02, Edmonton, January 1996.
- [73] S. Loualiche, A. Le Corre, A. Ginudi, L. Henry, C. Vaudry, F. Clerot, "Pseudomorphic GaInP Schottky diode and MSM detector on InP", *Electronics Letters*, vol. 26, no. 7, pp. 487-488, March 1990.
- [74] J.I. Davies, A.C. Marshall, M.D. Scott, R.J.M. Griffiths, "Ga-Al-In-As ternary and quaternary alloys lattice matched to InP for electronic, optoelectronic and optical device applications, by LP-MOVPE", *Journal of Crystal Growth*, vol. 93, pp. 782-791, 1988.
- [75] L.P. Sadwick, C. Kim, K. Tan, D. Streit, "Schottky barrier heights on n-type and p-type $\text{Al}_{0.48}\text{In}_{0.52}\text{As}$ ", *IEEE Electron Device Letters*, vol. 12, no. 11, pp. 626-628, November 1991.
- [76] S. Fujita, S. Naritsuka, T. Noda, A. Wagai, Y. Ashizawa, "Barrier height lowering of Schottky contacts on AlInAs layers grown by metal-organic chemical-vapor deposition", *Journal of Applied Physics*, vol. 73, no. 3, pp. 1284-1287, February 1993.
- [77] P. Kordos, M. Marso, R. Meyer, H. Luth, "Schottky barrier height enhancement on n- $\text{In}_{0.53}\text{Ga}_{0.47}\text{As}$ ", *Journal of Applied Physics*, vol. 72, no. 6, pp. 2347-2355, September 1992.
- [78] E.T. Yu, J.O. McCaldin, T.C. McGill, "Band offsets in semiconductor heterojunctions", *Solid State Physics*, vol. 46, p. 1, 1992.
- [79] R. Yuang, H. Shieh, Y. Chien, Y. Chan, J. Chyi, W. Lin, Y. Tu, "High-performance large-area InGaAs MSM photodetectors with a pseudomorphic InGaP cap layer", *IEEE Photonics Technology Letters*, vol. 7, no. 8, pp. 914-916, August 1995.
- [80] J.I. Chyi, T. Wei, J. Hong, W. Lin, Y. Tu, "Low dark current and high linearity InGaAs MSM photodetectors", *Electronics Letters*, vol. 30, no. 4, pp. 355-356, February 1994.

- [81] E. Sano, "A device model for metal-semiconductor-metal photodetectors and its applications to optoelectronic integrated circuit simulation", *IEEE Transactions on Electron Devices*, vol. 37, no. 9, pp. 1964-1968, September 1990.
- [82] *Properties of Gallium Arsenide, second edition*, INSPEC, The Institution of Electrical Engineers, London, 1990.
- [83] R.G. DeCorby, "Epitaxial proposals for simple MSM photodetectors operating in the 800 nm wavelength region", TRILabs Internal Report, Edmonton, July 1996.
- [84] M. Shur, *GaAs Devices and Circuits*, Plenum Press, New York, 1987.
- [85] P.M. Mooney, "Deep donor levels (DX centers) in III-V semiconductors", *Journal of Applied Physics*, vol. 67, no. 3, p. R1, February 1990.
- [86] K.W. Nauka, "Deep level defects in epitaxial III/V materials", *Semiconductors and Semimetals*, vol. 38, Academic Press, inc., New York, 1993, pp. 343-396.
- [87] H. Ito, T. Ishibashi, "Selective and non-selective chemical etching of InGa(As)P/GaAs heterostructures", *Journal of the Electrochemical Society*, vol. 142, no. 10, pp. 3383-3386, October 1995.
- [88] R.K. Ahrenkiel, "Minority-carrier lifetime in III-V semiconductors", *Semiconductors and Semimetals*, Vol. 39, Academic Press Inc., New York, 1993, pp. 38-150.
- [89] Y. Cho, B. Choe, "Band offset transitivity in AlGaAs/InGaP/InGaAsP heterostructures on a GaAs substrate", *Applied Physics Letters*, vol. 69, no. 24, pp. 3740-3742, December 1996.
- [90] M.S. Faleh, J. Tasselli, J.P. Bailbe, A. Marty, "Transistor-based evaluation of conduction-band offset in GaInP/GaAs heterojunction", *Applied Physics Letters*, vol. 69, no. 9, pp. 1288-1290, August 1996.
- [91] S.D. Kwon, H.K. Kwon, B. Choe, "Investigation of electrical properties and stability of Schottky contacts on $(\text{NH}_4)_2\text{S}_x$ -treated n- and p-type $\text{In}_{0.5}\text{Ga}_{0.5}\text{P}$ ", *Journal of Applied Physics*, vol. 78, no. 4, pp. 2482-2488, August 1995.
- [92] C. Lee, H. Shiao, N. Yeh, C. Tsai, Y. Lyu, Y. Tu, "Thermal reliability and characterization of InGaP Schottky contact with Ti/Pt/Au metals", *Solid State Electronics*, vol. 41, no. 1, pp. 1-5, January 1997.
- [93] F. Bechstedt, R. Enderlein, *Semiconductor Surfaces and Interfaces*, Akademie-Verlag, Berlin, 1988.
- [94] W. Monch, "On the physics of metal-semiconductor interfaces", *Reports on Progress in Physics*, vol. 53, pp. 221-278, 1990.

- [95] W.E. Spicer, "Defects in Metal/III/V heterostructures", *Semiconductors and Semimetals*, vol. 38, Academic Press, Inc., New York, 1993, pp. 449-491.
- [96] J. Woodall, P. Kirchner, J. Freeouf, D. McInturff, M. Melloch, E. Pollak, "The continuing drama of the semiconductor interface", in *Semiconductor Growth, Surfaces and Interfaces*, G. Davies, R. Williams, eds., Chapman and Hall, London, 1994, pp. 79-90.
- [97] T. Sands, A.S. Schwarz, "Contacts", *Characterization in Compound Semiconductor Processing*, G. McGuire, Y. Strausser, eds., Butterworth-Heinemann, Boston, 1995, pp. 41-56.
- [98] D. Kim, C. Chao, K. Beyzavi, P. Burrows, S. Forrest, "Surface passivation of InP/In_{0.53}Ga_{0.47}As heterojunction bipolar transistors for opto-electronic integration", *Journal of Electronic Materials*, vol. 25, no. 3, pp. 537-540, 1996.
- [99] J. Dickmann, H. Haspeklo, A. Geyer, H. Daembkes, H. Nickel, R. Losch, "High performance fully passivated InAlAs/InGaAs/InP HFET", *Electronics Letters*, vol. 28, no. 7, pp. 647-649, March, 1992.
- [100] A.M. Green, W.E. Spicer, "Do we need a new methodology for GaAs passivation", *Journal of Vacuum Science and Technology A*, vol. 11, no. 4, pp. 1061-1069, July/August 1993.
- [101] F. Capasso, G. Williams, "A proposed hydrogenization/nitridization passivation mechanism for GaAs and other III-V semiconductor devices, including InGaAs long wavelength photodetectors", *J. Electrochem. Soc.*, vol. 129, no. 4, pp. 821-824, April 1982.
- [102] H.H. Weider, "Dielectric Insulating Layers", chapter 4 of *Characterization in Compound Semiconductor Processing*, G. McGuire, Y. Strausser, eds., Butterworth-Heinemann, Boston, 1995, pp. 57-81.
- [103] J.F. Wager, C.W. Wilmsen, "The deposited insulator/III-V semiconductor interface", chapter 3 in *Physics and Chemistry of III-V Compound Semiconductor Interfaces*, C.W. Wilmsen, ed., Plenum Press, New York, 1985, pp. 165-211.
- [104] G.P. Schwartz, "Analysis of native oxide films and oxide-substrate reactions on III-V semiconductors using thermochemical phase diagrams", *Thin Solid Films*, vol. 103, pp. 3-16, 1983.
- [105] S. Habibi, M. Totsuka, J. Tanaka, S. Matsumoto, "Dry sequential process of photochemical etching and surface passivation of In_{0.52}Al_{0.48}As using HBr and H₂S", *Journal of Vacuum Science and Technology, B*, vol. 13, no. 4, pp. 1466-1472, July/August 1995.
- [106] E. Sano, M. Yoneyama, T. Enoki, T. Tamamura, "Performance dependence of InGaAs MSM photodetectors on barrier-enhancement layer structures", *Electronics Letters*, vol. 28, no. 13, pp. 1220-1221, June 1992.

- [107] J.H. Burroughes, M. Hargis, "1.3 μm InGaAs MSM photodetector with abrupt InGaAs/AlInAs interface", *IEEE Photonics Technology Letters*, vol. 3, no. 6, pp. 532-534, June 1991.
- [108] E. Sano, "Theoretical Analysis of the influences of barrier enhancement layers on transient responses of MSM photodetectors", *IEEE Transactions on Electron Devices*, vol. 39, no. 6, pp. 1355-1362, June 1992.
- [109] T. Miyoshi, H. Tsuchiya, M. Ogawa, "Quantum hole transport at the heterointerface of long wavelength avalanche photodiodes", *IEEE Journal of Quantum Electronics*, vol. 28, no. 1, pp. 25-30, January 1992.
- [110] A.F. Salem, K.F. Brennan, "Influence of hot carrier transport on the transient response of an InGaAs/InAlAs metal-semiconductor Schottky diode structure", *IEEE Transactions on Electron Devices*, vol. 43, no. 4, pp. 664-665, April 1996.
- [111] M. Suzuki, H. Tanaka, S. Akiba, "Effect of hole pileup at heterointerface on modulation voltage in GaInAsP electroabsorption modulators", *Electronics Letters*, vol. 25, no. 2, pp. 88-89, January 1989.
- [112] D.M. Gvozdic, J.B. Radunovic, J.M. Elazar, "An analytical expression for the electric field in MSM structures", *International Journal of Infrared and Millimeter Waves*, vol. 14, no. 7, pp. 1485-1493, 1993.
- [113] D.M. Gvozdic, "Analysis and transfer function of metal-semiconductor-metal photodetector equivalent circuit", *Applied Physics Letters*, vol. 70, no. 3, pp. 286-288, January 1997.
- [114] M. Lundstrom, *Fundamentals of Carrier Transport*, Modular Series on Solid State Devices, Volume X. Addison-Wesley, New York, 1990, Chapter 8.
- [115] K. Brennan, K. Hess, "Theory of high-field transport of holes in GaAs and InP", *Physical Review B*, vol. 29, no. 10, pp. 5581-5590, May 1984.
- [116] R. Scholz, "Stationary lattice mobility of holes in gallium arsenide", *Journal of Applied Physics*, vol. 77, no. 7, pp. 3232-3242, April 1995.
- [117] R.G. DeCorby, "1996 MSM photodetector mask set: summary and process description", TRILabs Internal Report, Edmonton, June 1996.
- [118] R.G. DeCorby, "Recommendations for selective wet-etch chemistry for InAlGaAs/InP MSM detectors", TRILabs Internal Report, Edmonton, April 1996.
- [119] R.G. DeCorby, "Wet-etchant recipes for mesa isolation of InAlGaAs and InGaAsP MSM photodetectors", TRILabs Internal Report, TR-96-09, July 1996.
- [120] R.G. DeCorby, R.I. MacDonald, R. Sharma, F. Gouin, J. Noad, N. Puetz, "Frequency-domain demonstration of transit-time-limited, large-area, InGaP-InP-InGaAs MSM photodetectors", *IEEE Photonics Technology Letters*, vol. 9, no. 7, pp. 985-987, July 1997.

- [121] R.G. DeCorby, R.I. MacDonald, J. Noad, F. Gouin, "Large (50 μm)² metal-semiconductor-metal photodetectors with 18 GHz bandwidth at 3 V bias; reduction of hole pileup", submitted to *Applied Physics Letters*, November 1997.
- [122] C. Gaonach, S. Cassette, M. Di Forte-Poisson, C. Brylinski, M. Champagne, A. Tardella, "A new realization of Schottky diodes on n-type InP", *Semicond. Sci. Technol.*, vol. 5, pp. 322-327, 1990.
- [123] P. Ambree, K. Wandel, E.H. Botcher, D. Bimberg, "Plasma enhanced chemical vapor deposited SiO₂ layers for passivation of InGaAs:Fe metal-semiconductor-metal photodetectors", *Journal of Applied Physics*, vol. 77, no. 2, pp. 945-947, January 1995.
- [124] Y. Xu, W.Y. Ching, "Electronic structure and optical properties of α and β phases of silicon nitride, silicon oxynitride, and with comparison to silicon dioxide", *Physical Review B*, vol. 51, no. 24, pp.17379-17389, June 1995.
- [125] J.H. Kim, H. Torsten, R.A. Friedman, E.Y. Char, S. Ray, "High-performance back-illuminated InGaAs/InAlAs MSM photodetector with record responsivity of 0.96 A/W", *IEEE Photonics Technology Letters*, vol. 4, no. 11, pp. 1241-1244, November 1992.
- [126] P. Phatak, N. Newman, P. Dreszer, E.R. Weber, "Experimental determination of the pressure dependence of the barrier height of metal/[n-type GaAs] Schottky contacts: A critical test of Schottky-barrier models", *Physical Review B*, vol. 51, no. 24, pp. 18003-18006, June 1995.
- [127] K.E. Mello, S.R. Soss, S.P. Murarka, T.M. Lu, S.L. Lee, "Epitaxial quality of thin Ag films on GaAs(100) surfaces cleaned with various wet etching techniques", *Applied Physics Letters*, vol. 68, no. 5, pp. 681-683, January 1996.
- [128] W.A. Wohlmuth, P. Fay, K. Vaccaro, E.A. Martin, I. Adesida, "High-speed InGaAs metal-semiconductor-metal photodetectors with thin absorption layers", *IEEE Photonics Technology Letters*, vol. 9, no. 5, pp. 654-656, May 1997.
- [129] M.S. Unlu, S. Strite, "Resonant cavity enhanced photonic devices", *Applied Physics Reviews, Journal of Applied Physics*, vol. 78, no. 2, pp. 607-639, July, 1995.
- [130] R. Yuang, J. Chyi, Y. Chan, W. Lin, Y. Tu, "High-responsivity InGaAs MSM photodetectors with semi-transparent Schottky contacts", *IEEE Photonics Technology Letters*, vol. 7, no. 11, pp. 1333-1335, November 1997.
- [131] M.A. Matin, K.C. Song, B.J. Robinson, J.G. Simmons, D.A. Thompson, F. Gouin, "Very low dark current InGaP/GaAs MSM photodetector using semi-transparent and opaque contacts", *Electronics Letters*, vol. 32, no. 8, pp. 766-767, April 1996.

- [132] E.H. Bottcher, E. Droge, D. Bimberg, A. Umbach, H. Engel, "Ultra-wide-band (>40 GHz) submicron InGaAs metal-semiconductor-metal photodetectors", *IEEE Photonics Technology Letters*, vol. 8, no. 9, pp. 1226-1228, September 1996.
- [133] T. Sheridan, H. Haidner, N. Streibl, "Increasing the efficiency of MSM detectors using a diffraction grating", *Measurement Science and Technology*, vol. 4, no. 12, pp. 1525-1527, 1993.
- [134] A. Strittmatter, S. Kollakowski, E. Droge, E.H. Bottcher, D. Bimberg, "High speed, high efficiency resonant-cavity enhanced InGaAs MSM photodetectors", *Electronics Letters*, vol. 32, no. 13, pp. 1231-1232, June 1996.
- [135] T.F. Kuech, "III-V compound semiconductor films for optical applications", in *Characterization in Compound Semiconductor Processing*, Butterworth-Heinemann, Stoneham, MA, 1995, pp. 17-39.
- [136] R.H. Stulen, R.R. Freeman, "Developing a soft x-ray projection lithography tool", *AT&T Technical Journal*, p. 37, Nov./Dec. 1991.
- [137] W. Strachan, J. Reiner, W. Goodhue, A. Karakashian, V. Casasanta, J. Geller, "Analysis of molecular beam epitaxy grown $\text{Ga}_{1-x}\text{Al}_x\text{As}/\text{Ga}_{1-y}\text{Al}_y\text{As}$ dielectric stack mirrors using complex indices of refraction", *Journal of Vacuum Science and Technology B*, vol. B14, no. 3, pp.2318-2321, May/June 1996, and references therein.
- [138] A. Moseley, J. Thompson, D. Robbins, M. Kearley, "High-reflectivity AlGaInAs/InP multilayer mirrors grown by low-pressure MOVPE for application to long-wavelength high-contrast-ratio multi-quantum-well modulators", *Electronics Letters*, vol. 25, no. 25, pp. 1717-1718, December 1989.
- [139] W. Kowalsky, J. Mahnss, "Monolithically integrated InGaAlAs dielectric reflectors for vertical cavity optoelectronic devices", *Applied Physics Letters*, vol. 59, no. 9, pp. 1011-1012, Aug. 1991.
- [140] P. Guy, K. Woodbridge, S. Haywood, M. Hopkinson, " A comparison of 1.55 μm distributed Bragg reflector stacks for use in multi quantum well micro resonator modulators", *Semicond. Sci. Technol.*, vol. 10, pp. 1283-1286, 1995.
- [141] F. Choa, K. Tai, W. Tsang, S. Chu, "High reflectivity 1.55 μm InP/InGaAsP Bragg mirror grown by chemical beam epitaxy", *Applied Physics Letters*, vol. 59, no. 22, pp. 2820-2822, November 1991.
- [142] S. Murtaza, R. Chelakara, R. Dupuis, J. Campbell, A. Dentai, "Resonant-cavity photodiode operating at 1.55 μm with Burstein-shifted $\text{In}_{0.53}\text{Ga}_{0.47}\text{As}/\text{InP}$ reflectors", *Applied Physics Letters*, vol. 69, no. 17, pp. 2462-2464, October 1996.
- [143] E. Hecht, *Optics*, Addison-Wesley Publishing co., Reading Mass., 1987.

- [144] M. Born, E. Wolf, *Principles of Optics, sixth edition*, Pergamon Press, New York, 1980.
- [145] S. Murtaza, K. Anselm, A. Srinivasan, B. Streetman, J. Campbell, J. Bean, L. Peticolas, "High-reflectivity Bragg mirrors for optoelectronic applications", *IEEE Journal of Quantum Electronics*, vol. 31, no. 10, pp. 1819-1825, October 1995.
- [146] A. Chin, T. Chang, "Enhancement of quantum efficiency in thin photodiodes through absorptive resonance", *Journal of Lightwave Technology*, vol. 9, no. 3, pp. 321-328, March 1991.
- [147] R. Enderlein, "Photoreflectance studies of (Al,Ga)As/GaAs heterostructures and devices", *Phys. Stat. Sol. B*, vol. 194, no. 1, pp. 257-265, 1996.
- [148] N. Peyghambarian, S.W. Koch, A. Mysyrowicz, *Introduction to Semiconductor Optics*, Prentice Hall, New Jersey, 1993, Chapter 13.
- [149] Z.M. Li, D. Landheer, M. Veilleux, D.R. Conn, R. Surridge, J.M. Xu, R.I. MacDonald, "Analysis of a resonant-cavity enhanced GaAs/AlGaAs MSM photodetector", *IEEE Photonics Technology Letters*, vol. 4, no. 5, pp. 473-476, May 1992.
- [150] J. Burm, K. Litvin, D. Woodard, W. Schaff, P. Mandeville, M. Jaspan, M. Gitin, L. Eastman, "High-frequency, high efficiency MSM photodetectors", *IEEE Journal of Quantum Electronics*, vol. 31, no. 8, pp. 1504-1508, August 1995.
- [151] A. Yariv, *Optical Electronics, Fourth Edition*, Saunders College Publishing, Philadelphia, 1991.
- [152] G. Ortiz, C. Hains, J. Cheng, H. Hou, J. Zolper, "Monolithic integration of In_{0.2}Ga_{0.8}As vertical-cavity surface-emitting lasers with resonance-enhanced quantum well photodetectors", *Electronics Letters*, vol. 32, no. 13, pp. 1205-1206, June 1996.
- [153] C. Kim, J. Garland, P. Raccah, "Modeling the optical dielectric function of the alloy system Al_xGa_{1-x}As", *Physical Review B*, vol. 47, no. 4, pp. 1876-1888, January 1993.
- [154] D. Jenkins, "Optical constants of Al_xGa_{1-x}As", *Journal of Applied Physics*, vol. 68, no. 4, pp. 1848-1853, August 1990.
- [155] C. Tsai, H. Shiao, C. Lee, Y. Tu, "High performances and reliability of novel GaAs MSM photodetectors with InGaP buffer and capping layers", *IEEE Photonics Technology Letters*, vol. 9, no. 5, pp. 660-662, May 1997.
- [156] J.R. Lothian, F. Ren, J.M. Kuo, J.S. Weiner, Y.K. Chen, "Pt/Ti/Pt/Au Schottky contacts on InGaP/GaAs HEMTs", *Solid State Electronics*, vol. 41, no. 5, pp. 673-675, 1997.

- [157] B. Saint-Cricq, A. Rudra, J.D. Ganiere, M. Ilegems, "High-reflectance GaInP/GaAs distributed Bragg reflector", *Electronics Letters*, vol. 29, no. 21, pp. 1854-1855, October 1993.
- [158] K. Shinoda, K. Hiramota, T. Tsuchiya, "High-reflectivity InGaP/GaAs multilayer reflector grown by MOCVD for high reliable 0.98- μm vertical-cavity surface-emitting lasers", *Japanese Journal of Applied Physics, part 1*, vol. 34, no. 2B, p. 1253, February 1995.
- [159] B.R. Bennett, R.A. Soref, J.A. Del Alamo, "Carrier-induced change in refractive index of InP, GaAs, and InGaAsP", *IEEE Journal of Quantum Electronics*, vol. 26, no. 1, pp. 113-122, January 1990.
- [160] D. Hahn, O. Jaschinski, H. Wehmann, A. Schlachetzki, M. Von Ortenberg, "Electron-concentration dependence of absorption and refraction in n-InGaAs near the band edge", *Journal of Electronic Materials*, vol. 24, no. 10, pp. 1357-1361, 1995.
- [161] C.J. Hwang, "Optical properties of n-type GaAs. I. Determination of hole diffusion length from optical absorption and photoluminescence measurements", *Journal of Applied Physics*, vol. 40, no. 9, pp. 3731-3738, August 1969.
- [162] D.D. Sell, H.C. Casey, K.W. Wecht, "Concentration dependence of the refractive index for n- and p-type GaAs between 1.2 and 1.8 eV", *Journal of Applied Physics*, vol. 45, no. 6, pp. 2652-2657, June 1974.
- [163] H.C. Casey, D.D. Sell, K.W. Wecht, "Concentration dependence of the absorption coefficient for n- and p-type GaAs between 1.3 and 1.6 eV", *Journal of Applied Physics*, vol. 46, no. 1, pp. 250-257, January 1975.
- [164] M. Schubert, V. Gottschalch, C.M. Herzinger, H. Yao, P.G. Snyder, J.A. Woollam, "Optical constants of $\text{Ga}_x\text{In}_{1-x}\text{P}$ lattice matched to GaAs", *Journal of Applied Physics*, vol. 77, no. 7, pp. 3416-3419, April 1995.
- [165] A. Hassine, J. Sapiel, P. le Berre, P. Legay, F. Alexandre, G. Post, "Acoustical and optical properties of $\text{Ga}_{0.52}\text{In}_{0.48}\text{P}$: a Brillouin study", *Journal of Applied Physics*, vol. 77, no. 12, pp. 6569-6571, June 1995.
- [166] S.S. Murtaza, J.C. Campbell, "Effects of variations in layer thickness on the reflectivity spectra of semiconductor Bragg mirrors", *Applied Physics Letters*, vol. 77, no. 8, pp. 3641-3643, April 1995.
- [167] S. Adachi, "Refractive indices of III-V compounds: key properties of InGaAsP relevant to device design", *Journal of Applied Physics*, vol 53, no. 8, pp. 5863-5869, August 1982.
- [168] J. Pan, J. Shieh, J. Gau, J. Chyi, J. Lee, K. Ling, "Study of the optical properties of $\text{In}_{0.52}(\text{Al}_x\text{Ga}_{1-x})_{0.48}\text{As}$ by variable angle spectroscopic ellipsometry", *Journal of Applied Physics*, vol. 78, no. 1, pp. 442-445, July 1995.

- [169] S. Nojima, H. Asahi, "Refractive index of InGaAs/InAlAs multiquantum-well layers grown by molecular-beam epitaxy", *Journal of Applied Physics*, vol. 63, no. 2, pp. 479-483, January 1988.
- [170] M. Mondry, D. Babic, J. Bowers, L. Coldren, "Refractive Indexes of (Al,Ga,In)As epilayers on InP for optoelectronic applications", *IEEE Photonics Technology Letters*, vol. 4, no. 6, pp. 627-630, June 1992.
- [171] W. Ho, M. Wu, Y. Tu, "Uniform and high performance of monolithically integrated 1x12 array of planar GaInAs photodiodes", *IEEE Transactions on Electron Devices*, vol. 44, no. 4, pp. 559-563, April 1997.
- [172] Y. Liu, S.R. Forrest, G.L. Tangonan, R.A. Jullens, R.Y. Loo, V.L. Jones, D. Persechini, J.L. Pikulski, M.M. Johnson, "Very-high-bandwidth In_{0.53}Ga_{0.47}As p-i-n detector arrays", *IEEE Photonics Technology Letters*, vol. 3, no. 10, pp. 931-933, October 1991.
- [173] Q.Z. Liu, "Design of metal-semiconductor-metal photodetector array with uniform 3-dB bandwidth", *Microwave and Optical Technology Letters*, vol. 9, no. 6, pp. 327-329, August 1995.
- [174] C.L. Goldsmith, G.A. Magel, R.J. Baca, "Principles and performance of traveling-wave photodetector arrays", *IEEE Transactions on Microwave Theory and Techniques*, vol. 45, no. 8, pp. 1342-1349, August 1997.
- [175] L.Y. Lin, M.C. Wu, T. Itoh, T.A. Vang, R.E. Muller, D.L. Sivco, A.Y. Cho, "High-power high-speed photodetectors – design, analysis, and experimental demonstration", *IEEE Transactions on Microwave Theory and Techniques*, vol. 45, no. 8, pp. 1320-1331, August 1997.
- [176] R. Sharma, R. Tholl, R. DeCorby, D. Clegg, "Frequency response characteristics of GaAs metal-semiconductor-metal (MSM) photodetector arrays", TR Labs Internal Report, TR-94-03, April 1994.
- [177] D.M. Pozar, *Microwave Engineering*, Addison-Wesley, New York, 1990.
- [178] A. Torabian, Y.L. Chow, "Method for analysing a microstrip sectorial power divider", *Electronics Letters*, vol. 33, no. 20, pp. 1713-1714, September 1997.
- [179] D. Maurin, K. Wu, "A compact 1.7-2.1 GHz three-way power combiner using microstrip technology with better than 93.8 % combining efficiency", *IEEE Microwave and Guided Wave Letters*, vol. 6, no. 2, pp. 106-108, February, 1996.
- [180] M.D. Abouzahra, K.C. Gupta, "Multiport power divider-combiner circuits using circular-sector-shaped planar components", *IEEE Transactions on Microwave Theory and Techniques*, vol. 36, no. 12, pp. 1747-1751, December 1988.
- [181] H.F. Taylor, O. Eknayan, C.S. Park, K.N. Choi, K. Chang, "Traveling wave photodetectors", *Proc. SPIE – Int. Soc. Opt. Eng.*, vol. 1217, pp. 59-63, 1990.

- [182] K.S. Giboney, M.J.W. Rodwell, J.E. Bowers, "Traveling-wave photodetector theory", *IEEE Transactions on Microwave Theory and Techniques*, vol. 45, no. 8, pp. 1310-1318, August 1997.
- [183] R.G. Walker, "High-speed III-V semiconductor intensity modulators", *IEEE Journal of Quantum Electronics*, vol. 27, no. 3, pp. 654-667, March 1991.
- [184] S. Ramo, J.R. Whinnery, T. Van Duzer, *Fields and Waves in Communication Electronics, second edition*, John Wiley & Sons, New York, 1984.
- [185] R. Nagarajan, *Diffraction Optics in Optoelectronic Switching*, Ph.D. thesis, University of Alberta, Spring 1997.
- [186] R.G. DeCorby, R.I. MacDonald, A.J.P. Hnatiw, D.B. Boertjes, J.N. McMullin, F. Gouin, J. Noad, "Packaged Array of eight MSM photodetectors with uniform 12 GHz bandwidth", *Electronics Letters*, vol. 34, no. 4, pp. 400-401, February 1998.

Appendix A: MSM Photodetectors for Optoelectronic Signal Processing – Bias Control of Responsivity

A.1. Introduction

The application of MSM photodetectors to optoelectronic switching and signal processing was discussed in Chapter 1. For switching applications, the sensitivity (minimum detectable power) of the detector or receiver circuit, for a given bit error rate, is a function of the signal to noise ratio. The signal to noise ratio is primarily affected by the detector's responsivity, capacitance, and low frequency gain characteristics. Essentially, the desired attributes for the MSM detector in switching applications are: high responsivity, low dark current shot noise, absence of excess noise due to low-frequency gain (shot noise) and gain-related trapping ($1/f$ noise), and low capacitance. These attributes must be obtained in a device having adequate bandwidth, for the desired bit rate of the system.

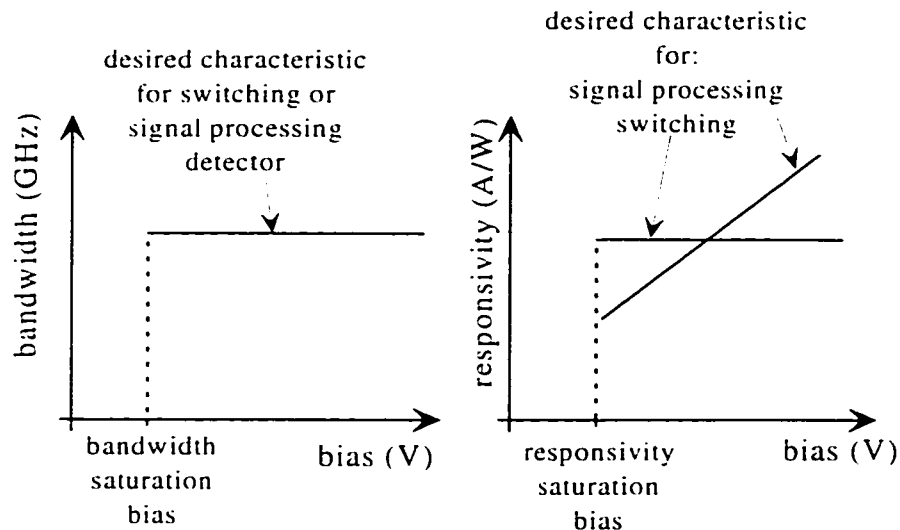


Figure A.1. The desired characteristics of MSM photodetectors for switching versus signal processing applications are illustrated schematically. For switching, it is desirable that the detector's bandwidth and responsivity saturate at low bias, so that a large and stable operating region is available. For signal processing, it is required that the detector has a bias-dependent responsivity, to accommodate the setting of tap weights. Ideally, this bias dependent responsivity is introduced without altering the bias-independent bandwidth of the switching detector.

An MSM detector with a flat photocurrent characteristic (for biases greater than a low saturation voltage) is most likely to meet the requirements described above. These points were discussed in detail in Chapters 1 and 2, and demonstrated experimentally in Chapter 3. The bandwidth of the ideal device also saturates, at a slightly higher bias, when the field throughout the absorption region is strong enough to drive holes at peak steady-state velocity (see the discussion in Section 2.7).

In direct conflict with the optimal attributes discussed above, optoelectronic signal processing elements [1],[2] require photodetectors with bias-

dependent responsivity (see Figure A.1). As discussed, in reference to Figure 1.5, the bias-controllable responsivity is used to set tap weights. Nitta et al. [3] suggested that the MSM photodetector was suitable for these types of applications. However, as recognized by Swekla and MacDonald [1], the bias-dependent responsivity exhibited by early MSM devices was a sign of deleterious physical mechanisms, incompatible with high-speed, low-noise optoelectronic systems. In particular, simple MSM photodetectors that exhibit bias-dependent responsivity also exhibit bias-dependent bandwidth.

In optoelectronic signal processing demonstrations to date, the bias dependent responsivity derived from a modulation of some aspect of carrier transport [4]. For example, bias-dependent carrier recombination or low frequency gain can be used to modulate responsivity. The problem with those approaches is that it is not possible to decouple the effects of carrier transport on device responsivity and speed. An alternative approach is suggested here. If the responsivity modulation is provided in the optical domain, for example by incorporating electro-optical materials into the device structure, then the transport properties of the device might be relatively unaffected. The proposed technique requires an increase in complexity, but only for the epitaxy. The basic electrode structure of the MSM detector is not changed. In this sense, none of the inherent advantages of the MSM detector are sacrificed, including simplicity of fabrication, low capacitance, and high speed.

The approach described in the following sections was motivated by previous research on quantum well-based optical logic gates [6], optical modulators [7-9], and wavelength-tunable photodetectors [10-12]. All of those previously reported devices were basically p-i-n photodetectors with a multiple quantum well (MQW) active region. By using a vertical structure, such as the p-i-n detector, the large electro-optic coefficients due to the quantum-confined Stark effect (QCSE) [5] are most efficiently exploited. Here, a similar approach is investigated, but with the MQW active region embedded in an MSM photodetector structure. The bias applied to the interdigitated electrodes of an MSM photodetector results in a two-dimensional field in the underlying epitaxial layers. As discussed in the following, this is not ideal in terms of exploiting the QCSE, as the lateral component of electric field between the fingers tends to ionize the band-edge excitonic features. However, the requirements for bias-dependent responsivity are less onerous than those for most of the p-i-n based devices mentioned above. For example, the device described by Lai et al. [11] was decidedly mediocre in terms of wavelength selectivity, but exhibited useful responsivity modulation over a fairly broad wavelength band (~ 20 nm).

In Section A.2, the nature of the electric field in the vicinity of interdigitated electrodes is discussed, and details affecting the operating bias range of the device are outlined. In Section A.3, some background theory on the optical and electro-optical properties of MQWs is reviewed. In Section A.4, a first-order simulation is presented, based on a semi-empirical model. The shortcomings of the model, and suggestions for improvement, are also discussed in Section A.4. In

Section A.5, the results are summarized, and conclusions are presented, relating to the long-term potential of the approach.

A.2. Electric Fields Near Interdigitated Electrodes

The field pattern near the interdigitated fingers of an MSM detector is approximately two-dimensional. This ignores the effects of fringing fields along the perimeter of the active region (at the outer edge of the outermost fingers), and also at the ‘finger tips’ (see Figure 1.3). Still, the two-dimensional approximation is very good, and has produced accurate estimates of the capacitance associated with the interdigitated electrodes. The equipotential surfaces and electric flux lines, near a single finger of an interdigitated electrode, are shown schematically in Figure A.2.

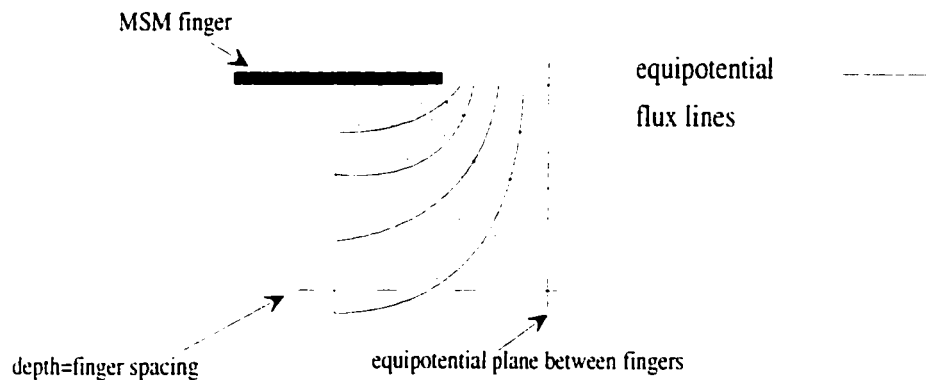


Figure A.2. A schematic illustration of the equipotential surfaces and electric field lines, near a single finger (shown in cross-section) of an interdigitated MSM detector, with finger spacing equal to finger width. The field lines are shown for a single unit cell only, with bias applied between the MSM finger and its neighboring finger (not shown). If background doping is neglected in the layers (zero space charge), an equipotential plane lies midway between adjacent fingers, as shown. In this case, all of the relevant information is contained in the unit cell shown (the field lines on the other side of the vertical equipotential plane are a mirror image). In reality, residual n-type dopants typically enhance the field near the cathode fingers, and reduce it near the anode fingers. Note that the field is strongest near the semiconductor surface, and especially near the peripheries of the electrodes. Also, the electric field is mostly lateral (parallel to the plane of the layers) in the non-shadowed regions between MSM fingers.

In all that follows, an MSM photodetector with 1 μm finger spacing and width (‘1x1’) is assumed. This geometry allows bandwidths as high as 20 GHz to be reached, as demonstrated in Chapter 3, and can be defined using standard UV lithography. As such, the 1x1 devices are a good choice for next generation optoelectronic systems.

The field pattern illustrated in Figure A.2 can be determined exactly, using one of two available sets of conformal transformations [13],[14]. The conformal transformations provide a solution of the Laplace equation ($\Delta^2\Phi=0$), rather than the Poisson equation ($\Delta^2\Phi=\rho$), so are accurate if the semiconductor is intrinsic or lightly doped. The conformal transformations are considered adequate for estimating the field distribution in real MSM structures, and have been applied to

the determination of geometrical capacitance and device speed. The conformal transformations of Gvozdic et al. [13] were employed here.

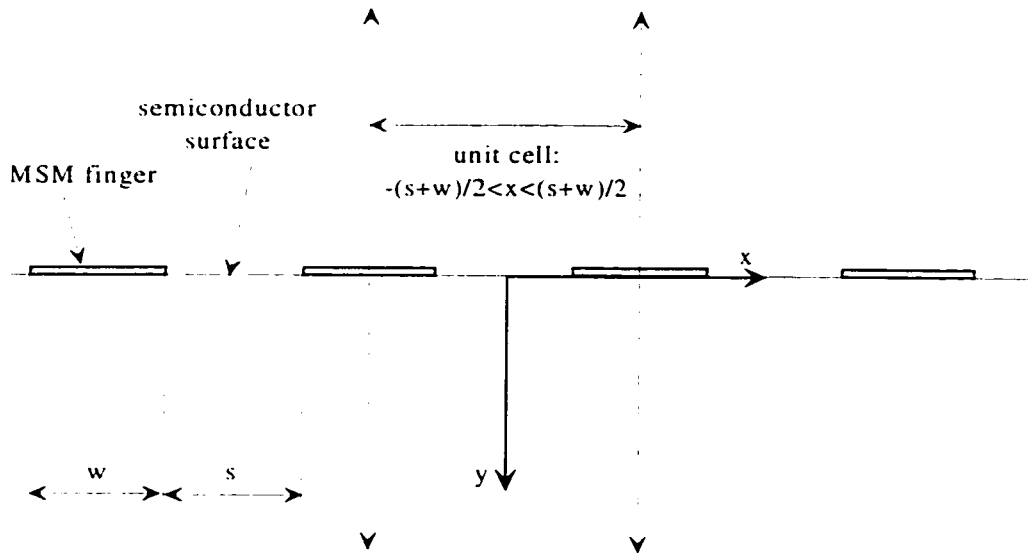


Figure A.3. The coordinate system is shown, for the conformal transformations used to determine the electric field in the vicinity of the MSM fingers. The transformations are valid for coordinates within the unit cell shown. The field pattern is identical in other unit cells. The origin lies at the semiconductor surface, midway between neighboring fingers. Lateral field components are directed along the x direction, and are also termed parallel (to the plane of the epitaxial layers). Vertical fields are directed along the y direction, and are also termed perpendicular (to the plane of the epitaxial layers).

The coordinate system, relevant to the transformations, is illustrated in Figure A.3. The origin lies at the semiconductor surface, midway between the fingers. The lateral dimension, parallel to the epitaxial layers, is labeled x . The vertical dimension is labeled y . The transformations provide the electrostatic potential, from which the fields can be derived, for any coordinate within the unit cell shown: $-(s+w)/2 < x < (s+w)/2$, where s is the finger spacing and w is the finger width. It should be noted that the transformations are derived under the assumption of zero-thickness fingers. Thus, the derived electric field exhibits a pole at the electrode peripheries ($x = \pm(s/2)$, $y = 0$). In a real device, with fingers of finite thickness, this would be the location of a high but finite electric field.

Figure A.4 is a three-dimensional plot of total electric field magnitude, for an MSM photodetector with $1 \mu\text{m}$ finger spacing and width and an applied bias of 10 V. Note the peaked fields at the finger peripheries. High fields in these locations are often responsible for the deleterious low frequency gain in MSM devices, discussed in Chapters 2 and 3. Also note that the total field magnitude is quite uniform away from those locations, and equal to about half the nominal value (bias/finger spacing). This was relevant to the discussion of bandwidth saturation, in Section 2.7.

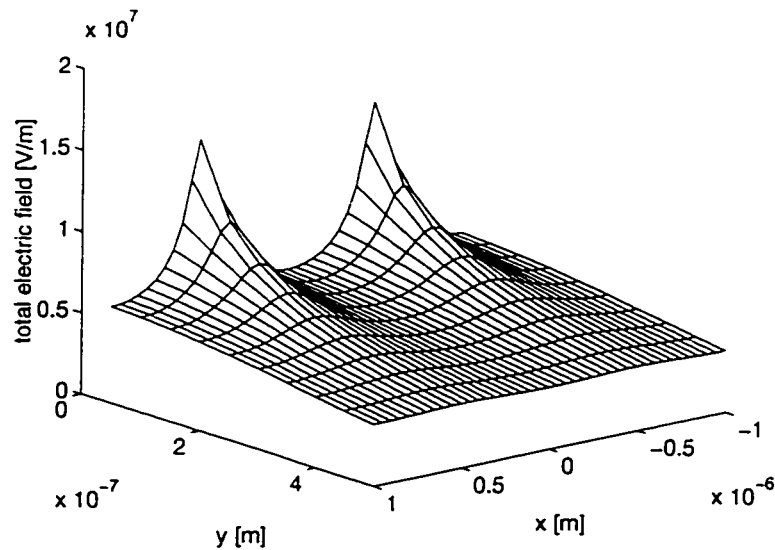


Figure A.4. The total electric field magnitude in the vicinity of adjacent MSM fingers. The coordinate system is as shown in Figure A.3, and the plot is for a 1×1 device, biased at 10 V. Data is plotted to a depth of $0.5 \mu\text{m}$, which represents a typical absorption region thickness for the devices in Chapters 3 and 4. The field is peaked at the semiconductor surface, near the peripheries of the fingers. Away from these locations, the total field magnitude is quite uniform, and about half the nominal value (bias/finger spacing).

For the simulations to follow, it is necessary to determine the components of electric field perpendicular and parallel to the plane of the epitaxial layers. This is because the electro-optic effects in semiconductor quantum wells are distinctly different for vertical and lateral fields [5]. In Figure A.5 and Figure A.6 respectively, the lateral and vertical field components are plotted for the same geometry as in Figure A.4.

As illustrated schematically in Figure A.2, the regions between MSM fingers tend to have high lateral fields and low vertical fields. Conversely, the regions beneath the fingers exhibit high vertical fields and relatively low lateral fields. As discussed in the following section, the electro-optic effects in semiconductor quantum wells are larger for fields perpendicular to the plane of the epitaxial layers. Thus, devices that absorb in the regions beneath the fingers, such as rear-illuminated or transparent-electrode devices, may be superior as electro-optic modulators. A more detailed discussion is provided in Section A.4.

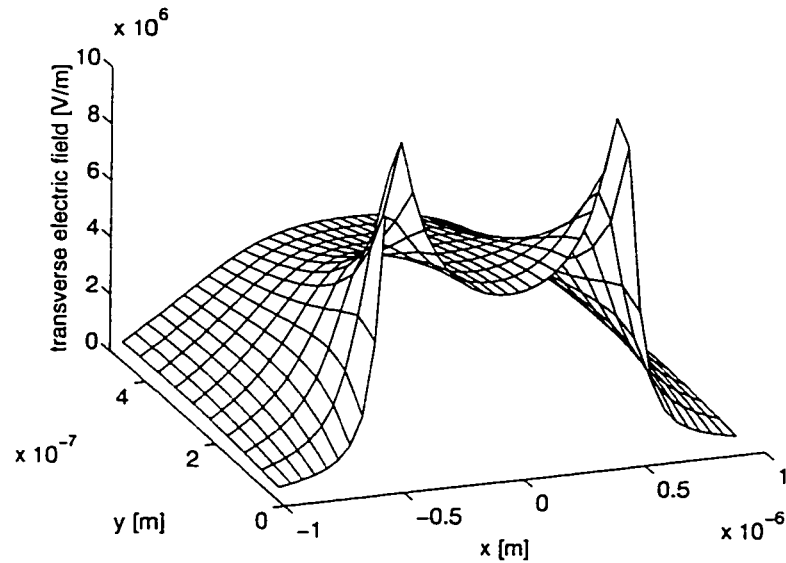


Figure A.5. The transverse (lateral) electric field is plotted, for the same geometry as in Figure A.4. Note that the lateral field is strongest in the regions between fingers, and is relatively weak beneath the fingers.

A.2.1. Device Operating Range – Bandwidth Saturation

As mentioned in Section A.1, the goal here is to design a device with bias-independent bandwidth and bias-dependent responsivity. Specifically, the responsivity should be variable over a bias range for which the device speed is constant and saturated. In order to fulfill the requirement of bias-independent bandwidth, it may be necessary to tailor the geometry and other properties of the device, such that the electro-absorptive effects occur over a bias range for which carrier velocities are saturated.

In the following, it is assumed that the devices of interest have finger spacing and width of $1\ \mu\text{m}$. Also, since the proposed devices are predicated on the resonant-cavity concepts discussed in Chapter 4, the absorption region thickness is typically $0.5\ \mu\text{m}$. Bandwidth saturation in a detector having this geometry was discussed in Section 2.7. It was found that in the absence of low-frequency gain, carrier trapping, or free-carrier pileup, 2 to 3 V bias should be sufficient to produce saturation bandwidth. Thus, it is necessary that electro-optic effects be manifested over the bias range of approximately 2 to 10 V. This would ensure bandwidth saturation over the operating range of interest, and is compatible with standard logic devices, an advantage for system integration.

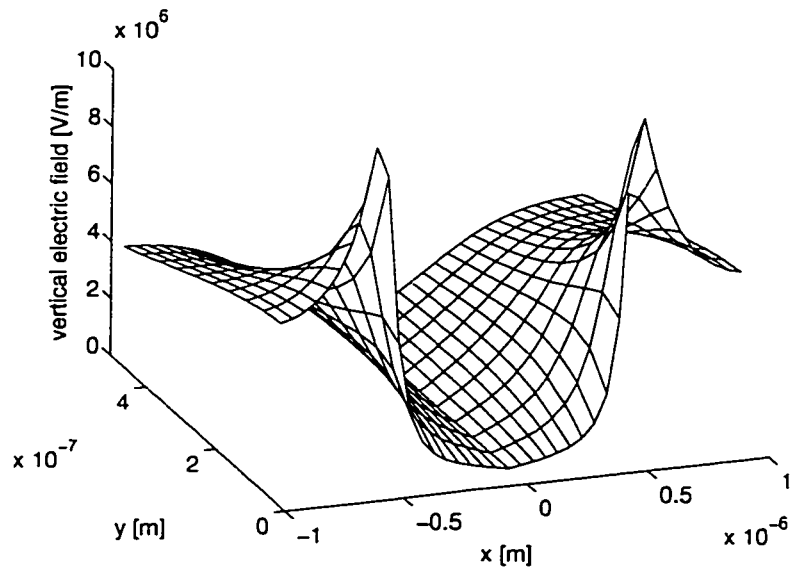


Figure A.6. The vertical electric field is plotted, for the same geometry as in Figure A.4. The strongest vertical fields exist in the regions beneath and near the MSM fingers. The regions between fingers primarily contain lateral fields (parallel to the plane of the epitaxial layers).

A.3. Semiconductor Quantum Wells

Semiconductor quantum wells have been the focus of intense research for the past two decades [6],[15]. The primary technological uses derive from the altered density-of-states characteristics, for electrons confined to two dimensions. This allows operational wavelengths to be tailored, as well as improving the efficiency of emitters, and has been commercially exploited in quantum well lasers [16], and recently in inter-sub-band infrared detectors [6]. Another consequence of two-dimensional confinement is that large electro-optical characteristics are present at the quantum well band edge. They are associated with strong, room-temperature exciton transitions. These electro-optic effects have been used to demonstrate various optical switches and modulators [8],[9], but the electro-optical devices are less established commercially.

Quantum confinement effects are manifested in semiconductor layers that are thinner than the de Broglie wavelength ($\lambda=h/p$) in the material. In such cases, the electrons behave approximately as if they exist in a two-dimensional solid. This has been of great interest both to theoretical physicists and device designers [17],[18]. A recent review by Fox [6] is a good introduction to the subject. The discussion that follows is not intended to be comprehensive, but rather is a brief review of the theory used in Section A.4.

A.3.1. Electronic States in Semiconductor Quantum Wells

The formation of discrete energy sub-bands in alternate narrow and wide band-gap semiconductor layers is illustrated schematically in Figure A.7. The dashed lines in Figure A.7 represent the allowed z-components of energy, for carriers in the layered solid. Since there is no confinement in the x and y

directions, there is actually a continuum of allowed energy levels between those indicated (for example, between $e1$ and $e2$), although in the ideal well no allowed states lie below the ground-state confinement energies ($e1$, $hh1$).

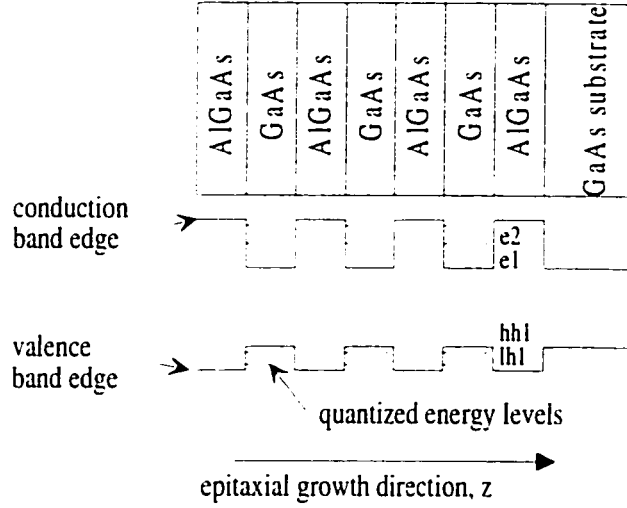


Figure A.7. Epitaxial layers (top) and band diagram (bottom) for a GaAs/AlGaAs multiple quantum well (MQW) structure. The quantized energy levels shown are labeled $e1$ and $e2$ for the electron states, $hh1$ for the lowest heavy-hole derived state, and $lh1$ for the lowest light-hole derived state.

Ignoring excitonic effects initially, the quantized energy levels can be estimated by treating electrons and holes independently. In this simple model, the carriers are single, non-interacting particles, moving in the periodic conduction and valence band potentials of the layered semiconductor. The three dimensional Schrodinger equation is generally simplified using the envelope function approximation (EFA) [15],[19]. The EFA is essentially a separation-of-variables technique, for which motion in the plane of the quantum well is treated independently of that perpendicular to the wells. Further, the effective mass approximation (EMA) [5] is generally adopted in first-order treatments, with careful attention to appropriate effective mass values.

In the EFA, the wavefunctions of the carriers in the MQW region take the form [15]

$$\psi = \sum_{\text{well,barrier}} e^{i\mathbf{k}_{xy} \cdot \mathbf{r}} u_{\text{well,barrier}}(\mathbf{r}) \chi_n(z) , \quad (\text{A.1})$$

where ψ is the total wavefunction, \mathbf{k}_{xy} is the transverse wave vector (in the plane of the layers), \mathbf{r} is the transverse positional vector (x,y), $u(\mathbf{r})$ is the Bloch function describing bulk transport in the well and barrier materials, and $\chi_n(z)$ is the so-called envelope wavefunction describing the z -dependence of the overall solution.

Given the EFA, $\chi_n(z)$ is accurately derived as the solution of a Schrodinger-like equation,

$$\left(\frac{-\hbar^2}{2m^*(z)} \frac{\partial^2}{\partial z^2} + V_{c,v}(z) \right) \chi_n(z) = E_n \chi_n(z), \quad (\text{A.2})$$

where $m^*(z)$ is position-dependent effective mass, $V_{c,v}(z)$ is the potential represented by the conduction or valence band edge in Figure A.7, and E_n are the z -direction eigen-energies of the electrons. The solutions are therefore those of the simple finite potential well, treated in elementary quantum-mechanics texts [20]. One caveat is that the potential mass is position-dependent here, and probability current density must be conserved. Thus, the boundary conditions are continuity of χ and $(1/m^*)(d\chi/dz)$, at each interface between well and barrier material.

The solutions take the form of sinusoids in the well and decaying exponentials in the barriers, as illustrated in Figure A.8.

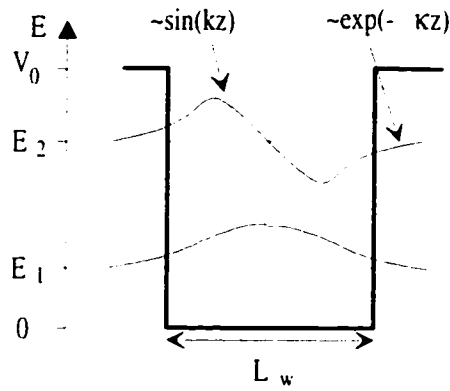


Figure A.8. Schematic illustration of the two lowest bound states in a finite quantum well. V_0 is the well depth. E_2 and E_1 are the eigen-energies, k and κ are wave-numbers in the well and barrier material, respectively, and L_w is the well width. Note that the overlap integral between states of opposite parity (symmetry about the well center) is nearly zero.

The solutions are conveniently divided into two groups, having odd ($n=2,4,\dots$) or even ($n=1,3,\dots$) symmetry about the well center. k_n and κ_n are the wave vectors in well and barrier, respectively, and are related to the eigen-energies, as

$$E_n = \frac{\hbar^2 k_n^2}{2m_w} = V_0 - \frac{\hbar^2 \kappa_n^2}{2m_b}, \quad (\text{A.3})$$

where m_w and m_b are the appropriate effective masses in well and barrier, respectively. Applying the boundary conditions to the solutions illustrated in Figure A.8 gives

$$\begin{aligned} \left(\frac{k_n}{m_w} \right) \tan\left(k_n L_w / 2 \right) &= \kappa_n / m_b ; n = 1, 3, 5, \dots \\ \left(\frac{k_n}{m_w} \right) \cot\left(k_n L_w / 2 \right) &= -\kappa_n / m_b ; n = 2, 4, 6, \dots \end{aligned} \quad (\text{A.4})$$

Equations (A.4) and (A.5) must be solved numerically or graphically, but yield the wavefunctions and their eigen-energies. The number of bound states, N , in a well, is given by [15]

$$N = 1 + \text{Int} \left[\left(\frac{2m_w V_0 L_w^2}{\pi^2 \hbar^2} \right)^{1/2} \right], \quad (\text{A.5})$$

where $\text{Int}[x]$ means the integer part of x . There is always at least one bound state.

For a given pair of component semiconductors, the parameters which must be independently known include the well width, the band offsets (which determine the well depth), and the appropriate effective masses in well and barrier. A numerical solution was obtained for GaAs/ $\text{Al}_x\text{Ga}_{1-x}\text{As}$ quantum wells, using the following definitions. The band offsets are [6]

$$\begin{aligned} V_c &= 1.255 * 0.65 * x \\ V_h &= 1.255 * 0.35 * x \end{aligned} \quad (\text{A.6})$$

where V_c and V_h are the conduction and valence band offsets, respectively. The effective masses are approximated as [5]

$$\begin{aligned} m_e &= 0.067 + 0.083x \\ m_h &= 0.34 + 0.42x \end{aligned} \quad (\text{A.7})$$

where m_e and m_h are the electron and heavy-hole effective masses, respectively, as a function of the Al concentration, x . The hole effective mass is anisotropic, and the value given is correct for transport in the (100) growth direction (perpendicular to the plane of the layers). For the electrons, non-parabolic band effects were introduced as described by Stevens et al. [21]. As an example, the e1 to hh1 transition wavelength, as a function of well width and Al concentration in the barriers, is plotted in Figure A.9.

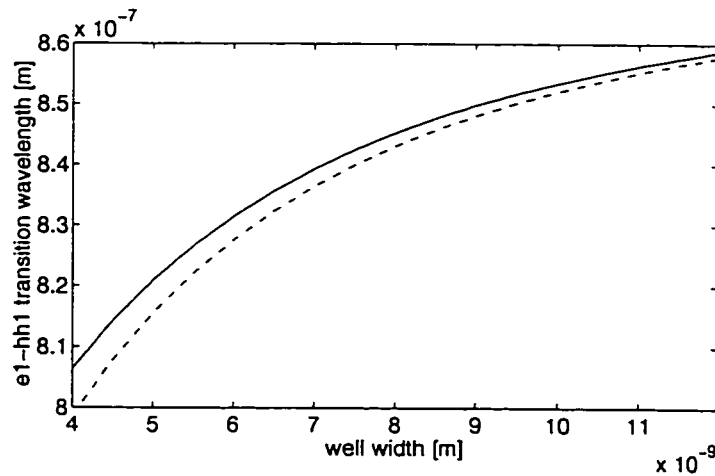


Figure A.9. The transition wavelength between ground state confinement energies, e1 to hh1, in a GaAs/ $\text{Al}_x\text{Ga}_{1-x}\text{As}$ quantum well. The data are plotted as a function of well width, for $x=0.2$ (dotted line), $x=0.3$ (solid line), and $x=0.4$ (dashed line).

A.3.2. Absorption in Quantum Wells

As a result of the altered band characteristics, the optical properties of quantum wells are much different than for the same material in bulk form. To illuminate the effects, Fermi's golden rule [20] is useful. It allows basic emission and absorption processes to be calculated as

$$W(i \rightarrow f) = \frac{2\pi}{\hbar} \left| \langle f | e r \cdot \xi | i \rangle \right|^2 g(\hbar\omega), \quad (\text{A.8})$$

where W is the rate of optical transitions from an initial state i to a final state f . The term in brackets is the overlap integral, er is the electric dipole vector, and ξ is the electric field vector for the photon involved in the transition. The effective density of states is given by g .

In the quantum well, optical transitions are between the sub-bands discussed in the preceding sub-section, according to established selection rules [15]. For example, the main transitions are between electron and hole states with the same quantum number, such as $e1$ - $hh1$ or $e1$ - $lh1$. In fact, for devices that rely on electro-absorption near the band edge, those two transitions dominate. In the semi-empirical model used here, which is similar to others [21],[22], only these transitions are considered. The band edge for optical transitions between continuum states is given by

$$h\nu_{\min} = E_{gw} + E_{e1} + E_{hh1}, \quad (\text{A.9})$$

where E_{gw} is the band-gap of the bulk well material, and E_{e1} and E_{hh1} are the electron and heavy-hole confinement energies, discussed in the preceding sub-section. The absorption edge has a step-like characteristic, and absorption is independent of photon energy up to the next allowed transition, $e1$ - $lh1$, where another step increase in absorption occurs. This is due to the step-like density of states for the confined electrons in the well. A good discussion is available in [6].

As in three-dimensional semiconductors, coulomb forces (between the electron and hole created in the annihilation of the photon) affect the absorption rate. An important result of quantum confinement is that electrons and holes, once generated, are in closer proximity. This increases the coulombic interaction of photogenerated carriers, and produces large excitonic features in the absorption spectra [6].

Optical transitions that create excitons occur at photon energies just beneath the corresponding band edge. For example, the transition energy for creation of the $e1$ - $hh1$ exciton is given approximately by [6]

$$h\nu_{exc1} = E_{gw} + E_{e1} + E_{hh1} - E_{exc}, \quad (\text{A.10})$$

where $h\nu_{exc1}$ is the photon energy associated with creation of the lowest-lying exciton, and E_{exc} is the ground-state binding energy of heavy-hole-derived excitons inside the well. Each sub-band has a similar associated exciton transition.

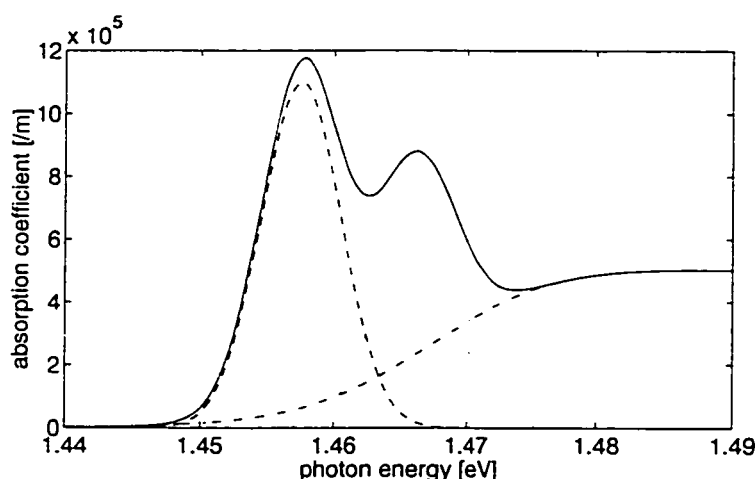


Figure A.10. A semi-empirical model for absorption at the band edge of a 9.6 nm wide GaAs/Al_{0.3}Ga_{0.7}As MQW. Three contributions to absorption are included as described in the text: heavy-hole exciton (dashed line), light-hole exciton (dotted line), and broadened continuum (dash-dotted line). The solid line represents total absorption. The fitting parameters are the peak absorption coefficients, the linewidths, and the energy position of each contribution. For the heavy-hole exciton, the assumptions are a peak absorption coefficient of $1.1 \mu\text{m}^{-1}$, a linewidth (half-width at half-maximum) of 3 meV, and a peak position of 1.4575 eV. For the light-hole exciton, the peak absorption is $0.63 \mu\text{m}^{-1}$, the linewidth is 3 meV, and the peak position is 1.466 eV. For the continuum, a linewidth of 5 meV was assumed, and the band edge is at 1.4675 eV. After reference [23].

At absolute zero temperature, in a defect-free quantum well, the absorption due to continuum transitions would be a perfect step function at each sub-band edge. Also, absorption at the exciton eigen-energies would appear as a series of spikes beneath the band edge, with zero linewidth. In reality, various homogeneous and inhomogeneous broadening mechanisms are present. At finite temperature, homogeneous (lifetime) broadening is due mainly to carrier and exciton collisions with phonons. In MQWs, the main cause of inhomogeneous broadening is layer thickness fluctuations [21].

In any case, many authors [21-23] have used a semi-empirical approach in modeling the absorption characteristics near the band-edge of a MQW. This is discussed in greater detail in Section A.4. The model of Chemla et al. [23] was adopted here. Three contributions to absorption near the band edge are included: a broadened Gaussian line-shape function for each of the e1-hh1 and e1-lh1 exciton transitions, and a single broadened two-dimensional continuum, incorporating both the e1-lh1 and e1-hh1 sub-band contributions. An example is shown in Figure A.10.

A.3.3. *Electro-Optic Effects in Semiconductor Quantum Wells*

Nearly all of the experimental and theoretical data in the literature are for fields applied perpendicular to the plane of the MQW layers, as is relevant to p-i-n devices. In p-i-n devices, an undoped MQW region is grown between p- and n-doped contacting layers, to form an essentially one-dimensional structure. In the MSM case, the applied field is two-dimensional, as discussed in Section A.2.

Thus, it is necessary to consider electro-optic effects for fields both perpendicular and parallel to the plane of the layers. To that end, the limited data available [5] for parallel field electro-optic effects were used to develop a first-order empirical model. In the following two sub-sections, electro-optical effects due to fields applied perpendicular and parallel to the plane of MQW layers are briefly reviewed.

A.3.3.1. Electro-Optic Effects Due to Perpendicular Fields

As described initially by Miller et al. [5], electric fields perpendicular to the plane of the layers produce extremely large and useful electro-optic effects near the band-edge in MQWs. This was termed the quantum-confined Stark effect (QCSE), due to analogous shift (and splitting) of electronic energy levels for hydrogenic atoms in electric fields. The analogy derives from the predominance of exciton effects in the band-edge optical characteristics of the MQW.

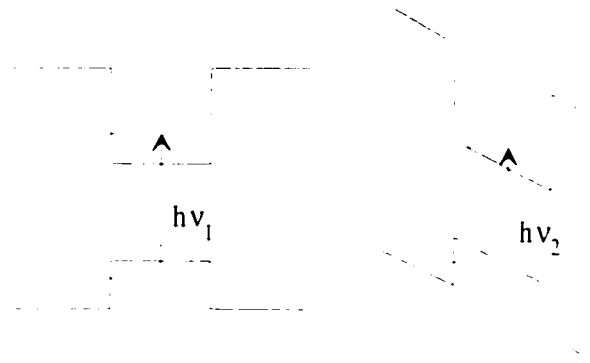


Figure A.11. Schematic illustration of the red-shift of the optical band-edge in a quantum-well. At zero field (left), the wells are rectangular in shape, and both the electron and hole ground state have highest probability at the center of the well. For a finite perpendicular field (right), the confined particles reside in a trapezoidal well, with sloping potential. The ground-state hole has highest probability near the left barrier, the ground-state electron near the right. The band edge is red-shifted by the field ($h\nu_2 < h\nu_1$), and the exciton oscillator strengths (peak absorption) are reduced, due to a reduction in the overlap of electron and hole wavefunctions in the well.

Under perpendicular field conditions, the quantum well absorption edge exhibits a marked red-shift. In addition, the exciton peaks remain resolvable, even for fields as high as a few tens of $\text{V } \mu\text{m}^{-1}$ [6]. The shift of the e1-hh1 exciton peak, representative of the band-edge, can be as much as a few times the zero-field exciton binding energy. This corresponds approximately to a band-edge shift of 10 to 20 nm for GaAs wells, with band edges in the 800 nm wavelength range. The shift is made possible by the confining band offsets of the barrier layers, which inhibit field ionization of the excitons. While the exciton is not ionized, the ground-state confinement energies of the electrons and holes are reduced in the perturbed well potential, and the optical transitions (see (A.10)) are shifted to lower energy. This is illustrated schematically in Figure A.11.

As shown, with an applied perpendicular field the carriers no longer reside in a square well, but rather in a trapezoidal well with sloping potential. The wave

functions in the well cease to have symmetry about the well center; rather the electron has highest probability density near the right barrier, and the holes near the left. This has several effects on the optical properties of the well, including a relaxation of the selection rules ($\Delta n=0$) [15] mentioned in Section A.3.2, so that previously forbidden transitions are observed. Also, the dominant zero-field transitions are weakened in the applied field, as electrons and holes reside increasingly near opposite sides of the well, and the overlap integral of the non-orthogonal wavefunctions is decreased.

The holes and electrons are not perfectly confined in a finite well, but rather escape due to thermionic emission and tunneling, at a rate that increases with field [6]. Carrier escape represents exciton ionization, and excitonic features are completely destroyed at very high fields.

The band-edge shift due to perpendicular fields has been modeled using variational, Monte Carlo, and perturbation techniques [21]. The technique employed here was the tunneling resonance method [5],[21],[24]. In the tunneling resonance technique, a single well and its adjacent barriers are modeled, as illustrated in Figure A.12. The bands are sloped, to reflect the applied field. Each layer is divided into a large number of steps, each step having a constant potential energy.

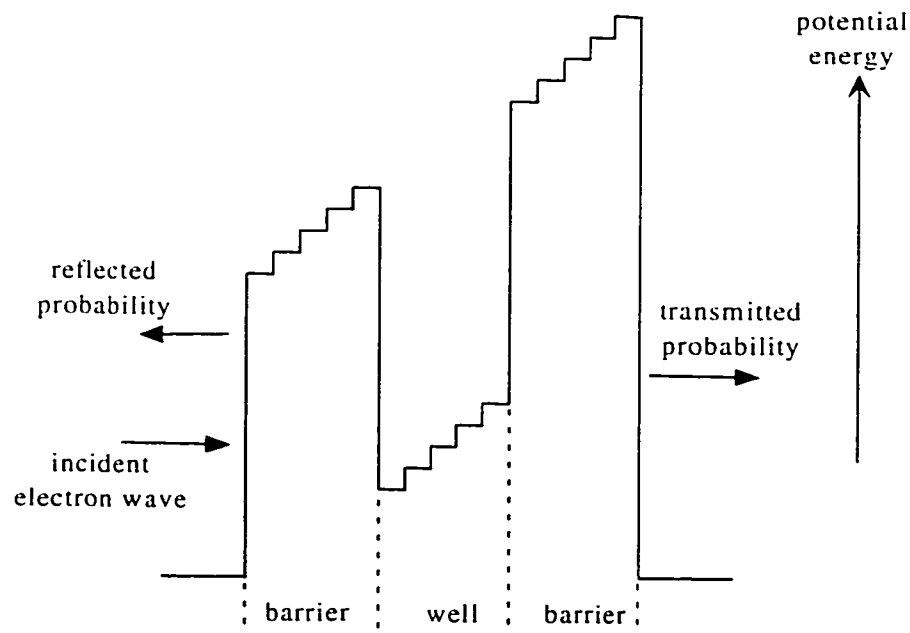


Figure A.12. The tunneling-resonance technique is illustrated schematically. The technique is used to estimate the quantized energy levels in a quantum well, with field applied perpendicular to the plane of the layers. Each layer is divided into multiple steps, each step having a constant potential. This allows simple exponential solutions to be assumed at each step. The energy of an incident electron wave is varied, and resonant peaks in the transmission or reflection spectra indicate the quantized energy levels in the well.

Because each step is characterized by a constant potential, the envelope functions can be approximated using simple exponentials.

$$\chi(z) = A \exp(ikz) + B \exp(-ikz) . \quad (\text{A.11})$$

A and B are the amplitudes of forward and reverse waves, which may be propagating or evanescent. The wavenumber is given by

$$k = \frac{\{2m(E - V(z))\}^{1/2}}{\hbar} , \quad (\text{A.12})$$

where m is the appropriate effective mass, E is the trial eigen-energy, and V is the position-dependent potential energy. The transmission or reflection spectra can be determined using a transfer-matrix formalism, identical to that used to determine the optical spectra of semiconductor layers, in Chapter 4. The same formalism is also used to treat wave propagation on periodically loaded lines, in Chapter 5. Here, the transfer-matrix relates the wave function and the probability density current at each interface:

$$\begin{bmatrix} \chi \\ 1/m \partial\chi/\partial z \end{bmatrix}_{out} = M_T \begin{bmatrix} \chi \\ 1/m \partial\chi/\partial z \end{bmatrix}_{in} . \quad (\text{A.13})$$

where m is the position-dependent effective mass, and M_T is the total transfer-matrix for the system of potential energy steps in Figure A.12. The transfer-matrix for each step is given by

$$M_T = \begin{bmatrix} \cos(k\Delta z) & m/k \sin(k\Delta z) \\ -k/m \sin(k\Delta z) & \cos(k\Delta z) \end{bmatrix} , \quad (\text{A.14})$$

where Δz is the width of the step. Similar to the derivation in Chapter 4, the reflection coefficient for the entire system of steps is obtained as

$$r = \frac{-i \left(\frac{k_{out}}{m_{out}} \right) M_{T11} - \left(\frac{k_{out} k_{in}}{m_{out} m_{in}} \right) M_{T12} - M_{T21} + i \left(\frac{k_{in}}{m_{in}} \right) M_{T22}}{i \left(\frac{k_{out}}{m_{out}} \right) M_{T11} - \left(\frac{k_{out} k_{in}}{m_{out} m_{in}} \right) M_{T12} + M_{T21} + i \left(\frac{k_{in}}{m_{in}} \right) M_{T22}} . \quad (\text{A.15})$$

k_{out} and k_{in} are the wavenumbers in the output and input layers, respectively, and m_{out} and m_{in} are the corresponding effective masses. A numerical simulation was implemented, based on these equations. As an example, Figure A.13 shows the tunneling resonance for a GaAs/Al_{0.3}Ga_{0.7}As combination, with a well and barrier width of 10 nm. The resonance shown is for the ground-state electron level, e1, with no applied field.

Note that the reflection coefficient falls to zero at the position of the allowed energy level. This reflects the fact that the equations are time-independent: an electron wave of infinite duration (perfectly defined energy) would have a tunneling probability of 1, at the resonant energy. The technique also provides information on the broadening of optical transitions, due to field-induced tunneling out of the well. This contribution is obtained directly from the linewidth

of the tunneling resonance [5]. For typical quantum wells, the broadening due to tunneling out of the wells is relatively negligible [21], compared to the phonon broadening mentioned in Section A.3.2.

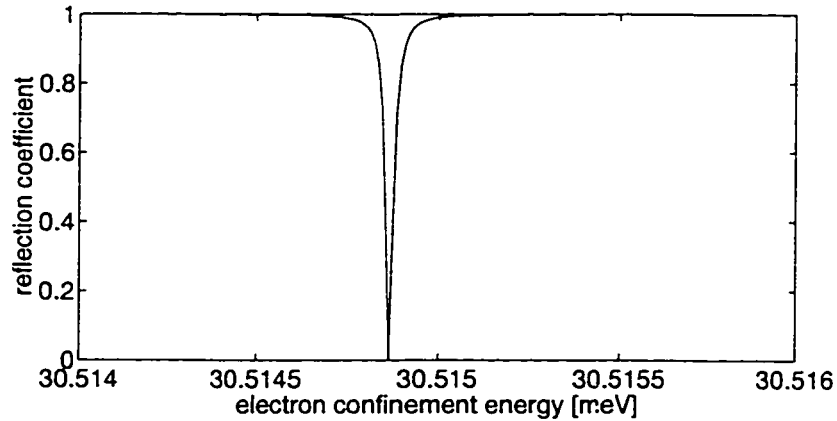


Figure A.13. The result of a tunneling resonance simulation, as described in the text, for a 10 nm GaAs well. A barrier width of 10 nm was used, and the barrier material was $\text{Al}_{0.3}\text{Ga}_{0.7}\text{As}$. The resonance shown indicates the approximate position of the ground-state confinement energy for electrons, e_1 , with no applied field.

The field-dependent sub-band gap was determined by applying the tunneling resonance technique to electrons and heavy holes, sequentially, and plugging the results in (A.9). This neglects excitonic effects, but is a good approximation of the shift of band-edge features with applied field. The exciton binding energy, introduced in (A.10), is relatively insensitive to perpendicular fields [5]. In Figure A.14, the sub-band gap is plotted as a function of perpendicular field, for the well parameters defined in Figure A.13.

Note that for the fields shown in Figure A.14, the band-edge shift is proportional to the square of the applied field (quadratic Stark shift [21]). For significant shifts, vertical fields in the 5 to $10 \text{ V } \mu\text{m}^{-1}$ range are necessary. Wider wells exhibit larger shifts at low fields, but their excitonic features are also destroyed at lower fields [22]. The data in Figure A.14 were used in the simulations of Section A.4.

A.3.3.2. Electro-Optic Effects due to Parallel Fields

The electro-optic effects due to fields parallel to the plane of quantum well layers have received relatively little attention. This can be understood qualitatively from the discussion in the preceding section: there is no confinement of carriers, to prevent exciton ionization, for fields applied in the transverse direction. However, large electro-optic features do occur at the excitonic transitions. This is due to lifetime broadening, which smears out the large peaks in the zero-field spectra.

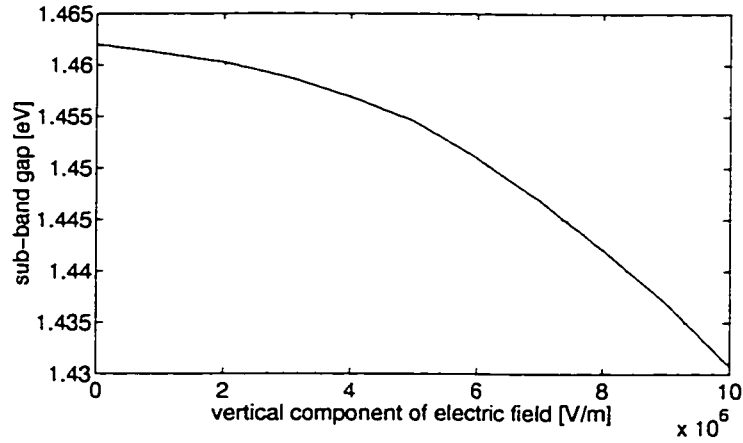


Figure A.14. The sub-band gap, given by (A.9), is plotted as a function of electric field applied perpendicular to the plane of the quantum well layers. The parameters of the well are the same as indicated for Figure A.13. The gap was determined using the tunneling resonance technique described in the text.

Of interest is the field required to ionize the exciton, closely related to the field at which excitonic features are completely destroyed, and beyond which only relatively small electro-optic effects are present. A first-order approximation for the ionization field is [5]

$$F_i = \frac{E_{exc}}{ea_{exc}} \quad , \quad (A.16)$$

where a_{exc} is the effective Bohr radius of the exciton in the well. Typical values [5] in a GaAs well are an exciton binding energy of 10 meV, and an effective radius of 10 nm, which suggests an ionization field of $1 \text{ V } \mu\text{m}^{-1}$. This is critical, because in the devices proposed here two-dimensional fields are present. It is desirable that the parallel field components do not completely destroy the exciton features, so that the large electro-optic effects engendered by the perpendicular fields can be used. The target operating range is 2 to $10 \text{ V } \mu\text{m}^{-1}$ (see Section A.2), so the conclusion from (A.16) is that large electro-optic effects are not likely to be available with two-dimensional fields. In other words, (A.16) predicts that the parallel field will destroy exciton features at low bias, before the device operating range is reached.

Fortunately, the available experimental data seem to indicate that (A.16) is overly pessimistic as an estimate of exciton ionization. Miller et al. [5] provided a detailed discussion of parallel field effects in GaAs/AlGaAs quantum wells. Their conclusion was that the electro-optic effects were qualitatively similar to those observed in bulk semiconductors: exciton resonances were broadened, by a reduction in lifetime due to field ionization.

Exact treatments are available for excitons in three- [5] and two- [25] dimensional semiconductors. A real quantum well lies between these limits, and the behavior of excitons in the well is not rigorously described by either theory. For the purposes of the semi-empirical model in Section A.4, it is necessary to

model the loss in peak absorption and the broadening, for each of the band-edge features. Miller et al. noted [5] that their experimental data were in closer agreement with the two-dimensional exciton theory. The confined excitons are resolvable at much higher fields than are their three-dimensional counterparts. They developed an analytical expression for the linewidth contribution due to field ionization (by fields in the plane of the well), for a two-dimensional exciton:

$$\Gamma_{2D} = \frac{64R_y}{\sqrt{\pi}} \left[\frac{R_y}{eF_{par}a_0} \right]^{1/2} \exp \left[\frac{-32R_y}{3eF_{par}a_0} \right]. \quad (\text{A.17})$$

R_y is the three-dimensional exciton Rydberg energy (approximately 4.2 meV in GaAs), and a_0 is the three-dimensional exciton Bohr radius (approximately 14 nm in GaAs). F_{par} is the electric field parallel to the plane of confinement. As mentioned, real wells do not exhibit perfect two-dimensional confinement. Thus, (A.17) is expected to underestimate the broadening with field in a real well. Nevertheless, it is possible to obtain good fits to the experimental data in [5], using the band-edge model described in Section A.4, and broadening contributions given by (A.17). This is illustrated in Figure A.15.

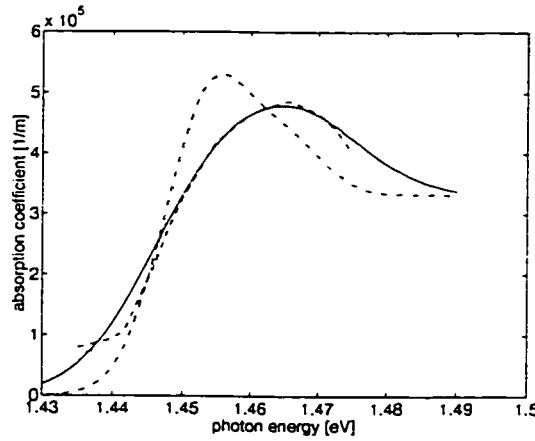


Figure A.15. Semi-empirical fits to the experimental data in [5] are shown. The data are for parallel fields in a 10 nm GaAs well: $1.6 \text{ V } \mu\text{m}^{-1}$ (dotted line), $4.8 \text{ V } \mu\text{m}^{-1}$ (dashed line). The fitted curves are similar to that shown in Figure A.10. A continuum band-edge at 1.465 eV, with linewidth (HWHM) of 5.5 meV, was used. The continuum parameters were assumed insensitive to the applied field. The heavy-hole exciton is located at 1.4532 eV, and the light-hole exciton at 1.4642 eV. The positions of the excitons were also assumed insensitive to parallel field. A zero-field exciton linewidth of 4.6 meV [5] was used, and they were broadened according to (A.17). The peak absorption of each exciton was subsequently adjusted to match the experimental data.

As shown in Figure A.15, the two-dimensional broadening theory seems to be in reasonable agreement with the limited experimental data available. Therefore, it was used in the simulations of Section A.4. It is important to note, however, that (A.17) is expected to be optimistic, in comparison with the behavior of real wells. This represents the least justified assumption in the model presented in Section A.4.

A.4. Semi-Empirical Simulations

Based on the theory developed in the preceding sections, a first-order, numerical simulation was developed. The goal was to investigate the possibility of employing band-edge electro-optic effects in multiple quantum wells, to obtain an MSM detector with bias-dependent responsivity. The proposed device is illustrated in Figure A.16. Essentially, a MQW active region is introduced in a resonant-cavity MSM detector (see Chapter 4). The device is similar to p-i-n optical modulators and detectors investigated by others [7-12]. The resonant cavity increases the optical interaction length, by multiple internal reflections, thereby maximizing the effectiveness of the electro-optic coefficients.

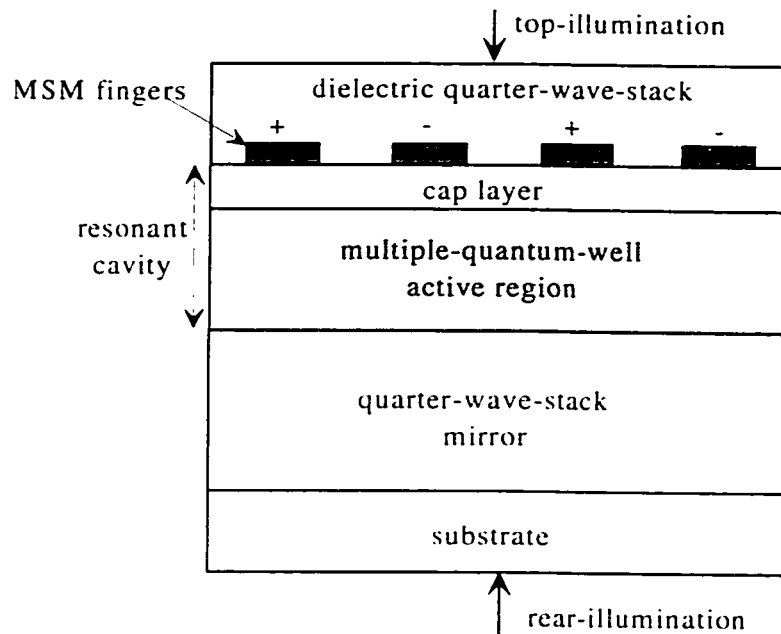


Figure A.16. Representative structure proposed to achieve bias-dependent responsivity for a gain-free MSM photodetector. Both front and back mirrors are included, to increase the quality factor of the resonant cavity as needed. Also, both top and rear illumination are considered, since the opaque fingers shadow regions of high vertical field (see Section A.2) in the top illumination case. For rear-illumination, the substrate must be transparent or removed.

To take advantage of extensive empirical data in the literature, 10 nm GaAs wells, with $\text{Al}_{0.3}\text{Ga}_{0.7}\text{As}$ barriers, were assumed. The details of the model are illustrated schematically in Figure A.17. A complete numerical simulation was implemented using Matlab, similar to the file contained in appendix B. The simulation determines the predicted absorption characteristics of the MQW active region, as a function of bias.

In brief, the model is based on dividing a representative cell of the MQW active region into a two-dimensional matrix of points. The electric field is calculated at each point in the matrix. Based on local electrical field components (parallel and perpendicular to the wells), the absorption characteristics at each point are estimated as discussed in Section A.4.1. Subsequently, the overall optical absorption, reflection, and transmission spectra are calculated, for each

column of the matrix in turn. Finally, the spectra of all columns are averaged, to obtain an estimate of the overall absorption characteristics of the MSM detector. The model contains many approximations, but is useful for estimating the feasibility of the concept.

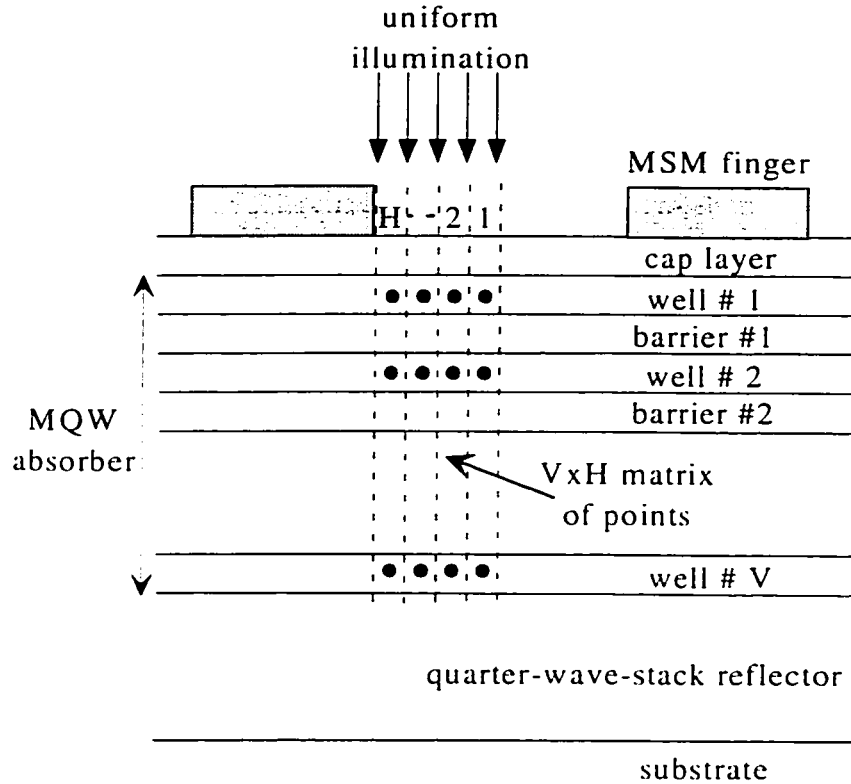


Figure A.17. Schematic illustration of the model used to estimate absorption in an MSM photodetector, with a MQW active region. The case shown is for top-illumination, with opaque metal fingers. A unit cell of the device (see Figure A.3) is divided into a two-dimensional matrix, with rows defined by the center point of each quantum well. The two-dimensional field is calculated at each point in the matrix, and the components are used to estimate the local absorption characteristics. Next, the total absorption spectra are calculated for each column of the matrix, separately, using the transfer-matrix technique described in Chapter 4. Finally, the spectra from all columns are averaged, to provide an estimate of the overall absorption spectra for the MSM detector.

A.4.1. Model for Absorption in Quantum Wells

The semi-empirical model of Chemla et al. [23] was used for absorption at the band-edge of a GaAs quantum well. An example was shown in Figure A.10. The model includes three contributions: two Gaussian curves to represent absorption by $e1-hh1$ and $e1-lh1$ excitons, and a single broadened continuum. The expression is

$$\alpha(h\nu) = \alpha_{hh} \exp\left[\frac{-(h\nu - E_{hh})^2}{2(\hbar\Gamma_{hh})^2}\right] + \alpha_{lh} \exp\left[\frac{-(h\nu - E_{lh})^2}{2(\hbar\Gamma_{lh})^2}\right] + \frac{\alpha_c}{1 + \exp\left(\frac{E_c - h\nu}{\hbar\Gamma_c}\right)} \times \frac{2}{1 + \exp\left\{-2\pi\left[\frac{|E_c - h\nu|}{R_y}\right]^{-1/2}\right\}} \quad (\text{A.18})$$

The peak absorption of the heavy-hole exciton, light-hole exciton, and continuum are α_{hh} , α_{lh} , and α_c , respectively. The linewidths (HWHM) are Γ_{hh} , Γ_{lh} , and Γ_c , respectively. The peak positions of the excitons are E_{hh} and E_{lh} , respectively. The continuum band-edge is located at E_c . The continuum absorption is enhanced by a Sommerfeld factor [15], which is the last term in (A.18). The Sommerfeld factor reflects the fact that coulomb interactions enhance absorption even above the band edge, where excitons are ionized. As a first-order approximation, the continuum contributions due to light and heavy hole sub-bands are not separated. Chemla et al. [23] were able to obtain excellent fits to experimental data, using (A.18).

The model contains nine fitting parameters. In the simulation of the MSM detector, the local electric field components were used to calculate an absorption characteristic at every point of a two-dimensional grid. As mentioned, 10 nm GaAs wells with 10 nm $\text{Al}_{0.3}\text{Ga}_{0.7}\text{As}$ barriers were assumed. Also, a typical zero-field absorption characteristic was assumed, based on experimental data in the literature. The heavy-hole and light-hole excitons were located at 1.4575 eV and 1.466 eV, respectively, and the continuum band edge at 1.4675 eV [23]. The peak absorption for the heavy-hole exciton was estimated as $2 \mu\text{m}^{-1}$ (normalized to width of well material [22]). From the ratios provided in [23], the light-hole exciton peak was estimated as $1 \mu\text{m}^{-1}$, and the continuum peak as $0.5 \mu\text{m}^{-1}$. Finally, the zero-field exciton line-widths were assumed to be 3 meV [21], and that of the continuum was assumed to be 5 meV [23]. Note that the resultant absorption characteristic is representative of a 10 nm GaAs/ $\text{Al}_{0.3}\text{Ga}_{0.7}\text{As}$ well, but the model is empirical and not based on a first-principles treatment.

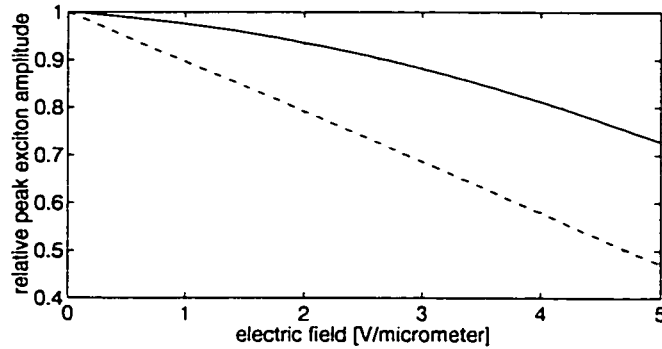


Figure A.18. The reduction in exciton peak amplitude is shown as a function of electric field perpendicular to the wells (solid line) and parallel to the wells (dashed line). The amplitude is expressed as a fraction of the zero-field peak amplitude. In the simulation, the contributions due to both field components are multiplied.

Field effects were also introduced in a semi-empirical manner. The effects were assumed to be equivalent for the heavy and light hole exciton, which is not rigorously accurate [5]. However, the devices simulated are designed to operate at or near the heavy-hole exciton, so the behavior of the light-hole exciton is of secondary importance [22]. It was assumed that parallel field components totally dominate the broadening of the exciton transitions, and the magnitude of broadening was estimated with (A.17).

Both the parallel and perpendicular fields were assumed to cause a reduction of peak exciton absorption, independently. The reductions used in the model are illustrated in Figure A.18. The curve for perpendicular fields was obtained from the experimental data of Lengyel et al. [22]. The curve for parallel fields was obtained from the fit to the data of Miller et al. [5], illustrated in Figure A.15. For two-dimensional fields, the overall reduction was assumed to be the product of the reductions for each field component. For example, for equal field components of $2 \text{ V } \mu\text{m}^{-1}$, the assumed exciton peak amplitude was approximately 76 % of the zero-field amplitude (the product of 0.8 and 0.95, see Figure A.18).

Finally, the positions of the excitons and the band edge were assumed to be a function of the perpendicular field component only [5]. The red-shifts of each exciton, and the continuum, were assumed approximately equal, and given by the data in Figure A.9. Again, this is not rigorously correct [21], but is reasonable since the heavy-hole exciton dominates the band-edge features.

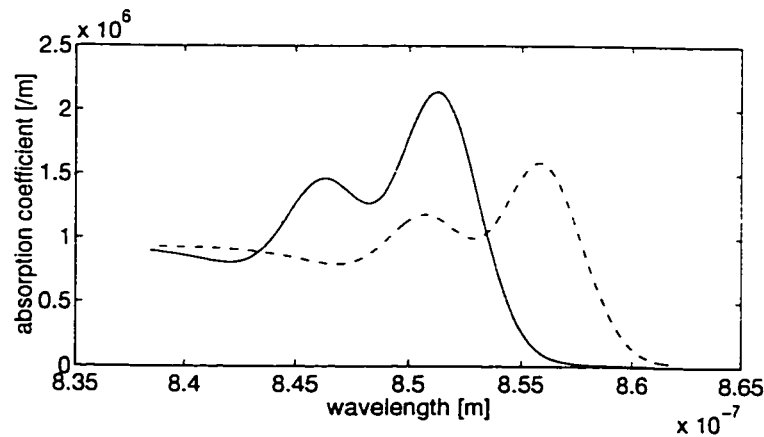


Figure A.19. Band-edge absorption features, as predicted by the semi-empirical model described in the text. The solid line is for no applied field. The dashed line is for a field of $5 \text{ V } \mu\text{m}^{-1}$, applied perpendicular to the plane of the wells. In that case, the band-edge shifts to the red. The dotted line is for field components of $5 \text{ V } \mu\text{m}^{-1}$, both perpendicular and parallel to the plane of the wells. While the band edge is red-shifted by the perpendicular field, the exciton features are broadened and obscured by the parallel field.

Figure A.19 is a plot of the modeled band-edge absorption features, for two different electric field conditions. In the first case, only a perpendicular field is present, and the absorption features exhibit the red-shift and reduction in exciton strength expected for the quantum-confined Stark effect. In the second case, a

parallel field is also present. The parallel field broadens the exciton features so that they cannot be resolved, but the entire band edge still shifts, due to the perpendicular field.

It should be noted that bulk refractive indices were used for the well and barrier layers in the simulation. This is a commonly employed simplification [26], but is not rigorously accurate [27]. The large absorption features due to band-edge excitons produce corresponding features in the refractive index near the band edge. This is expected, since the absorption coefficient and refractive index are interdependent, via the Kramers-Kronig relations. The devices proposed here are designed to operate on the long wavelength side of the e1-hh1 exciton, where the associated error is small [27]. Nevertheless, a more complete model would incorporate the changes in the refractive index due to confinement, and the electro-refractive effects of parallel and perpendicular fields.

A.4.2. Predicted Results for a Rear-Illuminated MSM Photodetector

From the discussion in Sections A.2 and A.3, it was apparent that a top-illuminated MSM detector may not be optimal in terms of exploiting the quantum-confined Stark effect. This was confirmed by simulation; the predicted results for a rear-illuminated device were superior, due to the strong vertical fields in regions beneath the MSM fingers. The simulated results for a rear-illuminated device are presented here.

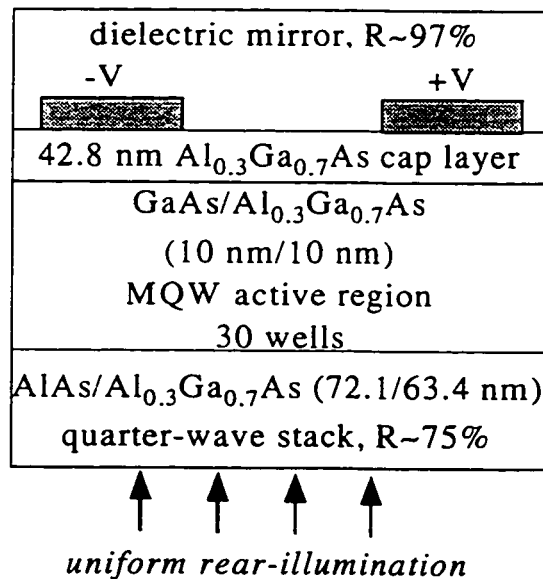


Figure A.20. MSM structure, in cross-section, used to simulate the electro-optic effects for rear-illumination. The entire structure is designed to resonate near the zero-field band edge of the quantum wells, at approximately 860 nm. The incident-side mirror is a semiconductor quarter-wave stack, with a reflectivity of approximately 75 %. The other mirror was assumed to have 97 % reflectivity, and to be constructed of a multi-layer dielectric coating. The mirror reflectivities were determined using (4.11), with the absorption coefficients modeled in Figure A.21. The MSM detector was assumed to have finger width and spacing of 1 μm .

The modeled device is shown in Figure A.20. The bulk refractive index data for GaAs and $\text{Al}_{0.3}\text{Ga}_{0.7}\text{As}$ were given in Chapter 4, and were used here. The

absorption features of the quantum wells were modeled as described in Section A.4.1. As an initial step, the absorption in the MQW active region was modeled in the absence of the mirrors. In this way, an average absorption coefficient could be determined, as a function of bias voltage. The results are shown in Figure A.21. The representative absorption coefficient was derived from the total thickness of absorbing material (30 wells, total thickness of 300 nm).

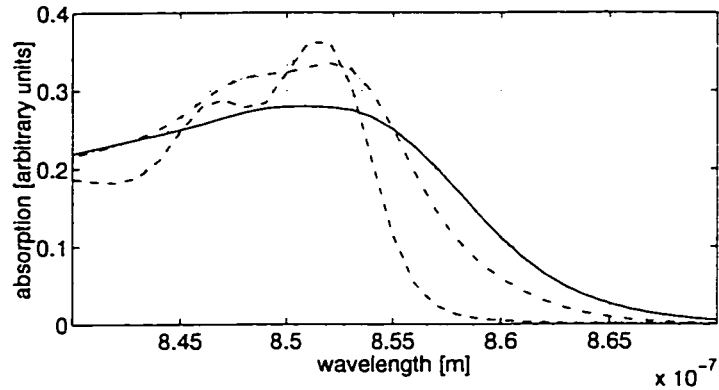


Figure A.21. The net absorption characteristics for the structure of Figure A.20, with no mirrors, as a function of bias: 2 V (dashed line), 4 V (dotted line), 6 V (dashed-dotted line), and 10 V (solid line). A representative absorption coefficient was determined from the data, using the total thickness of absorbing material (300 nm).

The criteria developed in Section A.2 were used to design the device of Figure A.20. The target operating range for the device is 2 to 10 V bias. The representative absorption at 10 V, from Figure A.21, was used in (4.11). This produced estimates for the required mirror reflectivities, such that the MQW detector would have nearly 100 % quantum efficiency at 10 V. The simulated, wavelength-dependent quantum efficiency for the device of Figure A.20 is shown in Figure A.22. Bias-dependent quantum efficiency (responsivity) is predicted for the idealized device, over a narrow wavelength band of approximately 5 nm. As an example, the quantum efficiency at a wavelength of 860 nm is plotted as a function of bias in Figure A.23.

The results indicate that it would be possible, in principle, to fabricate a device with the desired bias-dependent responsivity. Unfortunately, growth errors are likely to prohibit the implementation of such a device in the near future. As shown in Figure A.21, the required electro-absorptive effects exist over a wavelength range of only 5 to 10 nm. Thus, the resonant cavity must be centered with an error of less than 5 nm, to produce a device with predictable attributes. From the results in Chapter 4, errors in the position of the resonant cavity can routinely be as high as 10 to 20 nm. Realization of the devices proposed here will await the arrival of refined growth techniques, especially in-situ monitoring of layer thickness. The same situation holds for many of the other quantum-well-based devices proposed in the literature [8].

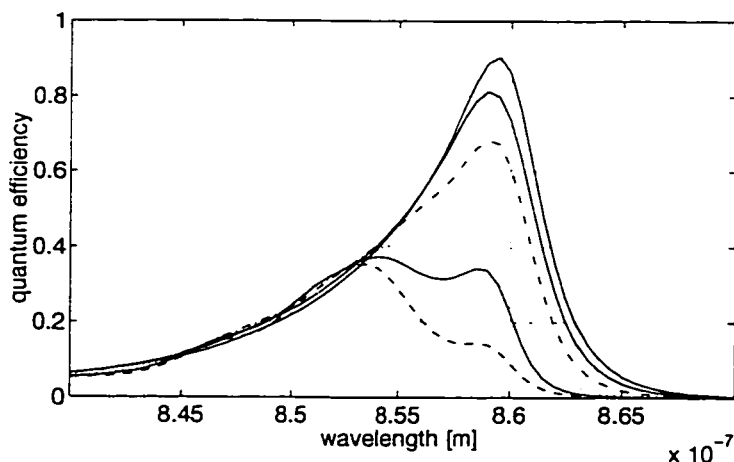


Figure A.22. The wavelength-dependent quantum efficiency, simulated for the device of Figure A.20. The data are for bias voltages of 2, 3, 4, 6, 8, and 10 V, from bottom to top. Bias-dependent quantum efficiency is predicted, over a wavelength band of approximately 5 nm.

A.4.3. Suggestions to Improve the Model

Some of the approximations used in the simulation are of a first-order nature. In particular, for electric fields in the plane of the quantum well layers, no exact theoretical treatment or reliable experimental data were available. It is known that (A.17) provides a low estimate of broadening in a real quantum well. With a better theoretical model, or good empirical data, the simulation would be refined. Similarly, the loss of oscillator strength for parallel fields (Figure A.18) was not known with great accuracy. Finally, electro-refractive effects should be included in an improved model. This becomes especially important if a high Q factor cavity is used, as suggested in the preceding section. Small changes in effective refractive index can shift the resonance peak by a few nm [11].

A.5. Summary and Conclusions

In this appendix, a novel MQW-based MSM detector was investigated theoretically. The proposed device is based on the resonant cavity techniques discussed in Chapter 4. By employing an electro-absorptive material in the cavity of the device, it was demonstrated that a bias-dependent responsivity might be achieved. This would be independent of the transport properties of the device, to fulfill the requirements for optoelectronic signal processing: bias-dependent responsivity and bias-independent bandwidth.

To model the proposed device, it was necessary to consider electro-optic effects in quantum wells, for fields both parallel and perpendicular to the plane of the layers. For parallel fields, very little experimental or theoretical data was available in the literature. A semi-empirical model was developed, to obtain a first-order approximation of the device attributes. This represents the first attempt to model a MQW-based MSM photodetector.

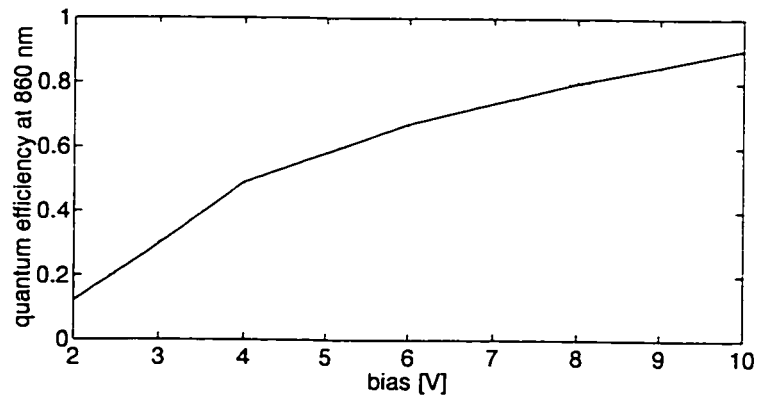


Figure A.23. Predicted quantum efficiency at 860 nm, as a function of bias, is shown. The quantum efficiency varies from 20 % to over 90 %, with increase of bias voltage from 2 to 10 V.

The simulated results confirm the intended operation of the device. Responsivity tuning was demonstrated over a 5 nm wavelength band, and for bias voltages in the 2 to 10 V range. However, it is concluded that the design is not robust enough, from a technological perspective. The reason is that growth errors less than 1% would be necessary, to align the resonance condition of the cavity with the band edge exciton features of the MQW. As demonstrated in Chapter 4, these errors are typically in the 2 to 5 % range at present. As with many other proposed MQW-based devices in the literature, practical realization awaits improved epitaxial techniques, especially in-situ layer thickness monitoring.

A.6. Appendix A References

- [1] B.E. Swekla, R.I. MacDonald, "Optoelectronic transversal filter", *Electronics Letters*, vol. 27, no. 19, pp. 1769-1770, September 1991.
- [2] R.I. MacDonald, "Optoelectronic equalisation", *IEEE Photonics Technology Letters*, vol. 6, no. 4, pp. 565-567, April 1994.
- [3] Y. Nitta, J. Ohta, M. Takahashi, S. Tai, K. Kyuma, "Optical neurochip with learning capability", *IEEE Photonics Technology Letters*, vol. 4, no. 3., pp. 247-249, March 1992.
- [4] B.E. Swekla, "An optoelectronic transversal filter", M.Sc. thesis, University of Alberta, Fall 1991.
- [5] D.A.B. Miller, "Electric field dependence of optical absorption near the band gap of quantum-well structures", *Physical Review B*, vol. 32, no. 2, pp. 1043-1060, July 1985.
- [6] A.M. Fox, "Optoelectronics in quantum well structures", *Contemporary Physics*, vol. 37, no. 2, pp. 111-125, 1996.
- [7] M. Whitehead, A. Rivers, G. Parry, "Low-voltage multiple quantum well reflection modulator with on:off ratio >100:1", *Electronics Letters*, vol. 25, no. 15, pp. 984-985, July 1989.

- [8] C.C. Barron, C.J. Mahon, B.J. Thibeault, L.A. Coldren, "Design, fabrication and characterization of high-speed asymmetric Fabry-Perot modulators for optical interconnect applications", *Optical and Quantum Electronics*, vol. 25, pp. S885-S898, 1993.
- [9] J.A. Trezza, J.S. Powell, J.S. Harris, "Zero-chirp asymmetric Fabry-Perot electroabsorption modulator using coupled quantum wells", *IEEE Photonics Technology Letters*, vol. 9, no. 3, pp. 330-332, March 1997.
- [10] T.H. Wood, C.A. Burrus, A.H. Gnauck, J.M. Wiesenfeld, D.A.B. Miller, D.S. Chemla, T.C. Damen, "Wavelength-selective voltage-tunable photodetector made from multiple quantum wells", *Applied Physics Letters*, vol. 47, no. 3, pp. 190-192, August 1985.
- [11] K. Lai, J.C. Campbell, "Design of a tunable GaAs/AlGaAs multiple-quantum-well resonant-cavity photodetector", *IEEE Journal of Quantum Electronics*, vol. 30, no. 1, pp. 108-114, January 1994.
- [12] J. Waclawek, J. Kovac, R. Rheinlander, V. Gottschalch, J. Skriniarova, "Electrically tunable GaAs/AlGaAs MQW RCE photodetector", *Electronics Letters*, vol. 33, no. 1, pp. 71-72, January 1997.
- [13] D.M. Gvozdic, J.B. Radunovic, J.M. Elazar, "An analytical expression for the electric field in MSM structures", *International Journal of Infrared and Millimeter Waves*, vol. 14, no. 7, pp. 1485-1493, 1993.
- [14] Y.C. Lim, R.A. Moore, "Properties of alternately charged coplanar parallel strips by conformal mappings", *IEEE Transactions on Electron Devices*, vol. ED-15, no. 3, pp. 173-180, March 1968.
- [15] C. Weisbuch, B. Vinter, *Quantum Semiconductor Structures, Fundamentals and Applications*, Academic Press, inc., Boston, 1991.
- [16] J.E. Geusic, R.L. Hartman, U. Koren, W. Tsang, D.P. Wilt, "Quantum well lasers in telecommunications", *AT&T Technical Journal*, pp. 75-83, January/February 1992.
- [17] L. Esaki, R. Tsu, "Superlattice and negative differential conductivity in semiconductors", *IBM Journal of Research and Development*, vol. 14, pp. 61-65, 1970.
- [18] R. Dingle, W. Wiegmann, C.H. Henry, "Quantum states of confined carriers in very thin $\text{Al}_x\text{Ga}_{1-x}\text{As-GaAs-Al}_x\text{Ga}_{1-x}\text{As}$ heterostructures", *Physical Review Letters*, vol. 33, pp. 827-830, 1974.
- [19] G. Bastard, J.A. Brum, R. Ferreira, "Electronic states in semiconductor heterostructures", *Solid State Physics*, vol. 44, H. Ehrenreich, D. Turnbull, eds., Academic Press, inc., Boston, 1991, pp. 229-415.
- [20] B.H. Bransden, C.J. Joachain, *Introduction to Quantum Mechanics*, Longman Scientific and Technical, London, 1989.

- [21] P.J. Stevens, M. Whitehead, G. Parry, K. Woodbridge, "Computer modeling of the electric field dependent absorption spectrum of multiple quantum well material", *IEEE Journal of Quantum Electronics*, vol. 24, no. 10, pp. 2007-2015, October 1988.
- [22] G. Lengyel, K.W. Jelley, R.W.H. Engelmann, "A semi-empirical model for electroabsorption in GaAs/AlGaAs multiple quantum well modulator structures", *IEEE Journal of Quantum Electronics*, vol. 26, no. 2, pp. 296-304, February 1990.
- [23] D.S. Chemla, D.A.B. Miller, P.W. Smith, A.C. Gossard, W. Wiegmann, "Room temperature excitonic nonlinear absorption and refraction in GaAs/AlGaAs multiple quantum well structures", *IEEE Journal of Quantum Electronics*, vol. QE-20, no. 3, pp. 265-275, March 1984.
- [24] A.S. Harwit, J.S. Harris, A. Kapitulnik, "Calculated quasi-eigenstates and quasi-eigenenergies of quantum well superlattices in an applied electric field", *Journal of Applied Physics*, vol. 60, no. 9, pp. 3211-3213, November 1986.
- [25] F.L. Lederman, J.D. Dow, "Theory of electroabsorption by anisotropic and layered semiconductors. I. Two-dimensional excitons in a uniform electric field", *Physical Review B*, vol. 13, no. 4, pp. 1633-1642, February 1976.
- [26] G. Livescu, G.D. Boyd, R.A. Morgan, L.M.F. Chirovsky, A.M. Fox, R.E. Leibenguth, M.T. Asom, M.W. Focht, "Role of electrorefraction in quantum-well Fabry-Perot modulators", *Applied Physics Letters*, vol. 60, no. 12, pp. 1418-1420, March 1992.
- [27] C.H. Lin, J.M. Meese, M.L. Wroge, C. Weng, "Effect of GaAs/AlGaAs quantum-well structure on refractive index", *IEEE Photonics Technology Letters*, vol. 6, no. 5, pp. 623-625, May 1994.

Appendix B: Matlab File for Calculating Optical Spectra of a Multi-Layer Semiconductor (InGaP/GaAs)

```

% Input vector of wavelengths. L
    Q=length(L)
%
% Calculate complex refractive index of each layer, at wavelength L(q)
    for q=1:Q
        % Calculate complex refractive index of heavily-doped. n-GaAs
        if L(q)<0.776E-6
            Nd2=(6.9611*(L(q)*1E6)^2-10.894*L(q)*1E6+7.9806)-i*(-
                31.8142*(L(q)*1E6)^3+75.4748*(L(q)*1E6)^2-59.9903*L(q)*1E6+16.0606);
        elseif L(q)<0.801E-6
            Nd2=(6.9611*(L(q)*1E6)^2-10.894*L(q)*1E6+7.9806)-i*(25.1831*(L(q)*1E6)^2-
                42.1553*L(q)*1E6+17.6436);
        elseif L(q)<0.838E-6
            Nd2=(152.4498*(L(q)*1E6)^3-392.6891*(L(q)*1E6)^2+335.1451*L(q)*1E6-91.1281)-
                i*(25.1831*(L(q)*1E6)^2-42.1553*L(q)*1E6+17.6436);
        else
            Nd2=(152.4498*(L(q)*1E6)^3-392.6891*(L(q)*1E6)^2+335.1451*L(q)*1E6-91.1281)-
                i*(-20.8991*(L(q)*1E6)^3+55.5457*(L(q)*1E6)^2-49.2119*(L(q)*1E6+14.53415);
        End
        % Calculate complex refractive index of intrinsic InGaP
        ncap=-37.8622*(L(q)*1E6)^3+95.5550*(L(q)*1E6)^2-81.0006*L(q)*1E6+26.3607;
        % Calculate complex refractive index of intrinsic GaAs
        if L(q)<0.827E-6
            Nabs=(-0.8566*(L(q)*1E6)^2+0.2609*L(q)*1E6+4.0108)-i*(-
                31.8142*(L(q)*1E6)^3+75.4748*(L(q)*1E6)^2-59.9903*L(q)*1E6+16.0606);
        elseif L(q)<0.862E-6
            Nabs=(16.8335*(L(q)*1E6)^2-28.5547*L(q)*1E6+15.7430)-i*(-
                31.8142*(L(q)*1E6)^3+75.4748*(L(q)*1E6)^2-59.9903*L(q)*1E6+16.0606);
        elseif L(q)<0.868E-6
            Nabs=(16.8335*(L(q)*1E6)^2-28.5547*L(q)*1E6+15.7430)-i*(0.5*L(q)*1E6-0.378);
        elseif L(q)<0.874E-6
            Nabs=(16.8335*(L(q)*1E6)^2-28.5547*L(q)*1E6+15.7430)-i*(97.2222*(L(q)*1E6)^2-
                174.3611*L(q)*1E6+78.1519);
        elseif L(q)<0.880E-6
            Nabs=(45.1083*(L(q)*1E6)^2-82.1970*L(q)*1E6+41.0290)-i*(97.2222*(L(q)*1E6)^2-
                174.3611*L(q)*1E6+78.1519);
        else
            Nabs=(45.1083*(L(q)*1E6)^2-82.1970*L(q)*1E6+41.0290)-i*(0.003*exp((0.88-
                L(q)*1E6)/0.005));
        end
        if imag(Nabs)>0
            Nabs=real(Nabs);
        end
        if imag(Nd2)>0
            Nd2=real(Nd2);
        end
        nd11=ncap;
        % Calculate refractive index of doped InGaP
        nd1=ncap-delnd1;
        Nsub=Nabs;
    %

```



```

% Calculate the propagation angles in each layer, for incident angle thetai
thetac=asin(sin(thetai)/ncap);
thetaabs=asin(sin(thetac)*ncap/real(Nabs));
thetad11=asin(sin(thetaabs)*real(Nabs)/nd11);
thetad2=asin(sin(thetad11)*nd11/real(Nd2));
thetad1=asin(sin(thetad2)*real(Nd2)/nd1);
thetas=asin(sin(thetad1)*nd1/real(Nsub));

%
% Calculate the transfer matrices for each layer, for polarization perpendicular to the plane of
incidence
md11pe=[cos(2*pi*nd11*td11*cos(thetad11)/L(q))
(sin(2*pi*nd11*td11*cos(thetad11)/L(q))/(nd11*cos(thetad11)))*i;
nd11*cos(thetad11)*sin(2*pi*nd11*td11*cos(thetad11)/L(q))*i
cos(2*pi*nd11*td11*cos(thetad11)/L(q))];
md1pe=[cos(2*pi*nd1*td1*cos(thetad1)/L(q))
(sin(2*pi*nd1*td1*cos(thetad1)/L(q))/(nd1*cos(thetad1)))*i;
nd1*cos(thetad1)*sin(2*pi*nd1*td1*cos(thetad1)/L(q))*i
cos(2*pi*nd1*td1*cos(thetad1)/L(q))];
md2pe=[cos(2*pi*Nd2*td2*cos(thetad2)/L(q))
(sin(2*pi*Nd2*td2*cos(thetad2)/L(q))/(Nd2*cos(thetad2)))*i;
Nd2*cos(thetad2)*sin(2*pi*Nd2*td2*cos(thetad2)/L(q))*i
cos(2*pi*Nd2*td2*cos(thetad2)/L(q))];
mabspe=[cos(2*pi*Nabs*tabs*cos(thetaabs)/L(q))
(sin(2*pi*Nabs*tabs*cos(thetaabs)/L(q))/(Nabs*cos(thetaabs)))*i;
Nabs*cos(thetaabs)*sin(2*pi*Nabs*tabs*cos(thetaabs)/L(q))*i
cos(2*pi*Nabs*tabs*cos(thetaabs)/L(q))];
mcappe=[cos(2*pi*ncap*tcap*cos(thetac)/L(q))
(sin(2*pi*ncap*tcap*cos(thetac)/L(q))/(ncap*cos(thetac)))*i;
ncap*cos(thetac)*sin(2*pi*ncap*tcap*cos(thetac)/L(q))*i
cos(2*pi*ncap*tcap*cos(thetac)/L(q))];
% Calculate the total transfer matrix for the system layers
Mtotpe=mcappe*mabspe*md11pe*(md2pe*md1pe)^z;
% Calculate the transfer matrix for the mirror layers only
Mmpe=md11pe*(md2pe*md1pe)^z;
% Calculate the transfer matrix for the non-mirror layers
Mtoppe=mcappe*mabspe;
%
% Calculate the reflection coefficient for the entire layer structure
rpe=(cos(thetai)*Mtotpe(1,1)+Nsub*cos(thetas)*cos(thetai)*Mtotpe(1,2)-Mtotpe(2,1)-
Nsub*cos(thetas)*Mtotpe(2,2))/(cos(thetai)*Mtotpe(1,1)+Nsub*cos(thetai)*cos(thetas)*Mtotp
e(1,2)+Mtotpe(2,1)+Nsub*cos(thetas)*Mtotpe(2,2));
% Calculate the reflection coefficient for the embedded mirror
rmpe=(Nabs*cos(thetaabs)*Mmpe(1,1)+Nabs*Nsub*cos(thetaabs)*cos(thetas)*Mmpe(1,2)-
Mmpe(2,1)-
Nsub*cos(thetas)*Mmpe(2,2))/(Nabs*cos(thetaabs)*Mmpe(1,1)+Nabs*Nsub*cos(thetaabs)*c
os(thetas)*Mmpe(1,2)+Mmpe(2,1)+Nsub*cos(thetas)*Mmpe(2,2));
% Calculate the transmission coefficient for the entire layer structure
tpe=2*cos(thetai)/(cos(thetai)*Mtotpe(1,1)+Nsub*cos(thetai)*cos(thetas)*Mtotpe(1,2)+Mtotpe
(2,1)+Nsub*cos(thetas)*Mtotpe(2,2));
% Calculate the transmission coefficient for the embedded mirror
tmpe=2*Nabs*cos(thetas)/(Nabs*cos(thetaabs)*Mmpe(1,1)+Nabs*Nsub*cos(thetaabs)*cos(th
etas)*Mmpe(1,2)+Mmpe(2,1)+Nsub*cos(thetas)*Mmpe(2,2));
% Calculate the transmission coefficient for the non-mirror layers
ttoppe=(1+rpe)/(Mtoppe(1,1)*(1+rmpe)+Mtoppe(1,2)*Nabs*(1-rmpe));
ttop2pe=(1-rpe)/(Mtoppe(2,1)*(1+rmpe)+Mtoppe(2,2)*Nabs*(1-rmpe));
%

```

```

% Calculate the percentage of incident power transmitted into the embedded mirror
  Ttoppe(q)=ttoppe*conj(ttoppe)*abs(Nabs);
% Calculate the percentage of incident power reflected at the top surface
  Rpe(q)=rpe*conj(rpe);
% Calculate the percentage of incident power transmitted into the substrate
  Tpe(q)=tpe*conj(tpe)*abs(Nsub*cos(thetas));
% Calculate the percentage of power reflected from and transmitted through the mirror
  Rmpe(q)=rmpe*conj(rmpe);
  Tmpe(q)=tmpe*conj(tmpe);
% Calculate the power absorbed in the entire structure, in the absorption region, and in the mirror
  Ape(q)=abs(1-Rpe(q)-Tpe(q));
  Ampe(q)=Ttoppe(q)*abs(1-Rmpe(q)-Tmpe(q));
  Aape(q)=abs(Ape(q)-Ampe(q));
%
% Calculate the transfer matrices for each layer, for polarization parallel to the plane of incidence
md1lpa=[cos(2*pi*nd1l*td1l*cos(thetad1l)/L(q))
(sin(2*pi*nd1l*td1l*cos(thetad1l)/L(q))*cos(thetad1l)/nd1l)*i;
nd1l*sin(2*pi*nd1l*td1l*cos(thetad1l)/L(q))*i/cos(thetad1l)
cos(2*pi*nd1l*td1l*cos(thetad1l)/L(q))];
mdlpa=[cos(2*pi*nd1*td1*cos(thetad1)/L(q))
(sin(2*pi*nd1*td1*cos(thetad1)/L(q))*cos(thetad1)/nd1)*i;
nd1*sin(2*pi*nd1*td1*cos(thetad1)/L(q))*i/cos(thetad1)
cos(2*pi*nd1*td1*cos(thetad1)/L(q))];
md2pa=[cos(2*pi*Nd2*td2*cos(thetad2)/L(q))
(sin(2*pi*Nd2*td2*cos(thetad2)/L(q))*cos(thetad2)/Nd2)*i;
Nd2*sin(2*pi*Nd2*td2*cos(thetad2)/L(q))*i/cos(thetad2)
cos(2*pi*Nd2*td2*cos(thetad2)/L(q))];
mabspa=[cos(2*pi*Nabs*tabs*cos(thetaabs)/L(q))
(sin(2*pi*Nabs*tabs*cos(thetaabs)/L(q))*cos(thetaabs)/Nabs)*i;
Nabs*sin(2*pi*Nabs*tabs*cos(thetaabs)/L(q))*i/cos(thetaabs)
cos(2*pi*Nabs*tabs*cos(thetaabs)/L(q))];
mcappa=[cos(2*pi*ncap*tcap*cos(thetac)/L(q))
(sin(2*pi*ncap*tcap*cos(thetac)/L(q))*cos(thetac)/ncap)*i;
ncap*sin(2*pi*ncap*tcap*cos(thetac)/L(q))*i/cos(thetac)
cos(2*pi*ncap*tcap*cos(thetac)/L(q))];
% Calculate the total transfer matrix for the system layers
Mtoppa=mcappa*mabspa*md1lpa*(md2pa*mdlpa)^z;
% Calculate the transfer matrix for the mirror layers only
Mmpa=md1lpa*(md2pa*mdlpa)^z;
% Calculate the transfer matrix for the non-mirror layers
Mtoppa=mcappa*mabspa;
%
% Calculate the reflection coefficient for the entire layer structure
rpa=(Mtotpa(1,1)/cos(thetai)+Nsub*Mtotpa(1,2)/(cos(thetai)*cos(thetas))-Mtotpa(2,1)-
Nsub*Mtotpa(2,2)/cos(thetas))/(Mtotpa(1,1)/cos(thetai)+Nsub*Mtotpa(1,2)/(cos(thetai)*cos(thetas))+Mtotpa(2,1)+Nsub*Mtotpa(2,2)/cos(thetas));
% Calculate the reflection coefficient for the embedded mirror
rmpa=(Nabs*Mmpa(1,1)/cos(thetaabs)+Nabs*Nsub*Mmpa(1,2)/(cos(thetaabs)*cos(thetas))-Mmpe(2,1)-
Nabs*Mmpa(2,2)/cos(thetas))/(Nabs*Mmpa(1,1)/cos(thetaabs)+Nabs*Nsub*Mmpa(1,2)/(cos(thetaabs)*cos(thetas))+Mmpe(2,1)+Nsub*Mmpa(2,2)/cos(thetas));
% Calculate the transmission coefficient for the entire layer structure
tpa=(2/cos(thetai))/(Mtotpa(1,1)/cos(thetai)+Nsub*Mtotpa(1,2)/(cos(thetai)*cos(thetas))+Mtotpa(2,1)+Nsub*Mtotpa(2,2)/cos(thetas));
% Calculate the transmission coefficient for the embedded mirror

```

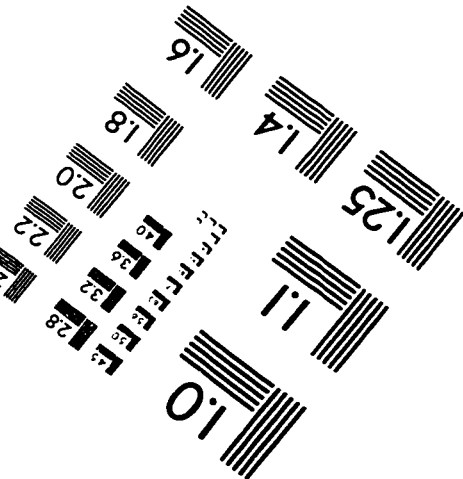
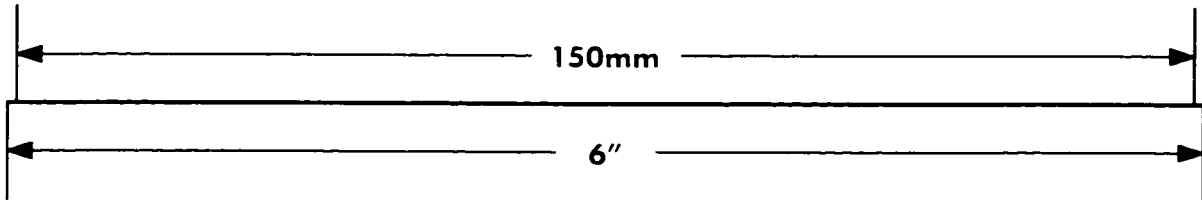
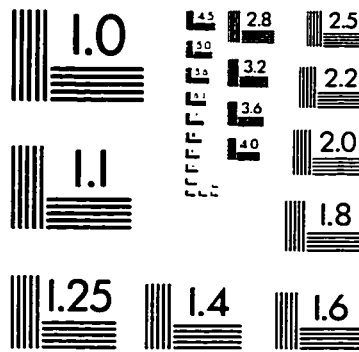
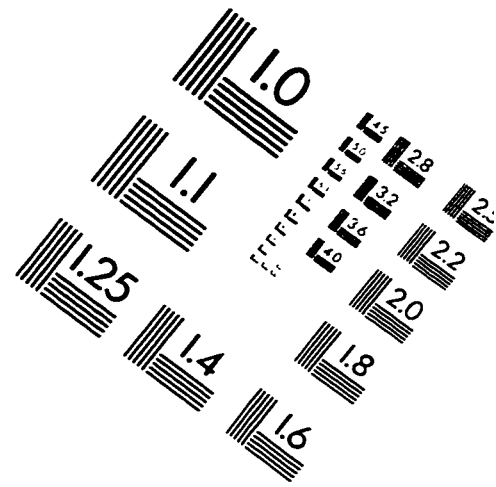
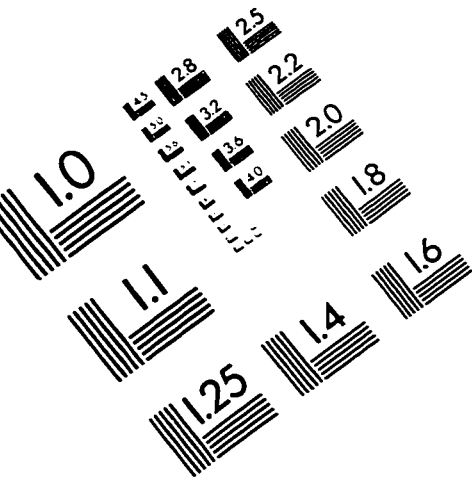
```

    tmpa=(2*Nabs/cos(thetaabs))/(Nabs*Mmpa(1,1)/cos(thetaabs)+Nabs*Nsub*Mmpa(1,2)/(cos(thetaabs)*cos(thetas))+Mmpa(2,1)+Nsub*Mmpa(2,2)/cos(thetas));
%
% Calculate the transmission coefficient for the non-mirror layers
    toppa=(1+rpa)/(Mtoppa(1,1)*(1+rmpa)+Mtoppa(1,2)*Nabs*(1-rmpa));
    top2pa=(1-rpa)/(Mtoppa(2,1)*(1+rmpa)+Mtoppa(2,2)*Nabs*(1-rmpa));
%
% Calculate the percentage of incident power transmitted into the embedded mirror
    Ttoppa(q)=toppa*conj(toppa)*abs(Nabs);
% Calculate the percentage of incident power reflected at the top surface
    Rpa(q)=rpa*conj(rpa);
% Calculate the percentage of incident power transmitted into the substrate
    Tpa(q)=tpa*conj(tpa)*abs(Nsub/cos(thetas));
% Calculate the percentage of power reflected from and transmitted through the mirror
    Rmpa(q)=rmpa*conj(rmpa);
    Tmpa(q)=tmpa*conj(tmpa);
% Calculate the power absorbed in the entire structure, in the absorption region, and in the mirror
    Apa(q)=abs(1-Rpa(q)-Tpa(q));
    Ampa(q)=Ttoppa(q)*abs(1-Rmpa(q)-Tmpa(q));
    Aapa(q)=abs(Apa(q)-Ampa(q));
%
% Average the spectra for parallel and perpendicular polarization
    A(q)=0.5*(Apa(q)+Ape(q));
    T(q)=0.5*(Tpe(q)+Tpa(q));
    R(q)=0.5*(Rpe(q)+Rpa(q));
End

plot(L,A,'r-',L,T,'b-',L,R,'g-')

```

IMAGE EVALUATION TEST TARGET (QA-3)



APPLIED IMAGE, Inc
1653 East Main Street
Rochester, NY 14609 USA
Phone: 716/482-0300
Fax: 716/288-5989

© 1993, Applied Image, Inc., All Rights Reserved

